SOILS and ROCKS

An International Journal of Geotechnical and Geoenvironmental Engineering

Soils and Rocks publishes papers in English in the broad fields of Geotechnical Engineering, Engineering Geology, and Geoenvironmental Engineering. The Journal is published quarterly in March, June, September and December. The first issue was released in 1978, under the name *Solos e Rochas*, being originally published by the Graduate School of Engineering of the Federal University of Rio de Janeiro. In 1980, the Brazilian Association for Soil Mechanics and Geotechnical Engineering took over the editorial and publishing responsibilities of *Solos e Rochas*, increasing its reach. In 2007, the journal was renamed Soils and Rocks and acquired the status of an international journal, being published jointly by the Brazilian Association for Soil Mechanics and Geotechnical Engineering, by the Portuguese Geotechnical Society, and until 2010 by the Brazilian Association for Engineering Geology and the Environment.

Soils and Rocks

1978,	1 (1, 2)
1979,	1 (3), 2 (1,2)
1980-1983,	3-6 (1, 2, 3)
1984,	7 (single number)
1985-1987,	8-10 (1, 2, 3)
1988-1990,	11-13 (single number)
1991-1992,	14-15 (1, 2)
1993,	16 (1, 2, 3, 4)
1994-2010,	17-33 (1, 2, 3)
2011,	34 (1, 2, 3, 4)
2012-2019,	35-42 (1, 2, 3)
2020,	43 (1, 2, 3, 4)
2021,	44 (1, 2, 3, 4)
2022,	45 (1, 2, 3, 4)

ISSN 1980-9743
ISSN-e 2675-5475 CDU 624.131.1

Soils and Rocks
An International Journal of Geotechnical and Geoenvironmental Engineering
ISSN 1980-9743 ISSN-e 2675-5475

Publication of
ABMS - Brazilian Association for Soil Mechanics and Geotechnical Engineering
SPG - Portuguese Geotechnical Society
Volume 45, N. 4, October-December 2022

Table of Contents

ARTICLES

Soils and Rocks
An International Journal of Geotechnical and Geoenvironmental Engineering
www.soilsandrocks.com
ISSN 1980-9743
ISSN-e 2675-5475

Performance evaluation of rigid inclusions for settlement control of grain silos in tropical soils

Juan Félix Rodríguez Rebolledo[1], Isabelle Moreira Santiago[1],
Heitor Cardoso Bernardes[1#], Thiago Augusto Mendes[2]

Article

Keywords
Grain silos
Rigid inclusions
Serviceability limit-state
3D numerical modeling
Finite element method
Tropical soils

Abstract

This study presents the evaluation of the performance of grain silos reinforced by rigid inclusions in soils of the Central-West region of Brazil, during its construction and operation. Therefore, a group of eight silos with 32.4 m in diameter, 30 m in height, and 12,000 t of storage capacity (each silo) was numerically analyzed using the three-dimensional Finite Element Method (FEM, Plaxis 3D). The stratigraphy of the Experimental Field of the University of Brasilia, Brazil (CEGUnB) was considered in the analysis. The performance of using a system of rigid inclusions to reinforce the soil beneath the raft was compared with the behavior of an isolated raft. Two models were developed: in the first one, an independent silo was considered, its behavior was analyzed during its construction and operation stages by varying the length of the inclusions; in the second model, the group of eight silos was considered and their behavior was studied for different combinations of loading. The rigid inclusions system proved to be an efficient foundation solution that allows controlling total and differential displacements during the construction and serviceability stages of the silo, helping to prevent the formation of cracks in the structural elements and grain contamination by the excessive opening of the raft-perimeter beam structural joint.

1. Introduction

Agriculture is one of Brazil's main economic drivers, and thus it is subject to constant infrastructure investments in the production, storage and distribution of grains throughout the country. In recent decades, the storage of grains has received special attention, with the increase in the construction of silos along the Central-West region of the country, which is responsible of around 50% of Brazil's total grain production (CONAB, 2022).

However, the combination of inadequate foundation design and difficult soil conditions is one of the main causes of pathologies in grain silos (Dogangun et al., 2009). Cylindrical metallic silos are common in Brazil. In this type of silo, the metallic superstructure is supported by a perimeter ring beam and a raft foundation placed directly on the ground (disconnected from the beam). Commonly, end-bearing piles are added to the ring beam and the central tunnel (used for the silo emptying), which leaves the soil beneath the raft without any type of reinforcement.

Large areas of the Brazilian Central-West region are covered by a detritus-laterite soil mantle from the Tertiary-Quaternary age called "porous clay". This superficial clay layer presents a porous and highly unstable structure, with high void ratio and low shear strength. Therefore, the most common pathologies observed in these conditions are related to the Serviceability Limit State (SLS), i.e., the development of total and differential settlements of the raft foundation and the opening of the structural joint between the raft and the perimeter beam. These displacements cause cracks in the structural elements, the contamination and wetting of the stored grain, and malfunction of the conveyor belts installed in the central tunnel, which are used for emptying the silo (Conciani, 2016), as shown by Bernardes et al. (2021) and in Figure 1.

Therefore, techniques to improve the foundation system are needed to ensure the proper functioning of the silos (Souza Filho, 2018). In this paper, the use of rigid inclusions technique is proposed and evaluated as a solution to control the total and differential settlements in silo foundations.

In addition to its common use as a foundation solution for road and railway embankments, due to its good performance (Briançon et al., 2015) and low cost compared to other solutions (Rodríguez-Rebolledo & Auvinet, 2006), rigid inclusions have been used more frequently as a deep foundation system for different types of structures, such as buildings (Combarieu,

#Corresponding author. E-mail address: heitor.bernardes@ifgoiano.edu.br
[1]Universidade de Brasília, Programa de Pós-graduação em Geotecnia, Brasília, DF, Brasil.
[2]Instituto Federal de Goiás, Departamento de Áreas Acadêmicas, Aparecida de Goiânia, GO, Brasil.

Submitted on May 5, 2022; Final Acceptance on August 1, 2022; Discussion open until Feb 28, 2023.
https://doi.org/10.28927/SR.2022.004822

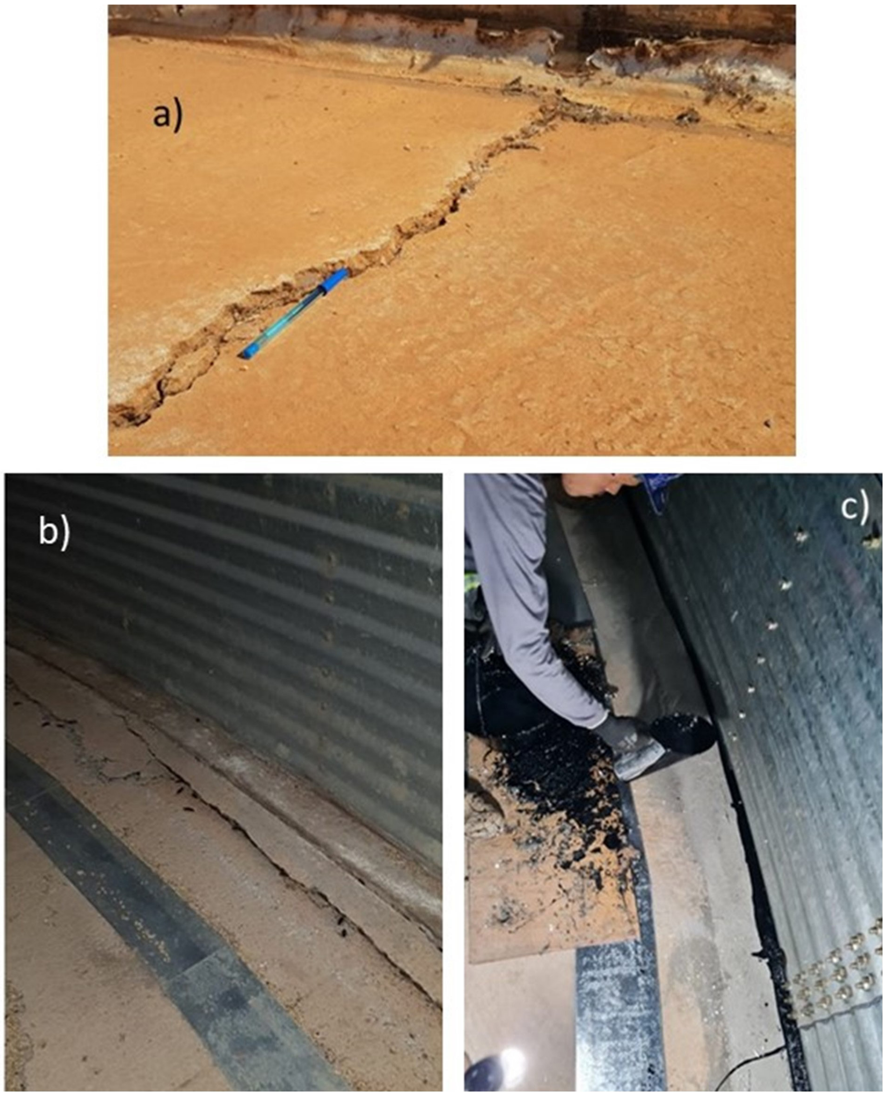

Figure 1. (a) Crack in the raft foundation; (b) structural joint opening between the raft and the beam ring; (c) sealing of the joint after opening.

1990; Santoyo & Ovando, 2006; Rodríguez-Rebolledo & Auvinet, 2006; Briançon et al., 2015), bridges (Pecker, 2004), and storage tanks (Bernuy et al., 2018).

This article presents the evaluation of the performance of grain silos reinforced by rigid inclusions in soils characteristic of the Central-West region of Brazil, during its construction and operational stages, using three-dimensional numerical modeling. A silo of 32.4 m in diameter, 30 m in height, and 12,000 t of storage capacity was analyzed. The stratigraphy of the Experimental Field of the University of Brasilia, Brazil (CEGUnB) was considered.

Two alternatives of foundations to the silo base slab, which receives the grain load, were analyzed and compared: an isolated raft, and a raft over a soil reinforced by a system of rigid inclusions. In both alternatives, the foundation of the perimeter ring beam and the central tunnel were kept the same, composed by conventional pile groups.

Two models were developed: in the first one, an independent silo was considered, its behavior was analyzed during its filling and emptying, by varying the length of the inclusions. In the second model, a group of eight silos was considered and their behavior was studied for different combinations of filling and emptying.

2. Model geometry and dimensions

The case selected for this investigation comprises a group of eight grain silos built in 2014, in São Félix do Araguaia, in the state of Mato Grosso, Brazil (Site 1 in Figure 2). According to Bernardes et al. (2021), after the first cycle of loading and unloading of the silos (only two silos were used in this period), several cracks and excessive settlement were observed at the silo's raft foundation.

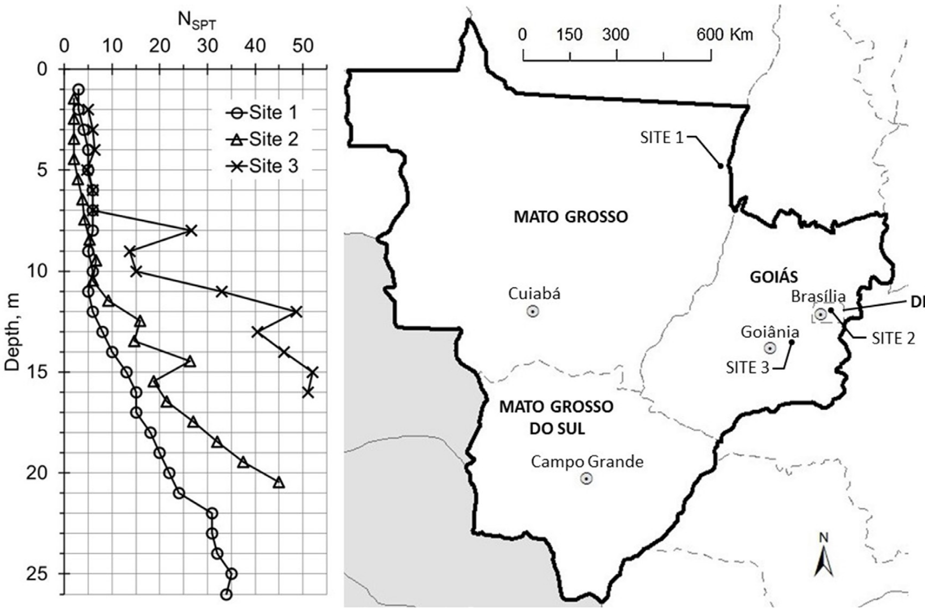

Figure 2. Standard penetration test results for different sites of silos projects within the Central-West region.

The wall and roof of each silo are made of a steel structure directly connected to a perimeter beam. Most of the grain weight is supported directly by a central raft, structurally disconnected from the perimeter beam and resting on an embankment of approximately 1.2 m thick (Figure 3). The raft is connected to a central tunnel and to eight aeration ducts, which provide a significant increase in the raft flexural stiffness. The foundation consists of continuous flight auger piles with 0.35 m in diameter and 20 m in length, disposed under the perimeter beam and the central tunnel, as shown previously in Bernardes et al. (2021).

The soil profile of the CEGUnB (Site 2 in Figure 2) was utilized in the analysis due to the stratigraphic conditions similar to the cases of silos with pathologies found in the Brazilian Central-West region (Sites 1 and 3 in Figure 2). Also, the large number of field and laboratory tests for the physical and mechanical characterization of the different soils of the CEGUnB contributed to a proper calibration of the soil constitutive model used in the numerical analysis considered herein (Perez, 1997; Jardim, 1998; Sales, 2000; Guimarães, 2002; Mota, 2003; Coelho, 2013; Sales et al., 2015).

Based on this information and the stratigraphic profiles proposed by Cruz (1987) and Cardoso (2002), Rodríguez-Rebolledo et al. (2019a) defined the soil profile of the CEGUnB. Superficially, an 8.5 m thick layer of detritus-lateritic soil composed mainly of red-yellow latosols. High degrees of weathering and leaching were responsible for the formation of this soil, which led to the development of a very porous, metastable aggregate structure with a large void ratio and, consequently, low density, called "porous clay" by local geotechnicians. Due to its high porosity and cementitious bond type, it has a highly unstable structure when subjected to increased moisture and/or changes in the stress state, which often lead to soil collapse. The end of the porous clay layer is identified in percussion drillings by the increase of N_{SPT} values from 8.5 to 10 m depth (transition layer), followed by the underlying saprolite soil.

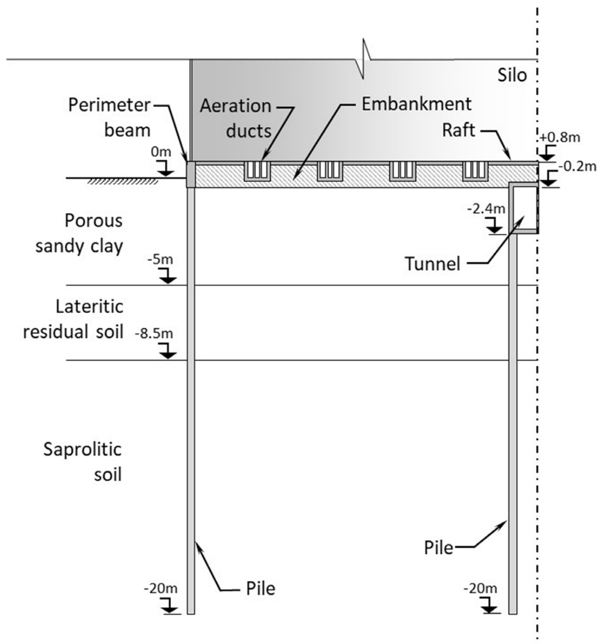

Figure 3. Original design of the silo's foundation.

3. Serviceability limit states

The Brazilian standard for foundations (ABNT, 2019) establishes that the serviceability limit value for a given deformation is the one corresponding to any condition that compromises the proper performance of the structure, e.g., unacceptable cracks. The standard does not establish limit values, but it does establish the criteria that must be considered for its definition. There is not much experience in the technical and scientific literature related to the behavior of grain silos that would help us to define a value for the SLS, however, as is shown in the following, it is possible to find information on similar structures, such as the case of storage tanks, built on other difficult soils conditions, such as loose sands or soft clays.

The standard for steel tanks for oil storage (ABNT, 1983), mentions that foundations must be designed to avoid differential settlements that can cause distortions in the tank structure. Also, the design must minimize the total settlement, so that the bottom of the tank remains above the ground after its loading, and the pipelines connected to the tank are not subjected to high additional forces caused by the tank settlement.

Becker & Lo (1979) present the results of a research program on the foundation behavior of five tower silos on clay deposits in Southwestern Ontario, Canada. After the first loading cycle, one of the instrumented silos developed a maximum settlement at the ring foundation of about 78 mm, and at the center of the silo equal to 89 mm. From the performance survey of four other silos, the maximum settlement of the ring foundation varies from 30 to 109 mm. The authors conclude that the silos presented satisfactory performance concerning total and differential settlement, and tilting.

Based upon 31 case histories of tanks settlement and damage, D'Orazio & Duncan (1987) concluded that the allowable angular distortion (the slope between two adjacent points or columns) of steel tanks on compressible soils depends mainly on the shape of the settlement profile, which is critical in cases were the maximum settlement occur off-center.

Bernuy et al. (2018) consider a maximum allowable angular distortion of 1/300 for the foundation design of large diameter (96 m) liquefied natural gas tanks, which foundation was reinforced by rigid inclusions. The authors assessed the tank settlements under various load cases, which were equal to 50 mm for the empty case, 150 mm for the full tank, and 110 mm after the tank unloading.

The Indian standard (IS, 1986) for the design and construction of foundations, indicates allowable values of maximum and differential settlements for silos with shallow foundations, on sand, hard clay, or plastic clay. For raft foundations on sand or hard clay layer, 100 mm maximum settlement and 1/400 angular distortion are allowed, and on plastic clay layer, the limit values are 125 mm of maximum settlement and 1/400 of angular distortion.

Bahar et al. (2013) present the settlement observations of a cylindrical steel tank and ten steel silos founded on a reconstituted and compacted granular fill, in Algeria. The authors concluded that the problems related to cracks and tilting in the monitored structures started from an angular distortion equal to 1/400.

Santrač et al. (2015) show the results of the measured and calculated settlements for a 17.7 m high silo, founded on a reinforced concrete slab, and subjected to a contact pressure of 190 kPa. The silo was constructed in Serbia, in a highly porous unsaturated layer of loess, which may exhibit collapse due to saturation. The total predicted settlement (initial compression, consolidation, and partial collapse) was equal to 183 mm, which is greater than the limit value established by the Serbia Technical Code (equal to 100 mm for the specified case). However, the settlements were uniform, not presenting potential damage to the silo's structure.

The literature review presented suggests that the maximum vertical settlement in silos and tanks remains between 89 and 183 mm, and the maximum angular distortion between 1/400 and 1/300. Therefore, this paper adopted the serviceability limit values of 150 mm and 1/400, for vertical settlement and angular distortion, respectively.

4. Numerical modeling description

Numerical modeling was developed using the Plaxis 3D software. The analysis was divided in two main parts: the individual behavior of a silo when changing the inclusions length, and the behavior of a group of eight silos considering different load combinations.

The rigid inclusions performance was evaluated by comparing the behavior of the silo's original foundation (piles only in the perimeter beam and in the tunnel, as described in Section 2) with one alternative solution, in which rigid inclusions were added under the silo's raft. As the objective of this research is to evaluate only the serviceability limit states, and the ultimate bearing capacity of the system was guaranteed by elements of the original foundation (Bernardes et al., 2021), this paper will not discuss the effect of the rigid inclusions on the foundation overall safety factor.

4.1 Stratigraphy and soil properties

Rodríguez-Rebolledo et al. (2019a) developed a methodology to obtain, adjust and validate the mechanical parameters of a typical soil profile (see the stratigraphy exposed in Figure 3) of the city of Brasília for the HS model (Hardening Soil Model), using laboratory and field test results obtained in previous studies conducted in the CEGUnB. The methodology presented began with the evaluation of the strength and compressibility parameters of triaxial CU tests (with isotropic and anisotropic consolidation) and one-dimensional consolidation tests, respectively (Guimarães, 2002). Then, the parameters obtained for the HS model were calibrated using the finite element method (FEM) and the SoilTest module of the Plaxis software. Based on the evaluation and calibration of these parameters, and the proposed soil profile, a geotechnical model for natural moisture conditions (Nat.) was proposed, as shown in Table 1.

This geotechnical model was validated through numerical modeling of the load testing of footings and piles conducted in the CEGUnB (Sales, 2000; Guimarães, 2002). Using the same methodology and with the triaxial and consolidation tests performed by Guimarães (2002), Pérez-León (2017) determined the HS model parameters for the first 3.5 m of the porous clay layer in saturated state (Sat.), as shown in Table 1.

4.2 Properties for the distribution layer

For the distribution layer (improved soil), the Mohr-Coulomb model was adopted. Research performed by Otálvaro (2013) provided the estimates of the parameters for tropical soil improved by compaction that was used in this study (Table 2). The compacted tropical soil, of the laterite type and highly weathered, was collected from the city of Brasília. The material was classified as ML (low plasticity silt) according to the Unified Soil Classification System (USCS). The γ value was obtained from the results of Proctor Standard testing. Parameters *E*, ϕ›, and *c'* were obtained from CD (consolidated-drained) triaxial tests performed on the same compacted soil. Echevarría (2006) obtained similar parameters for numerical simulations of tropical porous compacted soil.

4.3 Properties for the structural elements

For the modeling of the structural elements, all in concrete, the linear elastic constitutive model was assumed. Raft, perimeter beam, tunnel, and inclusions caps were modeled by plate elements; aeration ducts by beam elements; and piles and inclusions by embedded beams. Table 3 presents the parameters of the constitutive model adopted for each concrete element. The concrete Young's modulus was calculated according to the equation proposed in the Brazilian standard NBR 6118 (ABNT, 2014) as a function of the strength characteristics of the concrete subjected to simple compression. Therefore, a compressive stiffness of 25 GPa was assumed for the raft, perimeter beam, tunnel, piles, and inclusions caps, and 17.7 GPa for the inclusions. The Poisson's ratio of the concrete was equal to 0.2 for all elements (ABNT, 2014; ASIRI National Project, 2011).

The ultimate load capacity of the piles and rigid inclusions was evaluated using 2D axisymmetric FEM simulations (Plaxis 2D). The stratigraphic profile of CEGUnB and the geotechnical model for the HS were considered (Table 1). Concrete elements of 5, 10, 15, and 20 m in length and 0.35 m in diameter were modeled. Concrete-soil interface elements were inserted in the shaft and the tip of the pile, applying load increments on the pile head until the soil failure. For each simulation, a graph of applied load *versus* settlement was generated, where the load at failure for the point of maximum

Table 1. Geotechnical model proposed by the CEGUnB for the HS model (modified from Rodríguez-Rebolledo et al., 2019a).

Parameters	Layer number							
	1		2		3	4	5	6
	Porous sandy clay					Lateritic residual soil		Saprolitic soil
Depth (m)	0 - 1.5		1.5 - 3.5		3.5 - 5.0	5.0 - 7.0	7.0 - 8.5	8.5 - 20.0
State	Nat.	Sat.	Nat.	Sat.	Nat.	Nat.	Nat.	Nat.
γ (kN/m³)	13.1	16.5	12.8	16.4	13.9	14.3	16.0	18.2
c' (kPa)	5	0	5	0	5	20	75	20
ϕ' (°)	25	26	25	26	26	32	20	22
ψ (°)	0	0	0	0	0	0	0	0
E_{50}^{ref} (MPa)	3.2	2.2	2.5	2.1	4.0	12.0	13.2	12.2
E_{oed}^{ref} (MPa)	4.9	1.0	1.5	0.8	2.2	6.9	7.0	5.7
E_{ur}^{ref} (MPa)	14.0	13.0	14.0	13.0	36.9	37.5	54.0	54.0
m	0.50	0.65	0.50	0.80	0.50	0.50	0.50	0.70
ν_{ur}	0.2	0.2	0.2	0.2	0.2	0.2	0.2	0.2
p^{ref} (kPa)	100	50	100	50	100	100	100	100
R_f	0.80	0.75	0.80	0.75	0.90	0.90	0.90	0.80
POP (kPa)	65.7	16.1	31.8	6.6	0.0	31.4	0.0	0.0
K_o^{nc}	0.58	0.56	0.58	0.56	0.56	0.47	0.66	0.63
K_o	1.37	0.75	0.77	0.75	0.56	0.56	0.66	0.63

γ: unit weight of moist soil, *c'* and ϕ›: the effective shear strength parameters, ψ: dilatancy angle, E_{50}^{ref} : the reference secant stiffness modulus for the drained triaxial test, E_{oed}^{ref}: the reference tangent stiffness modulus for oedometric loading, E_{ur}^{ref} : the reference stiffness modulus for unloading and reloading conditions, *m*: the exponent that defines the strain dependence of the stress state, ν_{ur}: unloading/reloading Poisson's ratio, p^{REF}: the reference isotropic stress, R_f: the failure ratio, *POP*: the pre-overburden pressure, K_o^{nc}: the coefficient of the earth pressure at rest for normal consolidation, and K_0: coefficient of earth pressure at rest.

curvature was calculated. Then, an axial load *versus* depth graph (for load at pile failure) was obtained, which allowed to define the tip and shaft resistances (Table 3).

Equations 1 and 2 (García-Buriticá et al., 2021) were used to determine the spacing between inclusions (S) and the diameter of the inclusion cap (a), considering the shear strength values indicated in Table 2 (c' = 80 kPa, ϕ› = 38°), a distribution layer thickness (H) of 1.2 m and a uniformly distributed load applied on the raft (q_s) of 135.3 kPa. The ultimate load-bearing capacity of the inclusion cap (q_{ult}) was calculated using Equation 3 (García-Buriticá, 2021).

$$\frac{S_{min}-a}{a}=\sqrt{\frac{q_{ult}}{q_1}}-1, \text{for } S=D \tag{1}$$

Table 2. Parameters for the distribution layer.

Parameter	Value
Unit weight, γ (kN/m³)	18.6
Young's modulus, E (MPa)	60
Cohesion, c' (kPa)	80
Friction angle, ϕ› (°)	38
Poisson's ratio, ν	0.33

where S_{min} is the minimum value of S (obtained for $S = D$), D is the diameter of the top surface of the load transfer cone (LTC), and q_1 is the total pressure transmitted to the inclusion cap in terms of q_s and the shape of the LTC.

$$H_{max}=\left(S_{min}-a\right)\frac{\tan\beta}{2} \tag{2}$$

where H_{max} is the maximum value of H, and β is the external angle of the LTC defined by Colomb's theory as 45° + ϕ' / 2.

$$q_{ult} \quad c' N_c s_c g_c \tag{3}$$

where s_c is the shape factor = 1 + N_q/N_c, g_c is the inclination factor of the LTC ≈ 0.13 for ϕ' = 38° (according to García-Buriticá, 2021), and N_q and N_c are the bearing capacity factors. According to the above, were obtained values of S = 2 m and a = 0.7 m, which avoid the penetration of the inclusion cap in the distribution layer by punching and the transfer of point loads in the raft.

Table 3. Parameters for the structural elements.

a) Parameters for plate elements

Parameter	Inclusion cap	Perimeter beam	Raft	Tunnel
Thickness, d (m)	0.1	0.4	0.2	0.2
Unit weight, γ (kN/m³)	24	24	24	24
Young's modulus, E (GPa)	25	25	25	25
Poisson's ratio, ν	0.2	0.2	0.2	0.2

b) Parameters for aeration ducts (beam elements)

Parameter	Value	Cross section
Young's modulus, E (GPa)	25	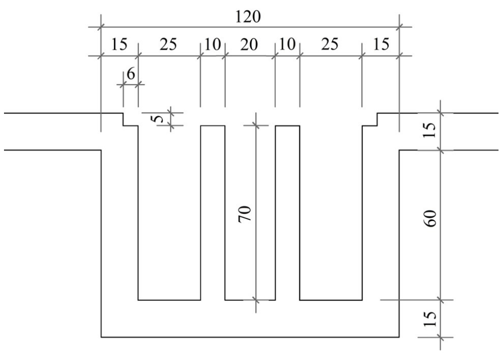
Unit weight, γ (kN/m³)	24	
Cross section, A (m²)	0.56	
Inertia around 2nd axis (m⁴)	0.0875	
Inertia around 3rd axis (m⁴)	0.0454	

c) Parameters for embedded beams

Parameter	Piles	Inclusions			
Length, L_{pile} (m)	20	5	10	15	20
Young's modulus, E (GPa)	25.0	17.7	17.7	17.7	17.7
Unit weight, γ (kN/m³)	24	23	23	23	23
Diameter, D (m)	0.35	0.35	0.35	0.35	0.35
Side friction resistance, T_{sf} (kN/m)	53.6	18.7	42.6	53.6	66.3
Base resistance, F_{max} (kN)	37.2	46.9	30.6	37.2	46.3
Total resistance, N_{pile} (kN)*	841.2	140.4	456.6	841.2	1372.3

$^{*}N_{pile}=F_{max}+L_{pile}T_{sf}$

4.4 Cases analyzed and stages

The finite element mesh developed for the silo's foundation is presented in Figure 4. For the simulation of the perimeter joint, a space of 200 mm was left between the raft and the perimeter beam, and an interface element was placed between the embankment (load transfer platform) and the perimeter beam.

For the case of the individual silo, after a sensitivity analysis, the lateral boundaries of the finite element mesh were placed at a distance of approximately three times the diameter of the silo (100 m from the silo axis in the x and y directions). The lower boundary was established at a depth of 25 m, beyond which the N_{SPT} was larger than 40 blows, and the soil was classified as very compact, according to the Brazilian standard NBR 6484 (ABNT, 2001).

Only a quarter of the silo's plan geometry could have been simulated, as adopted by Móczár et al. (2016) in a sugar silo analysis, but it was decided to model the complete silo because it served as a calibration for its use in the group modeling, i.e., for the generation of the model that considers a group of silos.

The medium was discretized by a finite element mesh with 71,409 10-node tetrahedral elements, which proved to be enough according to sensitivity analyses. The lateral boundary conditions were fixed in the horizontal direction, and the bottom boundary conditions were fixed in both directions.

As shown in Figure 5, for modeling of the interaction between the group of eight silos during the filling and emptying processes, the symmetry conditions of the problem were considered and three possible combinations were defined. The lateral boundaries of the finite element mesh were placed at a distance approximately three times the diameter of the silo (100 m from Silo 01 axis in the x direction and 100 m from Silos 01 and 02 in the y direction). The boundary conditions were set as the same used for the isolated silo model.

Table 4 shows the stages of analysis used for all the studied cases. The loads on the raft and the perimeter beam were obtained from the original project and correspond to the service loads for the silo working at its maximum capacity.

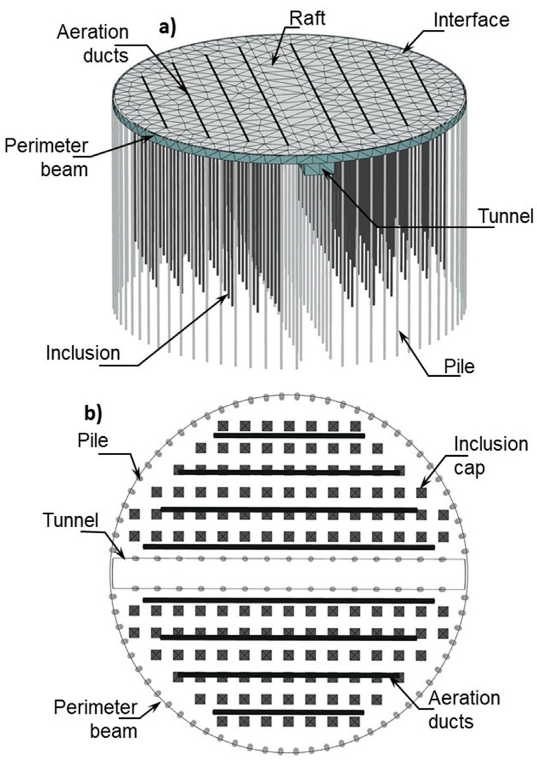

Figure 4. General configuration of the finite element mesh developed for the silo's foundations: (a) 3D; (b) plan view.

5. Analysis of the results

5.1 Case 1: individual behavior

The maximum vertical displacements (ρ^{MAX}) obtained at the silo raft, for the cases with the original foundation

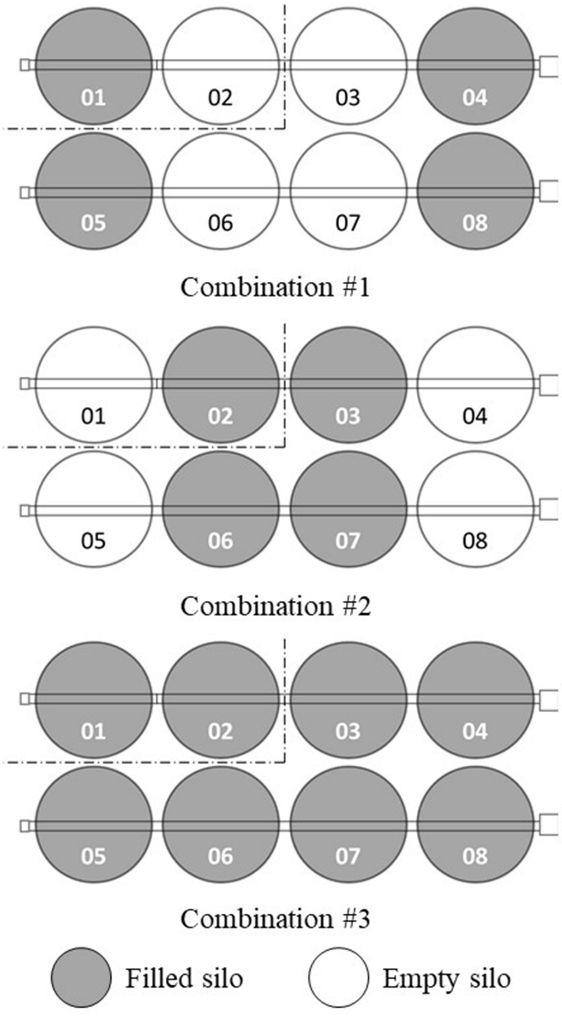

Figure 5. Possible combinations for the analysis of the interaction between the eight silos.

Table 4. Stages of analysis.

Stage	Characteristics
1	Initial stress conditions
2	Silo construction. Applied load on the perimeter beam = 183.1 kN/m
3	Total filling of the silo. Applied load on the silo raft = 135.3 kPa
4	Total discharge of the silo raft.

solution and reinforced with rigid inclusions, for stages 3 and 4 (total filling and discharge of the silo, respectively), and for stratigraphic conditions of natural and saturated moisture states, are shown in Figure 6.

It is possible to observe that for the original foundation solution, considering the natural condition (Figure 6a), ρ^{MAX} = 34 cm when the silo is completely filled, and when it is completely emptied a ρ^{MAX} = 24 cm remains. This means that after the loading of the silo a permanent (plastic) displacement is developed, equivalent to 70% of the total, and an elastic value remains of approximately 10 cm that may develop during the loading-unloading cycles of the silo.

In a saturated condition (Figure 6b) the settlement increases to ρ^{MAX} = 46 cm when the silo is loaded, and ρ^{MAX} = 37 cm after unloading, which corresponds to an increase of 35% in the total settlements and 54% in the permanent ones. It is possible to say that all these displacement values considerably exceed the adopted limit-state for total vertical displacements (15 cm).

When rigid inclusions of 15 m length are added, the ρ^{MAX} values are reduced by 78%, i.e., to 10 cm and 8 cm (Figure 6c), for total and permanent, respectively, and therefore the remaining elastic displacement is only 2 cm.

Figure 7 shows the vertical displacements obtained at the silo raft, at the perimeter beam, and the tunnel, for the cases with the original foundation solution and reinforced with rigid inclusions, for stage 3 (total filling), and for the natural condition.

For the original foundation (Figures 7a) occurs the development of displacements with considerably different magnitudes within each structural element and between them. For the raft, as mentioned before, when the silo is loaded, the maximum displacement is equal to 340 mm (located in the center of the black zone); and the minimum displacement (ρ^{MIN}) is about 120 mm, located at the ends of the tunnel (in the greyish zone), at a distance (L) of about 7.5 m. These results generate an angular distortion in the silo raft ($\delta_{max} = \left(\rho^{max} - \rho^{min}\right) / L$) equal to 1/34, well above the adopted limit-state (1/400). For the tunnel structure, despite being reinforced with piles, total displacements of ρ^{MAX} = 17 cm and δ^{MAX} = 1/326 were obtained, both values above the limit state. For the case of the perimeter beam, due to the reinforcement with piles and the low magnitude of transmitted load (compared to the tunnel) a total displacement of 10 cm and angular distortion of 1/796 were obtained.

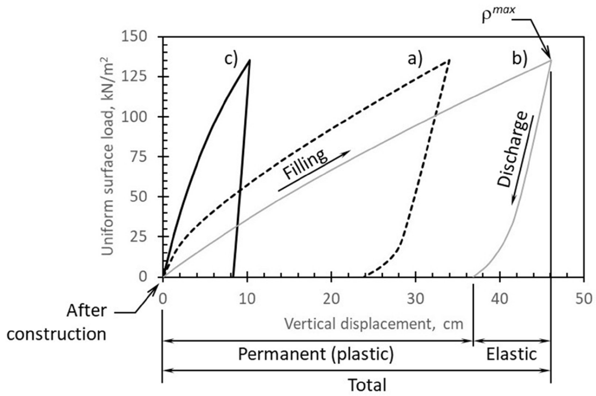

Figure 6. Maximum vertical displacement obtained at the silo raft, for the original foundation solution considering: (a) natural; (b) saturated conditions; (c) reinforced with rigid inclusions considering both moistures states.

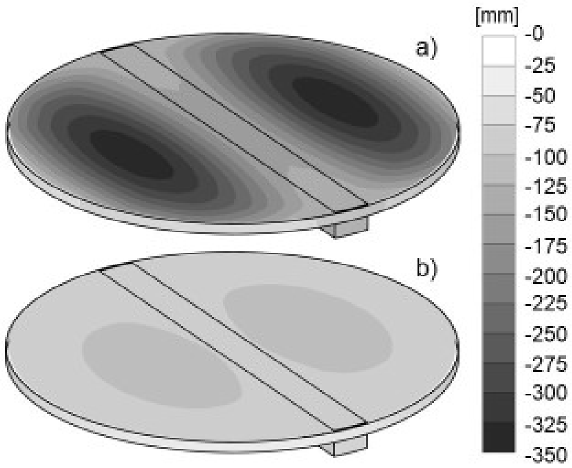

Figure 7. Vertical displacements computed for stage 3 at the silo raft, perimeter beam, and tunnel, considering a natural moisture state: (a) for the original foundation solution; (b) when reinforced with rigid inclusions.

When the rigid inclusions are added (Figure 7b) there is a significant reduction in differential displacements on the raft, i.e., ρ^{MAX} reduces to 10 cm, ρ^{MIN} to 8 cm, and L increases to 10.2 m, leading to an angular distortion of only 1/510, and for the tunnel, ρ^{MAX} reduces to 9.5 cm and δ^{MAX} to 1/1000 (i.e., both structures below the established limits).

Another important differential displacement that is observed in the silo (Figure 8), is the one that develops between the perimeter beam and the raft. Since the perimeter beam is strongly reinforced by piles, the vertical displacement is considerably lower than that developed in the perimeter of the raft, generating a gap between both elements when the silo is filled. This gap may cause grain contamination and structure service failure (Figure 1b).

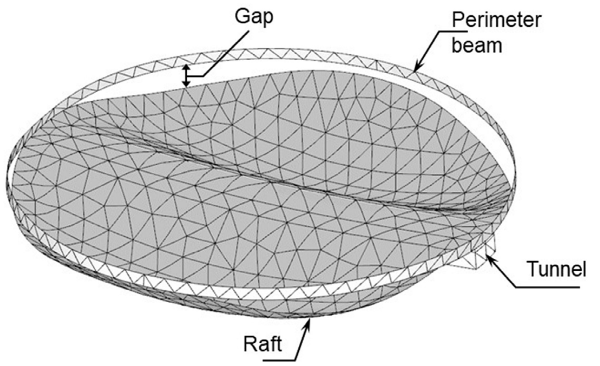

Figure 8. Deformed mesh obtained when the silo is filled (scaled up 20 times).

According to the obtained results, the maximum gap value obtained (G^{MAX}) is about 15.2 cm (stage 3, total displacement), and 11.5 cm when empty (stage 4, permanent displacement). For the foundation reinforced by rigid inclusions, G^{MAX} = 2.4 cm for stage 3 and G^{MAX} = 1.4 cm for stage 4, hence, a remaining elastic displacement of only 1 cm. It means that the inclusions allow the raft and beam to settle more uniformly, allowing the value of the gap to be reduced by approximately 85%.

For a better understanding of the foundation's performance when the rigid inclusions are added, a parametric analysis was performed by varying the length of these elements. Then, the results of the maximum displacement predictions were compared with those obtained when using the original foundation solution. According to Rodríguez-Rebolledo et al. (2019b), three relationships can be proposed that allowed evaluating the performance of the foundation with rigid inclusions, these are: settlement reduction factor (*SRF*, Equation 4), angular distortion reduction factor (*DRF*, Equation 5) and raft-perimeter beam gap opening reduction factor (*GRF*, Equation 6).

$$SRF = 1 - \frac{\rho_{w/i}^{max}}{\rho_{w/o}^{max}} \tag{4}$$

where $\rho_{w/i}^{max}$ is the maximum vertical displacement obtained when rigid inclusions are included and $\rho_{w/o}^{max}$ is the maximum vertical displacement obtained for the original foundation solution. When *SRF* = 1, the settlement is fully reduced, and the performance of the inclusion system is at the maximum; when *SRF* = 0, the settlement reduction is null, and the performance of the system is at the minimum.

$$DRF = 1 - \frac{\delta_{w/i}^{max}}{\delta_{w/o}^{max}} \tag{5}$$

where $\delta_{w/i}^{max}$ is the maximum angular distortion obtained when rigid inclusions are added and $\delta_{w/o}^{max}$ is the maximum angular distortion obtained for the original foundation solution.

$$GRF = 1 - \frac{G_{w/i}^{max}}{G_{w/o}^{max}} \tag{6}$$

where $G_{w/i}^{max}$ is the maximum gap opening obtained with the use of rigid inclusions and $G_{w/o}^{max}$ is the maximum gap opening obtained for the original foundation.

The graphs in Figure 9 show the total and permanent values obtained for *SRF* and *DRF*, for the raft, the tunnel, and the perimeter beam, for inclusions lengths from 5 to 20 m. For the case of the raft, it is possible to observe that, from 10 m in length, a good performance of the proposed foundation system is obtained. The value of *SRF* ranges from 0.50 to 0.81 and from 0.38 to 0.79 for total and permanent displacements, respectively. This means that the inclusions were able to reduce the maximum vertical displacement by up to 80%, and to meet the serviceability limits for total displacements value (T-SLS) from a length of approximately 12 m, and from 10 m for the permanent ones (P-SLS).

For the case of *DRF*, the performance of the solution increases significantly, since, for the same lengths, total values of 0.63 to 0.97 and permanent values of 0.55 and 0.97 are obtained, showing that the inclusions are able to reduce almost completely the differential displacements. Even inclusions of only 5 m in length allow reducing the maximum differential displacement by 30%.

For the tunnel, inclusions of 5 m in length would be enough to meet the limit states, both for total settlements and angular distortion. For the perimeter beam, the piles are sufficient for the limit states not to be exceeded.

The performance of the inclusions for settlement control of the tunnel and the perimeter beam, compared to that of the raft, is lower, since these elements are already reinforced with piles, i.e., the inclusions work together with the piles to reduce the settlements. Figure 10 shows the axial load developed in a central pile of the perimeter beam and tunnel, and in a central rigid inclusion, for the analyzed cases. It is possible to observe that when the inclusions are added, the load on the piles substantially decreases, mainly in the tunnel zone (Figure 10b), where the maximum load goes from 1162 kN to 833 kN, i.e., a reduction of approximately 30%. This reduction is due to the stiffness increase caused by the presence of rigid inclusions, which absorbs a significant portion of the external load when the silo is filled (Figure 10c).

The good performance observed in reducing the raft settlements is also reflected in the behavior of the raft-perimeter beam structural joint (gap opening), as shown in Figure 11. For the case of the original foundation, a gap opening of up

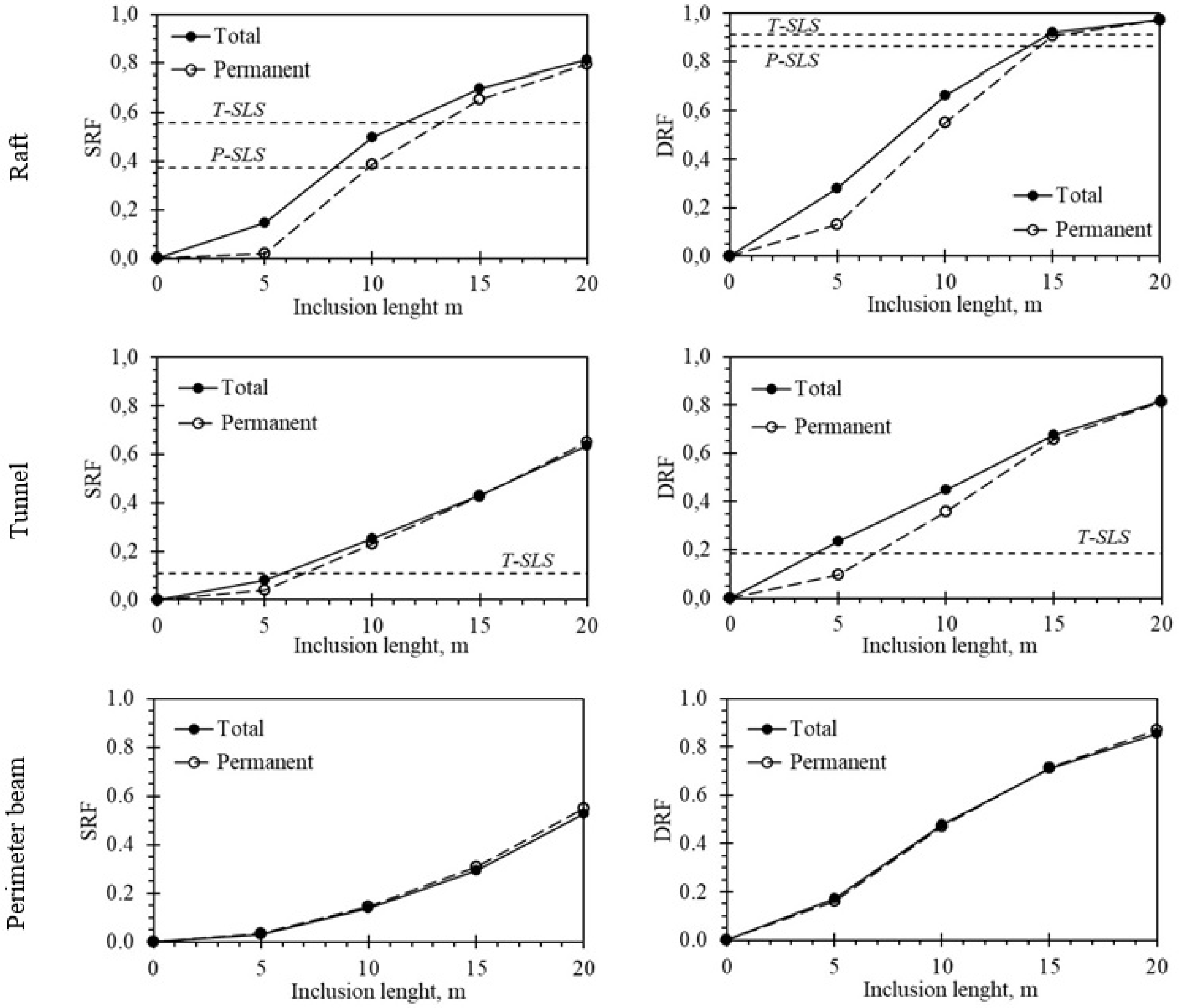

Figure 9. *SRF* and *DRF* factors obtained for different inclusion lengths, at the raft, tunnel, and perimeter beam for total and permanent displacements.

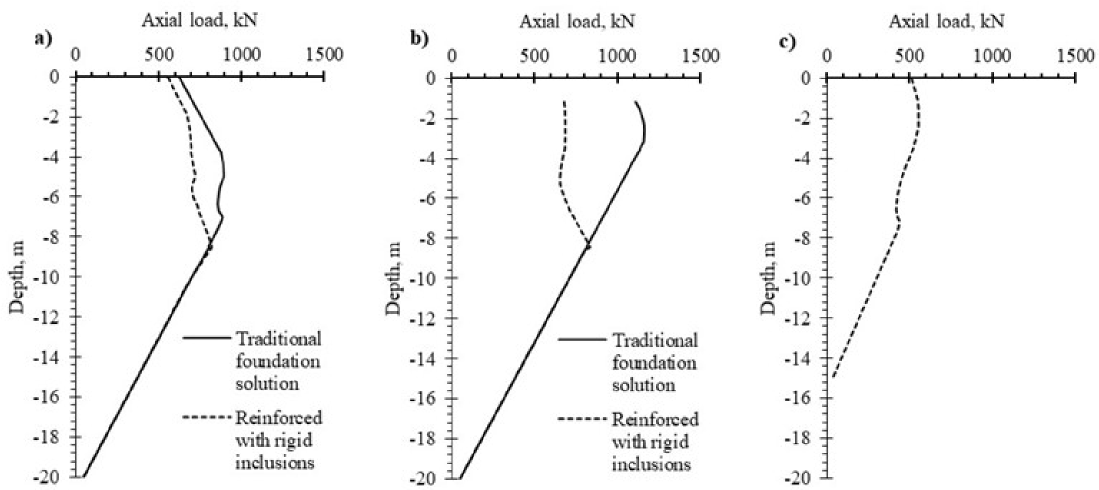

Figure 10. Axial load developed at: (a) perimeter beam piles; (b) tunnel piles; (c) inclusions.

to 15.2 cm was calculated. When the inclusions are placed, this value drops considerably to 5.7 cm (*GRF* = 0.62) and 1.3 cm (*GRF* = 0.91), for 10 and 20 m lengths, respectively.

5.2 Case 2: group behavior

According to the combinations defined in Figure 5, the vertical displacements obtained for the three load combinations, considering the natural moisture state and the original foundation are shown in Figure 12. In general, for the filled silos, vertical displacements increase mainly in the direction of the axes of symmetry X, and for the empty ones in the direction of the filled silo.

When compared to the values obtained for the individual silo, the maximum vertical displacement (ρ^{MAX}) for combination 1 (Figure 12a) increases by 5% (from 34 to 35.6 cm) for the external silos (filled), and for the internal ones (empty) ρ^{MAX} = 4.1 cm. For combination 2 (Figure 12b) ρ^{MAX} increases by 8% (up to 36.6 cm) for the internal ones, and again ρ^{MAX} = 4.1 cm for the empty ones. Finally, for combination 3 (Figure 12c, all silos filled), ρ^{MAX} increases by 11% (up to 37.8 cm) for the internal ones, and by 8% for the external.

When rigid inclusions are considered, the vertical displacement increase follows the same tendency verified for the original foundation. In the alternative solution compared to the individual silo analysis, ρ^{MAX} values increase more significantly for the filled silos, for combinations 1, 2, and 3, ρ^{MAX} increases by 15%, 23%, and 29% (from 10 to 11.5 cm, 12.3 cm, and 12.9 cm), respectively, but all of them below the established limit-state. For the empty silos ρ^{MAX} = 3.3 cm, for both cases (combinations 1 and 2).

Table 5 summarizes the values of the *SRF*, *DRF*, and *GRF* obtained for the performance evaluation of the group of silos for all the analyzed combinations. Although the values of ρ^{MAX} increased by up to 29% in relation to the analysis of an individual silo, the *SRF* values decreased by only 6% (from 0.70 to 0.66), while *DRF* and *GRF* remained practically the same. Small performance values were obtained for the empty silos, because the calculated total and differential vertical displacements, both with and without inclusions, were low, i.e., both cases were well below the established limit-state.

The results show that, for the analyzed case, the performance of the foundation reinforced with rigid inclusions is little affected by the operation of a group of silos.

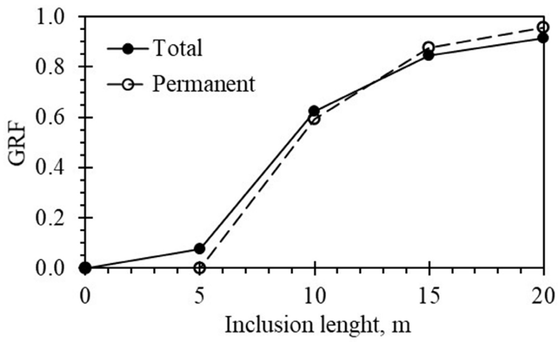

Figure 11. *GRF* factor obtained for total and permanent displacements.

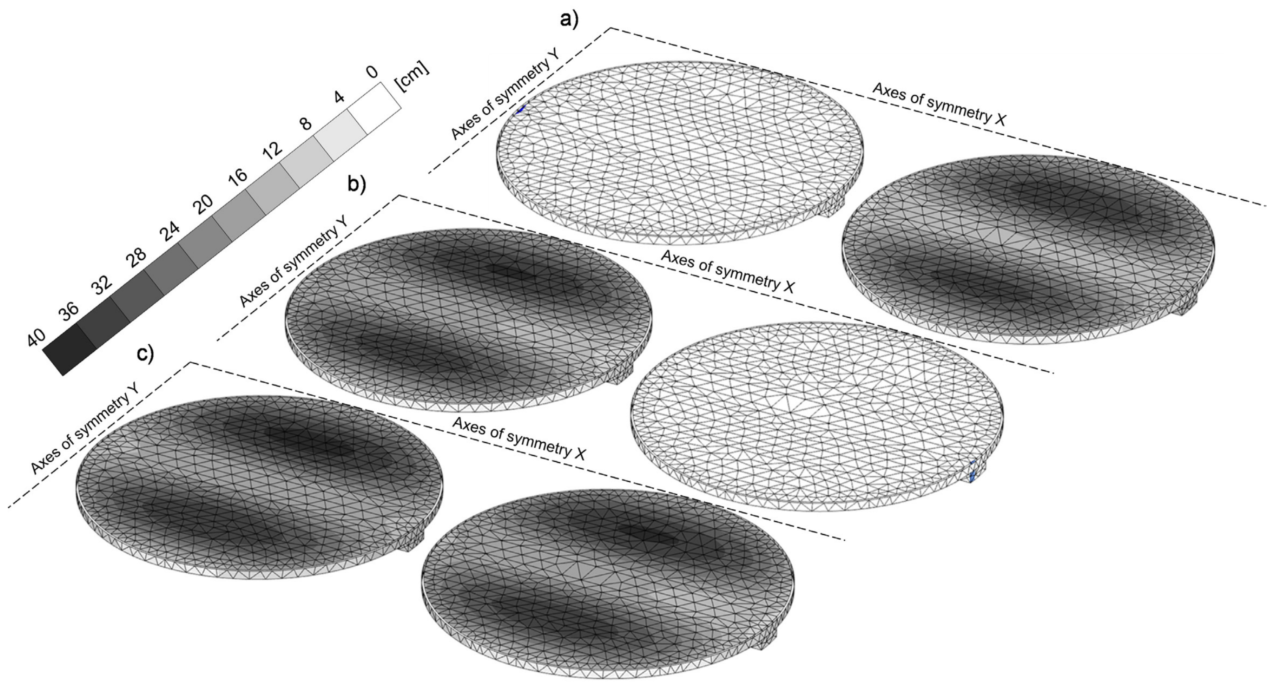

Figure 12. Vertical displacements computed for the silos group with the original foundation, when a) external silos are filled (combination 1), b) when internal silos are filled (combination 2) and c) when all silos are filled (combination 3).

Table 5. Performance evaluation of silos group for different filling combinations.

Comb.	Silos	*SRF*	*DRF*	*GRF*
Individual silo behavior		0.70	0.92	0.84
1	External (01, 04, 05, 08)	0.67	0.90	0.83
	Internal (02, 03, 06, 07)	0.17	0.17	0.09
2	External (01, 04, 05, 08)	0.20	0.20	0.13
	Internal (02, 03, 06, 07)	0.66	0.90	0.84
3	External (01, 04, 05, 08)	0.66	0.92	0.84
	Internal (02, 03, 06, 07)	0.66	0.93	0.85

6. Conclusions

This article presents the evaluation of the performance of grain silos reinforced by rigid inclusions in soils characteristic of the Central-West region of Brazil, during its construction and operation, through three-dimensional numerical modeling. The main conclusions are summarized below:

a) SLS values of 150 mm and 1/400, for vertical settlement and angular distortion, respectively, are suggested for the foundation design of grain silos.
b) For the original foundation solution, the calculated displacement values considerably exceed the adopted limit state for total vertical displacements. When rigid inclusions were added, it was possible to observe that, from 10 m in length, a good performance of the foundation system was obtained. The inclusions were able to reduce the maximum total and differential displacements by around 80%. Even inclusions of only 5 m in length allow to reduce the maximum differential displacement by 30%.
c) It was shown that the maximum performance obtained with the inclusions was in the control of the differential displacements for all the structural elements of the foundation, thus, reducing the probability of structural failures.
d) The presence of rigid inclusions causes a reduction (of approximately 30%) in the load absorbed by the tunnel piles, due to the stiffness increase beneath the raft. Hence, the quantity of piles could be optimized, or even totally replaced by rigid inclusions.
e) The good performance observed in reducing the raft settlements was also reflected on the behavior of the structural joint (gap opening), obtaining a reduction of the gap opening up to 91%. It is possible to say that one way to further reduce this value would be to reduce the length or number of the piles beneath the perimeter beam, which will lead to an optimized design.
f) For the analyzed case, the performance of the foundation reinforced with inclusions is little affected when considering the silos working as a group. Thus, the execution of the parametric analysis for the foundation design, i.e., to determine the length, diameter, and the number of inclusions and/or piles, can be done using an isolated silo. However, for the final review of the SLS, the foundations should be analyzed considering the silos working as a group.

The rigid inclusion system proved to be an efficient foundation solution that allows controlling total and differential settlements during the serviceability stage of the silo, helping to prevent the formation of cracks in the structural elements and grain contamination by the excessive opening of the raft-perimeter beam joint.

Acknowledgements

The authors acknowledge the Coordination for the Improvement of Higher Education (CAPES), the National Council for Scientific and Technological Development (CNPq) and the Federal District Development Support Fund (FAPDF, *Edital Nº 04/2021 - Demanda Espontânea, Processo nº* 00193-00000229/2021-21) for their financial support and partnership.

Declaration of interest

The authors have no conflicts of interest to declare. All co-authors have observed and affirmed the contents of the paper and there is no financial interest to report.

Authors' contributions

Juan Félix Rodríguez Rebolledo: conceptualization, formal analysis, funding acquisition, investigation, methodology, project administration, resources, software,

supervision, validation, visualization, writing – original draft. Isabelle Moreira Santiago: conceptualization, formal analysis, investigation, methodology, software, validation, visualization, writing – original draft. Heitor Cardoso Bernardes: conceptualization, investigation, methodology, validation, visualization, writing – review & editing. Thiago Augusto Mendes: investigation, methodology, visualization, writing – review & editing.

List of symbols

A	Cross section area
a	Diameter of the inclusion cap
c'	Effective soil cohesion
D	Diameter
d	Plate thickness
DRF	Angular distortion reduction factor
E	Young's modulus
E_{50}^{ref}	Reference secant stiffness modulus for the drained triaxial test
E_{oed}^{ref}	Reference tangent stiffness modulus for oedometric loading
E_{ur}^{ref}	Reference stiffness modulus for unloading and reloading conditions
F_{max}	Pile base resistance
g_c	Inclination factor of the load transfer cone
G^{MAX}	Maximum gap between the perimeter beam and the raft
GRF	Gap opening reduction factor
H	Distribution layer thickness
K_o^{nc}	Coefficient of the earth pressure at rest for normal consolidation
K_0	Coefficient of earth pressure at rest
L	Distance / length
m	Exponent that defines the stress-strain dependence
N_c, N_q	Bearing capacity factors
POP	Pre-overburden pressure
q_1	Total pressure transmitted to the inclusion cap
q_s	Uniformly distributed load over the raft
q_{ult}	Ultimate load-bearing capacity of the inclusion cap
p^{REF}	Reference isotropic stress
R_f	Failure ratio
S	Spacing between inclusions
s_c	Shape factor
SRF	Settlement reduction factor
T_{sf}	Pile side friction resistance
β	External angle of the load transfer cone
γ	Soil unit weight
Δ	Variation / difference of a variable with respect to two points
δ	Angular distortion
ν	Poisson's ratio
ν_{ur}	Unloading/reloading Poisson's ratio
ρ	Vertical displacement / settlement
ϕ›	Effective shear angle
ψ	Dilatancy angle

References

ABNT NBR 6118. (2014). *Design of Structural Concrete - Procedure*. ABNT - Associação Brasileira de Normas Técnicas, Rio de Janeiro, RJ (in Portuguese).

ABNT NBR 6122. (2019). *Design and Construction of Foundations*. ABNT - Associação Brasileira de Normas Técnicas, Rio de Janeiro, RJ (in Portuguese).

ABNT NBR 6484. (2001). *Soil - Standard Penetration Test - SPT - Soil Sampling and Classification - Test Method*. ABNT - Associação Brasileira de Normas Técnicas, Rio de Janeiro, RJ (in Portuguese).

ABNT NBR 7821. (1983). *Tanques soldados para armazenamento de petróleo e derivados - Anexo C: Fundações*. ABNT - Associação Brasileira de Normas Técnicas, Rio de Janeiro, RJ (in Portuguese).

ASIRI National Project. (2011). *Recommendations for design, construction and control of rigid inclusion ground improvements*. Presses des Ponts.

Bahar, R., Sadaoui, O., & Amzal, D. (2013). Differential settlements of cylindrical steel storage tanks: case of the marine terminal of Bejaia. In *Proceedings International Conference on Case Histories in Geotechnical Engineering*, Chicago. Retrieved in May 5, 2021, from https://scholarsmine.mst.edu/icchge/7icchge/session02/12.

Becker, D.E., & Lo, K.Y. (1979). Settlement and load transfer of ring foundation for tower silos. *Canadian Agricultural Engineering*, 21(2), 97-110. Retrieved in May 5, 2021, from https://library.csbe-scgab.ca/docs/journal/21/21_2_97_ocr.pdf

Bernardes, H.C., Souza Filho, H.L., Dias, A.D., & Cunha, R.P. (2021). Numerical analysis of piled raft foundations designed for settlement control on steel grain silo in collapsible soils. *International Journal of Civil Engineering*, 19, 607-622. http://dx.doi.org/10.1007/s40999-020-00586-5.

Bernuy, C., Hor, B., Kim, S., Song, M., & Alqoud, S.Y. (2018). LNG tanks on rigid inclusions: kuwait. *Innovative Infrastructure Solutions*, 3(80), 1-12. http://dx.doi.org/10.1007/s41062-018-0186-8.

Briançon, L., Dias, D., & Simon, C. (2015). Monitoring and numerical investigation of a rigid inclusions-reinforced industrial building. *Canadian Geotechnical Journal*, 52(10), 1592-1604. http://dx.doi.org/10.1139/cgj-2014-0262.

Cardoso, F.B.F. (2002). *Properties and mechanical behavior of soils of the Brazilian Central Plateau* [Doctoral thesis, University of Brasilia]. University of Brasília's repository (in Portuguese). https://repositorio.unb.br/handle/10482/31224.

Coelho, R.S. (2013). *Relatório das sondagens executadas na área destinada à construção da obra casa do professor*. FUNDEX. Brasília. (in Portuguese).

Combarieu, O. (1990). Amelioration of soils by vertical rigid piles, for shallow foundation. *Revue Française de Géotechnique*, 53, 33-44. http://dx.doi.org/10.1051/geotech/1990053033. (in French).

Companhia Nacional de Abastecimento – CONAB. (2022). *Boletim da Safra de Grãos - 5º Levantamento. Safra 2021/22: Tabela de dados - Produção e balanço de oferta e demanda de grãos*. CONAB (in Portuguese). Retrieved in March 5, 2022, from https://www.conab.gov.br/info-agro/safras/graos/boletim-da-safra-de-graos

Conciani, W. (2016). *Possíveis melhoramentos no projeto e construção de silos* [Candidature Thesis for Full Professor]. Instituto Federal de Educação, Ciência e Tecnologia de Brasília. (in Portuguese).

Cruz, P.T. (1987). Solos residuais: algumas hipóteses de formulações teóricas de comportamento. In *Seminário em Geotecnia de Solos Tropicais* (pp. 79-111). ABMS-UnB. (in Portuguese).

D'Orazio, T.B., & Duncan, J.M. (1987). Differential settlements in steel tanks. *Journal of Geotechnical Engineering*, 113(9), 967-983. http://dx.doi.org/10.1061/(ASCE)0733-9410(1987)113:9(967).

Dogangun, A., Karaca, Z., Durmus, A., & Sezen, H. (2009). Cause of damage and failures in silo structures. *Journal of Performance of Constructed Facilities*, 23(2), 65-71. http://dx.doi.org/10.1061/(ASCE)0887-3828(2009)23:2(65).

Echevarría, S.P. (2006). *Soil arching effects due to earth fills supported by piles foundations* [Master's dissertation, University of Brasilia]. University of Brasília's repository (in Portuguese). https://repositorio.unb.br/handle/10482/3776.

García-Buriticá, J.A. (2021). *Study of the load-transfer mechanism in the distribution layer of foundations reinforced by rigid inclusions* [Doctoral thesis, University of Brasilia]. University of Brasília's repository (in Portuguese). https://repositorio.unb.br/handle/10482/41295.

García-Buriticá, J.A.B., Rodríguez-Rebolledo, J.F., Mutzenberg, D.V., Caicedo, B., & Gitirana Junior, G.F.N. (2021). Experimental investigation of a load-transfer material for foundations reinforced by rigid inclusions. *Journal of Geotechnical and Geoenvironmental Engineering*, 147(10), 04021110. http://dx.doi.org/10.1061/(ASCE)GT.1943-5606.0002649.

Guimarães, R.C. (2002). *Analysis of properties and behavior of a lateritic soil profile applied to the study of the bearing capacity of bored piles* [Master's dissertation]. University of Brasília (in Portuguese).

IS 1904. (1986). *Code of practice for design and construction of foundations in soils: general requirements*. Indian Standard, New Delhi.

Jardim, N.A. (1998). *Metodologia de previsão de capacidade de carga vertical e horizontal com o dilatômetro de Marchetti* [Master's dissertation]. University of Brasília. (in Portuguese).

Móczár, B., Mahler, A., Lódör, K., & Bán, Z. (2016). Back analysis of settlements beneath the foundation of a sugar silo by 3D finite element method. *Plaxis Bulletin*, 39, 12-17.

Mota, N.M.B. (2003). *Ensaios avançados de campo na argila porosa não saturada de Brasília: interpretação e aplicação em projetos de fundação* [Doctoral thesis]. University of Brasília (in Portuguese).

Otálvaro, I.F. (2013). *Comportamento hidromecânico de um solo tropical compactado* [Doctoral thesis, University of Brasilia]. University of Brasília's repository (in Portuguese). https://repositorio.unb.br/handle/10482/13591.

Pecker, A. (2004). Design and construction of the rion antirion bridge. In *Proceedings Geotechnical Engineering for Transportation Projects*, Los Angeles, California. (Vol. 1, pp. 216-240). Reston: ASCE. https://doi.org/10.1061/40744(154)7.

Perez, E.N.P. (1997). *O uso da teoria da elasticidade na determinação do módulo de Young de solo adjacente a estacas carregadas verticalmente na argila porosa de Brasília* [Master's dissertation]. University of Brasília (in Portuguese).

Pérez-León, R.F. (2017). *Rigid Inclusions for controlling settlement in collapsible soils of the Federal District* [Master's dissertation, University of Brasilia]. University of Brasília's repository (in Portuguese). https://repositorio.unb.br/handle/10482/24065.

Rodríguez-Rebolledo, J.F., & Auvinet, G. (2006). Rigid inclusions in Mexico City soft soils. In *International Symposium Rigid Inclusions in Difficult Soft Soil Conditions* (ISSMGE TC-36, Vol. 1, pp. 197-206), Mexico City.

Rodríguez-Rebolledo, J.F., Pérez-León, R.F., & Camapum De Carvalho, J. (2019a). Obtaining the mechanical parameters for the hardening soil model of Tropical soils in the city of Brasília. *Soils and Rocks*, 42(1), 61-74. http://dx.doi.org/10.28927/SR.421061.

Rodríguez-Rebolledo, J.F., Pérez-León, R.F., & Camapum de Carvalho, J. (2019b). Performance evaluation of rigid inclusion foundations in the reduction of settlements. *Soils and Rocks*, 42(3), 265-279. http://dx.doi.org/10.28927/SR.423265.

Sales, M.M. (2000). *Análise do comportamento de sapatas estaqueadas* [Doctoral thesis]. University of Brasília (in Portuguese).

Sales, M.M., Vilar, O.M., Mascarenha, M.M.A., Silva, C.M., Pereira, J.H.F., & Camapum de Carvalho, J. (2015). Fundações em solos não saturados. In J.C. Carvalho, G.F.N. Gitirana Junior, S.L. Machado, M.MA. Mascarenha & F.C. Silva Filho (Eds.), *Solos não saturados no contexto geotécnico* (pp. 651-685). ABMS. (in Portuguese).

Santoyo, E., & Ovando, E. (2006). Geotechnical considerations for hardening the subsoil in Mexico City's Metropolitan Cathedral. In *International Symposium Rigid Inclusions in Difficult Soft Soil Conditions* (ISSMGE TC-36, Vol. 1, pp. 171-178), Mexico City.

Santrač, P., Bajić, Ž., Grković, S., Kukaras, D., & Hegediš, I. (2015). Analysis of calculated and observed settlements of the silo on loess. *Hrčak Technical Gazette*, 22(2), 539-545. http://dx.doi.org/10.17559/TV-20140615132437.

Souza Filho, H.L. (2018). *Estudo da técnica de sistemas em radier estaqueado para fundações de silos graneleiros do Centro-Oeste* [Master's dissertation, University of Brasilia]. University of Brasília's repository (in Portuguese). https://repositorio.unb.br/handle/10482/34449

Soils and Rocks
An International Journal of Geotechnical and Geoenvironmental Engineering
www.soilsandrocks.com
ISSN 1980-9743
ISSN-e 2675-5475

Influence of suction on the parameters of the Marchetti Dilatometer Test on a compacted residual soil

Cândida Bernardi[1], Orlando Martini de Oliveira[1#], Murilo da Silva Espíndola[1], Rafael Augusto dos Reis Higashi[1],

Article

Keywords
Site characterization
Marchetti dilatometer test
Compacted residual soil
Unsaturated soils
Soil suction

Abstract

This study had the objective to evaluate the application of the Marchetti Dilatometer Test (DMT) on compacted residual soil, analyzing the influence of suction on the parameters obtained. For this, a sample of residual diabase soil was collected and compacted in the laboratory at its optimum moisture content. Granular matrix suction sensors (GMS) were installed inside the compacted sample to monitor the suction during the experiment. The GMS allowed the monitoring of suction profile variations during the drying of the specimen submitted to ambient conditions. The DMT blade was statically inserted at 6 different points of the specimen surface with measurement of parameters *A* and *B* at every 10 cm deep. It was observed that with the increase of suction, there is an increase in both: material index value (I_D) and dilatometric module (E_D), but a reduction in the horizontal stress index (K_D) value. The increase in E_D value and reduction in K_D value indicates that there is an increase in deformability modulus (E) and a decrease in coefficient of at-rest earth pressure (K_0). The DMT correctly detected the trend in variations in geotechnical parameters as a function of variation in soil suction profiles.

1. Introduction

Technological control of soil embankment is a great importance during and after construction. This control is verified by determining the compaction humidity in relation to the optimum moisture content, as well as the degree of compaction reached. However, the information provided by this technique does not always reflect the authentic behavior of the soil, in addition to being applicable only during the construction stage. Thus, there is a need for more representative tests for the provision of control parameters of compacted soils.

The Marchetti Dilatometer Test (DMT) is a good alternative, among field tests, to assess the behavior of embankments, since it is a relatively simple test, easy to perform, and allows to estimate the geotechnical parameters of the soils (Marchetti & Monaco, 2018).

Initial studies with the DMT were based on readings and interpretations made in sedimentary soils (Marchetti, 1980). The DMT showed to be very useful to estimate the geotechnical parameters of these soils, such as overconsolidation ratio (*OCR*), the effective angle of internal friction (ϕ') and undrained shear strength (*Su*).

There are several studies in residual soils (Cruz & Fonseca, 2006; Borden et al. 1985; Giacheti et al. 2006; Silva, 2008), but only a few have proposed correlations. In general, it is common to apply the correlations of sedimentary soils to residual soils, resulting in inconsistent interpretations of its geotechnical behavior. This problem is evidenced in the studies by Cruz (2010, 2012), which explain that residual soils present unconventional mechanical behavior when compared with sedimentary soils. The presence of cementation and suction interferes with the interpretation of the results obtained in field tests.

Cruz et al. (2014) obtained a correlation to obtain the cohesion intercept that takes into account the *OCR* value obtained from the DMT, which proved to be satisfactory in relation to the experimental results obtained for a residual granite soil. A reduction in the values of p_1, E_D, I_D and K_D was also observed as the tests with DMT were closer to the water level inside the soil, thus decreasing the suction value.

Rocha et al. (2021) incorporated the effect of suction in the equations proposed by Marchetti et al. (2001) following a different path from the research proposal presented here, noting that the mean values of K_D and E_D were twice as high in the active zone of the soil due to the influence of suction with smaller variations in *Id* values. This research was developed with the objective to better understand the influence of suction on the behavior of compacted soils, by analyzing the parameters obtained through the DMT. This

[#]Corresponding author. E-mail address: oliveira.orlando@ufsc.br
[1]Universidade Federal de Santa Catarina, Departamento de Engenharia Civil, Florianópolis, SC, Brasil.

Submitted on October 17, 2021; Final Acceptance on August 31, 2022; Discussion open until February 28, 2023.
https://doi.org/10.28927/SR.2022.075921

research was developed with the objective to better understand the influence of suction on the behavior of compacted soils, by analyzing the parameters obtained through the DMT.

2. Dilatometer Marchetti Test - DMT

Developed by Silvano Marchetti in the mid-1970s in Italy, the DMT is commonly used in the area of geotechnical investigations. The original articles published by Marchetti (1975, 1980) provide a detailed description of the test and a series of empirical correlations between test results and common geotechnical parameters. According to Lutenegger (1988), the DMT is a simple tool, quick measurement and has low acquisition and installation costs, besides being resistant and used in several types of soils. Marchetti et al. (2001) state that the DMT is suitable for a wide range of soils, from sands, soft soils, rigid clays to soft rocks, natural or even compacted soils. The test provides estimates of soil parameters, which can be used to predict the performance of engineering structures.

The DMT equipment consists of a flat stainless-steel blade with a flexible circular membrane on one side of the blade. The blade is connected to the control unit, located on the ground surface, through a pneumatic-electric cable inserted inside the thrust rods. This control unit reads the pressures, A and B, required to just begin to move the membrane ('lift-off' pressure) and expand the membrane center of 1.1 mm against the soil (ASTM, 2015).

Pressure readings A and B are corrected by the membrane stiffness, which was inferred prior to the start of the test, yielding the values of p_0 and p_1 as described in Equations 1 and 2.

$$p_0 = 1.05 \cdot \left(A - z_m + \Delta A \right) - 0.05 \cdot \left(B - z_m - \Delta B \right) \quad (1)$$

$$p_1 = B - z_m - \Delta B \quad (2)$$

2.1 Intermediate parameters of the DMT

By obtaining the corrected pressure readings, p_0 and p_1, along with the estimate of the vertical effective stress (σ'_v) and the pore pressure (u_0), Marchetti (1980) defined three interpretation indexes of the dilatometer test: the material index (I_D), the horizontal stress index (K_D) and the dilatometer modulus (E_D), respectively presented in Equations 3, 4 and 5.

$$I_D = \frac{p_1 - p_0}{p_0 - u_0} \quad (3)$$

$$K_D = \frac{p_0 - u_0}{\sigma'_v} \quad (4)$$

$$E_D = 34.7 \cdot \left(p_1 - p_0 \right) \quad (5)$$

The parameter I_D is related to soil type, and the K_D parameter is related to the overconsolidation ratio (OCR) and coefficient of earth pressure at-rest (K_0) and the parameter E_D relates to the soil deformability modulus.

2.2 Correlations with geotechnical parameters

There are several semi-empirical correlations using the K_D and E_D values to estimate the geotechnical parameters of the soil. In the literature, there are correlations to obtain the coefficient of earth pressure at-rest (K_0), overconsolidation ratio (OCR), deformability or Young's modulus (E) and oedometric modulus (M_{DMT}), effective angle of internal friction (ϕ'), among others. In this paper, emphasis will be given to parameter K_0, a parameter that relates to the stresses acting on the soil in the at-rest condition.

There are some proposals de correlations to obtain the K_0 parameter, using the data found with the DMT. Equation 6 was proposed by Marchetti (1980) for clay soils. According to Jamiolkowski et al. (1988), this correlation can only be used for soft or median clays, without signs of aging, cementation or preconsolidation, with $I_D \leq 1.2$. For Lacasse & Lunne (1988), the Marchetti equation provides overestimated K_0 values for $1.5 < K_D < 4$. They suggest that Equation 6 is valid for $K_D > 4$.

$$K_0 = \left(\frac{K_D}{1.5} \right)^{0.47} - 0.6 \quad (6)$$

With the advances in the study of unsaturated soils, formulations for the definition of parameter K_0 appeared, considering the variable suction, with the objective of describing their geotechnical behavior more realistically.

According to Lu & Likos (2004), the relationship between the different stress components, such as horizontal and vertical stresses, is based on constitutive stress-deformation laws. The commonly used linear stress-deformation equation in elasticity is Hooke's Law.

Hooke's Law can be extended to the concept of suction stress. Two general conditions can be imposed for homogeneous unsaturated soil. Assuming that $\sigma_x = \sigma_y = \sigma_h$ and that the deformations $\varepsilon_x = \varepsilon_y = \varepsilon_h = 0$ gives Equation 7. This equation gives the value of the coefficient of earth pressure at-rest, or K_0, as a function of suction and vertical stress.

$$K_0 = \frac{\upsilon}{1-\upsilon} - \frac{1-2\upsilon}{1-\upsilon} \cdot \frac{\chi \cdot \left(u_a - u_w \right)}{\left(\sigma_v - u_a \right)} \quad (7)$$

The parameter χ of Equation 7 was proposed by Bishop (1959) to represent the effective stresses in unsaturated soils. The value is 1 for saturated soil and 0 for dry soil. The value depends mainly on the degree of saturation, and secondarily it is a function of soil structure and drying and wetting cycles (Bishop et al., 1960). Bishop's (1959) proposal is presented in Equation 8.

$$\sigma' = (\sigma - u_a) + \chi \cdot (u_a - u_w) \tag{8}$$

Applying the Mohr-Coulomb criterion for the effective stress equation proposed by Bishop (1959), the shear strength for unsaturated soils is represented by Equation 9. When the soil is saturated the value of $u_a = u_w$ and Equation 9 is reduced to Equation 10. The difference between Equations 9 and 10 represents the increase in resistance attributed to matrix suction. This difference is given by Equation 11.

$$\tau = c' + \left[(\sigma - u_a) + \chi \cdot (u_a - u_w)\right] \cdot tg\phi' \tag{9}$$

$$\tau_0 = c' + (\sigma - u_a) \cdot tg\phi' \tag{10}$$

$$\tau - \tau_0 = \chi \cdot (u_a - u_w) \cdot tg\phi' \tag{11}$$

Thus, the parameter χ can be obtained from Equation 11 being the same represented by Equation 12. Using this equation, the variation of χ as a function of suction can be obtained by performing shear strength tests. Figure 1 shows how this parameter is graphically obtained for different suction values. The τ_0 value shown in this figure represents the effective soil cohesion obtained from the test under the saturated condition. The relationship between shear strength and suction is obtained through unsaturated shear strength tests.

$$\chi = \frac{\tau - \tau_0}{(u_a - u_w) \cdot tg\phi'} \tag{12}$$

The parameter χ is dependent on the degree of saturation and the void ratio of the soil. For soils where the water retention curve is independent of the void ratio, the parameter χ can be considered equal to the degree of saturation S, however this is not normally found (Einav & Liu, 2020; Vaunat & Casini, 2017). In the work presented by Jennings & Burland (1962) it was verified for several types of soil that the variation of the parameter value χ in function of the suction is different from the variation of the saturation degree. Pereira et al. (2010) point out that the relationship χ=S should be viewed with caution as it loses its validity for silty and clayey soils.

In this research was determined the cohesion intercept that represents the relationship between shear strength and suction for zero net normal stress (σ - u_a = 0). This cohesion intercept was obtained by performing unconfined compressive strength tests using specimens with different initial suction values. For the definition of the cohesion intercept there is a need to determine the effective cohesion (c') and effective angle of internal friction (ϕ›) obtained from direct shear tests performed under the saturated condition. The cohesion intercepts were defined by the intersection of the rupture surface with the plane represented by shear strength as a function of suction (σ - u_a = 0). According to Figure 2, the cohesion intercepts were determined by the intersection of the lines that are tangent to the Mohr circle obtained by unconfined compressive strength tests with the shear strength plane as a function of the suction. These straight lines have a slope equal to ϕ', effective angle of internal friction of the soils, considered constant as the suction increases. This constant value of the effective angle of internal friction was obtained in studies carried out by Massocco (2017) on the same residual diabase soil of this research.

Equations 3 and 4 were modified based on the effective stress equation (see Equation 8) proposed by Bishop (1959). The value of u_0, related to the pore water pressure for the saturated soil, was replaced by the term $(\upsilon / 1 - \upsilon).\chi.(u_a - u_w)$ which will be added to the value of p_0. The modifications proposed to obtain parameters I_D and K_D are shown in Equations 13 and 14.

$$I_D = \frac{p_1 - p_0}{p_0 + \left(\frac{\nu}{1-\nu}\right) \cdot \chi \cdot (u_a - u_w)} \tag{13}$$

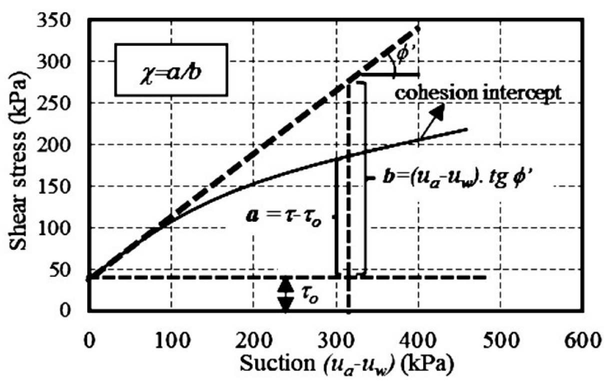

Figure 1. Graphical representation of the determination of the variation of the parameter χ as a function of suction using the cohesion intercept (modified from Khalili & Khabbaz,1998).

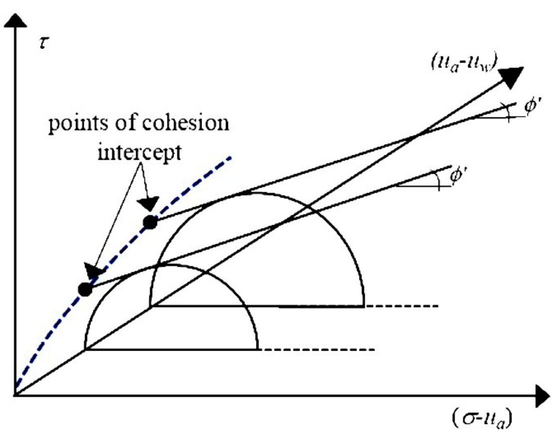

Figure 2. Determining the cohesion intercepts, Pecapedra et al. (2018).

$$K_D = \frac{p_0 + \left(\frac{v}{1-v}\right) \cdot \chi \cdot (u_a - u_w)}{(\sigma - u_a) + \chi \cdot (u_a - u_w)} \tag{14}$$

Fredlund & Rahardjo (1993) and Fredlund et al. (2012), also consider that elastic behavior within a soil mass may provide some information on the earth pressure at-rest of the soil. According to the authors, the theory of elasticity can be used to calculate the changes of stress acting on the soil, with Young's modulus and Poisson's ratio added to the equations. For the authors, in the resting condition, the K_0 parameter of a homogeneous and unsaturated soil mass takes the form of Equation 15.

$$K_0 = \frac{v}{1-v} - \frac{E}{(1-v) \cdot H} \cdot \frac{(u_a - u_w)}{(\sigma_v - u_a)} \tag{15}$$

Equations 7 and 15 show that the coefficient of earth pressure at-rest decreases with the increasing of suction value. This soil behavior, based on the theory of elasticity, has been experimentally proven by several researchers using different techniques to obtain K_0 as a function of suction (Mesri & Hayat, 1993; Daylac, 1994; Machado & Vilar, 1998; Oliveira, 1998; Peixoto, 1999; Zhang et al., 2009; Oh et al., 2013; Pirjalili et al., 2016; Abrantes & Campos, 2019).

Pirjalili et al. (2016) investigated the variation of parameter K_0 as a function of the suction of a compacted clay soil with two different void ratios. The tests were performed with the soil sample molded inside a metal ring instrumented with strain gauges to monitor lateral deformations, being the suction imposed on a triaxial test cell. Figure 3 presents the results obtained, indicating the reduction linear of the K_0 value with the increase of the suction. The highest values of K_0 were obtained for the specimen with a higher void ratio (e = 0.92).

The interpretation of the DMT in saturated sands and clays is well established, with many studies and methodologies, but the interpretation of the tests in unsaturated soils still needs further studies.

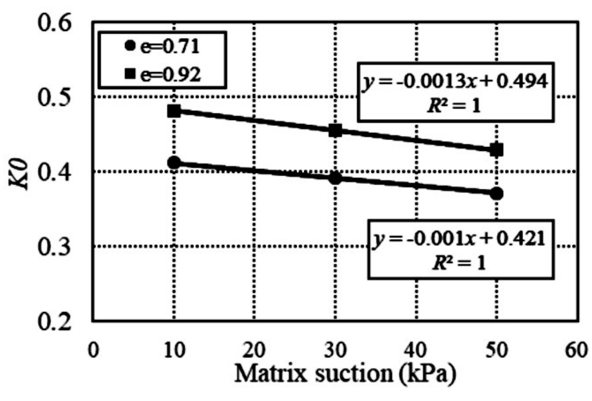

Figure 3. Variations of K_0 as a function of suction (modified from Pirjalili et al., 2016).

Frequently, the interpretation of field tests in unsaturated soils neglecting the contribution of suction. Failure to consider the influence of suction on the results may lead to an inadequate definition of the stratigraphic profile, and in particular, incorrect estimation of soil geotechnical parameters.

3. Materials and methods

This section presents the methodology used to perform the tests. It explains the procedures for conducting direct shear and unconfined compressive strength tests, detailing the procedure for the compaction and execution of the DMT in the laboratory and the procedures for suction monitoring.

3.1 Shear strength tests

To determine the soil resistance parameters, direct shear and unconfined compressive strength tests were performed. The direct shear strength test was performed in consolidated and drained conditions to determine cohesion (*c'*) and effective angle of internal friction (ϕ›), following the recommendations of ASTM (2011). For the procedure, a soil sample at optimum moisture conditions was compacted in a Proctor cylinder. From this sample, three specimens were molded with the aid of metallic shear molds, which present dimensions of 101.6 x 101.6 x 20.0 mm. The test specimens were submitted to the stages of flooding, consolidation and subsequent rupture, adopting the vertical normal stresses of 32.7, 77.4 and 126.8 kPa. The unconfined compressive strength test follows normative ASTM (2016). The samples were compacted in a steel three-part mold, with an internal diameter of 38 mm and height of 80.2 mm, in five equal layers, in optimum moisture conditions. Subsequently, they were submitted to different suction values, by wetting and/or drying process. Suction was determined using the filter paper method. For each specimen, two suction values were determined, and the mean value was adopted.

The initial suction values of the specimens were obtained with the use of Whatman No. 42 quantitative filter paper placed in direct contact with the surface of the specimen, being then involved in plastic film and aluminum paper, remaining at rest in a styrofoam box for a minimum period of 7 days. To determine the matrix suction value, the calibration proposed by Chandler et al. (1992) was used. Following this methodology, the cohesion intercept was obtained for the initial suction of the specimen, considering that its value remains constant during the test.

3.2 Experiment equipment – GMS and DMT

The mechanical equipment of the Large-Scale Triaxial (LST) test, located at the Soil Mechanics Laboratory at Federal University of Santa Catarina (UFSC), was adapted to perform the DMT in compacted soil. This equipment is used to obtain resistance and compressibility parameters of rockfill dams, to test specimens with dimensions of 66 cm in diameter and 165 cm in height (Hummes & Maccarini, 2009; Espíndola, 2016).

The reaction gantry, the hydraulic cylinder and the compaction mold were used for the experiment, with dimensions of 66 cm in diameter and 86 cm in height, formed by 16 windows screwed together and supported on a circular steel base. The soil sample was compacted within the mold using the socket of the Proctor compaction test. The sample had a total height of 72 cm, divided into 24 equal layers of 3 cm each. Were applied 293 blows per layer to achieve the level of compaction required in normal energy and optimum moisture content.

Four granular matrix suction sensors (GMS), manufactured by Irrometer Company, model 200SS sensors were installed in the center of the compacted sample at the depths of 9, 27, 45 and 63 cm. The GMS were screwed into PVC pipes where the wire that should be connected to the data acquisition system. This set was inserted into the holes that were hand-drilled with an earth auger with the same diameter of the GMS. To ensure good hydraulic continuity between the water present in the soil structure and the GMS, a mud was produced with the same soil, and it was used before the installation. The data acquisition was through Monitor 900M, via RS232 connection, using the Watergraph software.

Figure 4a presents the equipment used for the conducting of DMT. Figure 4b shows a schematic representation of the test indicating the position where the GMS was installed and the depths where it was taken as DMT readings. The nominal dimensions of the DMT blade, made of stainless steel, are 22 cm high and 9.3 cm wide. On one side has a flat expandable steel membrane with 6 cm in diameter. The reading intervals were defined every 10 cm, and seven readings were taken at 5, 15, 25, 35, 45, 55 and 65 cm deep. These test depths correspond to the center of the expandable membrane of the DMT blade.

For the process of inserting the DMT blade, it was necessary to make a piece of solid steel, 35 cm long, 10 cm high and 8 cm wide. One end of the piece was bolted to the hydraulic cylinder of the portico and the other end was connected to the dynamometer ring, along with the connections for setting the rods with the blade. The function of the steel piece was to enable driving in the blade from different positions within the mold. Figure 5a presents the schematic drawing of the pieces made. The picture of the moment at the beginning of the insertion of the DMT slide is presented in Figure 5b. Figure 6 shows the locations where the DMTs were performed. It is observed that the expansion of the steel membrane is directed to the center of the specimen. This avoids possible interference with the test results since it is close to the mold wall (10 cm).

Changes in soil structure related to the process of inserting the DMT blade and its influence on test results are not well known. However, the thickness of the DMT blade

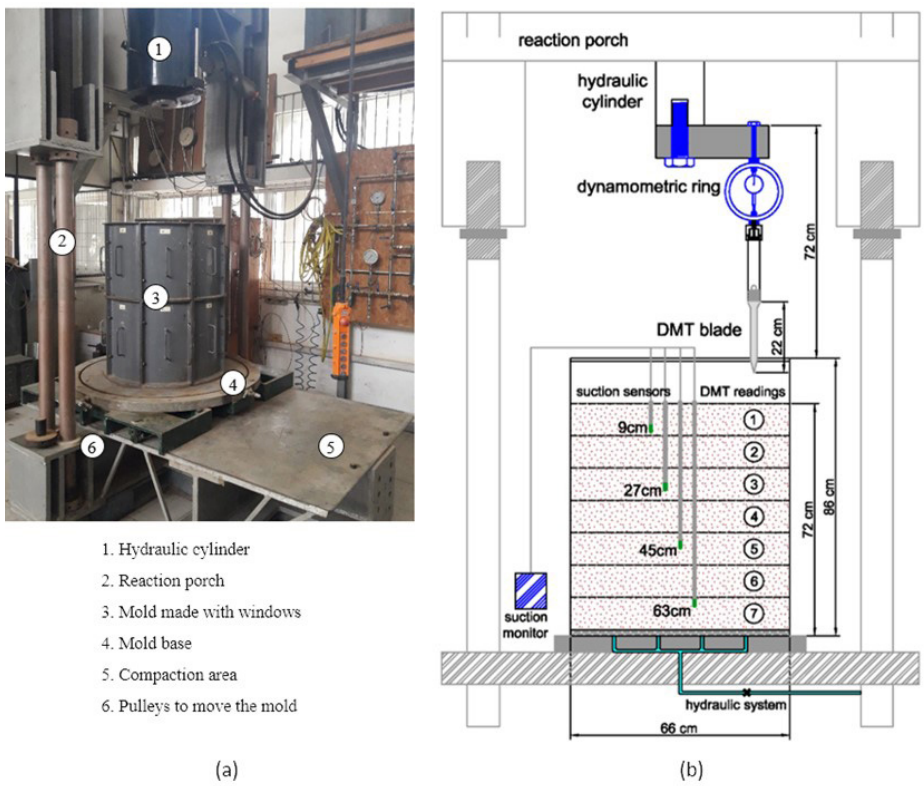

Figure 4. Equipment used for conducting the DMT in the laboratory: (a) general view; (b) schematic section.

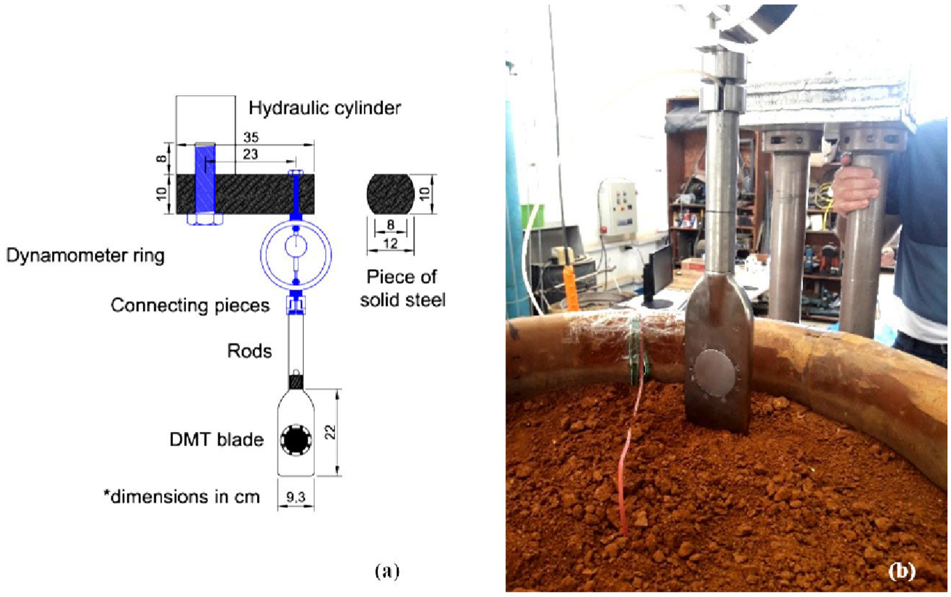

Figure 5. Parts made for driving in the DMT blade: (a) schematic layout (b) DMT blade.

(10-15 cm), the shape of its tip and the measuring system on the side minimize changes to the soil structure. Some experimental studies in sandy soils and mathematical modeling have been carried out to quantify the effect of DMT blade insertion in the soil (Zhongqing et al., 2021; Frost et al., 2016; Melnikov & Boldyrev, 2014). Zhongqing et al. 2021 measured horizontal displacements of 2 mm at a distance of 70 mm from the DMT blade with vertical displacements of 1 to 3 mm in the region close to the diaphragm.

Six tests were performed with the DMT positioned at different locations on the specimen surface (Figure 6), obtaining in each of them 7 readings of parameters *A* and *B*. The first test was performed for the molding conditions, corresponding to the optimum moisture content and maximum dry density of the compaction curve determined with Proctor normal energy.

The second DMT was carried out after sample saturation. The sample saturation was performed with the aid of water flow valves located at the base of the mold, where the water was inserted by low pressure (36 kPa) in the base and top directions of the sample. Saturation was confirmed when all GMS presented suction values are equal to zero. The other 4 DMT were performed as the specimen lost moisture and started to present different suction profiles. The suction profile was continuously monitored and the timing of the DMTs was selected, considering the GMS limit that can measure suctions up to 200 kPa. The insertion of the DMT blade was made statically with a velocity of 20 mm/s, this value being within the range of variation recommended by different standards (TC16 DMT, 2001; ASTM, 2015; Eurocode, 1997; ISO, 2017). In this laboratory experiment, many of the variables could be controlled, such as specimen homogeneity, better control of DMT slide insertion, and ambient conditions

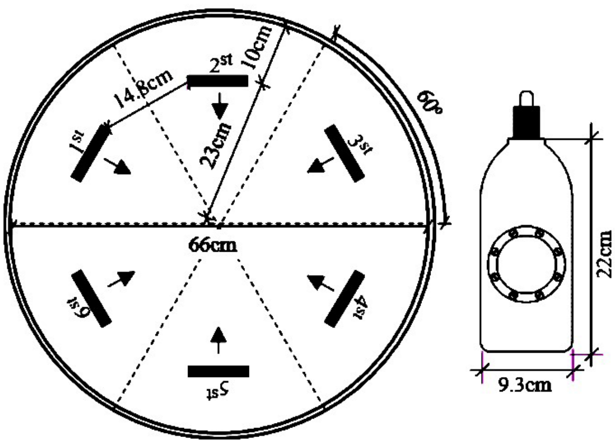

Figure 6. DMT blade insertion position.

related to temperature and relative humidity. There are some limitations such as the small specimen height that allows readings to a depth of 65 cm where the vertical stresses are small. However, the purpose of DMTs is to verify the influence of suction on test results that are all subjected to the same boundary conditions. Thus, suction is the only variable of the tests.

4. Results and discussions

4.1 Characterization of the soil

The soil sample collection point is in the city of Florianópolis/SC, Brazil. According to the geological map by Tomazzoli & Pellerin (2018), in the exact location of the collection point is a diabase dike. The surrounding geological unit is granite.

The laboratory tests carried out had the objective of characterizing the sample collected for the research. Table 1 presents a summary of the results of the granulometric curve, Atterberg limits, unit weight of solids, compaction test, direct shear test and soil classifications. The results of the saturated direct shear tests, obtained for the compacted specimens under the optimum moisture content conditions, are presented in Figure 7. The effective cohesion value and effective angle of internal friction were respectively 8.1 kPa and 34.7°.

4.2 Determination of vertical effective stress profiles

Figure 8 shows the results of the unconfined compressive strength tests as a function of the respective initial suction values obtained with the filter paper technique. The experimental points of this figure represent the projection of each of the 17 tests in the plane defined by the shear strength as a function of suction. This procedure is shown schematically in Figure 2. The curvilinear envelope (Figure 8) fitted to these experimental points represents the cohesion intercept.

For the compacted diabase residual soil used in this study, the variation of the parameter χ, obtained by the relationship between “a” and “b”, presented in Figure 8, for different suction values, was defined by Equation 16. This equation was substituted in Equation 14 to determine the effective vertical stress. The effective vertical stresses, given by Equation 17, were obtained by substituting the value of χ, represented by Equation 16, in Equation 8.

$$\chi = -0.201 \cdot \ln\left(u_a - u_w\right) + 1.5194 \quad (16)$$

$$\sigma'_v = \left(\sigma - u_a\right) + \left[-0.201 \cdot \ln\left(u_a - u_w\right) + 1.5194\right] \cdot \left(u_a - u_w\right) \quad (17)$$

The suction profiles obtained with the GMS and the effective vertical stress profiles are shown in Figure 9. The suction values were defined for the depths of the DMT by interpolation of the GMS readings. It can be observed in Figure 9 that the suction profiles present small variations of values. This indicates that for the maximum depth of the tests (0.65 m) the specimen drying occurred homogeneously. As expected, the effective vertical stresses increase with increasing depth and suction, reaching a maximum value of 85 kPa.

Figure 10 shows the suction monitoring during the 182 days period of the experiment. The results presented in this figure demonstrate the good functioning of the GMS. After the first DMT was performed, for the compaction condition, the specimen saturation was performed. GMS indicated a rapid reduction in suction value to zero. After this step, the specimen was closed to homogenize the moisture content in all its volume. During this period, an initial suction profile was defined, and the top of the specimen was opened.

No variations were observed in the suction values measured by the MSG after the DMT insertion. This can be

Table 1. Summary of the soil characterization tests.

Grain Size Analysis	Clay (%)	27.8
	Silt (%)	29.8
	Fine Sand (%)	16.3
	Medium Sand (%)	20.0
	Coarse Sand (%)	3.9
	Gravel (%)	2.2
Atterberg Limits	W_L (%)	47
	W_P (%)	44
	I_P (%)	3
	GI (Group Index)	3
Unit weight of solids	γ_s (kN/m^3)	28.0
Compaction Test	W_{opt} (%)	30
	γ_d (kN/m^3)	13.9
Direct Shear Test	c' (kPa)	8.1
	ϕ' (°)	34.7
Classifications	HRB	A-5
	USCS	ML

Legend: see List of Symbols

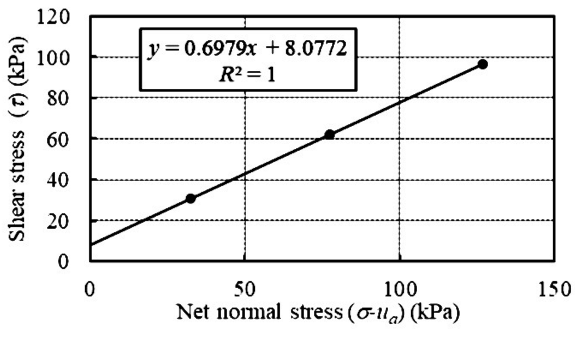

Figure 7. Results of direct shear tests performed under saturated conditions.

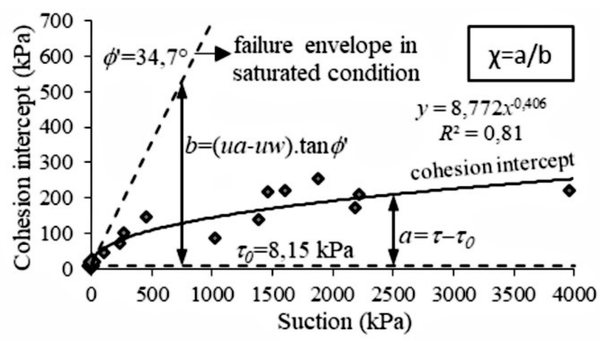

Figure 8. Obtaining parameter χ using the results of unconfined compressive strength tests.

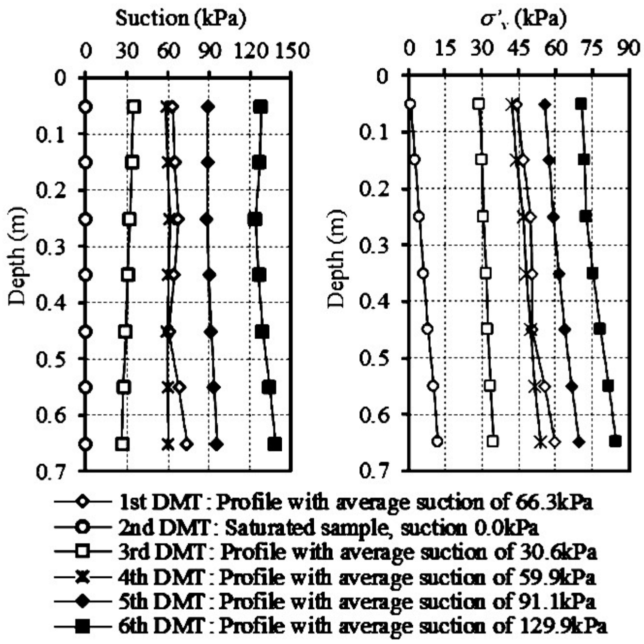

Figure 9. Profiles of suction and effective vertical stress.

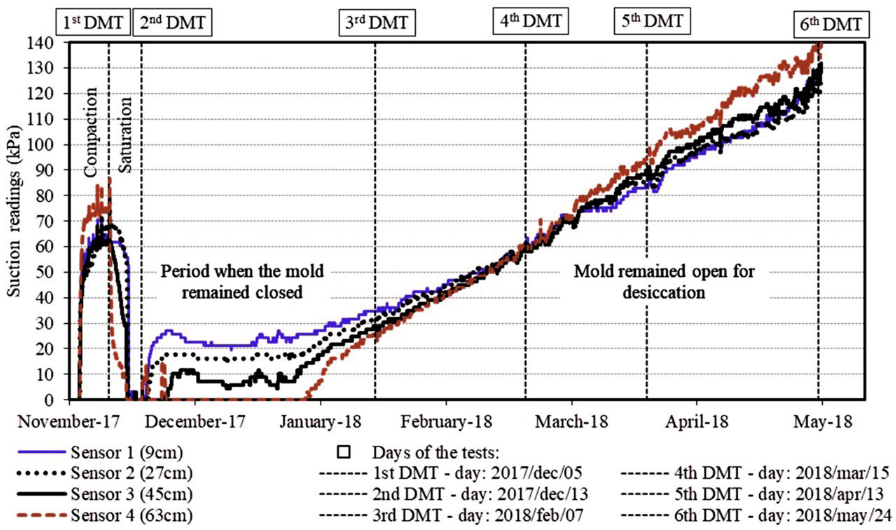

Figure 10. Monitoring of the suction sensors during the experiment.

seen in Figure 10 where the increase in suction in all GMS occurred at a constant rate. This fact indicates that there were no changes in the soil structure at a distance from the DMT blade of the order of 20 cm. Therefore, the distance between the DMT insertion points, indicated in Figure 6, is sufficient to prevent interference between the tests performed on each of the 6 suction profiles. At the end of the tests, the metallic compaction mold was removed, and no cracks were observed on the lateral surface of the specimen, which is at a distance of 10 cm from the DMT driving points (see Figure 6).

4.3 Results of the DMT

This item presents and analyzes the results of the DMT performed on compacted soils for different suction profiles. The results of all tests performed are presented in Table 2. In this table are the test parameters proposed by Marchetti (1980) and the suction profiles associated with each of the 6 DMTs.

Figure 11 presents the values of the pressure readings p_0 and p_1 and q_D, obtained from the DMT blade thrust

Table 2. Parameters of DMT obtained for different suction profiles.

Test	Depth (m)	A (kPa)	B (kPa)	Suction (kPa)	I_D	K_D	E_D (MPa)
1st DMT (Molding)	0.05	160	750	63.3	3.32	3.64	18.6
	0.15	485	1340	64.7	1.72	10.11	28.2
	0.25	490	1370	67.6	1.76	9.55	29.1
	0.35	540	1570	64.6	1.92	10.31	34.6
	0.45	330	1200	60.8	2.62	6.29	28.8
	0.55	550	1540	67.9	1.79	9.58	33.1
	0.65	490	1650	73.6	2.44	7.75	39.3
2nd DMT (Saturation)	0.05	155	610	0.0	2.77	157.50	13.9
	0.15	400	1000	0.0	1.45	138.88	19.2
	0.25	340	960	0.0	1.79	70.03	19.9
	0.35	465	1050	0.0	1.20	69.76	18.6
	0.45	360	1000	0.0	1.75	41.21	20.6
	0.55	440	1080	0.0	1.42	41.64	20.6
	0.65	290	970	0.0	2.37	22.49	22.1
3rd DMT (Drying)	0.05	155	640	34.7	2.80	5.34	15.0
	0.15	410	1080	33.8	1.57	13.24	21.7
	0.25	330	1020	32.2	2.03	10.27	22.5
	0.35	495	1230	30.8	1.44	15.06	24.1
	0.45	380	1040	29.0	1.67	11.32	21.4
	0.55	410	1040	27.6	1.46	11.93	20.3
	0.65	380	1130	26.5	1.95	10.51	24.6
4th DMT (Drying)	0.05	300	1040	58.8	2.40	6.95	24.3
	0.15	480	1330	59.6	1.75	10.55	28.3
	0.25	435	1430	61.2	2.33	8.86	33.6
	0.35	630	1660	60.4	1.65	12.59	34.9
	0.45	510	1400	59.4	1.73	9.98	29.8
	0.55	500	1350	59.9	1.68	9.42	28.3
	0.65	485	1490	60.4	2.11	8.65	34.0
5th DMT (Drying)	0.05	245	780	88.9	1.91	4.55	16.8
	0.15	410	1300	88.8	2.14	6.97	29.7
	0.25	450	1580	88.5	2.59	7.24	38.5
	0.35	580	1770	89.8	2.11	9.04	40.7
	0.45	445	1520	91.3	2.46	6.68	36.5
	0.55	520	1640	93.7	2.20	7.49	38.1
	0.65	580	1730	95.7	2.02	8.06	39.2
6th DMT (Drying)	0.05	440	1000	128.1	1.13	6.43	17.7
	0.15	455	1410	126.7	2.06	6.24	32.1
	0.25	470	1550	124.0	2.31	6.28	36.7
	0.35	530	1780	126.2	2.43	6.76	42.9
	0.45	460	1710	129.0	2.81	5.63	42.9
	0.55	645	1850	134.2	1.89	7.68	41.2
	0.65	580	1920	138.4	2.39	6.56	46.1

resistance with the dynamometric ring, mounted on the thrust rods. There is an influence of suction both in the pressure profiles p_0 and p_1, and in the DMT blade thrust resistance (q_D). Regarding pressures p_0 and p_1, the values of p_1 have the highest variations concerning suction increase. Parameter p_0 presents the lowest variations, probably because the reading being carried out in a region of the sample disturbed by the insertion of the blade. The value of the parameter p_1, obtained when the movement of the membrane center reaches 1.1 mm, is directly associated with the stiffness of the soil resulting from the compaction process. It can be observed in Figure 11c that the tip resistance (q_D) increases with depth. This fact is associated with the increase in confining pressure and suction. However, suction has a greater influence on the increase in tip resistance (q_D). The values of p_0 and p_1 of each of the profiles presented in Figure 11, obtained for different

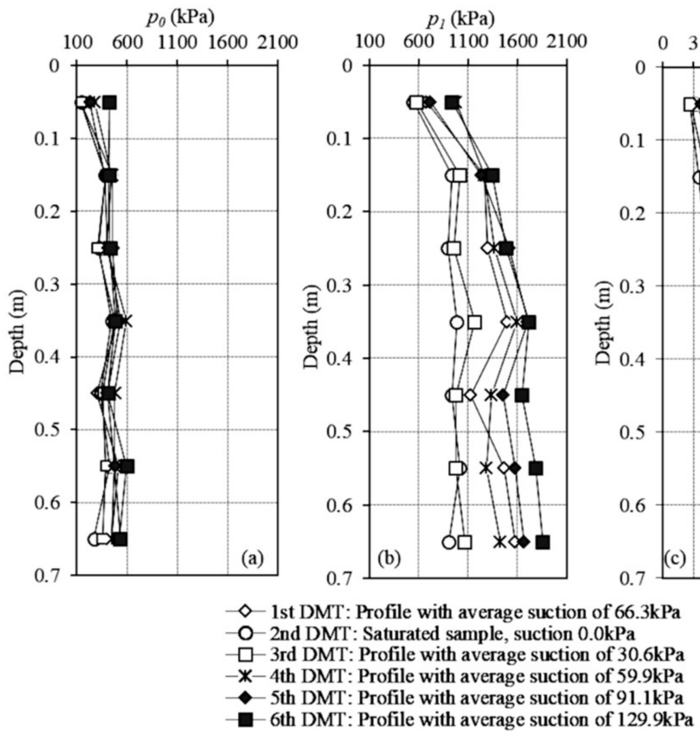

Figure 11. Readings of pressures (a) p_0 and (b) p_1 and tip resistance (c) q_D.

levels of suction, are plotted in Figure 12. This graph shows an increasing trend for pressures p_0 and p_1 as a function of suction when compared to the linear adjustments applied to the experimental points.

Figure 13 presents the profiles for the intermediate parameters I_D, K_D and E_D, obtained from the data from the DMT. The I_D and K_D parameters were obtained by Equations 13 and 14, respectively. When the suction value is equal to zero (2nd DMT) these equations become equal to the equations proposed by Marchetti (1980) for saturated soils.

For the calculation of I_D and K_D, the value of Poisson's ratio (ν), in Equations 13 and 14, was considered constant and equal to 0.3. This value was obtained by equating the equation for the value of K_0, proposed by Jaky (1944), with Equation 15 considering suction equal to zero in this equation. In this way, the value of Poisson's ratio was calculated by Equation 18.

$$K_0 = 1 - sen\phi' = \frac{\nu}{1-\nu} \tag{18}$$

The material index parameter (I_D), presented in Figure 13a, varies around an average value for each of the suction profiles, without presenting an increasing or decreasing trend according to depth. However, there is a slight influence of suction, and so the I_D values are higher for higher suction values, as can be seen in Figure 14.

The parameter I_D classified the compacted sample between sandy silt and silty sand, different from the particle size distribution test conducted in the soil sample, which classified the soil as silty clay. This behavior is justified by the fact that the I_D parameter reflects the mechanical performance of the soil.

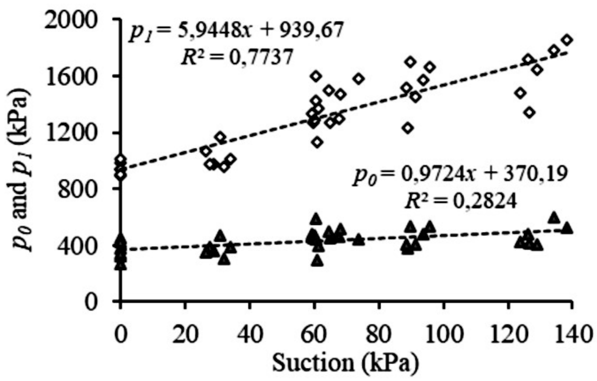

Figure 12. Relationship between the readings p_0 and p_1 and suction.

As for the horizontal stress index parameter (K_D), presented in Figure 13b, the values obtained experimentally show a great influence from increases in suction values. The results of 2nd DMT are not plotted in this figure. The profile of the 2nd DMT, in the saturated condition, shows a value of 157.5 on the surface of the specimen followed by a reduction of value to 22.5 at a depth of 0.65 m. Those values are very high and are directly related to the small values of vertical stresses (σ'_v) limited by the maximum depth of the laboratory test,

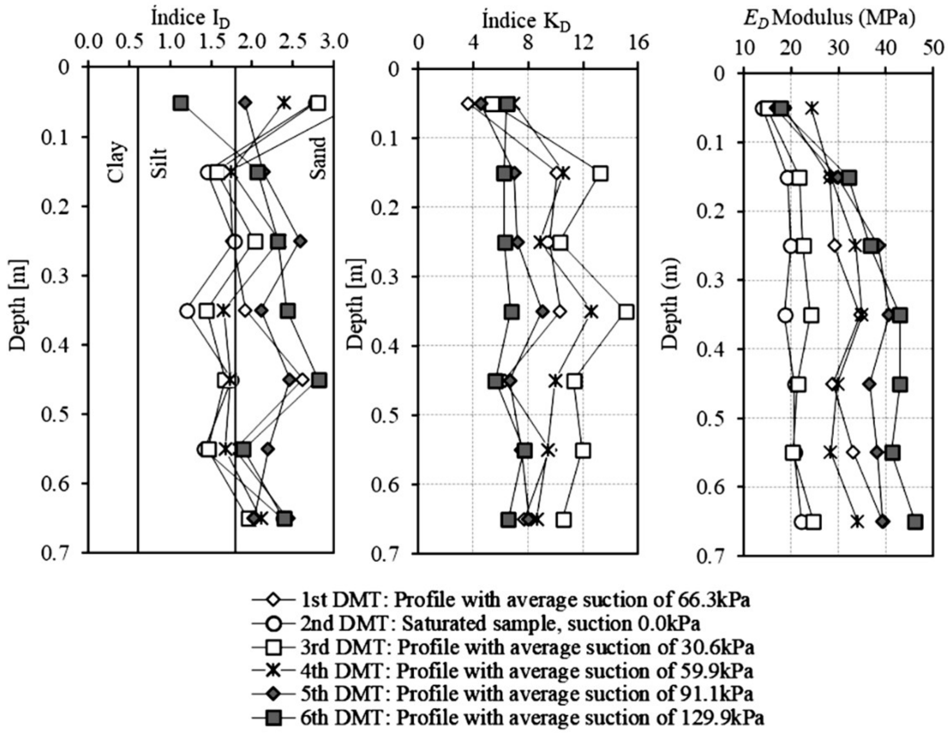

Figure 13. Profiles for the parameters: (a) I_D, (b) K_D and (c) E_D.

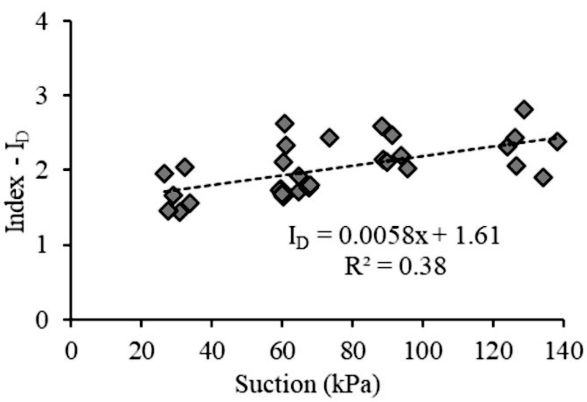

Figure 14. Relationship between I_D and suction.

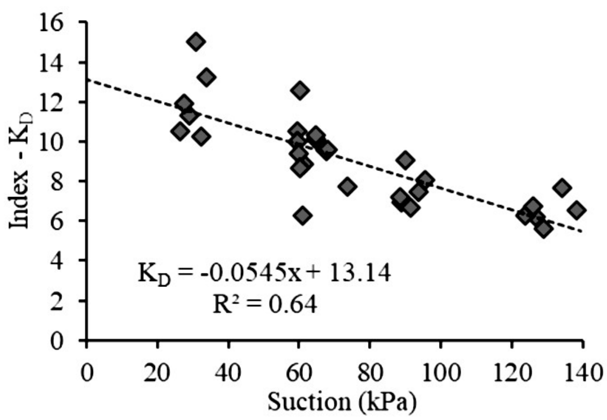

Figure 15. Relationship between K_D and suction.

which is a limitation of this research. To avoid anomalous K_D values, they are often plotted to depths greater than 1 m.

For profiles that have a specific suction value, the K_D values do not tend to increase or decrease with depth, oscillating around an average value. The K_D values of these profiles ranged from 4.2 to 15.5. However, as can be observed in Figure 15, there is a tendency of decreasing K_D values with an increase of suction. As the matrix suction of the soil increases, there is a reduction in horizontal stress (Fredlund & Rahardjo, 1993). This reduction in horizontal stress, which varies as a function of depth, causes a reduction in the K_0 value.

The profiles for the dilatometer modulus parameter (E_D), presented in Figure 13c, show that E_D increases up to the depth of 35 cm, with a tendency to remain constant at further depths. The E_D range varied between 13.9 and 46.1 MPa, with a mean of 28.8 MPa. In Figure 16 are plotted the values of E_D as a function of suction in all the experimental points. The E_D values increase with increasing suction, showing a good correlation coefficient (R^2 = 0.82). Many studies have verified an increase in the modulus of deformability and shear resistance in compacted residual soils as a function of an increase in suction (Oliveira, 2004; Pecapedra, 2016; Bernardi, 2018).

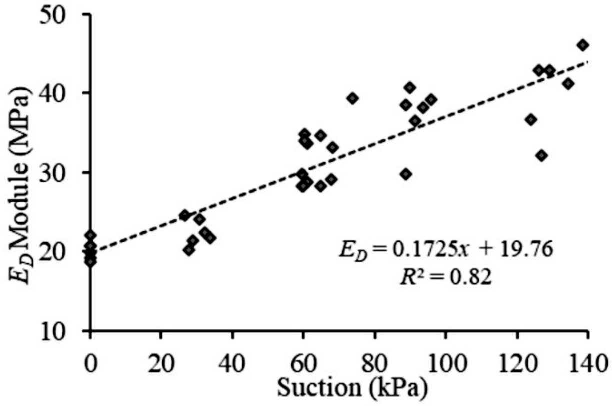

Figure 16. Relationship between E_D and suction.

5. Conclusions

The experimental results of this research verified the suction influence on the readings measured during the DMT in the compacted soil. It was suggested that the equations for material index I_D and horizontal stress index K_D should be adapted, inserting the variable suction in them. This had the objective to adapt the equation to be used in data from tests carried out on unsaturated soils. The use of the effective vertical stress equation proposed Bishop (1959), which incorporates suction, has also been suggested. In this equation, the variation of the parameter *c'* as a function of suction was defined using the cohesion intercept obtained with the results of uniaxial compression tests. In this equation, the variation of the parameter χ as a function of the suction was defined using the cohesion intercept obtained with the results of uniaxial compression tests. In these tests, the initial suction of the specimens were determined using the filter paper technique. As a simplifying hypothesis, the value of Poisson's ratio of the equations obtained for I_D and k_D was considered constant and equal to 0.3.

With the increase in the suction value, the parameters I_D and E_D showed a tendency to increase values and the K_D value showed a tendency to decrease in value. When going from the saturated condition (2nd DMT) to the suction of the order of 130 kPa (6th DMT) the Id value changed from 1.8 to 2.1, showing an increase of 18%. For this same suction interval, the value of *Ed* increased from 19.3 kPa to 37.1 kPa, showing an increase of 92%. The K_D value obtained for the saturated condition was equal to 12, reducing to 6.5 when the average suction of the soil profile was equal to 130 kPa, thus presenting a reduction of 46%. The variations in the I_D, K_D and E_D values, with the increase of suction, are compatible with the mathematical models and the experimental results obtained by other researchers. The relationships proposed in this research for the calculation of I_D and K_D, incorporating the suction value, provided coherent values. It was found that the DMT correctly detected the influence of suction on the geotechnical parameters analyzed.

Acknowledgements

The authors are grateful to the Soil Mechanics Laboratory of the Federal University of Santa Catarina where the tests were performed. Additional thanks to the third author for his participation in conducting the tests and to the fourth author who provided the granular matrix suction sensors.

Declaration of interest

There were no competing interests or conflicts of interest associated with the conduct of this research or the development of this paper.

Authors' contributions

Cândida Bernardi: conceptualization, data curation, formal analysis investigation, methodology, resources, project administration, supervision, validation, visualization, writing – original draft, writing – review & editing. Orlando Martini de Oliveira: conceptualization, investigation, methodology, resources, project administration, supervision, validation, writing – review & editing. Murilo da Silva Espíndola: investigation, resources. Rafael Augusto dos Reis Higashi: funding acquisition, resources.

List of symbols

c'	Effective cohesion
DMT	Marchetti dilatometer test
E_D	Parameter related to the soil deformability modulus
E	Modulus of elasticity for the soil structure related to a change in (σ-u_a)
HRB	Highway Research Board soil classification
H	Modulus of elasticity for the soil structure related to a change in (u_a-u_w)
I_D	Parameter related to soil type
I_p	Plasticity index
K_D	Parameter related to the over-consolidation ratio (OCR) and coefficient of earth pressure at-rest (K_0)
K_0	Coefficient of earth pressure at-rest
K_D	Horizontal stress index
OCR	Overconsolidation ratio
p_1	Pressure obtained from the DMT
p_0	Pressure obtained from the DMT
USCS	Unified Soil Classification System
u_a	Air pressure
u_w	Pore water pressure
$(u_a$-$u_w)$	Suction
w_l	liquid limit
$w_{opt.}$	Optimum moisture content
w_p	Plastic limit
Z_m	Gage reading when vented to atmospheric pressure
Z	Reading depth

ΔA	DMT membrane calibration readings
ΔB	DMT membrane calibration readings
ϕ'	Effective angle of internal friction
γ_d	Dry unit weight
γ_s	Unit weight of the solid particles
σ'	Effective stress
σ	Total stress
σ_v	Normal vertical stress
S	Degree of saturation
Su	Undrained shear strengths
τ	Shear strength
τ_0	Shear strength in saturated conditions
υ	Poisson's ratio
χ	Coefficient related to the degree of saturation of the soil

References

Abrantes, L.G., & Campos, T.M.P. (2018). Evaluation of the coefficient of earth pressure at rest (Ko) of a saturated-unsaturated colluvium soil. In *7th International Symposium on Deformation Characteristics of Geomaterials* (Vol. 92, pp. 07006). Les Ulis: EDP Sciences. https://doi.org/10.1051/e3sconf/20199207006.

ASTM D2166M-16. (2016). *Standard test method for unconfined compressive strength of cohesive soil*. ASTM International, West Conshohocken, PA. http://doi.org/10.1520/2166_D2166M-16.

ASTM D3080M-11. (2011). *Standard test method for direct shear test of soils under consolidated drained conditions*. ASTM International, West Conshohocken, PA. http://doi.org/10.1520/D3080_D3080M-11.

ASTM D6635-15. (2015). *Standard test method for performing the flat plate dilatometer*. ASTM International, West Conshohocken, PA. http://doi.org/10.1520/D6635-15.

Bernardi, C. (2018). *Study of the use of the Marchetti Dilatometer test in a compacted residual soil with evaluation of the influence of suction* [Master's dissertation]. Federal University of Santa Catarina (in Portuguese).

Bishop, A.W. (1959). The principle of effective stress. *Teknisk Ukeblad*, 106(39), 859-863.

Bishop, A.W., Alpan, J., Bligth, G.E., & Donald, I.B. (1960). Factors controlling the strength of partly saturated cohesive soils. In *Research Conference Shear Strength of Cohesive Soils* (pp. 503-532). USA: ASCE.

Borden, R.H., Lowder, W.M., & Khosla, N.P. (1985). Evaluation of pavement subgrade support characteristics by dilatometer test. *Transportation Research Record: Journal of the Transportation Research Board*, (1012), 120-127.

Chandler, R.J., Crilly, M.S., & Montgomery-Smith, G. (1992). A low-cost method of assessing clay desiccation for low-rise buildings. *Proceedings - Institution of Civil Engineers*, 92(2), 82-89.

Cruz, N. (2010). *Modelling geomechanics of residual soils with DMT tests* [PhD thesis]. University of Porto. https://hdl.handle.net/10216/60207.

Cruz, N., & Fonseca, A.V. (2006). Characterization of stiff residual soils by dynamically push-in DMT. *Geotechnical Special Publication*, 149, 261-268.

Cruz, N., Rodrigues, C., & Fonseca, A. V. (2012). Design parameters of Portuguese granitic residual soils obtained from DMT tests. *International Journal of Geotechnical Engineering*, 6(2), 239-244. http://dx.doi.org/10.3328/IJGE.2012.06.02.239-244.

Cruz, N., Rodrigues, C., & Viana da Fonseca, A. (2014). An approach to derive strength parameters of residual soils from DMT results. *Soils and Rocks*, 37(3), 195-209. Retrieved in October 17, 2021, from https://soilsandrocks.com/sr-373195

Daylac, R. (1994). *Development and use of a cell for K0 measurement with suction control* [Master's dissertation]. PUC Rio de Janeiro (in portuguese).

Einav, I., & Liu, M. (2020). The effective stress of unsaturated soils: thermodynamic connections to intrinsic and measured suctions. In: P. Giovine, P.M. Mariano & G. Mortara (Eds.), *Views on microstructures in granular materials: advances in mechanics and mathematics* (Vol. 44). Birkhäuser. https://doi.org/10.1007/978-3-030-49267-0_3.

Espíndola, M. (2016). *Large-scale triaxial tests on rock samples from the Machadinho UHE* [PhD thesis]. Federal University of Santa Catarina (in Portuguese).

Eurocode 7. (1997). *Geotechnical design - Part 3: Design assisted by field testing, Section 9: Flat dilatometer test (DMT)*. European Committee for Standardization (CEN).

Fredlund, D.G., & Rahardjo, H. (1993). *Soil mechanics for unsaturated soils.* John Wiley & Sons Inc.

Fredlund, D.G., Rahardjo, H., & Fredlund, M.D. (2012). *Unsaturated soil mechanics in engineering practice.* John Wiley & Sons.

Frost, J.D., Matinez, A., Su, J., & Xu, T. (2016) Discrete Element Method modeling studies of the interactions between soils and in-Situ testing devices. In *International Conference on Geotechnical and Geophysical site Characterizations* (Vol. 1, pp. 431-436). London: ISSMGE.

Giacheti, H.L., Mio, G., & Carvalho, D. (2006). Flat dilatometer testing in brazilian tropical soils. In *The Second International Flat Dilatometer Conference* (pp. 102-110). London: ISSMGE.

Hummes, R.A., & Maccarini, M. (2009). *Development of a large triaxial equipment for rockfills*. ANEEL P&D Tractebel Energia S.A. (in portuguese).

ISO 22476-11:2017(E). (2017). *Geotechnical investigation and testing – Field testing – Part 11: Flat dilatometer test*. International Organization for Standardization, Geneva, Switzerland.

Jaky, J. (1944). The coefficient of earth pressure at rest. *Journal of Society of Hungarian Architects and Engineers*, 78(22), 355-358.

Jamiolkowski, M., Ghionna, V.N., Lancellotta, R., & Pasqualini, E. (1988). New correlations of penetration test for design practice. In *International Symposium on Penetration Testing* (Vol. 1, pp. 263-296). Rotterdam: Balkema.

Jennings, J.E.B., & Burland, J.B. (1962). Limitations to the use of effective stresses in partly saturated soils. *Geotechnique*, 12(2), 125-144. http://dx.doi.org/10.1680/geot.1962.12.2.125.

Khalili, N., & Khabbaz, M.H.A. (1998). Unique relationship for χ for the determination of the shear strength of unsaturated soils. *Geotechnique*, 48(5), 681-687. Retrieved in October 17, 2021, from https://www.icevirtuallibrary.com/doi/abs/10.1680/geot.1998.48.5.681

Lacasse, S., & Lunne, T. (1988). Calibration of dilatometer correlations. In *International Symposium on Penetration Testing* (Vol. 1, pp. 537–548). Rotterdam: Balkema.

Lu, N., & Likos, W.J. (2004). *Unsaturated soil mechanics.* John Wiley & Sons.

Lutenegger, A.J. (1988). Current status of the Marchetti dilatometer test. In *International Symposium on Penetration Testing* (Vol. 1, pp. 137–155). Rotterdam: Balkema.

Machado, S.L., & Vilar, O.M. (1998). Shear strength of unsaturated soils: laboratory tests and expeditions determination. *Soils and Rock*, 21(2), 65-78. [in portuguese]

Marchetti, S. (1975). A new in situ test for the measurement of horizontal soil deformability. In *Proceedings of the Conference on In Situ Measurement of Soil Properties* (pp. 255–259). Raleigh: ASCE.

Marchetti, S. (1980). In situ tests by flat dilatometer. *Journal of Geotechnical Engineering*, 106(3), 299-321. Retrieved in October 17, 2021, from https://ascelibrary.org/doi/10.1061/AJGEB6.0000934

Marchetti, S., & Monaco, P. (2018). Recent improvements in the use, interpretation, and applications of DMT and SDMT in practice. *Geotechnical Testing Journal*, 41(5), 837-850. http://dx.doi.org/10.1520/GTJ20170386.

Marchetti, S., Monaco, P., Totani, G., & Calabrese, M. (2001). The flat dilatometer test (DMT) in soil investigations: a report of the ISSMGE Technica1 Committee TC16. In *Proceedings from the Second International Flat Dilatometer Conference*. London: ISSMGE.

Massocco, N.S. (2017*). Determination of geotechnical parameters of residual soils with emphasis on the mechanics of unsaturated soils* [Master's dissertation]. Federal University of Santa Catarina (in Portuguese).

Melnikov, A.V., & Boldyrev, G.G. (2014). Experimental study of sand deformations during a CPT. In P.K. Robertson & K.L. Cabal (Eds.), *The 3rd International Symposium on Cone Penetration Testing*, Vegas, Nevada (pp. 339-345). Las Vegas, Nevada, USA: ISSMGE.

Mesri, G., & Hayat, T.M. (1993). The coefficient of earth pressure at rest. *Canadian Geotechnical Journal*, 30(4), 647-666. http://dx.doi.org/10.1139/t93-056.

Oh, S., Lu, N., Kim, T.K., & Lee, Y.H. (2013). Experimental validation of suction stress characteristic curve from non-failure triaxial *K0* consolidation tests. *Journal of Geotechnical and Geoenvironmental Engineering*, 139, 1490-1503. http://dx.doi.org/10.1061/(ASCE)GT.1943-5606.0000880.

Oliveira, O.M. (2004). *Study on the shear strength of a compacted residual soil unsaturated* [Doctoral thesis]. University of São Paulo (in portuguese).

Oliveira, S.A.G. (1998). *An odometric cell for measuring horizontal stress in unsaturated soils* [Master's Dissertation]. University of Brasilia (in Portuguese).

Pecapedra, L.L. (2016). *Study of the resistance to unsaturated shearing of residual soils of granite and diabase of Florianópolis/SC* [Master's Dissertation]. Federal University of Santa Catarina (in Portuguese).

Pecapedra, L.L., Oliveira, O.M., & Higashi, R.A.R. (2018). Analysis of the cohesion intercepts of a compacted diabase residual soil in three different molding conditions. In *XIX Congresso Brasileiro de Mecânica dos Solos e Engenharia Geotécnica* (pp. 1–9). Salvador, Brazil: ABMS. (in Portuguese).

Peixoto, R.J. (1999). *Application of constitutive models in the evaluation of the mechanical behavior of the federal district collapsible porous clay* [Master's Dissertation]. University of Brasilia (in portuguese).

Pereira, J.M., Coussy, O., Alonso, E.E., Vaunat, J., & Olivella, S. 2010. Is the degree of saturation a good candidate for Bishop's χ parameter? In *Proceedings of the 5th International Conference on Unsaturated Soils*, Barcelona, Spain (pp. 913-919). Boca Raton: CRC Press.

Pirjalili, A., Golshani, A., & Mirzaii, A. (2016). Experimental study on the coefficient of lateral earth pressure in unsaturated soils. In *Proceedings of the 3rd European Conf on Unsaturated Soil* (Vol. 9, p. 05003). Les Ulis: EDP Sciences.

Rocha, B.P., Rodrigues, R.A., & Giacheti, H.L. (2021). The flat dilatometer test in an unsaturated tropical soil site. *Journal of Geotechnical and Geological Engineering*, 39, 5957-5969. http://dx.doi.org/10.1007/s10706-021-01849-1.

Silva, F.K. (2008). *Dilatometric tests - DMT in Santa Catarina soils: comparative study with CPT and SPT* [Master's dissertation]. Federal University of Santa Catarina (in Portuguese).

TC16 DMT. (2001). *The Flat Dilatometer Test (DMT) in Soil Investigations: a report by the ISSMGE Committee TC16*, Washington, DC.

Tomazzoli, E.R., & Pellerin, J.R.G.M. (2018). Geology of the Santa Catarina Island, Santa Catarina state, Brazil. *Geociências*, 37(4), 715-731. [in Portuguese]

Vaunat, J., & Casini, F. (2017). A procedure for direct determination od Bishop's χ parameter from changes in pore size distribution. *Geotechnique*, 67(7), 631-636. http://dx.doi.org/10.1680/jgeot.15.T.016.

Zhang, R., Zheng, J.L., & Yang, H.P. (2009). Experimental study on K0 consolidation behavior of recompacted unsaturated expansive soil. In *GeoHunan International Conference* (Vol. 192, pp. 27-32). EUA: ASCE. https://doi.org/10.1061/41044(351)5.

Zhongqing, H.E.N., Tianyu, W.U., Yanbin, G.A.O., Yue, L.Y.U., & Shuai, L.I.U. (2021). An experimental study of the displacement characteristics of dry sand under dilatometer penetration. *Journal Hydrogeology & Engineering Geology*, 48(3), 119-125. Retrieved in October 17, 2021, from https://kns.cnki.net/kcms/detail/detail.aspx?doi=10.16030/j.cnki.issn.1000-3665.202008046

Soils and Rocks
An International Journal of Geotechnical and Geoenvironmental Engineering
www.soilsandrocks.com
ISSN 1980-9743
ISSN-e 2675-5475

Desiccation characteristics and direct tension attributes of thin clayey soil containing discrete natural fibers

Abu Taiyab[1#], Nazmun Naher Islam[2], Mokhlesur Rahman[3]

Article

Keywords
Desiccation coefficient
Desiccation crack
Fiber reinforcement
Tensile strength
Toughness

Abstract
The use of thin clayey soil as a liner plays an important role in many geotechnical and geo-environmental engineering applications, such as open channel and reservoir sealant, contaminant barrier etc. Their functional performance and sustainability depend primarily on the desiccation characteristics of these liners and barriers. A number of studies have been undertaken to quantify the degree of improvement achieved by using natural and synthetic fiber reinforcement. However, there is a lack of studies to understand the desiccation behavior of reinforced clay. This study aimed to explore the desiccation and cracking behavior of clayey soil reinforced with two natural fibers (coir and jute fiber) in addition to the degree of improvement in tensile strength. A series of direct tension and desiccation cracking tests have been conducted in the laboratory on clay-coir and clay-jute fiber mixes. The results demonstrate that when coir and jute fibers are used, the tensile strength of fiber-reinforced soil rises by up to 475 percent and 215 percent, respectively, when compared with the tensile strength of unreinforced soil at the same moisture content. Desiccation test results also show that blending of fibers reduces the breadth and depth of cracks significantly. The characteristics of unreinforced and fiber-reinforced clayey soil under desiccation and direct tension are briefly discussed in this paper. Findings of the present study will be important for professionals dealing with clay liners and trying to reduce cracking problems associated with drying soil.

1. Introduction

Desiccation cracking of clayey soils is a worldwide problem in many engineering applications such as earthen embankments for roads and dams, open channels, reservoirs, sanitary landfill barriers, etc. Such cracking causes notable problems with earthen roads, embankments, slopes, and foundations (Li et al., 2009). Desiccation cracks in clay liners underlying sanitary waste landfills cause serious geo-environmental concerns (Daniel & Brown, 1987; Peron et al., 2009b). Failures of clay levees are found to be initiated by penetrating water into desiccation fissures (Utili et al., 2008). As documented in literature, desiccation cracks are initiated when the minor principal stress exceeds its tensile strength (Albrecht & Benson, 2001; Konrad & Ayad, 1997).

Many researchers investigated the mechanism of cracking of unreinforced clay under various conditions (Lau, 1987; Morris et al., 1992; Colina & Roux, 2000; Vogel et al., 2005; Kodikara & Choi, 2006; Peron et al., 2009a; Tang et al., 2011a; Li & Zhang, 2011; Lakshmikantha et al., 2012; Costa et al., 2013; Li, 2014; Shokri et al., 2015; Khatun et al., 2015). The factors influencing desiccation cracking are soil mineral composition, clay content, initial moisture content and soil density (Albrecht & Benson, 2001; Tang et al., 2008; Shinde et al., 2012; Silva et al., 2013; Lu et al., 2015; Jayanthi et al., 2017). The boundary conditions, temperature and humidity also have influences on the desiccation cracking behavior of unreinforced clay (Tang et al., 2010; Uday & Singh, 2013; DeCarlo & Shokri, 2014; Uday et al., 2015; Lakshmikantha et al., 2018).

The desiccation rate of unreinforced clay is higher at smaller thicknesses. Cracking water content is higher for thicker clay layers (Nahlawi & Kodikara, 2006; Tang et al., 2011c; Tollenaar et al., 2017). The average length and width of cracks as well as crack density increase with the increase in clay layer thickness (Tang et al., 2008; Guo et al., 2018). Initiation of desiccation crack will be delayed due to the inclusion of fiber reinforcement in clayey soil. The addition of discrete fiber in clayey soil reduces shrinkage, extent of desiccation cracking and total cracked area (Chaduvula et al., 2017; Jayasree et al., 2015; Ziegler et al., 1988). A number of

[#]Corresponding author. E-mail address: mataiyab@duet.ac.bd
[1]Dhaka University of Engineering & Technology, Department of Civil Engineering, Gazipur, Bangladesh.
Submitted on August 21, 2021; Final Acceptance on August 21, 2022; Discussion open until February 28, 2023.
https://doi.org/10.28927/SR.2022.074421

researchers (Anggraini et al., 2015a, b; Capilleri et al., 2019; Correia et al., 2015; Enokela & Alada, 2012; Li et al., 2014) investigated the strength and toughness of fiber reinforced clayey soil in direct and indirect tension. A significant improvement in the tensile strength and toughness of reinforced soil has been reported from their studies.

It is evident that a number of studies have been undertaken to realize the extent of desiccation cracking of fiber reinforced clayey soil. But, the desiccation characterization of clayey soil mixed with randomly distributed fibers is yet to be explored. An understanding of desiccation and direct tension behavior of thin clayey soil containing fiber reinforcement will be helpful for proper use of discrete fiber as reinforcement in clay liners and covers. In this paper, the desiccation rate, cracking water content, tensile strength, toughness etc. of thin clayey soil of varying thicknesses with a range of fiber contents are presented. Relationships among the reinforced clay layer thickness, cracking water content, and desiccation rate have been developed. Details of the investigation program and outcomes are presented in the following sections.

2. Materials and methods

2.1 Materials

The raw materials used for the current investigation were clayey soil, coir and jute fiber. The clayey soil was collected from the marshy land of Gazipur City Corporation, Bangladesh. The properties of the soil are shown in Table 1. Coir was extracted from coconut husks. The collected coir was cleaned with potable water without the use of chemical additives and dried at room temperature. Before fixing the length of fibers, different lengths of fiber were used in the trial samples. Based on their consistent results, the length of the fibers has been fixed. Then the fibers were cut into the required lengths by scissors. The jute fiber used in this study was collected from the local market and cut into desired lengths. Figure 1 and Figure 2 show the coir and jute fibers used in the present study. The properties of coir and jute fiber are listed in Table 2.

2.2 Direct tension sample preparation and testing

This study aimed at exploring direct tension behavior at and around the optimum moisture content of reinforced clayey soil. So, a number of compaction tests are conducted following the ASTM standard method (ASTM, 2007) on base soil and soil-fiber mixtures to determine the *OMC*. The test results of compaction tests are summarized in Table 3. The direct tension test is an appropriate method to determine the tensile strength of clayey soil as the tensile stress and strength can be directly obtained (Tang et al., 2015). A simplified direct tension test mold was fabricated for this study. A photograph of the direct tension test mold is shown in Figure 3(a). The length and thickness of the test specimen are 90 mm and 25.5 mm respectively. The cross-

Figure 1. A photograph of the coir used in this study.

Figure 2. A photograph of the jute fibers used in this study.

Table 1. Properties of soil used in this study.

Item	Natural moisture content (%)	Specific gravity	Liquid limit (%)	Plastic limit (%)	Optimum moisture content (%)	Maximum dry unit weight (kN/m³)	Unconfined compressive strength (kN/m²)	Unified soil classification
Symbol	w_n	G_s	LL	PL	OMC	$\gamma_{d(\max)}$	q_u	-
Result	23.6	2.63	38	21	17	16.67	73.2	CL

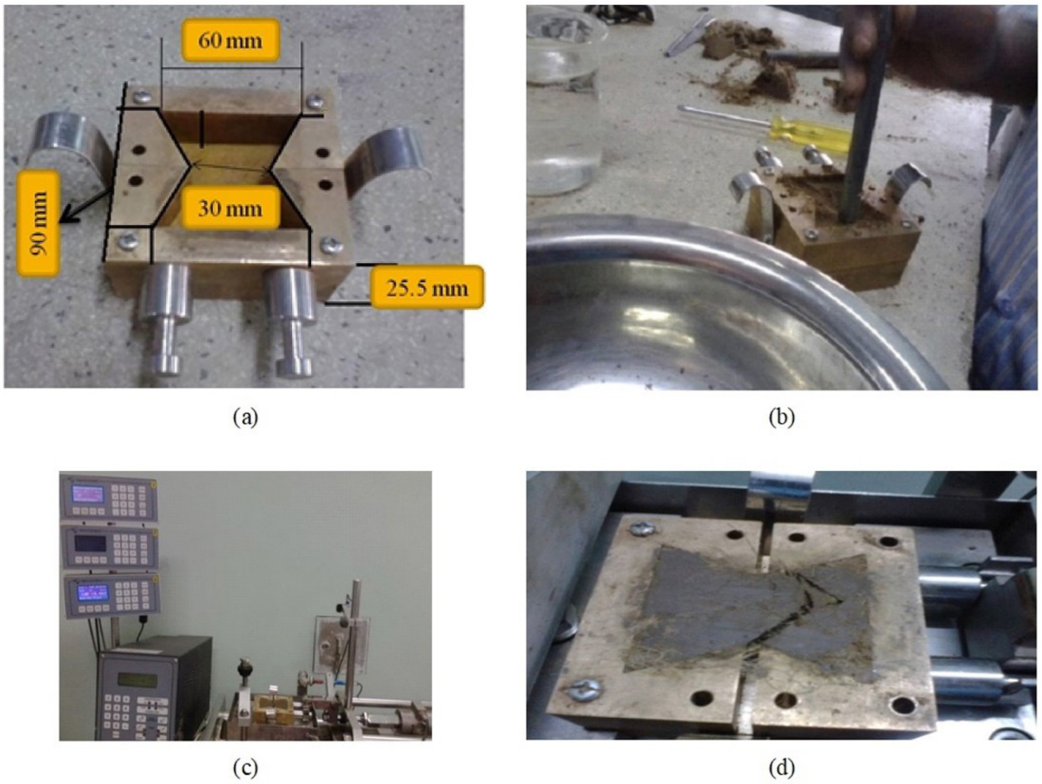

Figure 3. (a) Dimensions of direct tension test mold, (b) compaction in the mold, (c) sample placed in direct tension test device, and (d) sample after test.

Table 2. Properties of coir and jute fiber used in this study.

Fiber type	Color	Mean diameter (mm)	Average length (mm)	Aspect ratio	Fiber contents (%)
Coir	Brown	0.25	25	100	1.0, 2.0, 3.0
Jute fiber	Brown	0.1	30	300	0.5, 1.0, 2.0

Table 3. Summary of compaction tests.

Specimen type	Maximum dry unit weight (kN/m^3)	Optimum moisture content (%)
Base Soil	16.67	17.0
Soil + 1% Coir	16.32	18.0
Soil + 2% Coir	15.21	19.0
Soil + 3% Coir	14.10	20.0
Soil + 0.5% Jute Fiber	16.58	18.5
Soil + 1% Jute Fiber	16.00	20.0
Soil + 2% Jute Fiber	15.33	22.0

sectional dimension of the specimen at the neck is 30 mm × 25.5 mm. To minimize friction between the soil and the bottom surface of the mold, the bottom surface of the mold was lubricated prior to placement of the testing materials at the time of preparing the test specimen. After the specimen was compacted, the sample with the compaction mold was placed into the testing equipment. Figure 3(b) to Figure 3(d) show the compaction of the specimen, test equipment and specimen after failure respectively. The stress and strain readings are recorded at an interval of 15 seconds. And, the rate of deformation was maintained at 1 mm/min throughout the test to have a sufficient number of readings to capture the shape of the stress-strain curve accurately. The total loading time required for the tests on reinforced samples was about 8 minutes. Finally, the tensile strength (σ_t) was calculated by dividing the maximum tensile load (P_{max}) by the cross-sectional area (i.e., 30 mm × 25.5 mm).

2.3 Desiccation testing procedure

The desiccation cracking tests were conducted using metal molds with a rectangular cross section. To induce parallel cracking during the drying of soil, the lengths of the molds were significantly larger than the widths. Table 4 shows the mold dimensions. The room temperature was maintained at 30 ^{0}C to 35 ^{0}C during these tests. During this testing, the relative humidity was kept between 62 percent and

Table 4. Summary of desiccation cracking tests.

Mold type	Mold dimensions ($L \times W \times D$) (mm)	Number of molds used	Initial water content (%)	Relative humidity (%)	Materials of mold used
A	600×25×30	5	38	62-65	Metal
B	600×25×20	5	38	62-65	Metal
C	600×50×10	5	38	62-65	Metal
D	600×25×5	5	38	62-65	Metal

Legend: L = Length, W = Width and D = Depth.

65 percent. To ensure moisture uniformity, the base soil and soil-fiber mixtures were completely mixed with water up to the liquid limit of the base soil and enclosed in an air-tight bag for 24 hours. Using a spatula, the soil mixes were then pressed into the molds to their full depth. The side walls of the mold were lubricated before the soil was placed to reduce soil adherence to the side walls. Five rectangular molds were utilized in each experiment. Some of these molds were utilized for crack initiation and evolution, while others were used to measure moisture content during drying. The formation of cracks is checked manually and their moisture contents have been determined at different intervals of time. The width of cracks is measured with the help of steel wires of various diameters. Throughout the test period, the moisture content at the top and bottom of the desiccation test specimens varied. Because the specimens were thin, the moisture content was calculated as the average moisture content based on the total weight of the specimens.

2.4 Toughness behavior at direct tension

The toughness behavior of reinforced soft clay in the post peak zone is studied for all the direct tension test specimens. The toughness index is determined from normalized curves. The load and the deformation axes were normalized with respect to the load and deformation respectively at the peak load. A dimensionless direct tension toughness index (*TI*) is defined in Equation 1 to understand the post peak behavior as proposed by Sobhan & Mashnad (2002).

$$TI = \frac{A_d - A_p}{\frac{d}{d_p} - 1} \tag{1}$$

where d_p = deformation at peak load P_{max}; d = any deformation that is greater than the d_p value; A_p = area under the normalized curve up to the peak; and A_d = area under the normalized curve up to the deformation ratio d/d_p.

2.5 Desiccation rate and desiccation coefficient

The moisture content at any time is proposed by Equation 2 given below for analysis of desiccation test data obtained from the current study. It is an exponential function, and is similar to that of Nahlawi & Kodikara (2006) except that the final moisture content term is factored by $\frac{2}{3}$.

$$w = \frac{2}{3} w_f + \left(w_0 - \frac{2}{3} w_f \right) e^{-kt} \tag{2}$$

Where, w = moisture content at any time, t of the desiccation test (%)
k = Coefficient of desiccation (per day)
w_0 = initial moisture content of the desiccation test (%)
w_f = final moisture content at the end of the desiccation test (%)

The desiccation rate may be defined as a change in moisture content with respect to time (i.e., $\frac{dw}{dt}$) can be expressed by Equation 3 given below. It is also an exponential function.

$$\frac{dw}{dt} = -k \left(w_0 - \frac{2}{3} w_f \right) e^{-kt} \tag{3}$$

3. Results and discussion

3.1 Tensile strength and toughness

The effect of fiber content on tensile strength of fiber reinforced soils is demonstrated in Figure 4. It is seen in Figure 4, that the tensile strength increases from 33 kPa to 71 kPa on increasing coir content from 0% to 2.0% for samples prepared at *OMC*. Similarly, the tensile strength increases from 76 kPa to 148 kPa when the coir content increases from 0% to 2.0% for samples compacted at water content of 5% less than *OMC*. Likewise, the tensile strength increases from 11 kPa to 59 kPa, for a change in coir content from 0% to 2.0% and compaction water content of *OMC*+5%. Figure 4 also shows that the tensile strength of jute fiber reinforced clay increases from 33 kPa to 55 kPa, 76 kPa to 161 kPa and 11 kPa to 23 kPa for samples prepared at *OMC*, *OMC*-5% and *OMC*+5% respectively on using 1% jute fiber. While comparing the tensile strength of coir reinforced clay with unreinforced clay, it can be seen that tensile strength increased by up to 214%, 232% and 475% for samples prepared at *OMC*-5%, *OMC* and *OMC*+5% respectively. Meanwhile, the tensile strength of jute reinforced clay is observed to be increased by up to 132%, 168% and 215%

respectively for samples at *OMC*-5%, *OMC* and *OMC*+5%. Therefore, it can be apprehended that the effect of coir is greater than the effect of jute fiber on increasing the tensile strength of clayey soil.

In comparison to the tensile strength of reinforced soils at different molding moisture contents, the impact of fiber is observed more for samples with higher moisture content. Figure 4 also indicates that the addition of discrete fibers up to 2% of coir and 1% of jute fiber increases the tensile strength of clayey soil significantly. An increase in tensile strength is caused by resistance to the slip of fibers in the soil matrix at the time of tensile loading. Li et al. (2014) studied the tensile strength of polypropylene fiber reinforced clay and reported that tensile strength is increased by the interfacial mechanical interactions between the fiber surface and soil particles. Conversely, a further increase in fiber content decreases the tensile strength of the soil-fiber matrix due to a reduction in bonding between fiber and soil. Therefore, the optimum fiber content for maximization of tensile strength of clayey soil can be considered as 2% for coir and 1% for jute fiber. Anggraini et al. (2015b) found maximum tensile strength at 1.5% coir content for soft marine clay, which is similar to that observed in the present study.

The average values of *TI* obtained from the direct tension test on laboratory-made samples are plotted against moisture content in Figure 5. For the purpose of *TI* calculation, the *d/dp* value was chosen up to 3 for all the specimens. Figure 5 indicates that the effect of moisture on the *TI* of studied fiber reinforced soil is negligible when compared to that of original clay. The *TI* of soft clay increases notably with an increase in moisture content. Whereas, such an increase in *TI* is not present in the case of the same clay reinforced with coir and jute fiber. Besides, the *TI* increases notably with a small amount of coir (1%) and jute fiber (0.5%) for samples prepared at their *OMC*-5% and *OMC*. But, the *TI* is observed to decrease by a small amount for the samples prepared at *OMC*+5% moisture content. The change in *TI* on further inclusion of fiber is insignificant.

The absolute toughness (*T*) of fiber mixed soft clay is defined as the area under the load-deformation curves up to failure, and it indicates the total energy absorbed by the material before failure. The variations of *T* with variation of moisture content are presented in Figure 6. It indicates that *T* decreases almost linearly with an increase in moisture content for both coir and jute fiber-reinforced clayey soil. This figure demonstrates that *T* increases with an increase in coir content of 2% and jute fiber content of 0.5%. Further increase in fiber decreases *T* at all the studied moisture content of coir-reinforced clay. This decrease in *T* is observed for the jute fiber reinforced sample prepared at *OMC*-5% only. A minor change in *T* for jute fiber reinforced samples at *OMC* and *OMC*+5% is observed for fiber content greater than 0.5%. The maximum improvement in the absolute toughness that is found for 2% coir-reinforced soil is 10 to 17 times greater when compared with that of unreinforced soil in the studied range of moisture content.

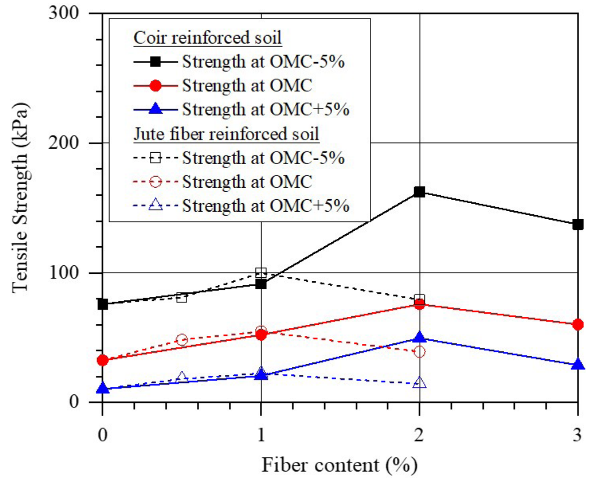

Figure 4. Effect of fiber content on the tensile strength of soil samples at various moisture and fiber contents.

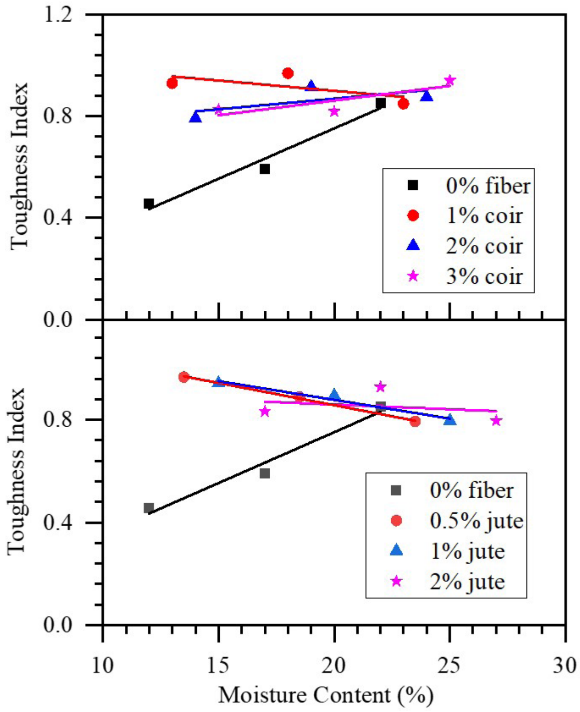

Figure 5. The effect of moisture content on the toughness index of coir and jute fiber reinforced soil (from laboratory tests on soil samples at various fiber contents).

3.2 Desiccation cracking of reinforced and unreinforced soil

Figure 7 displays typical cracking patterns observed at the end of desiccation cracking tests for clayey soil without any reinforcement and with different percentages of fiber reinforcement. It is evident from these photographs that the

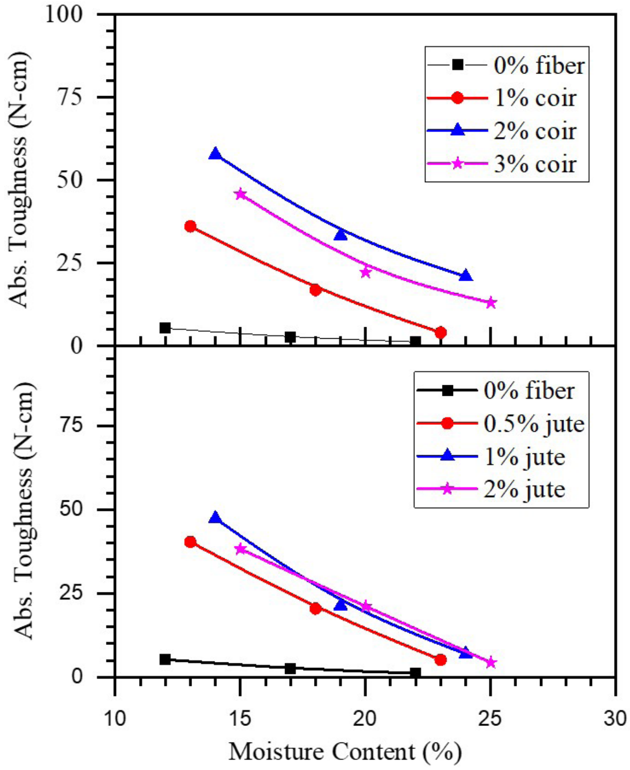

Figure 6. Effect of moisture content on the absolute toughness of coir and jute fiber reinforced soil (from laboratory tests on soil samples at various fiber contents).

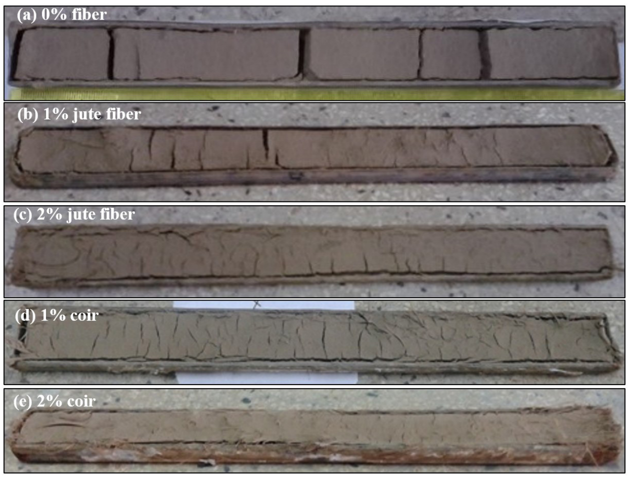

Figure 7. The cracking pattern of clayey soil of different fiber content after a desiccation cracking test.

crack width of unreinforced samples is higher than the crack width of reinforced samples. The number of cracks is fewer in the case of unreinforced samples compared to the number of cracks in reinforced samples. It is also remarkable that the crack width becomes smaller with an increase in fiber content. The length of cracks was smaller for higher fiber content. Chaduvula et al. (2017) studied the desiccation cracking behavior of polyester fiber reinforced clay and observed similar results. Comparing Figure 7(b) with Figure 7(d) and Figure 7(c) with Figure 7(e), it can be said that coir controls the crack more efficiently than jute fiber.

3.3 Desiccation characteristics of reinforced and unreinforced soil

The variation of moisture content with desiccation time is shown in Figure 8 for unreinforced Gazipur clay. It indicates that the moisture content reduces rapidly at the initial stage of desiccation and decreases slowly towards the end of the desiccation test. Past studies (Corte & Higashi, 1964; Nahlawi & Kodikara, 2006) on the desiccation characteristics of slurry clay reported similar results. Desiccation curves for thin (5mm and 10mm thick) samples are very close to each other, while significant differences can be observed for thick (20mm and 30mm thick) samples. It can be seen that desiccation ended earlier for thinner samples. It may be due to desiccation starting at the top surface first and then it propagating toward the bottom of the samples. Lifting up of the cracked cells with respect to middle cracked cells at the latter stages of desiccation was observed. This behavior indicates differential desiccation rates between the top and bottom parts of the soil layer at different stages of desiccation. Figure 9 shows desiccation curves for coir and jute fiber reinforced clay. Comparing Figure 9(a) to Figure 9(d), the effect of fiber content is more prominent for samples of 10mm to 30mm in thickness. Fiber causes delay in the drying process of reinforced clay. It can be seen from Figure 9(d) that the effect of thickness is very small for thicknesses of 10mm to 30mm. However, the desiccation curves in the compacted clay tests mentioned here appear to approach identical water content at the end of the testing. This is because the soil finally reaches a moisture content that is in balance with the surrounding environment, as measured by relative humidity and air temperature. Final moisture content (w_f) is observed more for greater thickness and larger fiber content. Exponential desiccation curve fitting has been conducted for all the samples. The resulted desiccation equations are shown with respective plots. The first derivatives of these equations (i.e., *dw/dt*) are considered as the desiccation rate at any time of desiccation.

Figure 10 and Figure 11 represent computed desiccation rate versus time plots obtained from fitted curves. It can be seen from these figures that the rate of desiccation is very high at the initial stage compared to that at finishing time. The more the thickness, the less the desiccation rate at the initial stage. But, the desiccation rate is higher for thicker samples at the end of the test. It may be caused by the higher moisture content of the thicker samples at the end of the test evaporating more than the thinner samples. At the initial stage of the tests, desiccation rates of 5mm thick jute fiber reinforced clay were higher than unreinforced clay, but desiccation rates of thicker (10mm to 30mm thick) jute

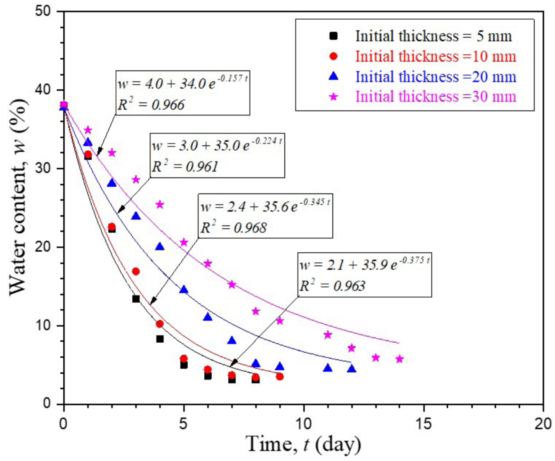

Figure 8. Desiccation curves for unreinforced Gazipur clay.

fiber reinforced clay samples were lower than unreinforced samples. The desiccation rates of coir reinforced clay, on the other hand, are shown to be lower than the unreinforced samples of all thicknesses at the initial stage of desiccation.

3.4 Effect of layer thickness on desiccation and cracking

Figure 12 and Figure 13 present the effect of thickness on the desiccation coefficient of unreinforced and fiber-reinforced clayey soil respectively. The main variables in these tests are the thickness of the soil specimen (initial thicknesses are 5mm, 10mm, 20mm and 30mm) and fiber content (0%, 1% and 2%). It can be seen that the specimens with larger depths generally exhibited a smaller desiccation coefficient for unreinforced and reinforced clayey soil. This occurs because

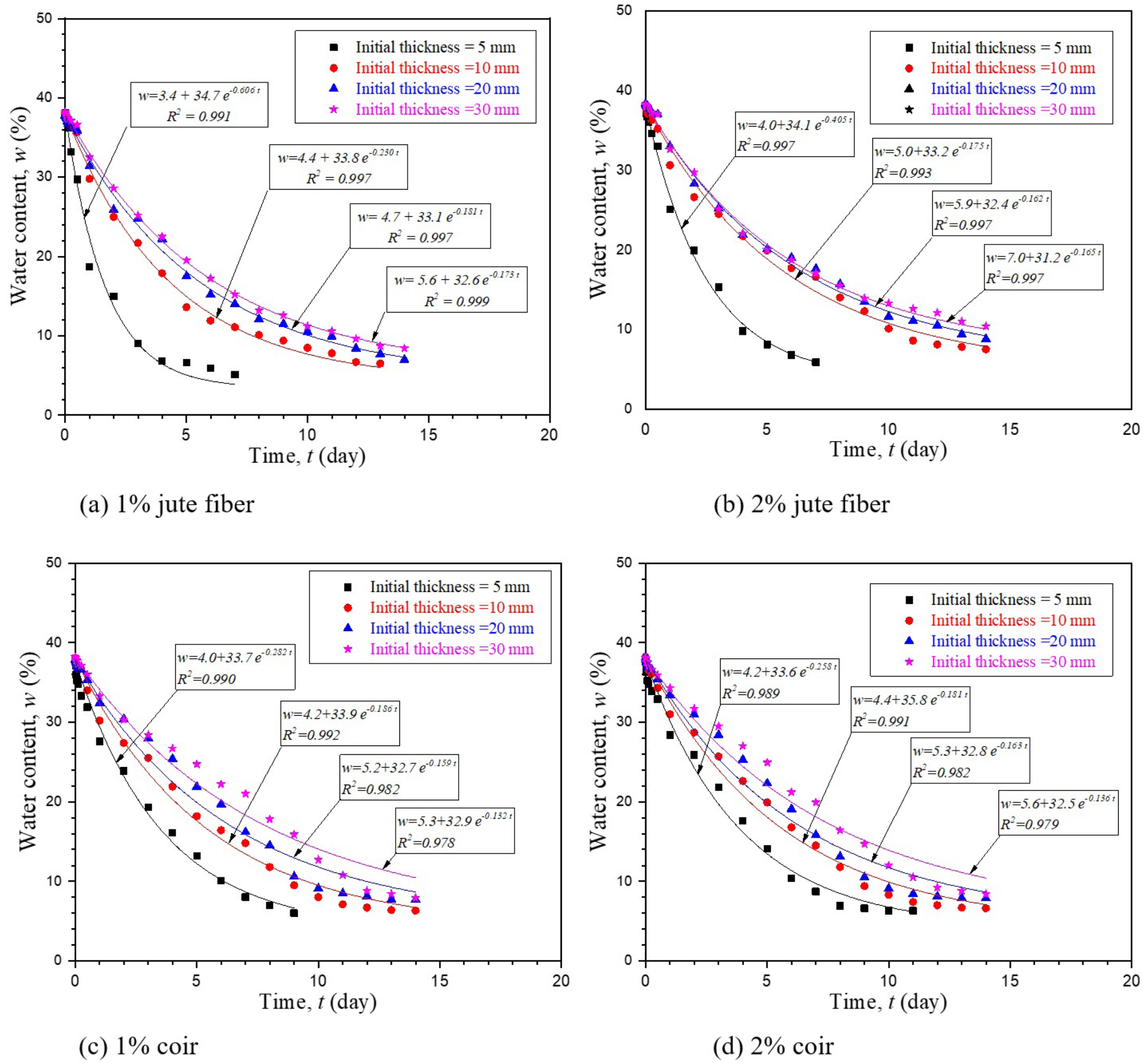

Figure 9. Desiccation curves for Gazipur clay with (a) 1% jute fiber, (b) 2% jute fiber, (c) 1% coir and (d) 2% coir as reinforcement.

the distance that moisture must travel for evaporation at the surface increases as the soil thickness increases.

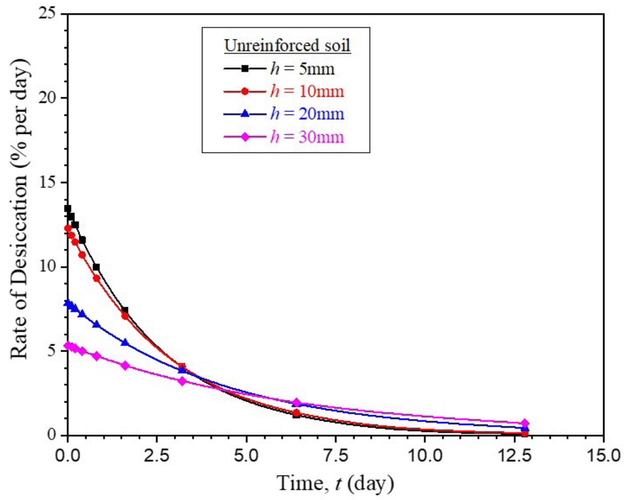

Figure 10. Desiccation rate for unreinforced Gazipur clay.

Figure 14 demonstrates the effect of sample thickness on the cracking water content of reinforced and unreinforced clayey soil. The cracking water content is less for reinforced clayey soil than for unreinforced clay. As a result, it can be claimed that employing discrete fibers as reinforcement can help to prevent cracks from forming in clayey soil. This is due to reinforced soil's higher tensile strength, which prevents the creation of cracks in soil that has reached a moisture content where unreinforced soil has cracked. A similar result was reported by Abu-Hejleh & Znidarcic (1995), where they reported that the soils start cracking during desiccation induced one-dimensional shrinkage when total lateral tensile stress at the crack tip reaches the tensile strength. It is also observed that the effect of coir is greater than jute fiber in resisting desiccation cracking. The effect of specimen thickness on the crack spacing to thickness ratio of unreinforced clayey soil is presented in Figure 15. The crack spacing to thickness ratio is calculated for the initial and final thickness of specimens. The crack spacing (s) mentioned here is the mean spacing, which is determined by the total spacing divided by the total number of cells when the soil was in dry condition.

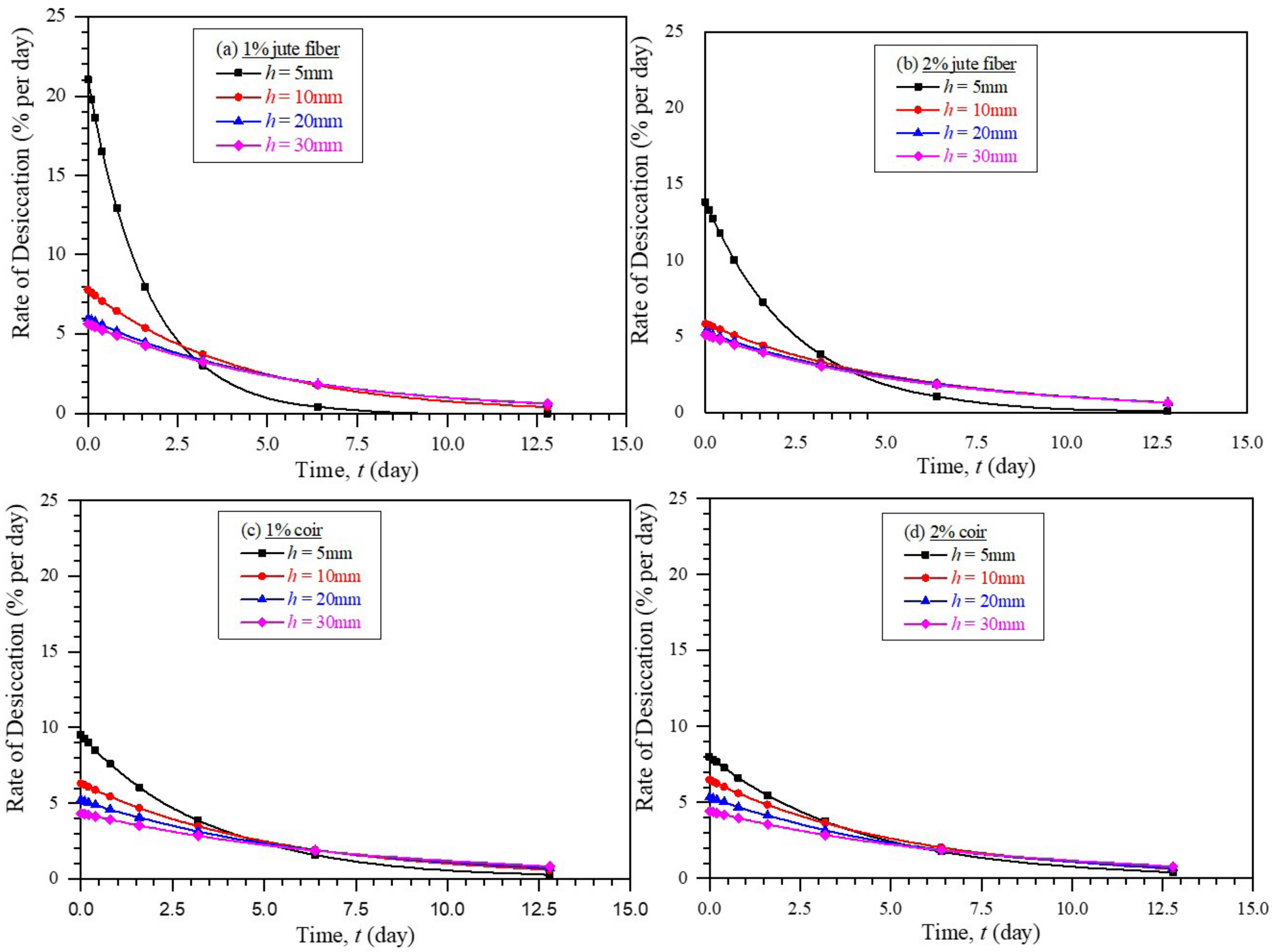

Figure 11. Desiccation rate for Gazipur clay with (a) 1% jute fiber, (b) 2% jute fiber, (c) 1% coir and (d) 2% coir as reinforcement.

This approach has been used to analyze the data of Corte & Higashi (1960) and Lau (1987). It can be marked that a straight line is obtained on a log-log plot for both cases.

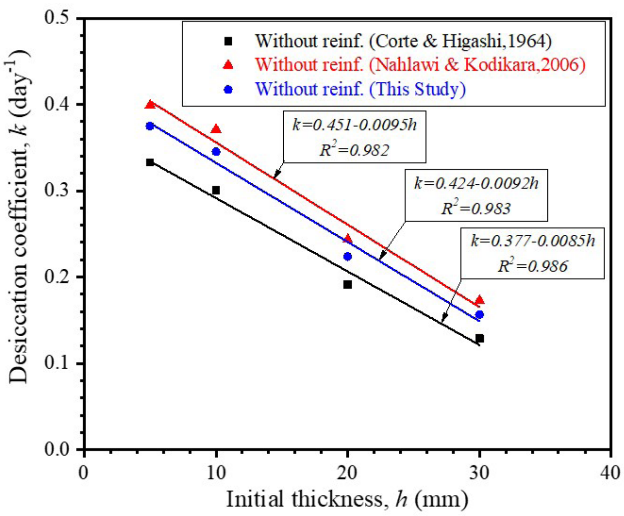

Figure 12. Effect of sample thickness on esiccation coefficient of unreinforced soil.

3.5 Relation between cracking water content and desiccation coefficient

Figure 16 shows the relationship between desiccation coefficient (k) and cracking water content (w_c), where linear regression lines are obtained for unreinforced clay. Figure 17 and Figure 18 illustrate the plots of cracking water content versus desiccation coefficient of reinforced clayey soil. Exponential relationships are observed in this case. The values of R^2 are found within 0.96 to 1, which indicates a good correlation between the selected parameters. It is clear that the cracking water content is lower because of the higher desiccation coefficient that happens for thinner samples. When comparing the results of this study to the desiccation equations proposed by past researchers (Corte & Higashi, 1964; Nahlawi & Kodikara, 2006), the equation proposed in this study lies between Corte & Higashi (1964) and Nahlawi & Kodikara (2006). As indicated in Figure 16, there is no significant change in desiccation coefficient between 5mm and 10mm thick unreinforced soil samples. Figure 17 and Figure 18 show that the desiccation coefficient for 5mm and 10mm thick reinforced soil samples varies considerably. This difference in desiccation coefficient between unreinforced

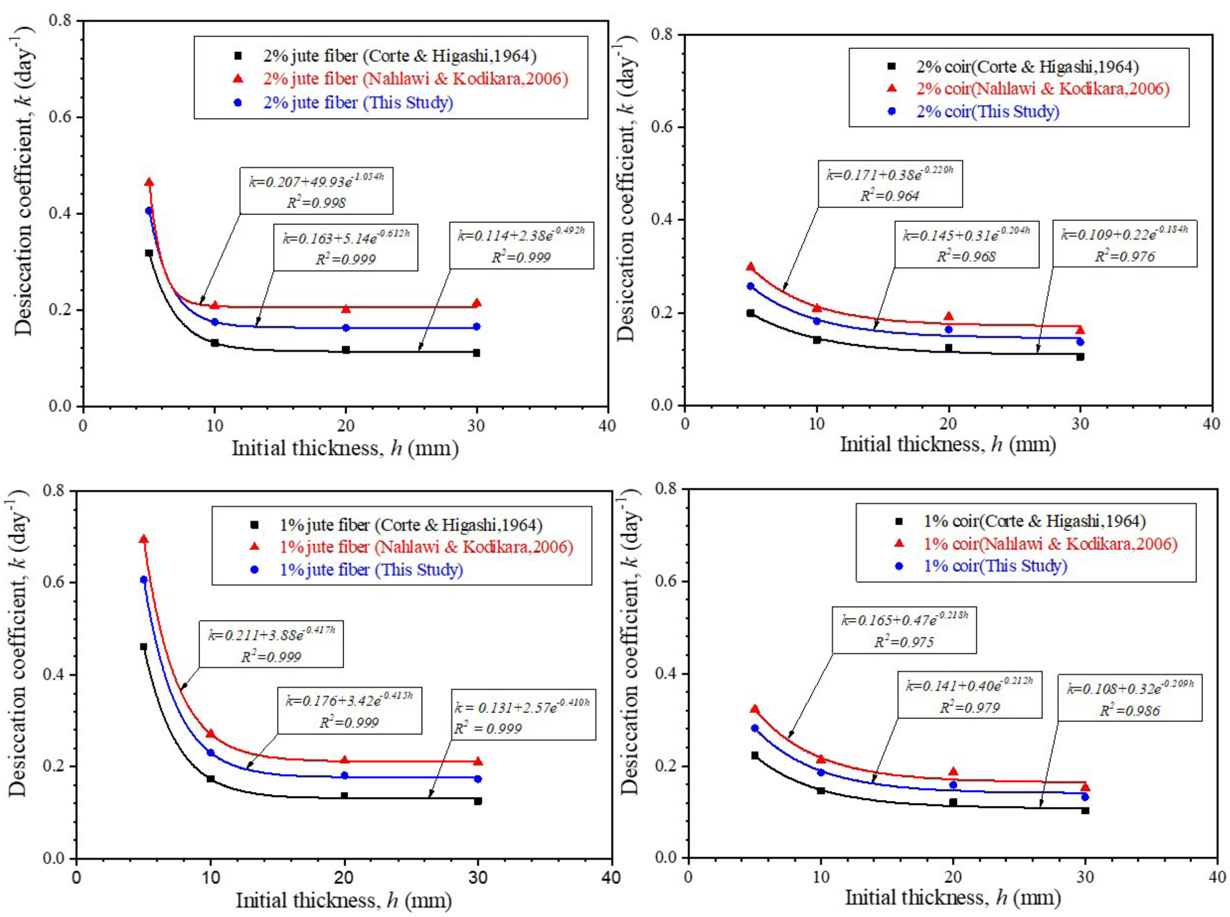

Figure 13. Effect of sample thickness on desiccation coefficient of reinforced clayey soil.

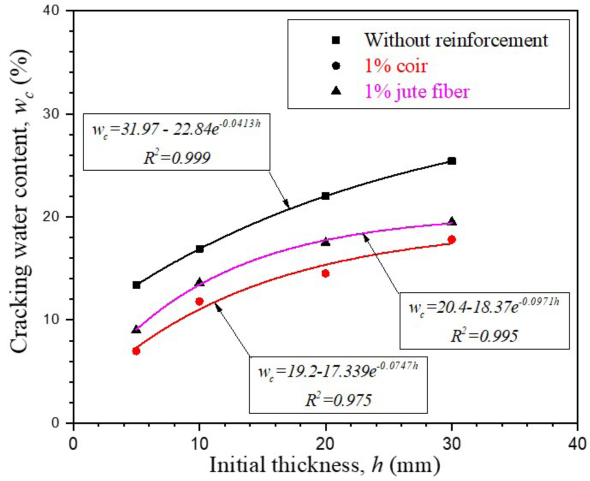

Figure 14. Effect of reinforcement and sample thickness on cracking water content of clayey soil.

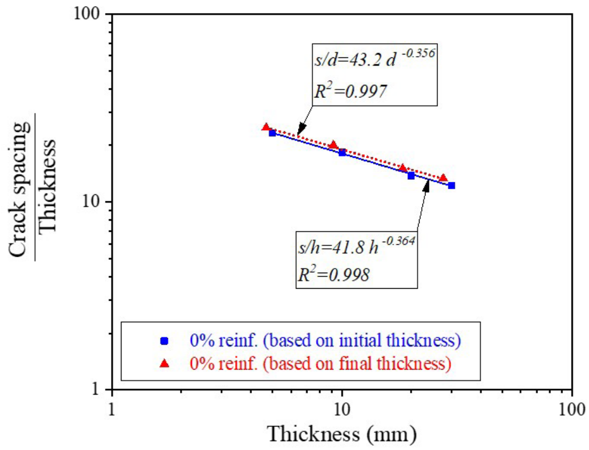

Figure 15. Effect of specimen thickness on the crack spacing to thickness ratio of unreinforced clayey soil.

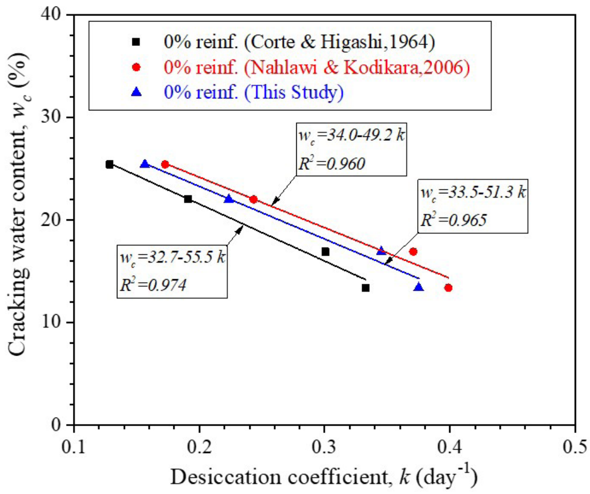

Figure 16. Relation between cracking water content and desiccation coefficient for unreinforced clayey soil.

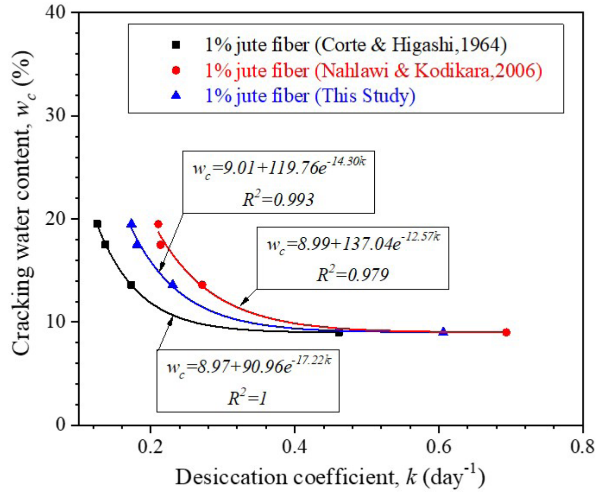

Figure 17. Relation between cracking water content and desiccation coefficient of 1% jute fiber reinforced clay.

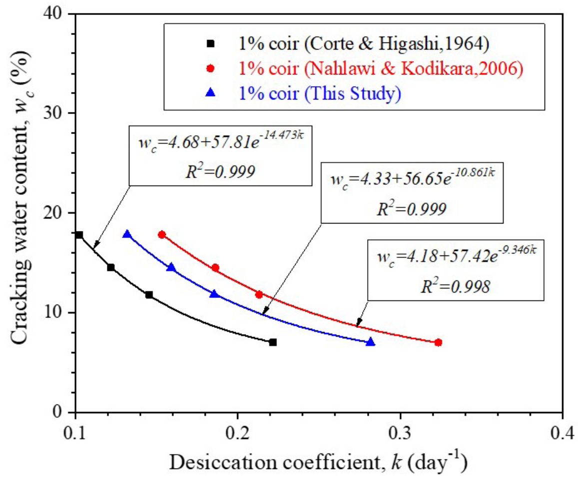

Figure 18. Relation between cracking water content and desiccation coefficient for 1% coir reinforced clay.

and reinforced thin samples could be due to reinforced soil having less crack width and depth when compared to unreinforced soil.

4. Conclusion

A series of laboratory desiccation tests have been conducted in addition to direct tension tests on a clayey soil with various proportions of natural fibers (coir and jute fiber). The test results are presented in the above sections. On the basis of the test results, the following conclusions can be drawn.

- The tensile strength increases on using discrete fiber of coir up to 2% and jute fiber up to 1%. Thus, optimum fiber content may be considered as 2% for coir and 1% for jute fiber to achieve maximum tensile strength.

- The tensile strength of coir reinforced soil increased by up to 214%, 232% and 475% respectively for samples prepared at *OMC*-5%, *OMC* and *OMC*+5%. Similarly, the tensile strength of jute fiber reinforced soil increased by up to 132%, 168% and 215% respectively for samples prepared at *OMC*-5%, *OMC* and *OMC*+5%.
- The absolute toughness is greatly improved by using reinforcement in a random distribution of up to 2% coir and 1% jute fiber. As the moisture content rises, the absolute toughness of both reinforced and unreinforced samples decreases. The toughness index of unreinforced soil improves as the moisture content rises. The use of coir and jute fiber improves the toughness index at low moisture level (*OMC*-5%). But, the reinforcing effect on the toughness index at higher moisture content (*OMC*+5%) is negligible.
- Discrete natural fibers reduce the crack width and length considerably. The higher the fiber content, the narrower the cracks and the more cracks there are.
- The moisture content drops quickly at first and then gradually as the desiccation test progresses. The desiccation rate is lower for thicker samples during the initial stage of the test. However, for thicker samples, it is higher at a certain point near the end of the test.
- The initial desiccation rates of jute fiber reinforced clay of 5mm thickness are higher and of 10mm to 30mm thickness are lower than unreinforced samples. The desiccation rates of coir reinforced clay of all thicknesses are lower than the unreinforced samples.
- Thinner clayey soil samples, whether reinforced or unreinforced, show lower cracking water content. When compared to unreinforced clay, reinforced clayey soil has reduced cracking water content. This is due to reinforced soil's stronger tensile strength, which prevents cracks from forming in soil that has reached a moisture content where unreinforced soil has cracked.
- For unreinforced clay, the relationship between cracking water content and desiccation coefficient is linear; for reinforced clay, the relationship is exponential.

Declaration of interest

The authors have no conflicts of interest. There is no financial interest to report.

Authors' contributions

Abu Taiyab: conceptualization, methodology and laboratory setup development, supervision, review and editing of the content and finalization, critical analysis and visualization. **Nazmun Naher Islam:** methodology and laboratory setup development, material collection, laboratory investigation, data analysis, writing draft and finalization. **Mokhlesur Rahman:** conceptualization, supervision, finalization and approval of the content.

List of symbols

A_d	Area under the normalized curve up to deformation ratio d/d_p
A_p	Area under the normalized curve up to peak
d	Any deformation that is greater than d_p
D	Depth of the desiccation mold
d_p	Deformation at peak load P_{max}
dw/dt	Desiccation rate
Gs	Specific gravity of soil grain
q_u	Unconfined compressive strength
k	Desiccation coefficient
L	Length of the desiccation mold
LL	Liquid limit of soil
OMC	Optimum moisture content
PL	Plastic limit of soil
P_{max}	Maximum tensile load
T	Absolute toughness
TI	Toughness Index
w	Moisture content at any time t of desiccation test
W	Width of the desiccation mold
w_c	Cracking water content
w_f	Final moisture content of desiccation test
w_n	Natural moisture content
w_0	Initial moisture content of desiccation test
$\gamma_{d(\max)}$	Maximum dry density
σ_t	Tensile strength

References

Abu-Hejleh, A.N., & Znidarcic, D. (1995). Desiccation theory for soft cohesive soils. *Journal of Geotechnical Engineering*, 121(6), 493-502. http://dx.doi.org/10.1061/(ASCE)0733-9410(1995)121:6(493).

Albrecht, B.A., & Benson, C.H. (2001). Effect of desiccation on compacted natural clays. *J. Geotech. and Geoenv. Eng. ASCE.*, 127(1), 67-75. http://dx.doi.org/10.1061/(ASCE)1090-0241(2001)127:1(67).

Anggraini, V., Asadi, A., Huat, B.B.K., & Nahazanan, H. (2015a). Effects of coir fibers on tensile and compressive strength of lime treated soft soil. *Measurement*, 59, 372-381. http://dx.doi.org/10.1016/j.measurement.2014.09.059.

Anggraini, V., Huat, B.B.K., Asadi, A., & Nahazanan, H. (2015b). Effect of coir fibers on the tensile and flexural strength of soft marine clay. *Journal of Natural Fibers*, 12(2), 185-200. http://dx.doi.org/10.1080/15440478.2014.912973.

ASTM D 0698. (2007). *Standard test method of laboratory compaction characteristics of soil using standard effort*. ASTM International, West Conshohocken, PA.

Capilleri, P.P., Cuomo, M., Motta, E., & Todaro, M. (2019). Experimental investigation of root tensile strength for slope stabilization. *Indian Geotech J.*, 49(6), 687-697. http://dx.doi.org/10.1007/s40098-019-00394-2.

Chaduvula, U., Viswanadham, B.V.S., & Kodikara, J. (2017). A study on desiccation cracking behavior of polyester fiber-reinforced expansive clay. *Applied Clay Science*, 142, 163-172. http://dx.doi.org/10.1016/j.clay.2017.02.008.

Colina, H., & Roux, S. (2000). Experimental model of cracking induced by drying shrinkage. *The European Physical Journal E*, 1(2–3), 189-194. http://dx.doi.org/10.1007/s101890050021.

Correia, A.A.S., Oliveira, P.J.V., & Custódio, D.G. (2015). Effect of polypropylene fibres on the compressive and tensile strength of a soft soil, artificially stabilised with binders. *Geotextiles and Geomembranes*, 43, 97-106. http://dx.doi.org/10.1016/j.geotexmem.2014.11.008.

Corte, A., & Higashi, A. (1960). *Experimental research on desiccation cracks in soil (Research Report)*. U.S. Army Snow Ice and Permafrost Research Establishment.

Corte, A., & Higashi, A. (1964). *Experimental research on desiccation cracks in soil (Research Report)*. U.S. Army Material Command Cold Region Research & Engineering.

Costa, S., Kodikara, J., & Shannon, B. (2013). Salient factors controlling desiccation cracking of clay in laboratory experiments. *Geotechnique*, 63(1), 18. http://dx.doi.org/10.1680/geot.9.P.105.

Daniel, D.E., & Brown, K.W. (1987). Landfill liners: how well do they work and what is their future? in J. R. Gronow, A. N. Schofield & R. K. Jain (Eds.), *Land disposal of hazardous waste: engineering and environmental issues* (pp. 235-244). Ellis Horwood Publishers.

DeCarlo, K.F., & Shokri, N. (2014). Effects of substrate on cracking patterns and dynamics in desiccating clay layers. *Water Resources Research*, 50(4), 3039-3051. http://dx.doi.org/10.1002/2013WR014466.

Enokela, O.S., & Alada, P.O. (2012). Strength analysis of coconut fiber stabilized earth for farm structures. *International Journal of Advancements in Research & Technology*, 1(2), 1-7.

Guo, Y., Han, C., & Yu, X. (2018). Laboratory characterization and discrete element modeling of shrinkage and cracking in clay layer. *Canadian Geotechnical Journal*, 55(5), 680-688. http://dx.doi.org/10.1139/cgj-2016-0674.

Jayanthi, P.N.V., Kuntikana, G., & Singh, D.N. (2017). Stabilization of fine-grained soils against desiccation cracking using sustainable materials. *Advances in Civil Engineering Materials*, 6(1), 36-67. http://dx.doi.org/10.1520/ACEM20160037.

Jayasree, P.K., Balan, K., & Peter, L. (2015). Shrinkage characteristics of expansive soil treated with coir waste. *Indian Geotechnical Journal*, 45, 360-367. http://dx.doi.org/10.1007/s40098-015-0144-8.

Khatun, T., Dutta, T., & Tarafdar, S. (2015). Topology of desiccation crack patterns in clay and invariance of crack interface area with thickness. *The European Physical Journal E*, 38(8), http://dx.doi.org/10.1140/epje/i2015-15083-6.

Kodikara, J.K., & Choi, X. (2006). A simplified analytical model for desiccation cracking of clay layers in laboratory tests. In *Fourth International Conference on Unsaturated Soils* (pp. 2558-2569). Reston: ASCE. http://dx.doi.org/10.1061/40802(189)218.

Konrad, J.M., & Ayad, R. (1997). An idealized framework for the analysis of cohesive soils undergoing desiccation. *Canadian Geotechnical Journal*, 34, 477-488. http://dx.doi.org/10.1139/t97-015.

Lakshmikantha, M.R., Prat, P.C., & Ledesma, A. (2012). Experimental evidence of size effect in soil cracking. *Canadian Geotechnical Journal*, 49(3), 264-284. http://dx.doi.org/10.1139/t11-102.

Lakshmikantha, M.R., Prat, P.C., & Ledesma, A. (2018). Boundary effects in the desiccation of soil layers with controlled environmental conditions. *Geotechnical Testing Journal*, 41, 675-697. http://dx.doi.org/10.1520/GTJ20170018.

Lau, J.T.K. (1987). *Desiccation cracking of soils* [MSc Thesis]. University of Saskatchewan. http://hdl.handle.net/10388/etd-03242010-112414.

Li, J., Tang, C., Wang, D., Pei, X., & Shi, B. (2014). Effect of discrete fibre reinforcement on soil tensile strength. *Journal of Rock Mechanics and Geotechnical Engineering*, 6, 133-137. http://dx.doi.org/10.1016/j.jrmge.2014.01.003.

Li, J.H., & Zhang, L.M. (2011). Study of desiccation crack initiation and development at ground surface. *Engineering Geology*, 123(4), 347-358. http://dx.doi.org/10.1016/j.enggeo.2011.09.015.

Li, J.H., Zhang, L.M., Wang, Y., & Fredlund, D.G. (2009). Permeability tensor and representative elementary volume of saturated cracked soil. *Canadian Geotechnical Journal*, 46(8), 928-942. http://dx.doi.org/10.1139/T09-037.

Li, X. (2014). *Shrinkage cracking of soils and cementitiously-stabilized soils: mechanisms and modeling* [Ph.D. Dissertation], Washington State University.

Lu, H., Li, J., Wang, W., & Wang, C. (2015). Cracking and water seepage of Xiashu loess used as landfill cover under wetting–drying cycles. *Environmental Earth Sciences*, 74(11), 7441-7450. http://dx.doi.org/10.1007/s12665-015-4729-4.

Morris, P.H., Graham, J., & Williams, D.J. (1992). Cracking in drying soils. *Canadian Geotechnical Journal*, 29(2), 263-277. http://dx.doi.org/10.1139/t92-030.

Nahlawi, H., & Kodikara, J.K. (2006). Laboratory experiments on desiccation cracking of thin soil layers. *Geotechnical and Geological Engineering*, 24, 1641-1664. http://dx.doi.org/10.1007/s10706-005-4894-4.

Peron, H., Hueckel, T., Laloui, L., & Hu, L.B. (2009a). Fundamentals of desiccation cracking of fine-grained soils: experimental characterisation and mechanisms identification. *Canadian Geotechnical Journal*, 46(10), 1177-1201. http://dx.doi.org/10.1139/T09-054.

Peron, H., Laloui, L., Hueckel, T., & Hu, L.B. (2009b). Desiccation cracking of soils. *European Journal of Environmental and Civil Engineering*, 13(7–8), 869-888. http://dx.doi.org/10.1080/19648189.2009.9693159.

Shinde, S.B., Uday, K.V., Kadali, S., Tirumkudulu, M.S., & Singh, D.N. (2012). A novel methodology for measuring the tensile strength of expansive clays. *Geomechanics and Geoengineering*, 7(1), 15-25. http://dx.doi.org/10.1080/17486025.2011.599867.

Shokri, N., Zhou, P., & Keshmiri, A. (2015). Patterns of desiccation cracks in saline bentonite layers. *Transport in Porous Media*, 110(2), 333-344. http://dx.doi.org/10.1007/s11242-015-0521-x.

Silva, W.P., Silva, C.M.D.P., Silva, L.D., & Oliveira, F.V.S. (2013). Drying of clay slabs: experimental determination and prediction by two-dimensional diffusion models. *Ceramics International*, 39(7), 7911-7919. http://dx.doi.org/10.1016/j.ceramint.2013.03.053.

Sobhan, K., & Mashnad, M. (2002). Tensile strength and toughness of soil–cement–fly-ash composite reinforced with recycled high-density polyethylene strips. *Journal of Materials in Civil Engineering*, 14(2), 177-184. http://dx.doi.org/10.1061/(ASCE)0899-1561(2002)14:2(177).

Tang, C., Shi, B., Liu, C., Zhao, L., & Wang, B. (2008). Influencing factors of geometrical structure of surface shrinkage cracks in clayey soils. *Engineering Geology*, 101(3–4), 204-217. http://dx.doi.org/10.1016/j.enggeo.2008.05.005.

Tang, C.S., Cui, Y.J., Shi, B., Tang, A.M., & Liu, C. (2011a). Desiccation and cracking behaviour of clay layer from slurry state under wetting–drying cycles. *Geoderma*, 166(1), 111-118. http://dx.doi.org/10.1016/j.geoderma.2011.07.018.

Tang, C.S., Cui, Y.J., Tang, A.M., & Shi, B. (2010). Experiment evidence on the temperature dependence of desiccation cracking behavior of clayey soils. *Engineering Geology*, 114(3–4), 261-266. http://dx.doi.org/10.1016/j.enggeo.2010.05.003.

Tang, C.S., Pei, X.J., Wang, D.Y., Shi, B., & Li, J. (2015). Tensile strength of compacted clayey soil. *Journal of Geotechnical and Geoenvironmental Engineering*, 141(4), 1-8. http://dx.doi.org/10.1061/(ASCE)GT.1943-5606.0001267.

Tang, C.S., Shi, B., Liu, C., Suo, W.B., & Gao, L. (2011c). Experimental characterization of shrinkage and desiccation cracking in thin clay layer. *Applied Clay Science*, 52(1), 69-77. http://dx.doi.org/10.1016/j.clay.2011.01.032.

Tollenaar, R.N., van Paassen, L.A., & Jommi, C. (2017). Observations on the desiccation and cracking of clay layers. *Engineering Geology*, 230, 23-31. http://dx.doi.org/10.1016/j.enggeo.2017.08.022.

Uday, K.V., & Singh, D.N. (2013). Investigation on cracking characteristics of fine-grained soils under varied environmental conditions. *Drying Technology*, 31(11), 1255-1266. http://dx.doi.org/10.1080/07373937.2013.785433.

Uday, K.V., Prathyusha, J.N.V., Singh, D.N., & Apte, P.R. (2015). Application of the Taguchi method in establishing criticality of parameters that influence cracking characteristics of fine-grained soils. *Drying Technology*, 33(9), 1138-1149. http://dx.doi.org/10.1080/07373937.2015.1015032.

Utili, S., Dyer, M., Redaelli, M., & Zielinski, M. (2008). Desiccation fissuring induced failure mechanisms for clay levees. In: *10th Int. Symp. on Landslides and Engineered Slopes*, Xian (China). http://dx.doi.org/10.1201/9780203885284-c175.

Vogel, H.J., Hoffmann, H., Leopold, A., & Roth, K. (2005). Studies of crack dynamics in clay soil: II. A physically based model for crack formation. *Geoderma*, 125(3–4), 213-223. http://dx.doi.org/10.1016/j.geoderma.2004.07.008.

Ziegler, S., Leshchinsky, D., Ling, H.I., & Perry, E.B. (1988). Effect of short polymeric fibers on crack development in clays. *Soil and Foundation*, 38(1), 247-253. http://dx.doi.org/10.3208/sandf.38.247.

Soils and Rocks
An International Journal of Geotechnical and Geoenvironmental Engineering
www.soilsandrocks.com
ISSN 1980-9743
ISSN-e 2675-5475

Soil-cement formation factor: methodological approach and relationship with unconfined compression strength

João Marcos Vaillant[1#], Rafaela Cardoso[2]

Article

Keywords
Archie's Law
Soil-cement
Absorption
Unconfined compression strength
Electrical conductivity

Abstract

This study investigated the use of the Formation Factor of the material as an alternative way to estimate soil-cement strength involving no destructive tests. This factor is obtained from Archie's Law and consists of the ratio of pore water electrical conductivity to saturated porous material electrical conductivity, being related to porosity by constant terms. In this study, the electrical conductivity of the pore solution was obtained from a soil-cement leaching test after curing, and the conductivity of the monolithic soil-cement, by applying continuous voltage between 12-35 V onto electrodes of 1 mm thick copper plates. The influence of cement content and dry density on the electrical properties and water absorption was studied and discussed for curing times of 7 and 28 days. The samples molded with higher dry densities and cement contents presented higher Formation Factor for Soil Cement and higher unconfined compression strength. The Formation Factor and the unconfined compression strength are linearly related. Due to the methodology adopted, the Formation Factor was predominantly influenced by the conductivity of the pore solution and was related to the open porosity by means of a power function. Therefore, the Archie's Law can be applied to soil-cement. In this case, the cementation coefficient varies until 28 days of curing, tending to stabilize around 8 from that age onwards. The volumetric coefficient can be adopted as a constant with a value of 10^{12}.

1. Introduction

Soil stabilization with the use of cement is used on a large scale in the production of earth bricks and in geotechnical works, such as pavement layers in roads and also in embankments (Bahar, et al., 2004; Cardoso & Maranha das Neves, 2012). Performance standards prescribe minimum values for unconfined compression strength and water absorption. These parameters are largely affected by the cement dosage and compaction dry density, which may vary during construction, and for this it is important to develop non-destructive monitoring tools during construction for quality control.

In this context, there are studies involving the relationship between the physical properties of soil-cement and electrical conductivity or resistivity (e.g., Khalil & Santos, 2011; Kibria & Hossain, 2012; Zhang et al., 2012; Hammad, 2013; Fallah-Safari et al., 2013; Bai et al., 2013; Vincent et al., 2017). The methods used to obtain electrical measurements are easy and quick to apply, in addition to being non-destructive and non-invasive, which justifies their increasingly frequent use in research.

The electrical conductivity of the monolithic material, when associated with the conductivity of the pore solution, provides a parameter known as the Formation Factor (Archie, 1942). This factor, originally conceived for rocks, has been largely used in soil studies mainly for geophysical prospection (Rinaldi & Cuestas, 2002; Lorenzo & Bergado, 2004; Shah & Singh, 2005; Song et al., 2008; Kahraman & Yeken, 2010). This factor (*FF*) is defined using Archie's equation (Equation 1), representing the relation between the electrical conductivity of the pore water and the saturated solid material (respectively K_w and K_0), being function of porosity ϕ and calibration constants *A* (volumetric coefficient) and *m* (cementation coefficient).

$$FF = \frac{K_w}{K_0} = A.\phi^{-m} \tag{1}$$

The electrical conductivity depends on soil structure and minerals, and chemical composition of the pore fluid. In fact, electrical current flows through the conductive liquid phase existing in soil voids and eventually through the surface of conductive minerals, being dependent on pore geometry, or tortuosity. This explains the fact that molding dry density and water content affect the electrical conductivity (Vaillant,

[1]Centro Federal de Educação Tecnológica de Minas Gerais, Departamento de Engenharia Civil, Belo Horizonte, MG, Brasil.
[2]Universidade de Lisboa, Instituto Superior Técnico, Departamento de Engenharia Civil, Lisboa, Portugal.
[#]Corresponding author: jmvaillant@gmail.com

Submitted on July 8, 2021; Final Acceptance on August 21, 2022; Discussion open until February, 28, 2023.
https://doi.org/10.28927/SR.2022.072421

2013; Vaillant & Cardoso, 2016). For the case of soil-cement mixtures, a combination of the porous net and the cement content of the mixture will contribute to introduce more tortuosity. This combination is also primarily responsible for the mechanical strength of the material. In addition, soluble elements from cement will affect the electrical conductivity of the pore solution. For this reason, it is important to evaluate the electrical conductivity of the pore fluid as it will change with cement dosage and curing time.

The relationship between the Formation Factor of the material and its mechanical strength has not been properly addressed in soil-cement research yet. This fact may be due to a difficulty in obtaining the measurement of the electrical conductivity of the pore solution or a scarcity of studies correlating the conductivity of the solid material with its compression strength. Only a few studies can be cited, especially Song et al. (2008), Zhang et al. (2012), Fallah-Safari et al. (2013) and Vincent et al. (2017).

Song et al. (2008) established relationships between the resistivity of a stabilized soil and its cement content, degree of saturation, moisture content, curing time and unconfined compression strength, as well as relationships with the soil SPT. They found a directly proportional linear function in the relation between resistivity (ρ) and resistance (q_u), as shown in Equation 2.

$$q_u = 286.\rho - 334 \tag{2}$$

A similar relationship between compression strength and resistivity can be found in the study by Kahraman & Yeken (2010) carried out on rocks. This study particularly highlights a model obtained from multiple regressions, relating the compression strength (σ_c, in MPa) with the electrical resistivity (ρ, in Ω.m), the apparent density (γ, in g/cm^3), and porosity (n, in %), according to Equation 3.

$$\sigma_c = -296 \cdot 16 + 0 \cdot 071\rho + 6.33n + 135 \cdot 8\gamma \quad r = 0 \cdot 97 \tag{3}$$

Zhang et al. (2012) studied the influence of cement content, porosity and curing time on the electrical resistivity and compression strength of soil-cement, before and after wet curing. In that study, the authors established relations of resistivity (ρ) and unconfined compression strength (UCS) with a synthetic parameter, combining total porosity (n_t), curing time (T) and cement content (a_w). It was suggested that this relationship is similar to Archie's Law and, therefore, this law can be applied to soil-cement. The relationships mentioned above have a linear correlation coefficient of 0.98 and are represented in Equations 4 and 5, respectively for electrical resistivity (ρ) and compression strength (UCS).

$$\rho = 33.65\left(\frac{n_t}{a_w.T}\right)^{-0,71} \tag{4}$$

$$UCS = 9.857.\left(\frac{n_t}{a_w.T}\right)^{-1,11} \tag{5}$$

Fallah-Safari et al. (2013) used different samples of compacted clay (without reuse) at different apparent molding densities, to observe the relation between UCS and electrical resistivity. They observed a non-linear relation between the variables - an increase in electrical resistivity for increases in apparent density. The results, on average, were not consistent, since the highest correlation coefficient (R^2) obtained was 0.829 for a bentonite sample, and for four other samples the obtained coefficient was lower than 0.7.

Vincent et al. (2017) studied four different samples of a soil stabilized with cement. They performed a multiple regression analysis between the unconfined compression strength and the electrical resistivity of the material before curing (fresh state), in the periods of 1 and 7 days of curing. The results are consistent with those obtained in other studies, observing increases in resistivity for proportional increases in cement content and curing time. This study presented only the equations for the initial stage of the mixture (before curing) and after a period of 1 day of curing, as it sought to obtain the UCS prediction at 7 days, that is, before hardening, to avoid losses. The type of curing adopted in this research was not mentioned.

In this context, this study proposes an easy-to-apply methodology to evaluate the compression strength of soil-cement composites based on relations with an Apparent Formation Factor of the soil-cement (henceforth called FF_{sc}). Using the Archie's Law, this Formation Factor was determined both from measurements of electrical conductivity in the solid material after determined curing times (K_f) and from measurements of the leached solution, named K_{sp} (Equation 6). Electrical conductivity is the physical parameter that rules FF_{sc}, which, in turn, is influenced by the material design parameters (dry volumetric weight or dry density at compaction, and cement content) and curing time.

$$FF_{sc} = \frac{K_{sp}}{K_f} = A.Abs^{-m} \tag{6}$$

In this work the soil-cement porosity was replaced by the water absorption (*Abs)* (or open porosity), found using the saturation process described in the methodology section of ABNT NBR 8492 (ABNT, 2012b). The water absorption is a parameter of quality control of soil-cement bricks at 7 days of age, whose value is limited to 20% (ABNT, 2012a).

The experimental conditions to measure the electrical conductivity of the solution, for which Archie's Law was postulated, were not obeyed in this study. This is because conductive clay minerals are dispersed in pore solution (Shale effect), and pore solution may be diluted. However, Archie's Law for this soil-cement is simple to use and allows obtaining a representative value of the "cementation" of the material. This law is being used as concept, because the formation factor depends on porosity, which comes from the connected porous network derived from dosing, molding, and curing conditions. Being associated with the presence of hydrated cement minerals, it will be latter possible to observe a relation between this factor and UCS.

Finally, this Apparent Formation Factor (FF_{sc}) for soil-cement was related with UCS to define relationships which may be useful as a non-destructive method for quality control. The relations were established to consider dry density and cement dosage, in addition to the curing time.

2. Materials and methods

2.1 Materials and sample preparation

The soil samples used were fragments of marl from the Portuguese region of Abadia, which were passed through a #4 sieve. The fines content passed through sieve #200 with diameter <0.075 mm was of 17%. The minerals present were carbonates (16-23% calcite and dolomite), quartz (5-10%), other non-clayey minerals (8-17%), clays (1 5% chlorite, 17-30% kaolinite, 21-35% illite, 0-1% smectite and 30-60% mixed layer clays) and a very small percentage of organic matter (0-2%) (Maranha das Neves & Cardoso, 2006). Liquid limit was 40% and plasticity index was 28% (classification CL) - values found using the fine fraction of the marl. The unit weight of solid particles was 27.5 kN/m^3. The Portland cement type II-32 with unit weight of solid particles of 31.0 kN/m^3 was used.

The specimens, molded in rectangular metallic forms with section of 4 × 4 cm^2 and length of 16 cm (CEN, 2007), as shown in Figure 1a, were manually compacted in four layers, one-centimeter thick each. The compaction moisture adopted was approximately 2% above the optimum moisture obtained in Proctor Normal test. A pilot test was carried out to find the maximum possible dry density to be achieved in manual compaction. Thus, four levels of dry volumetric weights were defined up to the maximum limit achieved in the test: 14, 15, 16 and 17 kN/m^3, respectively G1, G2, G3 and G4. Four cement dosages were mixed with each dry unit weight of marl: 5% (D1), 10% (D2), 15% (D3) and 20% (D4). The choice of these cement percentages was based on the most used content in the literature consulted. To individually identify each of the 16 combinations of density (G) and cement content (D), variable C was created. It represents the dosage of cement per volume or the cement content per m^3 of mixture which values are shown in Table 1.

The samples were immediately extracted from the mold after compaction, weighted and their initial electrical conductivity was recorded. Then, curing was carried out in a humid chamber with a relative humidity greater than or equal to 95%. Curing times were established to be 7 days (ABNT, 2012a) and 28 days, being different specimens prepared for each period. The 28-day curing was included to observe the hydration process and its influence on electrical measurements. Considering the reference samples (without cement), a total of 108 specimens were manipulated for study.

After curing, the specimens were prepared for compression and leaching/absorption tests, which were performed after a

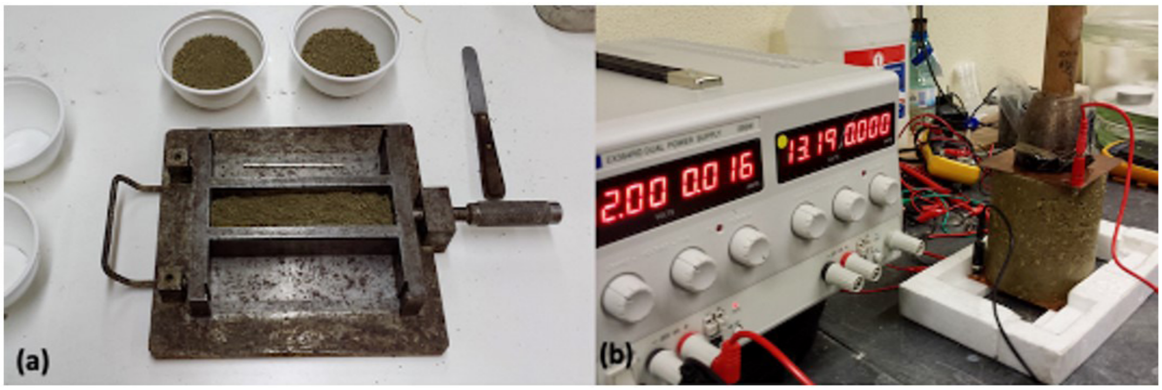

Figure 1. (a) specimen molding; (b) electric current reading procedures.

Table 1. Cement content (C) per m^3 of soil-cement (kg/m^3).

(C) cement content (kg/m^3)					
		(G) dry density (kg/m^3)			
		G1 (1400)	G2 (1500)	G3 (1600)	G4 (1700)
(D) cement dosage (%)	D1 (5)	72.15	77.30	82.46	90.63
	D2 (10)	152.27	163.16	174.06	191.29
	D3 (15)	241.84	259.14	276.45	303.79
	D4 (20)	342.62	367.11	391.64	430.39

new measurement of the electrical conductivity. This is the electrical conductivity of the saturated soil-cement (K_0, or K_f if measured for different curing times). Each specimen of 4 cm × 4 cm × 16 cm was cut into three parts, being the cubic central part (4 × 4 cm^2) reserved for the leaching and water absorption tests, and the two extremes (6 × 4 cm^2) reserved for the simple compression tests (load applied along the larger dimension). The specimens reserved for the compression tests were wrapped in plastic wrap to prevent edge breaks.

2.2 Electrical conductivity of the treated compacted marls

The procedure adopted to measure the electrical conductivity of the treated compacted marls is presented in Figure 1b. A source of continuous tension between 12-35 V and one-millimeter-thick copper plate electrodes (10 × 10 cm^2) was used to measure the electrical conductivity in the solid samples.

Electrical conductivity was computed using the well-known Ohm's law. The electric current was measured using the voltage source in the central part of the sample, applied perpendicularly to bedding layers formed in the compaction. The contact between the electrodes and the soil was ensured using a small weight, and a standard time for current stabilization of 15 seconds was adopted to consider capacitive effect of the material. Capacitive properties were not explored further. The soil-cement conductivity was taken in the saturated material with dry surface, i.e., superficially dried (ABNT, 2012b).

2.3 Leaching, electrical conductivity and water adsorption joint tests

The central part of each sample was wrapped in filter paper to avoid possible loss of solid material (Figure 2a) after measuring the electrical conductivity. Then the sample was totally submerged in distilled water whose volume was defined to be 7.5 times the volume of the sample. It remained submerged (Figure 2b) until full saturation. Saturation was determined by controlling the sample weight along the leaching test.

The experimental conditions to measure the electrical conductivity of the pore solution were not postulated as in Archie's Law. They were adapted in this study from the sample leaching. Two factors, then, probably affected the electrical conductivity measures obtained: the dispersion of clay minerals in pore solution, and the dilution of pore solution. However, the expectation is to validate Archie's Law for soil-cement under simplified experimental conditions and to obtain a representative value of the "cementation" of the material, that is, of the connected porous network derived from dosing, molding, and curing conditions

The electrical conductivity of the leached solution was measured using a CRISON conductivity meter (Figure 2c) (reading range of 0.2 μS/cm). The electrical conductivity of the pore solution of the samples (K_{sp}) was obtained from the relation between the accumulated conductivity and the leaching period, according to Vaillant (2013). The correlation curve presents a linear zone that is representative of the conductivity of the pore solution. Thus, the K_{sp} value was calculated from the slope of that line.

At the end of the leaching test the open porosity was determined after curing, at 7 and 28 days, by measuring the difference between total masses measured after saturation and after oven drying.

2.4 Unconfined compression tests

The unconfined compression tests were done following CEN EN 1015-11 (CEN, 2007). The load was applied adopting a constant rate of 0.5 mm/min for axial deformation. The precision of the equipment is 0.01 kN. The specimens tested were cut from the ends of the main sample (6 cm × 4 cm) and were subjected to saturation for four hours before the compression test. Figure 3 shows the steps followed for samples preparation.

2.5 Electron scanning microscope images and mercury intrusion porosimetry tests

Complementary mercury intrusion porosimetry (MIP) tests were performed in 1 × 1 × 1 cm^3 cubic portions extracted from some samples after 28 days curing to evaluate changes

Figure 2. (a) sample packaging; (b) submersion for leaching test; (c) measurement of the leachate electrical conductivity.

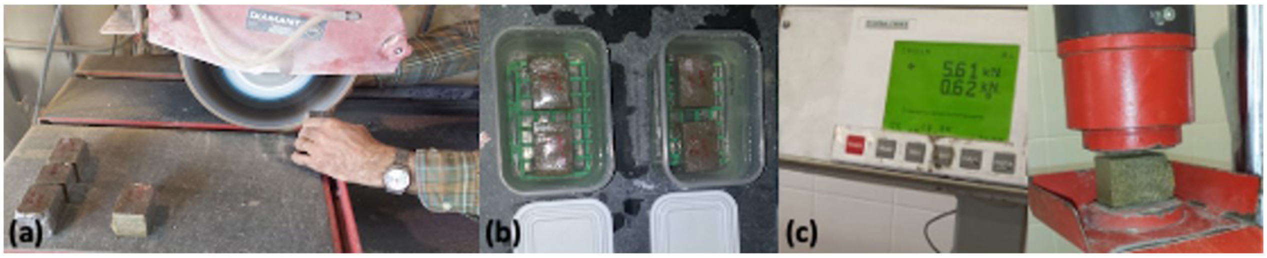

Figure 3. Sample preparation for the UCS tests: (a) cutting; (b) saturation; (c) compression.

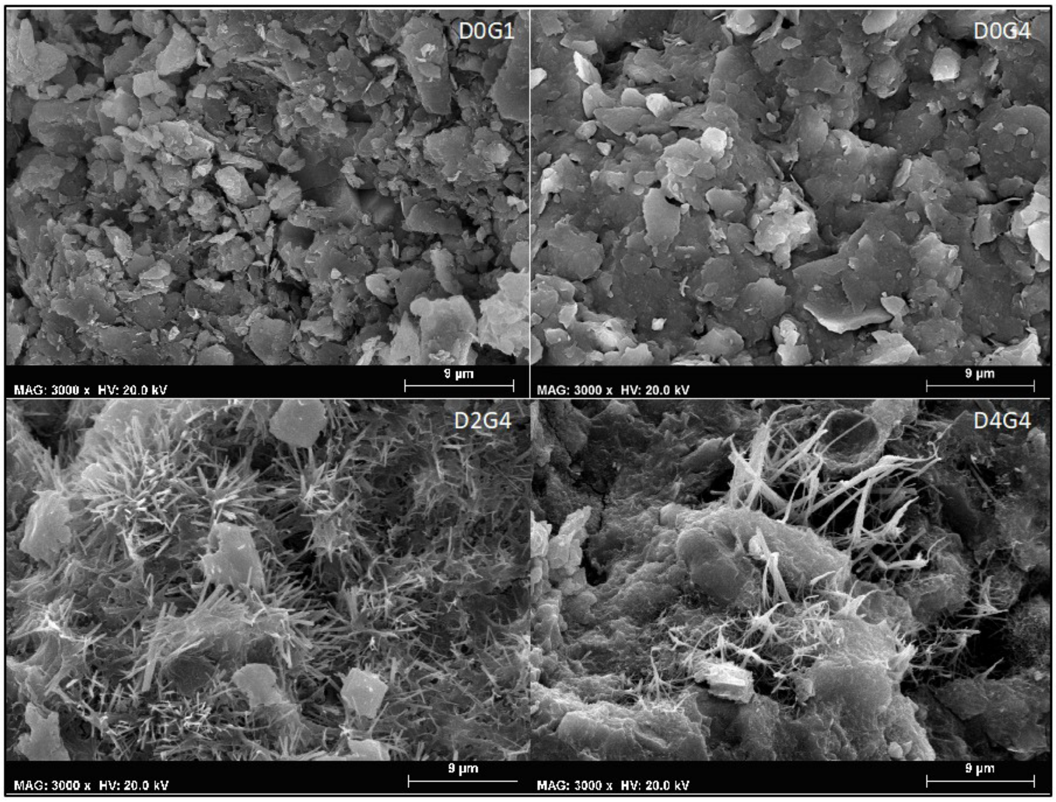

Figure 4. Microscopy of treated (bottom images) and untreated (top images) marls at different cement contents and molding density.

in pore sizes due to compaction and cement dosage. Electron scanning microscope images allowed to visualize the hydrated cement minerals formed for the different dosages adopted.

3. Results and discussion

3.1 Electron scanning microscope images

Figure 4 presents some electron scanning microscope images of the soil-cement structures modified by the compaction density (top photos) and stabilization with cement for 28 days of curing (bottom photos). The presence of the hydrated cement minerals is obvious in both samples, being more disperse and less thick in sample D2G4 than in sample D4G4. Their presence confirms pore clogging of the compacted material, interfering with electrical conductivity of the material because electrical current flows mainly through the liquid phase, i.e., by the pore fluid.

3.2 Influence of cement content on the conductivity of solid material (K_f)

Figure 5 presents the relation between cement content and saturated material electrical conductivity for 7 and 28 days of curing. In general, the electrical conductivity for a given curing period (K_f) tends to decrease with the increase of both cement content (C) and dry density (G) at compaction. This same behavior can be observed in other studies (e.g. Khalil & Santos, 2011; Kibria & Hossain, 2012; Zhang et al., 2012; Hammad, 2013; Fallah-Safari et al., 2013; Bai et al., 2013; Vincent et al., 2017).

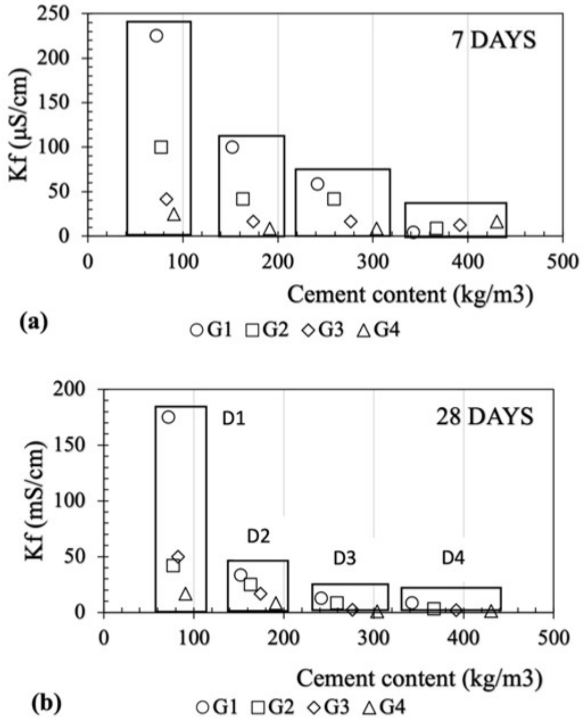

Figure 5. Influence of cement content on the conductivity of the solid material for (a) 7 days and (b) 28 days of curing.

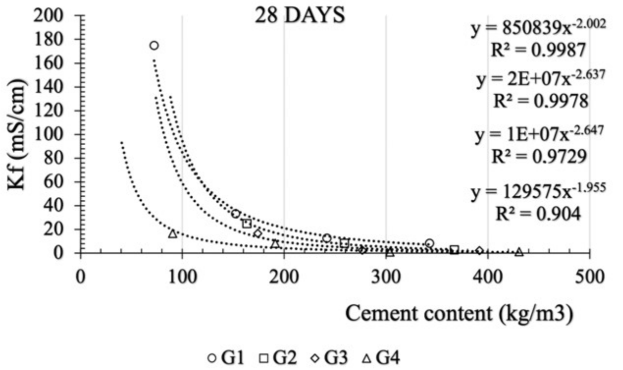

Figure 6. Influence of cement content on the conductivity of the solid material.

This behavior was expected, because the hydrated cement paste creates a new porous network in the material, with less quantity of pores and also disconnecting them (see the bottom images in Figure 4). This structural change has a direct impact on the material conductivity because the electrical current flows through the liquid phase and the path followed depends on the geometry of the connected pores. In addition, the amount of liquid present in the porous material is reduced by decreasing porosity and, for this reason, the conductivity decreases with the increase of dry density.

This reduction in conductivity is more marked for 28 days of curing, when the hydrated cement minerals are expected to be completely formed and therefore the quantity of ions dissolved in the pore water is reduced. Indeed, assuming the same amount of cement minerals for the same dosage (D), a consistent trend of behavior can be observed, indicating a power function whose exponent is close to 2.0 (Figure 6). This also seems to be the behavior trend observed in the work by Zhang et al. (2012), for three samples studied at six different curing times.

There was a great dispersion for samples with seven days of curing, mainly for the highest cement dosages, which may be due to hydration reactions still in progress, with a greater amount of hydrated calcium compounds present in the system. This fact can also be observed and explained in other studies already mentioned (Liu et al., 2008; Chen et al., 2011; Zhang et al., 2012; Vincent et al. (2017). For this reason, the regressions for the seven-day-curing samples were not presented.

3.3 Influence of cement content on the conductivity of the pore solution (K_{sp})

The presence of cement contributes to increase the conductivity of the pore solution (K_{sp}) due to dissolved ions. This conductivity is different from that of distilled water even for the untreated material due to the presence of dissolved clay minerals. The contribution of the cement is evident in the values of K_{sp} measured for the lowest curing age (7 days), when there is intense chemical activity (cement hydration reactions) impairing the diffuse ion transport. This can be seen in Figure 6, in which the relations were more dispersed at this early age than after 28 days of curing. It is assumed that, in the latter, the pore water system is chemically more stable and, therefore, there is a well-defined trend between the variables. For 28 days the values of K_{sp} are linearly related to the cement content (slope close to 0.4, in Figure 7b).

By keeping cement dosage (D) constant there is an increase in K_{sp} for increasing dry density (G). The increase in dry density imposes an increase in cement content to adjust to the required percentual dosage. For this reason, there will be a greater concentration of ions in the pore solution which, in turn, will have their volume reduced because of the reduction of large pores produced by the higher density. It seems that this may have accelerated the ion transport mechanism, increasing its concentration in the leached solution and, consequently, increasing its conductivity.

3.4 Influence of cement content on the soil-cement Formation Factor (FF_{sc})

The FF_{sc} represents the structural arrangement of the material at its "formation". For soil-cement, therefore, this factor will influence dosage parameters (cement content and compaction density), type and curing time. The mathematical relations between the FF_{sc} and cement content (C), defined in kg/m^3, are presented in Figure 8. The regressions were performed as a function of the samples dry density, which, in this case, also represents an increase in the cement content,

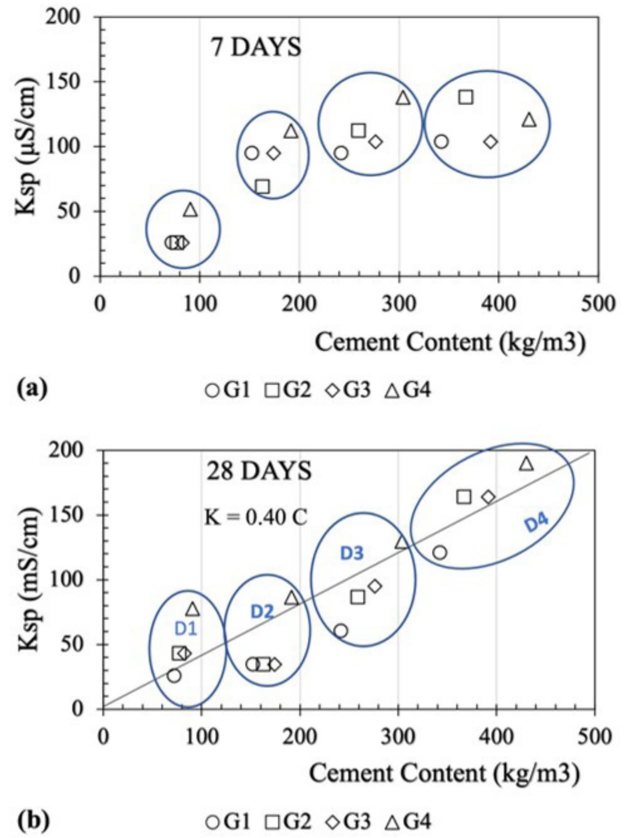

Figure 7. Influence of cement content on the conductivity of the pore solution for (a) 7 days and (b) 28 days of curing.

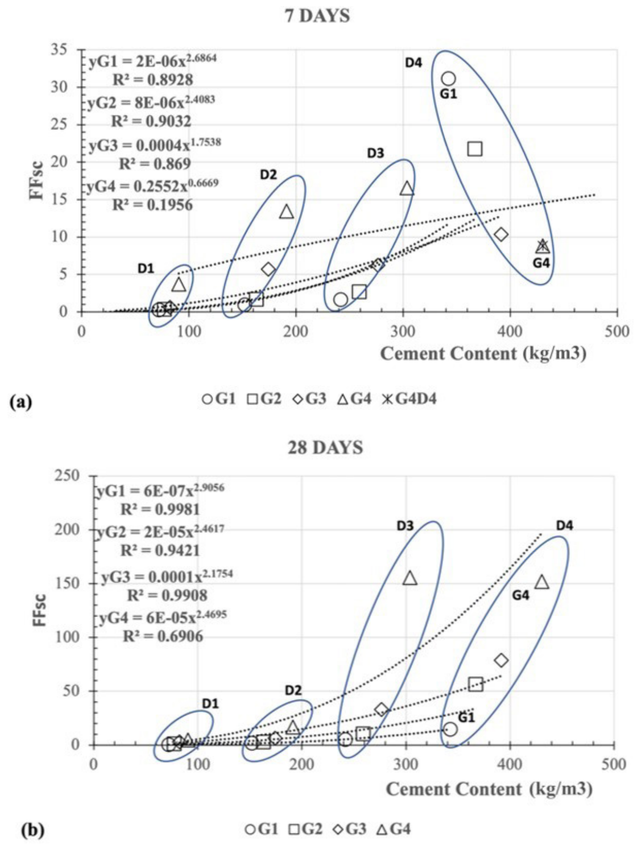

Figure 8. Influence of cement content on the soil-cement Formation Factor for (a) 7 days and (b) 28 days of curing.

as indicated by the deviations of the points to the right. The groups of samples for the different cement dosages (D) were highlighted with circles in the graphs.

Similar trends relating the two variables can be seen, except for sample D4 for 7 days of curing. The differences found for this sample are possibly due to the presence of larger amounts of non-hydrated cement particles. In other words, the sample with 20% of cement (D4) seems to indicate a disproportionate hydration process, suggesting that the relationship between water and cement was not ideal, with not enough water to hydrate the existing amount of cement particles. This caused a kind of "delay effect" in the hydration process at this age, which interfered with the conductivity readings, reversing the trend presented for the other groups of samples, with lower cement contents. At 28 days of curing, however, there was greater stability in the formation of the porous network, and the slope of the curve tended to be constant for any dosage, as indicated by the equations in Figure 8b. This suggests that, for cement contents above 15%, it would be prudent to have a curing time longer than 7 days to ensure that the measurements of the treated materials will no longer be affected by this hydration delay.

No study was found in the literature on the application of the electrical conductivity of soil-cement for a content of 20%. There were also no studies of this material associated with Archie's Law, involving electrical conductivity reading of the pore solution. There are many studies on the application of Archie's Law to concretes and mortars, associated with porosity, permeability, setting time and ion diffusion, as reported in Vaillant (2013). These differences in porosity can be observed in the mercury intrusion porosimetry (MIP) tests, which indicated a minor difference in the porous network for samples D2 e D4. The curves presented in Figure 9, for samples D0G4, D2G4 and D4G4, indicate the expected overall reduction of the pore size with increasing density, being more visible for the smallest pores because the peak displaced from dimensions around 120 nm to 80 nm and to 50 nm, for increasing dosages D0, D2 and D4, respectively.

Finally, as observed in Figure 8, samples with a higher cement content showed a higher FF_{sc}, represented by the points shifting up and to the right. Those samples with a higher density had a higher FF_{sc}, represented by the upward shift of samples G1-G4 (except for group D4, as already discussed). Curing time concurs to reduce electrical conductivity of the solid sample (K_f) and, therefore, the higher it is, the greater is the FF_{sc}.

3.5 Influence of K_f and K_{sp} on the FF_{sc}

Figure 10 presents the relations between the conductivities of the solid material and the pore solution, K_f and K_{sp}, and the

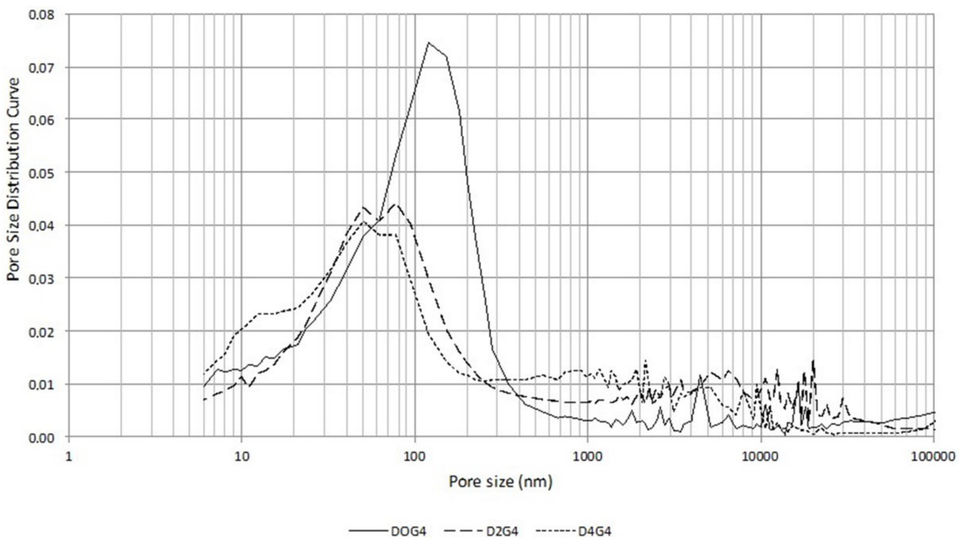

Figure 9. Mercury intrusion porosimetry for the samples with dry density G4 with different cement dosage.

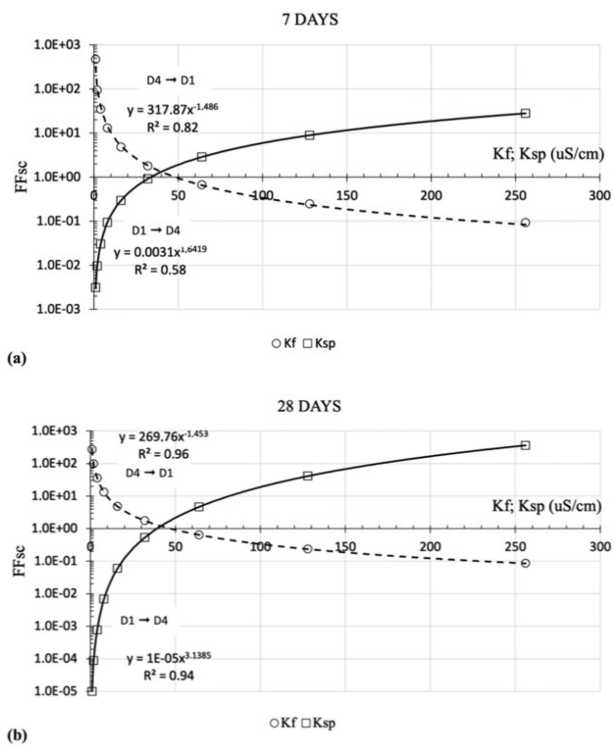

Figure 10. Influence of conductivities (K_{sp} and K_f) on the value of the formation factor (FF_{sc}) for (a) 7 days and (b) 28 days of curing.

FF_{sc} value. The conductivity of the solid sample is lower for higher cement contents and higher for low contents (D4→D1). Thus, the FF_{sc} increases when the conductivity of the solid decreases. On the other hand, the conductivity of the pore solution is lower for lower cement contents and higher for high cement contents (D1→D4). Therefore, the FF_{sc} increases when the conductivity of the pore solution is increased.

However, FF_{sc} is more sensitive to K_{sp} than to K_f: when K_f increases by a ratio of two (2), FF_{sc} decreases by a ratio close to three (3) times or 37%; when K_{sp} increases in the same proportion, the FF_{sc} increases in the rate of ten (10) times on average, or 1000%. This fact is certainly related to the lower resistance of the liquid medium to the passage of electric current, and also to the method used to obtain K_{sp} from the leaching test, as discussed above. The FF_{sc} will be unitary when the conductivities of the solution and the solid are equal. For the studied soil, this occurred for the value of 45 µS/cm, as can be seen in Figure 10.

3.6 Influence of open porosity on the FF_{sc}

FF_{sc} is inversely proportional to the open porosity (Figure 11), represented here by the absorption of water, in compliance with Archie's Law. The only exception was observed in sample D4 at 7 days.

The results show small variations in open porosity for increases in cement content. These variations are more consistent when the mold density is increased, except for the D4 sample. Considering only samples with 28 days of curing, the minimum open porosity achieved for the soil-cement in this study was close to 20% (D2G4), and the maximum close to 32% (D1G1). The FF_{sc} is close to 5 for samples D1G4, 17 for D2G4 e reaches 150 in samples D4G4, indicating the influence of cement content on this factor.

It seems that the cementation coefficients (m) tend to stabilize for cement contents above 10%. This occurred with the samples with 7 and 28 days, demonstrating an independence of curing time from that dose onwards. The cement content influences the FF_{sc} due to the hydration products, and its value varies if there are hydration reactions taking place, as indicated by the results (Figure 8). However, the increase

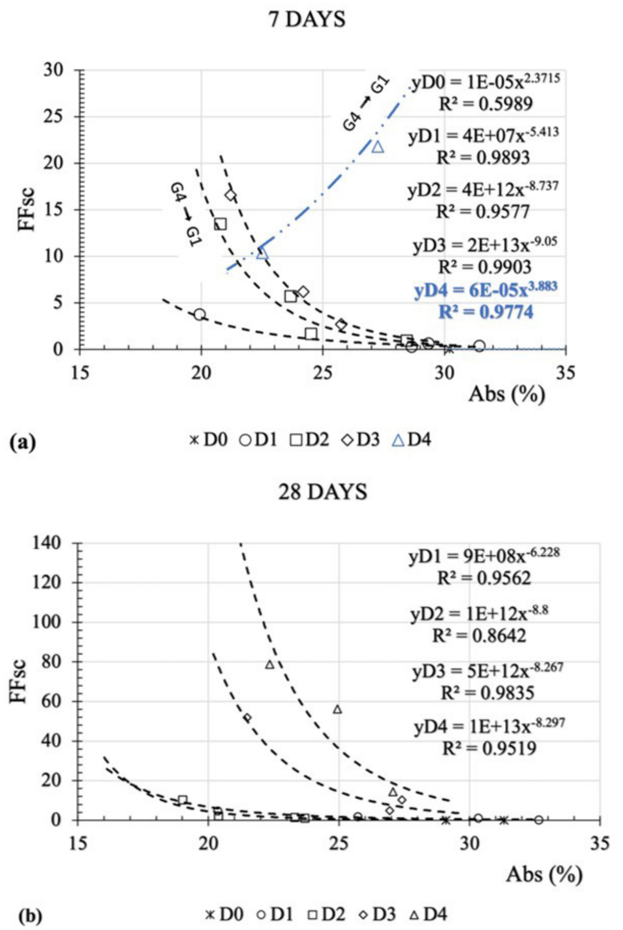

Figure 11. Influence of open porosity (*Abs*) on the soil-cement FF_{sc} for (a) 7 days and (b) 28 days of curing.

in cement content does not represent a reduction in open porosity, in general. This will also depend on the mold density, as exemplified in Table 2.

The value of the cementation coefficient was close to 8 for the samples D3 and D4, being close to 9 and 6 for samples D2 and D1, respectively. These values for *m* constant are similar to those found for soil-cement mixtures (Backe et al., 2001) and hardened mortars (Garboczi, 1990; Christensen et al., 1994; Backe et al., 2001) and sand-cement mixtures (Cardoso, 2016), higher than the values found for soils and rocks (between 1 and 3, if Archie´s law is used). An acceptable explanation given by Christensen et al. (1994) for such high value is that the pore structure of cement slurries is much more tortuous and less porous than that of rocks. Similar explanation was given by Bryant & Pallatt (1996) in the interpretation of the results found for very low-porosity rocks.

The other constant in Archie's equation (*A*) represents a volumetric factor and its value has an extensive range of variations attributed to a series of intervening factors (Worthington, 1993). For the soil-cement samples in this study, this coefficient did not show significant variations for samples above 10%. The values

Table 2. Variation of open porosity (*Abs*) with cement content for the samples G3 and G4.

	Abs (%)	
	7 days	28 days
D1G3	29.4	25.7
D2G3	23.7	20.4
D3G3	24.2	21.0
D4G3	22.5	21.5
D1G4	19.9	20.4
D2G4	20.8	19.0
D3G4	21.2	21.5
D4G4	20.8	21.0

were very high, in the order of magnitude of 10^{12}, indicating that the FF_{sc} tends to infinity when porosity tends to zero. On the other hand, experimental data reveal the tendency of the curve to tangent the porosity axis. It means that when it reaches its maximum value, the FF_{sc} value reaches zero, theoretically.

4. *FFsc* and UCS

4.1 Influence of the soil-cement formation factor on UCS

The relation between the UCS of the soil-cement mixtures and the Formation Factor is presented in Figure 12. The samples dosed with 20% of cement (D4) were excluded from the analysis, due to the deviations presented by the FF_{sc} in the samples with 7 days of curing. Although this dispersion was minimized in the 28-day samples, as previously mentioned. UCS increases linearly with FF_{sc}, which in turn increases with cement content (D1→D4) and molding density (G1→G4), as shown in Figure 12.

The logarithmic scale was adopted to favor the visualization of the trend curves, with indicate good linear relations between the variables. A good fitting is also found if all samples are considered in a unique relationship (Figures 12b and 12d), with angular and linear coefficients with values of 0.08 and 0.11 for curing of 7 days, and 0.02 and 0.53 for curing of 28 days.

Considering that the FF_{sc} is lower for the largest porosities (Figure 11), then the UCS will be higher for higher values of FF_{sc}, as expected due to this mechanical property of the material. Note that there is also a progression of strength in relation to the cement dosage, which can be verified on the right part of the plot (Figures 12a and 12c).

The FF_{sc} is a parameter obtained after curing the soil-cement in saturation condition and should not vary for periods over 28 days. So, it can be an alternative to control this material strength after its production, in addition to the usual way that relates strength to the design parameters (GC). Nevertheless, it is best to consider each dosage to minimize error, as discussed next.

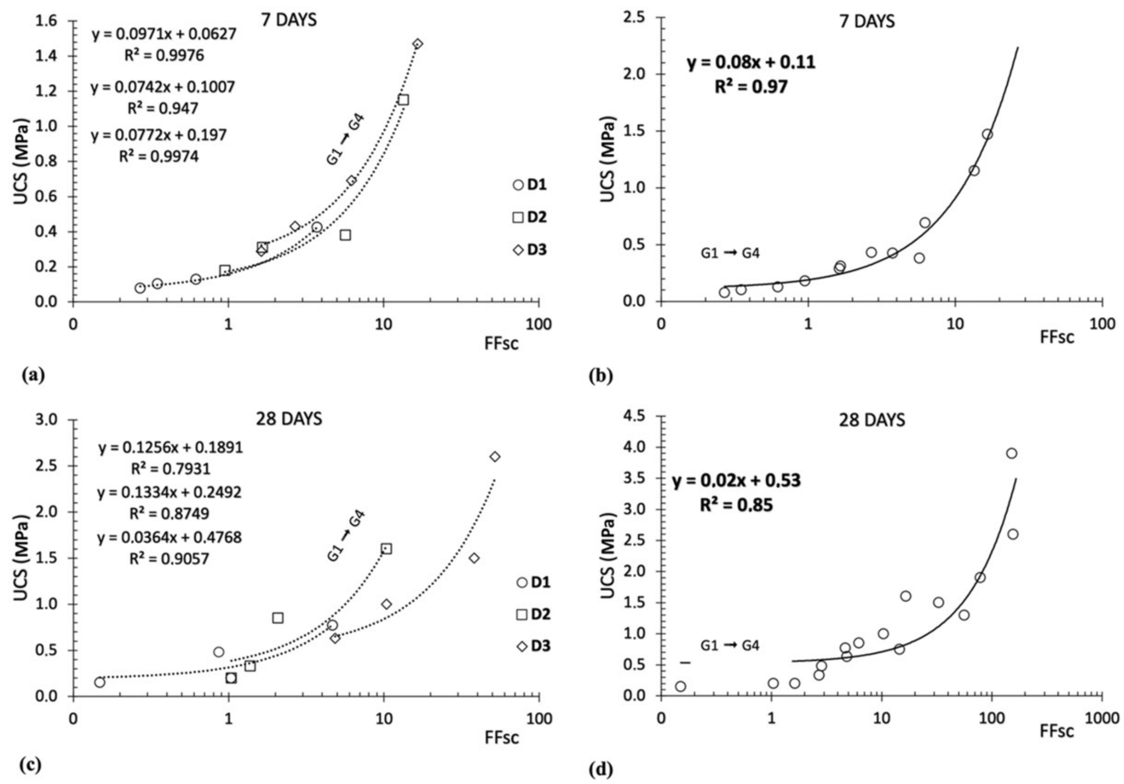

Figure 12. Relation between FF_{sc} and UCS for: (a) 7 days for each cement content; (b) 7 days for any content; (c) 28 days for each cement content; (d) 28 days for any content.

Considering the soil characteristics and the manual molding conditions adopted in this study, the unconfined compression strength reached minimum values (2 MPa) only at the curing time of 28 days, for samples molded close to dry density of 1.7 (G4) and cement content equal to or above 15% (D3 and D4).

The equation in Figure 12b indicates that to obtain a minimum value of UCS = 2 MPa at 7 days, the FF_{sc} should be close to 24 or greater. Thus, by the graph of Figure 10, it is possible to know which value of electrical conductivity of the solid and of the solution must be obtained in the measurements. Applying the equation, the values found are, respectively, 5 μS/cm and 113 μS/cm, approximately.

4.2 Influence of design parameters on soil-cement UCS

The values of soil-cement UCS can be mathematically related with the cement contents, as it is usually done for mortars and concrete. This is presented in Figure 13. In this figure it is also shown that there is a direct relationship between the soil-cement UCS and its molding density.

The slope of the regression line corresponds to an increase in the UCS when dry density and cement content increase. Regarding the constant cement content (C), the UCS grows vertically with the dry mold density. The small slope of the correlation line is due to the cement content that was increased with the density. On the other hand, for constant molding density (G), the UCS values also increase vertically with dosage. Relationships such as these are useful to quantify UCS using this non-destructive technique.

From the plots in Figure 13, the UCS is obtained for any combination of cement consumption (C) and mold density (G) for the cement-stabilized soil. Table 3 presents the calculations obtained for a UCS = 2 MPa, including the control parameters, confirming that high dry densities are required in molding for low cement contents. It seems relevant to remember that more unfavorable conditions were adopted in this study, such as manual compaction, immediate demolding and curing in a wet chamber.

The calculations show the possible combinations in dosing parameters to achieve the desired strength, both at 7 and 28 days. In some cases, it is still necessary to meet a water absorption requirement at 7 days of curing, which is 20% on average. Thus, the most economical dosage in this context would be for a cement consumption of 337.3 kg/m^3 and molding density of 2059.2 kg/m^3. However, this density would not be obtained manually.

The calculations also indicate the variation of FF_{sc} as a function of curing time. This factor was calculated based on the good general relations shown in Figure 12. Therefore, it is constant for all combinations. The volumetric constant

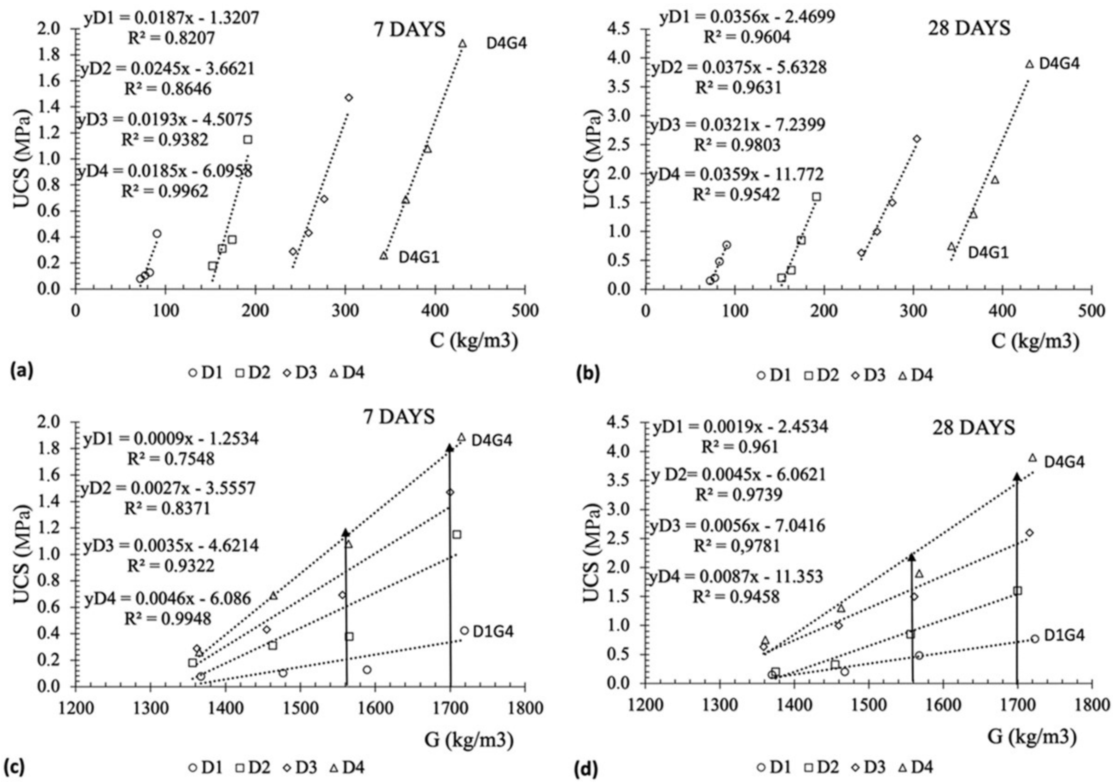

Figure 13. Influence of cement content on soil-cement UCS for: (a) 7 days and (b) 28 days. Influence of the dry density on soil-cement UCS for: (c) 7 days and (d) 28 days.

Table 3. Results of dosing and control parameters for UCS = 2 MPa.

D (kg/m³)	G (kg/m³)	*Abs* (%)	K_{sp} (μS/cm)	K_f (μS/cm)	FF_{sc} (min)	*A*	*m*
			7 days				
177.5	3611.0	13.8	210	6	24	1E+12	9.3
231.0	2059.2	19.0					8.3
337.3	1891.4	20.5					8.0
437.8	1758.7	28.0					7.3
			28 days				
125.6	2342.1	16.8	102	6	20	1E+12	8.7
203.5	1791.1	16.6					8.7
163.2	1614.3	23.9					7.8
383.6	1534.8	25.3					7.7

(*A*) of Archie's Law was also considered constant for all sample combinations because it is "volumetric factor" with a value of a high order of magnitude. Small variations in the "cementation coefficient" (*m*) can be observed for each variation in dosage. Also, this coefficient tends to stabilize at the end of the "formation" of the definitive structure of the material at 28 days of curing.

The K_f values were obtained from the equations in Figure 10 and they presented a constant value along curing time. The K_{sp} value was calculated from this conductivity and the FF_{sc}. Thus, minimum values were obtained for this variable and equations with poor correlation coefficients were avoided, as seen in Figure 10a.

5. Conclusions

A methodology is proposed to evaluate the UCS of compacted soil-cement mixtures by using a non-destructive technique, in which the electrical conductivity of the material and that of the fluid from a leaching test are measured to compute the parameter FF_{sc}. This Formation Factor of the soil-cement varies for each combination of dosage/dry density. These parameters contribute to the variations in the electrical conductivity of the material (K_f) and of the pore solution (K_{sp}). This last measure increases with increasing cement content, and the second decreases. However, FF_{sc} is more sensitive to K_{sp} than to K_f, in a proportion 5 times greater. Curing time concurs to reduce electrical conductivity of the solid sample (K_f) and, therefore, the higher it is, the greater is the FF_{sc}. The cement content influences the FF_{sc} from the porous network formed with the hydration products, and its value varies as long as there are hydration reactions taking place. However, the increase in cement content does not represent a reduction in open porosity in general. This will also depend on the mold density.

The cementation coefficient is not constant for the material up to 7 days of curing, but it seems to stabilize at 28 days. At this age, the value of the cementation coefficient was close to 8 for the samples D3 and D4, and close to 9 and 6 for the samples D2 and D1, respectively. The same occurred to the volumetric factor (A), whose values were very high, in the order of magnitude of 10^{12} on average. Therefore, the higher the FF_{sc} of the soil-cement, the higher its UCS. It was seen that UCS increases with both mold density and cement content.

Therefore, it is possible to design the material quality control parameters of the soil-cement and, consequently, the dosage parameters to obtain a specific UCS using the methodological conditions proposed by this study.

Acknowledgements

We are thankful to Instituto Superior Técnico of Lisbon University for having supported the conduct of the research and the Brazilian sponsoring agency CAPES (Coordenação de Aperfeiçoamento de Pessoal de Nível Superior) for the funding.

Declaration of interest

The authors have no conflicts of interests that could inappropriately bias this work. There is no financial interest to report.

Authors´ contributions

João Marcos Vaillant: conceptualization, data curation, formal analysis, funding acquisition, investigation, methodology, visualization, writing. Rafaela Cardoso: resources, supervision, validation, writing.

List of symbols

m	cementation coefficient of the Archie's Law
A	volumetric coefficient of the Archie's Law
Abs	water absorption or open porosity
C	cement content in kg/m^3
CL	clay low
D	cement content in percentage
FF	Archie's Formation Factor for conductivity
FF_{sc}	Apparent Factor Formation for soil-cement
G	molding dry volumetric weight (kN/m^3)
K_0	electrical conductivity of saturated material
K_f	electrical conductivity of soil-cement saturated after curing
K_{sp}	electrical conductivity of soil-cement pore solution
K_w	electrical conductivity of material pore solution
UCS	unconfined compression strength of the soil
ϕ	porosity of the material

References

ABNT NBR 8491. (2012a). *Soil-cement brick – Requirements*. ABNT – Associação Brasileira de Normas Técnicas, Rio de Janeiro, RJ. (in Portuguese).

ABNT NBR 8492. (2012b). *Soil-cement brick — Dimensional analysis, compressive strength determination and water absorption — Test method*. ABNT – Associação Brasileira de Normas Técnicas, Rio de Janeiro, RJ. (in Portuguese).

Archie, G.E. (1942). The electrical resistivity log as an aid in determining some reservoir characteristics. *Petroleum Transactions of AIME*, 146(1), 54-62. https://doi.org/10.2118/942054-G.

Backe, K.R., Lile, O.B., & Lyomov, S.K. (2001). Characterizing curing cement slurries by electrical conductivity. *SPE Drilling & Completion*, 16(4), 201-207. http://dx.doi.org/10.2118/74694-PA.

Bahar, R., Benazoug, M., & Kenai, S. (2004). Performance of compacted cement-stabilized soil. *Cement and Concrete Composites*, 26, 811-820. http://dx.doi.org/10.1016/j.cemconcomp.2004.01.003.

Bai, W., Kong, L., & Guo, A. (2013). Effects of physical properties on electrical conductivity of compacted lateritic soil. *Journal of Rock Mechanics and Geotechnical Engineering*, 5, 406-411. http://dx.doi.org/10.1016/j.jrmge.2013.07.003.

Bryant, S., & Pallatt, N. (1996). Predicting formation factor and resistivity index in simple sandstones. *Journal of Petroleum Science Engineering*, 15(2-4), 169-179.

Cardoso, R. (2016). Porosity and tortuosity influence on geophysical properties of an artificially cemented sand. *Engineering Geology*, 211(23), 198-207. http://dx.doi.org/10.1016/j.enggeo.2016.07.009.

Cardoso, R., & Maranha das Neves, E. (2012). Hydro-mechanical characterization of lime-treated and untreated marls used in a motorway embankment. *Engineering*

Geology, 133-134, 76-84. http://dx.doi.org/10.1016/j.enggeo.2012.02.014.

CEN EN 1015-11. (2007). *Methods of test for mortar for masonry. Part 11 - Determination of flexural and compression strength of hardened mortar*. CEN – European Committee for Standardization, Brussels.

Chen, L., Du, Y., Liu, S., & Jin, F. (2011). Evaluation of cement hidration properties of cement stabilized lead contaminated soils using electrical resistivity measurement. *Journal of Hazardous, Toxic and Radioactive Waste*, 15(4), 312-320. http://dx.doi.org/10.1061/(ASCE)HZ.1944-8376.0000073.

Christensen, B.J., Coverdale, T., Olson, R.A., Ford, S.J., Garboczi, E.J., Jennings, H.M., & Mason, T.O. (1994). Impedance spectroscopy of hydrating cement-based materials: measurement, interpretation, and application. *Journal of the American Ceramic Society*, 77(11), 2789. http://dx.doi.org/10.1111/j.1151-2916.1994.tb04507.x.

Fallah-Safari, M., Hafizi, M. K., & Ghalandarzadeh, A. (2013). The relationship between clay geotechnical data and clay electrical resistivity. *Bolletino di Geofisica ed Applicata*, 54(1), 23-38. http://dx.doi.org/10.443/bgta0070.

Garboczi, E.J. (1990). Permeability, diffusivity, microstructural parameters: a critical review. *Cement and Concrete Research*, 20(4), 591-601. http://dx.doi.org/10.1016/0008-8846(90)90101-3.

Hammad, A.H. (2013). *Evaluation of soil-cement properties with electrical resistivity* [Master, Dalhousie University]. Department of Civil Engineering, Dalhousie University. Retrieved in July 8, 2021, from http://hdl.handle.net/10222/21920

Kahraman, S., & Yeken, T. (2010). Electrical resistivity measurement to predict uniaxial compression and tensile strength of igneous rocks. *Bulletin of Materials Science*, 33(6), 731-735. http://dx.doi.org/10.1007/s12034-011-0137-x.

Khalil, M.A., & Santos, F.A.M. (2011). Influence of degree of saturation in the electrical resistivity-hidraulic conductivity relationship. In O. Dikinya (Ed.), *Developments in hydraulic conductivity research* (Chap. 2, pp. 49-70). IntechOpen. Retrieved in July 8, 2021, from https://vdoc.pub/documents/developments-in-hydraulic-conductivity-research-3um1p1earg3g

Kibria, G., & Hossain, M.S. (2012). Investigation of geotechnical parameters affecting electrical resistivity of compacted clays. *Journal of Geotechnical and Environmental Engineering*, 138, 1520-1529. http://dx.doi.org/10.1061/(ASCE)GT.1943-5606.00007222.

Liu, S., Du, Y., Han, L., & Gu, M. (2008). Experimental study on the electrical resistivity of soil-cement admixtures. *Environmental Geology*, 54(6), 1227-1233. http://dx.doi.org/10.1007/s00254-007-0905-5.

Lorenzo, G.A., & Bergado, D.T. (2004). Fundamental parameters of cement-admixed clay: new approach. *Journal of Geotechnical and Geoenvironmental Engineering*, 130, 1042-1050. http://dx.doi.org/10.1061/(ASCE)1090-0241(2004)130:10(1042).

Maranha das Neves, E. & Cardoso, R. (2006). *Research project for BRISA on the mechanical behaviour of embankments from A10 Motorway. Department of Civil Engineering, Report ICIST EP 23/06 and 23/08*. Instituto Superior Tecnico. in Portuguese.

Rinaldi, V.A., & Cuestas, G.A. (2002). Ohmic conductivity of a compacted silty clay. *Journal of Geotechnical and Geoenvironmental Engineering*, 128(10), 824-835. http://dx.doi.org/10.1061/(ASCE)1090-0241(2002)128:10(824).

Shah, P.H., & Singh, D.N. (2005). Generalized Archie's law for estimation of soil electrical conductivity. *Journal of ASTM International*, 2(5), 1-19. http://dx.doi.org/10.1520/JAI13087.

Song, Y.L., Yan, J.D., Han, L.H., & Gu, M.F. (2008). Experimental study on the electrical resistivity of soil–cement admixtures. *Environmental Geology*, 54, 1227-1233. http://dx.doi.org/10.1007/s00254-007-0905-5.

Vaillant, J.M.M. (2013). *Avaliação dos parâmetros de lixiviação de metais pesados em matriz de cimento Portland por meio da condutividade elétrica* [Doctoral Thesis, Federal University of Santa Catarina]. Federal University of Santa Catarina's repository (in Portuguese). https://repositorio.ufsc.br/handle/123456789/107025

Vaillant, J.M.M., & Cardoso, R. (2016). Comportamento da condutividade elétrica mediante variações nos parâmetros de compactação dos solos. In *Anais do 15º Congresso Nacional de Geotecnia e 8º Congresso Luso-Brasileiro de Geotecnia: A Geotecnia e os desafios societais*, Porto.

Vincent, N.A., Shivashankar, R., Lokesh, K.N., & Jacob, J.M. (2017). Laboratory electrical resistivity studies on cement stabilized soil. *International Scholarly Research Notices*, 2017, 8970153. https://doi.org/10.1155/2017/8970153.

Worthington, P.F. (1993). The uses and abuses of Archie equations, 1: the formation factor-porosity relationship. *Journal of Applied Geophysics*, 30(3), 215-228. http://dx.doi.org/10.1016/0926-9851(93)90028-W.

Zhang, D., Chen, L., & Liu, S. (2012). Key parameters controlling electrical resistivity and strength of cement treated soils. *Journal of Central South University*, 19(10), 2991-2998. http://dx.doi.org/10.1007/s11771-012-1368-8.

Soils and Rocks

An International Journal of Geotechnical and Geoenvironmental Engineering

www.soilsandrocks.com

ISSN 1980-9743
ISSN-e 2675-5475

Geostatistical-based enhancement of RFEM regarding reproduction of spatial correlation structures and conditional simulations

Jean Lucas dos Passos Belo[1#], Paulo Ivo Braga de Queiroz[1], Jefferson Lins da Silva[2]

Article

Keywords
Spatial variability
Conditional simulation
Probabilistic analysis
Geostatistics
Random finite element
Reliability

Abstract

Engineering always deals with uncertainties, and efforts are needed to quantify them. A probabilistic analysis considers the statistical information of the problem to this quantification. In the geotechnical area, uncertainties play a particular role in structure design because it deals with naturally formed materials. Evaluating spatial variability has become progressively important. However, studies on the correct reproduction of this variability and conditional simulations are limited. In this paper, a geostatistical-based enhancement of the Random Finite Element Method (RFEM) is presented. The main aim of this study is to incorporate an advanced multivariate geostatistical technique (i.e., Turning Bands Co-simulation, TBCOSIM) to reproduce the coregionalization model of soil properties correctly in order to investigate the effects regarding this reproduction. It is illustrated in a real case of soil slope. The results showed that, for the unconditional simulation, the presented approach reached a perfect agreement with the coregionalization model, while the conditional simulation inserted some disturbances to this agreement, but it still satisfactorily reproduced the model. The original RFEM failed to reproduce this structure, leading to lower variances than the presented approach, which would cause a non-conservative design. Furthermore, disregarding the local uncertainty (i.e., the nugget effect) may introduce bias to analysis and, depending on its magnitude, may also lead the conditional analysis to not show a worthwhile reduction in variances of results. Finally, this paper shows that correctly determining the coregionalization model and reproducing it on probabilistic analysis may meaningfully influence the results.

1. Introduction

Although we (engineers) are typically used to considering engineering as an exact science, we do not always treat it as such. All engineering areas deal with uncertainties (e.g., inherent, spatial, temporal, from measurements or from a model), however we do not always take them into account. Considering and quantifying these uncertainties enables us to evaluate the precision threshold of our estimations (calculated results). When engineers understand the importance of uncertainty quantification and start considering it in their designs and analysis, only then will engineering be conducted as an exact science, within its limitations. Efforts to determine these thresholds should not be overlooked, such as currently observed in practice and even in academic applications, unfortunately. Therefore, this topic requires due attention and may lead to a lengthy discussion.

For Geotechnical Engineering, uncertainties and variabilities associated with material properties, which make up a geotechnical structure, have substantial influences on its safety and behavior. This sensitivity is significant in this area of study because it deals with naturally formed materials (i.e., soils and rocks), sources of large variances and heterogeneity.

Nowadays, many commercial programs allow the realization of probabilistic analysis to evaluate geotechnical structures. Usually, these programs apply the Monte Carlo simulation (MCS) technique, associated with the Limit Equilibrium Method (LEM) or the Finite Element Method (FEM), to perform this analysis. However, today, these programs hold limited resources, such as the number of random variables, the type of probability density functions, the spatial variability consideration, the high computational cost, among others (Belo & Silva, 2020; Belo et al., 2022).

#Corresponding author. E-mail address: belo.jeanlucas@gmail.com
[1]Instituto Tecnológico de Aeronáutica, Departamento de Infraestrutura Aeroportuária, São José dos Campos, SP, Brasil.
[2]Universidade de São Paulo, Escola de Engenharia de São Carlos, São Carlos, SP, Brasil.

Submitted on October 23, 2021; Final Acceptance on August 3, 2022; Discussion open until February 28, 2023.
https://doi.org/10.28927/SR.2022.076121

In the literature, studies have proposed various probabilistic approaches for the geotechnical area. The Random Finite Element Method (RFEM), proposed by Griffiths & Fenton (1993), is the most accepted and used approach for this purpose. RFEM reconciles the FEM with the Random Field Theory (RFT) to simulate the spatial variability of soil properties. It correctly searches for the weakest path through heterogenous material and leads to probabilities of failure higher than would be estimated by disregarding the spatial variability (Sayão et al., 2012). Nevertheless, RFEM disregards known field data, usually determined by sampling material or site investigation. It is the major disadvantage of this approach and, disregarding these data and their positions within the field, can cause fluctuations in variance of analysis and hence produce an incompatible design, touching safety and economy. Therefore, its application (unconditional to data) is useful in generic geotechnical design, e.g., in terms of code or standard provisions.

Approaches aiming to consider known field data make use of the Conditional Random Field (CRF). Despite the fact that studies regarding CRF have increased in recent years, studies using this technique in geotechnical engineering remain limited in number. Mrabet & Bouayed (2000) used the CRF to reduce the uncertainty on the probabilistic results of a dam analysis, more specifically regarding the properties of the compacted soil masses. Folle et al. (2006) presented the main statistical and geostatistical methods in geotechnics to deal with quantification regarding the heterogeneity of soil properties. Then, they evaluated a case study using Sequential Gaussian Simulation (SGS). Griffiths et al. (2009) investigated the influence of spatial variability on slope reliability using the RFEM. However, the spatial correlation function was assumed to be fixed, described by an exponentially decaying (Markov) function. Monteiro et al. (2009) approached the problem of rock characterization using drill measurements. The authors incorporated the spatial relationship using the CRF to infer the geology of the neighboring regions. Kim & Sitar (2013) applied the CRF to a homogeneous soil slope to investigate its stability, assuming the deterministic critical slip surface as fixed for the probabilistic analysis.

Lately, Schöbi & Sudret (2015) combined the CRF with the framework of sparse polynomial chaos expansions to analyze response quantities in geotechnical problems, illustrated by applying the approach to a strip foundation problem on a two-layer soil mass. Li et al. (2016) presented a method that combined 3D kriging with a random field generator to develop the CRF. The authors applied this for a slope stability analysis, aiming to identify the best locations for site investigations and compare different candidate slope designs. Liu et al. (2017) applied the CRF to investigate a cohesion-frictional slope using a MATLAB developed code. The CRF was generated using the kriging method and the Cholesky decomposition technique. Yang et al. (2017) used the CRF to investigate undrained slope stability based on the RFEM and a kriging method. Despite not considering conditional simulations, Muñoz et al. (2018), as Griffiths et al. (2009), investigated the influence of spatial variability of the soil parameters on the factor of safety (FoS) of a hypothetical slope. However, the analysis assumed no correlations between variables (univariate analysis, i.e., independent random variables), spatial variability followed normal and lognormal distribution, by using Monte Carlo simulations and Kriging process, and found the FoS with the LEM. Johari & Gholampour (2018) developed a MATLAB code to apply the CRF to a stochastic analysis of an unsaturated soil slope. Yang et al. (2019) used the CRF to investigate the "optimal" site investigation scope for a slope design, combining the analysis of the cost of site investigation with the cost of slope failure. Johari & Fooladi (2020) presented a probabilistic analysis of a real soil slope using the concepts of the CRF, coded in MATLAB. Jurado et al. (2020) proposed a rational approach to test the spatial variance of soil based on site investigation and on the CRF.

Incorporating the data known from the field and its spatial positions in the analysis can be performed by using geostatistical concepts and techniques. Geostatistical simulations enable the generation of random fields that agree with their statistical information and eventual conditioning data. Liu et al. (2019) showed that, among the random field generation methods, seven cover most studies, i.e., sequential Gaussian simulation (SGS), local average subdivision (LAS), turning bands simulation (TBS), spectral method (SM), Karhunen-Loève expansion (KLE), matrix decomposition method (MD) and moving average method (MA).

KLE and MD present the highest algorithm complexity, followed by MA, SM, TBS, SGS and LAS. Furthermore, the algorithm complexity can be powered in cases of multivariate applications. Although KLE has been widely used in stochastic approaches, it poses a problem in applications, where complex geometry will be encountered or when assuming high dimension covariance matrix, and some problems have been identified regarding heterogeneity of the generated sample functions (Sudret & Der Kiureghian, 2000; Stefanou & Papadrakakis, 2007). MD, as it is, suffers from several deficiencies, e.g., like KLE, problems with a considerable number of nodes or somehow increasing the dimension of covariance matrix will likely run out of memory and, even if that does not happen, the whole processing computation cost is high, including Cholesky decomposition and matrix-vector multiplication. MA involves decomposition in the convolution sense of covariance function, which may influence the applicability regarding computational cost and memory requirements. Although the limitation of TBS had been overcome with computational developments, it was usually associated with the use of few lines to generate random fields, which may introduce artifact effects into them (Emery & Lantuéjoul, 2006). Before each conditional simulation, SGS requires the computation of expected mean and variance. Moreover, SM and LAS are limited to only rectangular grids (simulation mesh), a condition that may be true for some of the above-mentioned methods when simplifications are assumed to relieve the computational processing.

Considering that, the main current techniques applied to geostatistical simulations are Sequential Gaussian Simulation (SGS) (Isaaks, 1990), Turning Bands Simulation (TBS) (Matheron, 1973), and their multivariate versions, Sequential Gaussian Co-simulation (COSGS) (Verly, 1993) and Turning Bands Co-simulation (TBCOSIM) (Emery, 2008). Multivariate simulations or co-simulations are highly recommended for cases with cross-correlated variables, commonly experienced for soil properties.

Some studies have emerged that compare these techniques. Ren (2005) published a short note on conditioning TBS. In this study, the author presented results that demonstrated that the TBS is a fast simulation method when multiple realizations are necessary. For example, performing only one realization of a conditional simulation, SGS was around 5 times faster than TBS. However, increasing this number to 100 realizations, SGS performed around 5.5 times slower than TBS, and this discrepancy presents an almost linear trend in favor of the TBS. Paravarzar et al. (2015) assessed the performance and accuracy of SGS and TBS for jointly simulating co-regionalized variables of a synthetic univariate case and a real multivariate one. The turning bands accurately reproduced the spatial correlation structure for both cases, while the sequential simulation produced some bias, which was more severe in the multivariate case.

The conclusions lead to the claim that TBCOSIM outperforms COSGS in terms of the cross-correlated reproduction, calculated by the spatial continuity and statistical parameters. In addition, the turning bands technique also surpassed other techniques in terms of lower computational costs, standing out more and more when the number of realizations increases. However, studies have not assumed the TBCOSIM technique for applications. Usually, studies have assumed the SGS or other techniques, even assuming fixed functions to describe the spatial correlation of soil properties. Studies have paid little attention to the correct reproduction of the spatial correlation structures of coregionalized variables - or, at least, they do not claim to present the evaluation of their structures. Studies that proposed to investigate the effects regarding spatial variability on probabilistic analysis have focused strictly on the influence of the correlation length (i.e., range) and paid no attention to the agreement between the simulated coregionalization model and the sample one.

Therefore, this paper presents an improved and efficient approach to address probabilistic analysis of geotechnical structures, a geostatistical-based enhancement of the Random Finite Element Method (RFEM) by incorporating an advanced geostatistical technique (i.e., Turning Bands Co-simulation, TBCOSIM), so far not jointly used. It also investigates the influence of correctly reproducing spatial variability on the multivariate probabilistic analysis of geotechnical structure. The primary aim of this work is to provide the correct consideration of the coregionalization model of the soil properties. We illustrate the sophisticated approach and those effects through an actual case of a soil slope, previously presented in the literature.

2. Geostatistical concepts

In reliability studies, geostatistics has gained increasing attention within the area of geotechnical structure design. Geostatistics was originally developed for mining purpose, aiming to characterize the concentrations of certain minerals in a field (Regionalized Variables Theory, RVT) (Matheron, 1973). This theory has two objectives: first, to describe the spatial correlation (theoretically) and, second, to solve estimation problems of a regionalized variable based on a minimal sample (in practice).

The application of a geostatistical technique begins by analyzing the sample data. First, we need to assume that there is a possibility that the value of the random variable for each point, $Z(x)$, in a field is correlated, to some extent, with the values of other nearby points, $Z(x+h)$. This means that the spatial continuity of a regionalized variable can be done with sample values based on two-points statistics. Then, the variogram function, $\gamma(h)$, - used to describe the behavior of spatial correlation in a field - depends only on two points, positioned at a distance h from each other. Analyzing all known data from different points gives the statistical inference for this function. The variogram is calculated as Equation 1.

$$\gamma(h) = \frac{1}{2n}\sum_{i=1}^{n}\left[Z(x+h) - Z(x)\right]^2 \tag{1}$$

Where n is the number of pairs of points separated by lag h. Likewise, the cross-variogram function for multivariate fields can be determined as Equation 2.

$$\gamma_{12}(h) = \frac{1}{2n}\sum_{i=1}^{n}\left[Z_1(x) - Z_1(x+h)\right]\cdot\left[Z_2(x) - Z_2(x+h)\right] \tag{2}$$

A theoretical variogram function must then fit the sample covariograms to be applied in simulations. The simple and cross-variograms compose the most important information for geostatistical simulations. However, conventional statistical information (i.e., mean, standard deviation, and probability density function) may also be required.

Determining statistical information requires some precautions, often neglected. For example, site investigations (boreholes) rarely have regular spacing in the field because of difficulty of access, topography, areas of environmental preservation, among other reasons. Thus, sampling may have clustered boreholes, which may introduce bias to statistical inferences. To address this “clustering problem”, the declustering technique is recommended (e.g., cell declustering and polygonal declustering methods). In brief, the declustering entails analyzing the "influence area" for each borehole of the campaign and calculates the weights for them (Chilès & Delfiner, 2012).

Once the analysis has determined the variogram function and conventional statistical information of the regionalized or coregionalized variables, geostatistical simulations can be performed. If conditional simulations are desired, it would also require the known data (from the site investigation, boreholes), and their position within the field.

2.1 Turning bands co-simulation - TBCOSIM

TBCOSIM was originally presented by Emery (2008) and developed in MATLAB. It is based on the COSIM program - proposed by Carr & Myers (1985) - and the TBSIM - proposed by Emery & Lantuéjoul (2006). TBCOSIM presents significant improvements compared to previous proposals, which are worth mentioning:

- it allows three-dimension simulations, by grid or scattered points;
- it imposes no restrictions on the number of nested structures, known data points or random variables;
- it works with heterotopic data sets;
- it uses stationary and intrinsic models;
- it uses simple kriging, ordinary kriging or intrinsic co-kriging, associated with the consideration of a unique or moving neighborhood, to condition the simulations to a data set;
- it accepts 15 commonly used covariance models (spherical, exponential, gamma, stable, cubic, Gaussian, cardinal sine, J-Bessel, K-Bessel, generalized Cauchy, exponential sine, linear, power, mixed power and spline), as illustrated in Figure 1;
- it backtransforms variables from Gaussian space to the original units of each variable;
- it can change the support (regularization) of simulations.

Besides adapting and modifying the TBCOSIM for this study, it was also entirely reprogrammed using the Fortran language to achieve the objectives. Next, the code was linked to the RFEM to compose the sophisticated approach used in this study (we will call it "sRFEM"). For further details on the TBCOSIM technique, readers are referred to Emery (2008).

3. Random Finite Element Method - RFEM

Originally, RFEM was proposed by Griffiths & Fenton (1993), and it is considered a powerful and rigorous tool to take the spatial variability of soil properties into account for probabilistic analysis. It uses random field theory (RFT) jointly with the finite element method (FEM).

The FEM is used to compute the plane strain deformation of elastic-perfectly plastic soils governed by the Mohr-Coulomb failure criterion. It is also based on the strength reduction method (SRM) and uses eight-node rectangular quadrilateral elements, with reduced integration (four Gauss points per element) in the generation of the gravity loads, the stiffness matrix and the stress redistribution phase. The adopted solution procedure, to model material non-linearity, is the "constant stiffness" (modified Newton-Raphson) method. For more details, readers are referred to Griffiths & Lane (1999) and Smith et al. (2013).

RFEM uses the Local Average Subdivsion (LAS) method, presented by Fenton & Vanmarcke (1990), to generate the

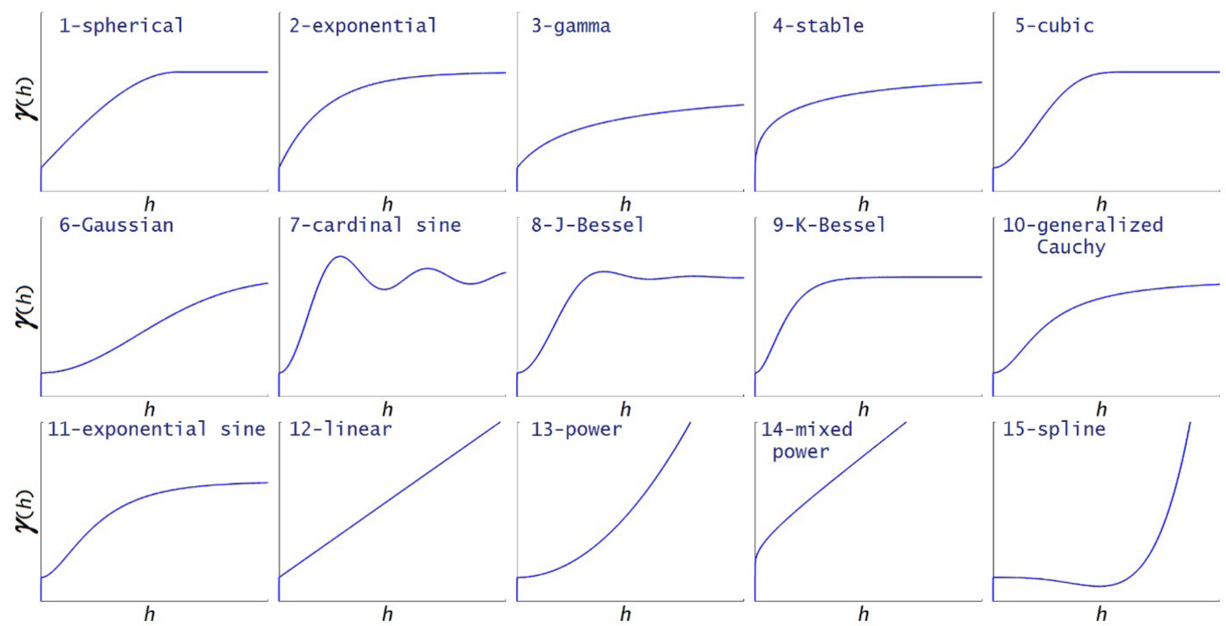

Figure 1. Theoretical fitting models accepted by the TBCOSIM technique.

random fields of simulations. In order to describe the spatial correlation between different spaced points in the field, the LAS method can be used assuming five covariance functions, almost all associated with an exponential decay, and already awarded in the code (RFEM). The most commonly used and recommended function is the Markovian covariance function, which calculates the correlation coefficient (C) between soil properties at different points in the field, as Equation 3.

$$C(h) = exp\left\{ -\sqrt{\left(\frac{2h_x}{a_x}\right)^2 + \left(\frac{2h_y}{a_y}\right)^2} \right\} \tag{3}$$

Where a_x and a_y are the spatial correlation ranges in x (horizontal) and y (vertical) directions, respectively. However, for assumed isotropic fields ($a = a_x = a_y$), it can be simplified to Equation 4.

$$C(h) = exp\left\{ -\frac{2h}{a} \right\} \tag{4}$$

Then, the RFEM analyzes the geotechnical structure via the FEM application for each simulated random field. For example, in order to test the probabilistic stability of a soil slope, the *mrslope2d* pack executes the strength reduction method. In each simulation, the analysis assumes the failure threshold condition to determine whether it is in the success or failure domains. Finally, the probability of failure (P_f) is obtained by the $(number\ of\ failures)/(number\ of\ realizations)$ ratio. In brief, RFEM uses the Monte Carlo simulation (MCS).

4. Sophisticated RFEM – sRFEM

Besides incorporating the TBCOSIM to enable an advanced geostatistical-based enhancement of the RFEM that, to the best of the authors' knowledge, has not been presented in the literature before, other improvements were also needed and integrated. They were needed to enable the evaluation of specific aspects of the probabilistic analysis that were not presented in the original approach. They are:

- Defining the experimental variograms generated by simulations:
  - o Evaluating the experimental variograms enables the investigation regarding the accordance with and the correct reproduction of the pre-defined coregionalization model (based on the sample one);
  - o Variograms are generated and analyzed in the Gaussian space.
- Defining the factor of safety (*FoS*) calculated for each simulation:
  - o The original source-code evaluates only the limit state condition (*FoS*=1), concluding if the simulated structure is or is not inside the failure domain;
  - o Evaluating the *FoS* for each simulation is done through an iterative process until convergence, considering a pre-defined tolerance value. This process was incorporated into RFEM regarding the probabilistic and deterministic analysis. In the deterministic analysis, the *FoS* used to be calculated by assuming some hypotheses values (low precision), not by an iterative process (convergence);
  - o Storing the *FoS* values, calculated for the structure for each simulation, enables the evaluation of the frequency distribution, or the probability density function (PDF), of the *FoS* of the analyzed structure;
  - o Evaluating the PDF of *FoS* enables revalidation of the calculated results because the variable's (*FoS*) variance can be graphically illustrated, just as the mean value and its behavior (distribution type), close to the peak or in the tailings;
  - o Many programs use the PDF of the *FoS* to estimate the reliability index (β) of the structure.
- Analyzing the convergence of the probability of failure (P_f) with simulations:
  - o The P_f's convergence is an important indicator that should be evaluated when performing a probabilistic analysis because it represents the precision of the calculated value;
  - o According to Melchers & Beck (2017), the MCS requires around $10^{(P+2)}$ simulation to obtain a good estimate of the P_f of a system, where p is the expected order of the P_f of the investigated structure (P_f=x×10^{-P}). Hence, when expecting a significantly low P_f, the total amount of required simulations would be clearly substantially high;
  - o Evaluating the P_f convergence with simulations can show a satisfactory stabilization for a lower or a higher amount than that recommended by Melchers & Beck (2017). Because of that, enabling this evaluation is really important.
- Updating parts of the open source-code with functions and update syntaxes that are more reliable and agile than its precursors:
  - o The functions and codes are constantly updated to attribute more agility and reliability to the programming. Therefore, revisions and updates of previous codes may be needed and recommend;
  - o Since the developed Fortran code, for the application of the TBCOSIM, is a recent programming (developed in this study), updating the available RFEM code ensures better compatibility between the algorithm frameworks.

The following steps summarize the process of performing a conditional probabilistic analysis of a geotechnical structure using the embraced sophisticated approach:

(1) treating and analyzing known data together with their locations in the field, which comprises:
  - organizing data in a text file;

- applying the declustering technique for data, which determines weights for each data and borehole (the *declus* algorithm from the Geostatistical Software Library, GSLIB, may be used for this step);
- constructing the histograms considering the declustering weights;
- determining conventional statistical information based on the previous step (mean, standard deviation or coefficient of variance, and type of distribution);
- transforming data from original units into Gaussian space (the *nscore* algorithm from the GSLIB may be used for this step);
- creating a text file with a table to allow the backtransformation of each random variable (needed in later steps);
- calculating the sample variograms (simple and crossed) based on the normalized data (the *gamv* algorithm from the GSLIB may be used for this step);
- fitting the sample variograms by theoretical variograms (using or not nested structures);
- identifying which data will condition the realizations and creating a text file with them.

(2) defining the geometry of the geotechnical structure (a slope in this paper), the mesh dimensions, element size, number of realizations and other parameters for the execution of RSLOPE2D (part of RFEM);
(3) discretizing the structure/field, storing the central position of each element that comprises the mesh;
(4) carrying out a deterministic analysis of the problem;
(5) generating the conditional random fields (one per realization), using the TBCOSIM technique, and storing them

- applying the turning bands technique to generate unconditional random fields;
- using the kriging technique and Equation 5 to condition these fields to the sample data.

$$Z_{cc}\left(\boldsymbol{x}\right)=Z_{ci}\left(\boldsymbol{x}\right)+\left(Z_{kc}\left(\boldsymbol{x}\right)-Z_{ki}\left(\boldsymbol{x}\right)\right) \tag{5}$$

where $\boldsymbol{x}$ finds the points in space, $Z_{cc}\left(\boldsymbol{x}\right)$ determines the value in the conditional random field, $Z_{ci}\left(\boldsymbol{x}\right)$ means the value in the unconditional random field, $Z_{kc}\left(\boldsymbol{x}\right)$ is the value in the kriging field based on the sample data, and $Z_{ki}\left(\boldsymbol{x}\right)$ represents the value in the kriging field assuming unconditional data replacing known data.

- backtransforming the simulated values from the Gaussian space to the original units;
- storing the realizations.

(6) analyzing the safety of the structure for each simulated conditional random field;
(7) concluding the probabilistic analysis identifying the probability of failure (P_f) - Monte Carlo simulation (MCS).

All the above-mentioned text files follow the same standardization formats according to the GSLIB's specifications (Deutsch & Journel, 1997).

5. Case study

In order to investigate and to illustrate the effects regarding the reproduction of the spatial correlation structures of soil properties on probabilistic analyses, this paper investigates a real soil slope previously presented in the literature by Johari & Fooladi (2020). According to the reference, the site is in the city of Shiraz, Iran. It has fifteen boreholes, with depths around 25 ~ 26 m from the ground surface. Figure 2 outlines the positioning of these boreholes in the investigated field. Johari & Fooladi (2020) presented all the sample data used in this paper. Readers are referred to this reference for more details.

The analysis assumed a plane strain model. Since the data and the site present a three-dimensional arrangement, the analysis assumed a simulation section. Figure 2 positions the section in the field, while Figure 3 represents it. It is worth mentioning that, for a real design intention, other sections should also be investigated.

For the conditional simulation, only the highlighted boreholes were assumed as conditioning data on its perpendicular projections on the section plane. The conditional

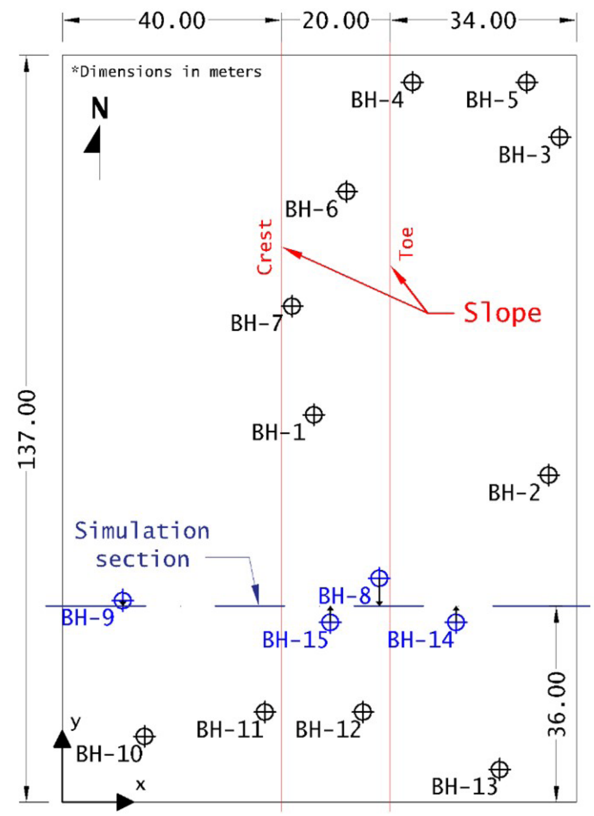

Figure 2. Site representation with borehole locations, slope and assumed simulation section. Modified from Johari & Fooladi (2020).

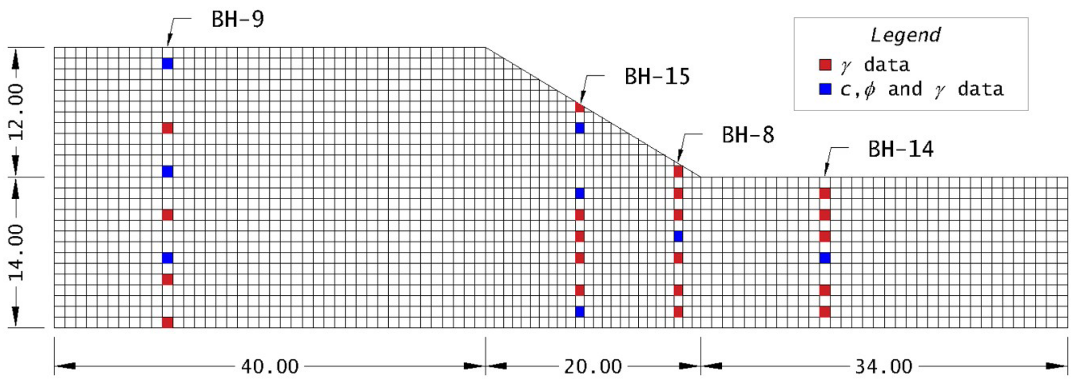

Figure 3. Simulation section with conditioning data locations (distances in meters).

Table 1. Conventional statistical data considering and not considering the declustering.

Soil parameters	Not declustering			Declustering		
	μ	σ	CoV	μ	σ	CoV
c (kPa)	14.89	8.487	0.57	14.02	9.379	0.67
ϕ (º)	25.21	6.050	0.24	25.12	5.782	0.23
γ (kN/m^3)	17.38	0.869	0.05	17.41	0.928	0.05
E and ν were deterministic parameters						
E (kN/m^2)	35,000					
ν	0.30					

μ – mean; σ – standard deviation; CoV – coefficient of variation.

simulation did not consider other boreholes because they were distant from this section, differing from the approach assumed by the cited reference. However, all boreholes were used to determine the statistical information on the site parameters.

5.1 Structural analysis

First, since it is an example of an illustration, the field was deemed as an isotropic soil layer. In other words, although the sophisticated approach can deal with this condition, for the sake of simplicity, the anisotropy of the spatial variability was not considered in this paper.

Then, it can be observed that the location of the boreholes, in Figure 2, demonstrates an irregular spatial investigation. As previously mentioned, clustered samples can introduce bias in statistical information. To deal with this condition, the cell declustering technique was performed. For this step, the analysis makes use of the well-known Geostatistical Software Library (GSLIB) (Deutsch & Journel, 1997), specifically the *declus* algorithm.

In agreement with Johari & Fooladi (2020), cohesion (c), friction angle (ϕ) and unit weight (γ) were assumed as random variables, or regionalized variables, while dilatation angle, elastic modulus (E) and Poisson's ratio (ν) were deterministic. Table 1 shows the statistical information presented by the reference (not declustering) and the recalculated one, considering the declustering technique. This shows that the mean and standard deviation values may vary significantly or not when declustering is considered. Although these variations can be low for this illustration, they may lead to different conclusions for the analysis.

The next step of the analysis comprises the generation of the transformation tables (from the original units to the Gaussian space, and vice versa). GSLIB was used once more for this task, specifically the *nscore* algorithm.

Once all the data were in the Gaussian space, they were analyzed to determine the variograms for the field. This determination used all the data from all the boreholes. GSLIB's *gamv* algorithm can calculate these variograms, therefore it was incorporated into the approach. Figure 4 shows the simple and cross-variograms for the sample data.

For the application, a theoretical fitting function to the sample variograms should be determined. To define this function, first it was assumed to be composed of a nugget effect jointly with two spherical nested structures. The spherical spatial correlation function can be expressed as Equation 6.

$$
\begin{aligned}
&C(h) = C\left\{\frac{2}{3}\left(\frac{h}{a}\right) - \frac{1}{2}\left(\frac{h}{a}\right)^3\right\}, \; if\ h < a \\
&C(h) = C, \; if\ h > a
\end{aligned}
\tag{6}
$$

Where h is the vector lag between points in the field, C is the sill variogram value, and a is its range or correlation length.

Then, the fitting parameters (of the coregionalization model) were defined thought (1st) a manual fitting, followed by (2nd) applying the weighted least squares method and (3rd) another manual fitting, as refinement, all assuming the requirement of obtaining a licit and positive semi-defined theoretical model. Therefore, the fitted linear function of the coregionalization model was described as Equation 7.

$$C(\boldsymbol{h}) = \begin{bmatrix} 0.00 & 0.00 & 0.00 \\ 0.00 & 0.48 & 0.26 \\ 0.00 & 0.26 & 0.55 \end{bmatrix} nugget + \begin{bmatrix} 1.00 & -0.48 & -0.57 \\ -0.48 & 0.30 & 0.30 \\ -0.57 & 0.30 & 0.40 \end{bmatrix} sph_{16.0}(\boldsymbol{h}) + \begin{bmatrix} 0.30 & -0.33 & -0.15 \\ -0.33 & 0.40 & 0.13 \\ -0.15 & 0.13 & 0.17 \end{bmatrix} sph_{34.0}(\boldsymbol{h}) \tag{7}$$

Where the first spherical structure persists for 16.0 meters in the range, while the second continues up to 34.0 meters.

5.2 Stochastic analyses

Three assembled configurations were applied to the case study. First, a probabilistic analysis was performed using the original RFEM approach, accordingly with the common seen applications. Second, a new assessment was performed but applying the sRFEM (incorporating the TBCOSIM technique) with no conditional data (unconditional simulation). Finally, the third configuration was similar to the second, but this time the conditioning data of the boreholes close to the simulation section were considered (conditional simulation).

For the conditional simulation, only the highlighted boreholes were assumed as conditioning data, specifically its perpendicular projections on the section plane, see Figure 2 and Figure 3. The conditional simulation did not consider other boreholes because they were distant from this section, differing from the approach assumed by the cited reference. However, all boreholes were used to determine the statistical information.

All configurations assumed the statistical information presented in Table 1, considering the declustering method. In addition, configurations performed 2,000 realizations each, but this amount would increase as needed.

Replicating the reference, the log-normal distribution type describes all the probability density functions (PDFs) of the random variables. However, the correlation length and the correlation matrix were based on the results of the structural analysis, Figure 4. The correlation length was 34.0 meters (range of the variograms), and the correlation matrix (sills of the variograms) was as Equation 8.

$$C(\boldsymbol{h}) = \begin{bmatrix} 1 & -0.81 & -0.72 \\ -0.81 & 1 & 0.43 \\ -0.72 & 0.43 & 1 \end{bmatrix} \tag{8}$$

Conversely, the other configurations used the transformation tables and the theoretical coregionalization function (Equation 7). For the conditional simulation, third configuration, the ordinary cokriging technique was selected to condition the simulated fields to the known data.

5.3 Spatial covariance reproduction

The first question that arises from the application of a geostatistical simulation is whether it complies with the reproduction of the spatial covariance model. A simple procedure to assess this condition is to analyze the experimental variograms generated by the simulations and compare them with the input model.

Figure 5 presents this evaluation for the second configuration (unconditional simulation using the sRFEM). Note that for each realization, the experimental variograms change, moving away from or closer to the theoretical model (cloud of simulation). However, when analyzing the average experimental variograms, they should agree with the theoretical coregionalization model. Therefore, the unconditional simulation via sRFEM satisfactorily reproduces the spatial covariance model as the average variograms, both simple and crossed, agree with the input model.

Figure 6 shows a comparison of the average variograms for all configurations and the theoretical coregionalization model. The first configuration, using the original RFEM, could not correctly reproduce the model of spatial covariance. Note that the generated variograms resulted in a lower covariance between the equispaced points compared with the theoretical model. Then, this condition can implicate in a random field with a lower variance when compared to the real one, leading to a non-conservative analysis. Despite not adhering to the theoretical structure behavior, the major contribution to the observed discrepancy is related to the nugget effect, which is ignored in this configuration (null nugget effect, with variograms starting from origin).

Otherwise, as previously mentioned, the unconditional simulation via sRFEM successfully reproduced the theoretical model. However, when analyzing the conditional simulation, note that a disturbance occurs for simple variograms. The agreement is hardly supported by conditional simulations. There are some reasons for this “disagreement”. The primary reason is that the conditioning data does not perfectly fit the theoretical model assumed for the simulation, as can be seen in Figure 4. In other words, the known data in the field introduce a certain “distortion” regarding the input or fitted model. Despite this effect, the cross-variograms for the conditional simulation were satisfactorily in accordance with the prior model.

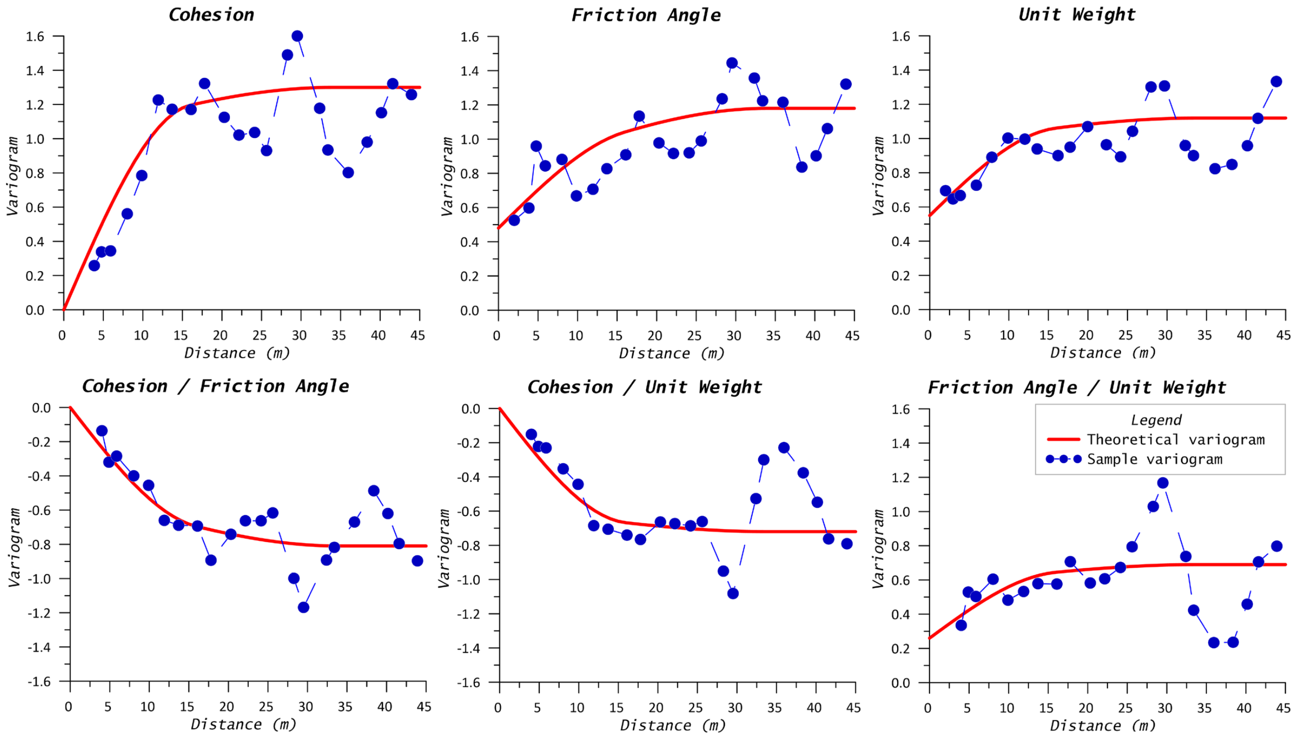

Figure 4. Fitting of sample variograms by theoretical nested structures - simple variograms (top) and cross-variograms (down).

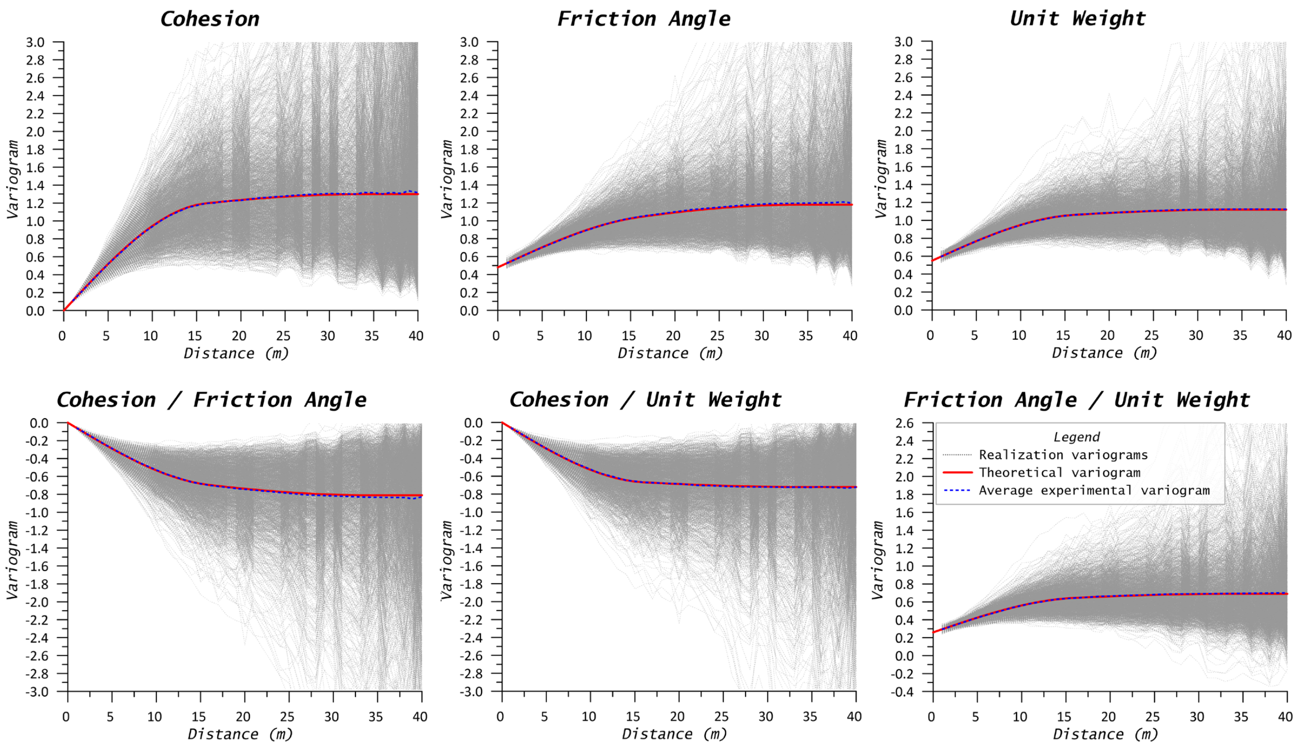

Figure 5. Comparison between the average experimental and the theoretical variograms for the unconditional simulation.

A section simulated example is shown in Figure 7. It illustrates the first realization of the conditional random field for the case study. In addition, the displaced FE mesh was jointly presented.

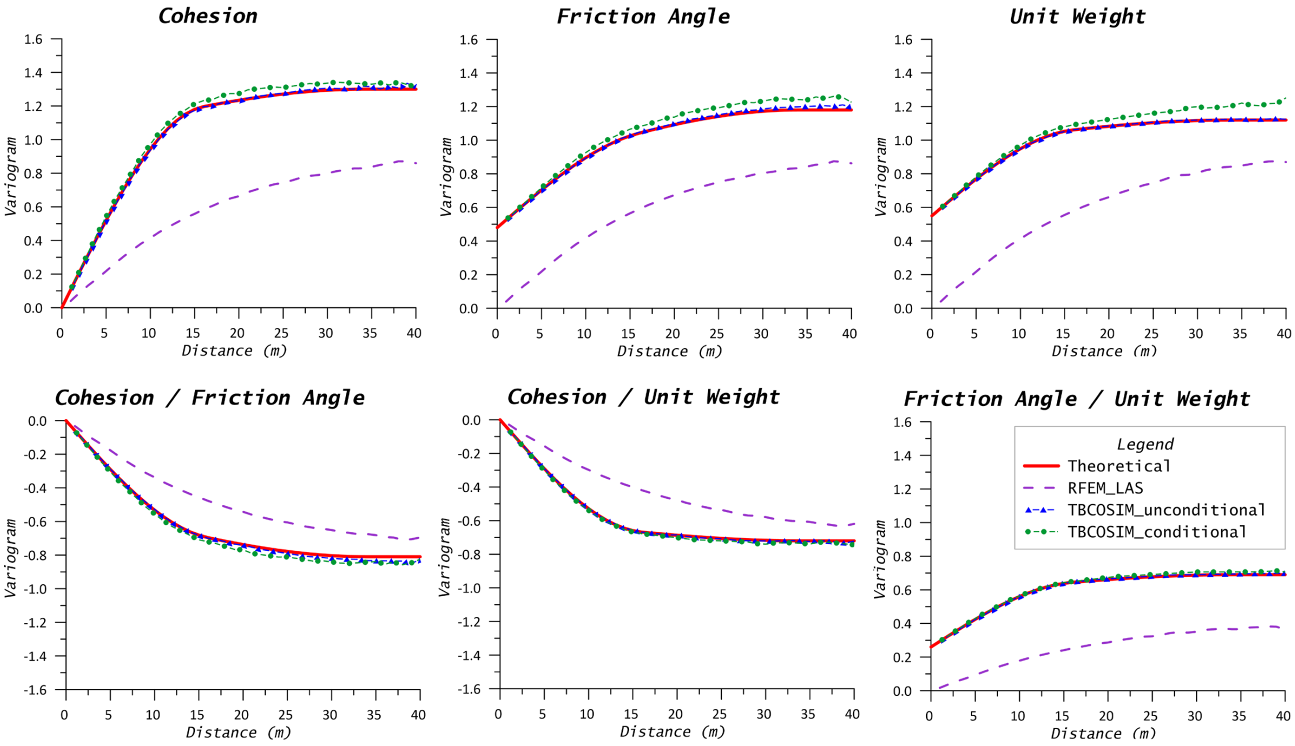

Figure 6. Comparison between the average experimental and theoretical variograms using three methods – Original RFEM, unconditional and conditional using sRFEM.

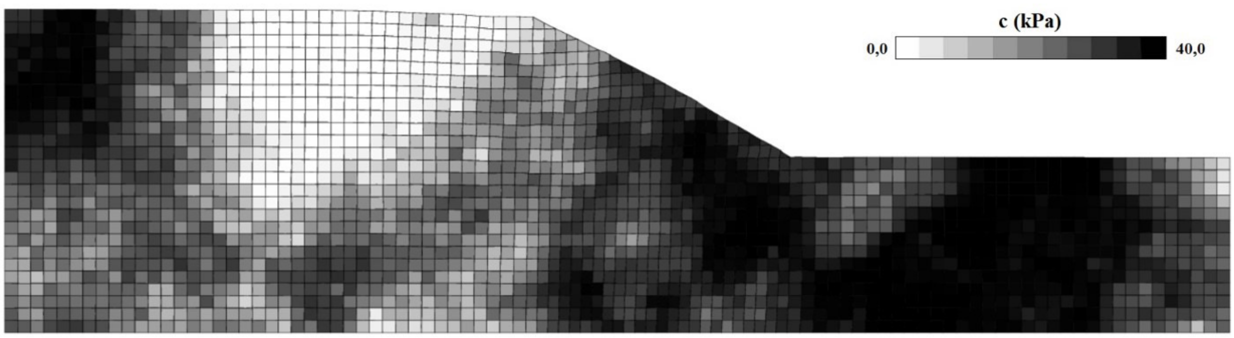

Figure 7. Simulation section of a conditional realization using the sRFEM, representing the displaced FE mesh and the random field in terms of the cohesion parameter.

5.4 Failure assessment

After performing the simulations, the MCS technique was jointly used to define the probability of failure (P_f) of the geotechnical structure. The stability analysis was carried out using the approach incorporated by the RFEM (the strength reduction method), with some adaptations, such as mentioned in the item 4. As the stability analyses were performed, the P_f was monitored, allowing the investigation of its convergence, as shown in Figure 8. A failure event is defined to occur when the factor of safety (FoS) is less than the unit ($FoS < 1$).

Storing the FoS for each realization also grants the investigation of its ensemble (PDF), as shown in Figure 8. Note that both the convergence of the P_f and the ensemble for the FoS were analyzed for the three configurations.

A deterministic stability analysis of this structure, using only the mean values presented in Table 1 (with declustering), resulted in the FoS equal to 1.56. In agreement with this deterministic result, the PDFs for FoS of the three configurations have the peak of their distributions around this value, and very close to the value presented by Johari & Fooladi (2020). However, the distributions showed different behaviors between them, mainly regarding the variance and the behavior of the upper

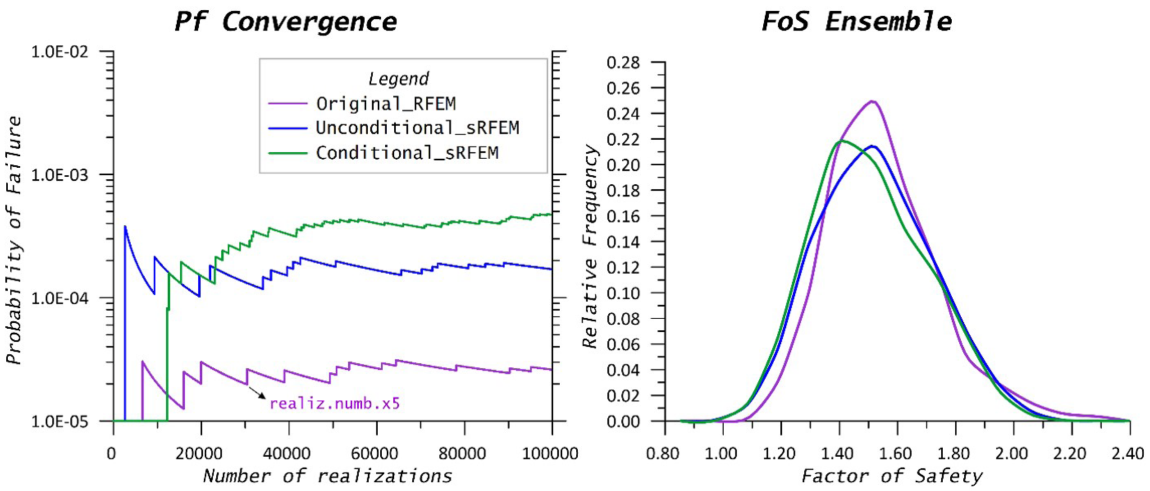

Figure 8. Convergence of the probability of failure and PDF of the factor of safety (FoS) through each method.

and lower tails. The first approach (using the original RFEM) led to a lower variance compared to both unconditional and conditional analysis using the sRFEM. In addition, the P_f for first approach was lower than the second one (around 0.003% and 0.017%, respectively), as expected when examining their distributions. The P_f for the first configuration was obtained from an MCS with 5×10^5 realizations, because of its lower value, while 10^5 simulations were assumed for the second and the third approaches.

In contrast to previous work exploring conditional simulations for this purpose, the conditional simulation (third configuration, using the sRFEM) led to a higher P_f compared with previous configurations (around 0.047%). A PDF analysis reaffirms this result, because the lower tail distribution for the conditional simulation presents a slightly larger area (for $FoS < 1$) than the unconditional one. In addition, the conditional approach also showed a marginally higher variance than the unconditional simulation. Usually, these results are unexpected because conditional simulations are used to reduce the uncertainties about the field variance. However, in this case study, this "unanticipated" condition can occur for a few reasons:

- as previously mentioned, conditional data are used to introduce a disturbance to the coregionalization model, which can be seen in Figure 6 mainly for the simple variograms. Then, note that this effect, in this case, shifted the simple variograms to higher values, so for the same lag vector between any two points, the variance is higher for the conditional than for the unconditional simulation;
- since the geostatistical parameters were defined based on all available data (three-dimensional field), the data in the simulated section may have a slight discrepancy regarding the generalized covariance model, e.g., conditioning data presents higher variance than the entire set of data regarding the investigated field;
- the behavior close to the origin of the spatial covariance models has a substantial influence in the final simulated variances. High nugget effects lead to higher variances in results. If the definition of this behavior is not well-founded, it may produce loss of efficiency of the kriging techniques, and the computed variance may be inaccurate. This effect has even more serious consequences for the conditional simulations, which aim to reproduce the variability in greater detail (Chilès & Delfiner, 2012);
- all the conditioning data assumed for the simulated section (boreholes 8, 9, 14 and 15) have values for the friction angle parameter lower than the mean value for the entire investigated field. Then, it can lead the conditional strength to a reduced average in lower tail realizations;
- perhaps, the number of investigations (boreholes) or points with known data was not enough to reduce the uncertainty level, as explored and presented by Yang et al. (2019).

In the meantime, it is worth mentioning that the PDF, for the conditional simulation, around the peak (close to the mean value of FoS) has a bottleneck format. It suggests that realizations around the mean values granted a lower variance than the peripheral ones.

6. Conclusion

This paper addressed the correct reproduction of the spatial coregionalization model and investigated the effects regarding this reproduction for probabilistic analysis of geotechnical structures. For this, it uses geostatistical concepts and advanced techniques (TBCOSIM) jointly with the most reliable and applied approach presented in the literature to deal with random fields associated with the FEM (RFEM). Based on the results for the illustrative case study, the following conclusions can be drawn:

- Determining the simple and cross-variograms, for the sample data and the fitting theoretical coregionalization function, is an important task in geostatistical treatments, hence also in a probabilistic analysis of geotechnical structures;
- The spatial covariance reproduction when using the sRFEM satisfactorily agrees with the input coregionalization model. The average variograms of the unconditional simulation almost perfectly agree with the theoretical ones, while the conditional one presents a small shifting factor of the variograms upwards (higher values of variance), since the known data rarely agree precisely with the "fitting" model. Otherwise, the original RFEM, as a common approach, failed in this reproduction, leading to lower variances than the sRFEM. Therefore, the RFEM would present a non-conservative design for this structure, resulting in an expressive low P_f, which may be a consequence of the failure in reproducing the spatial variability, for this case;
- Neglecting the investigation distribution in the field may lead to bias statistical information about it. The declustering technique is an important tool to deal with clustered investigations, often seen in practice;
- Disregarding the nugget effect, simulations cannot characterize the local uncertainty (e.g., uncertainties regarding measurements, equipment, tests, correlation formulas, and other sources). It affects the reproduction of the coregionalization model, hence may lead the analysis to biased results;
- Although previous studies often associating the conditional simulation with lower variances and probability of failure, this "expected" condition was not observed for this case study. This is because of some factors presented at the end of Section 5.4;
- Depending on amount and location of the conditioning data, jointly with the geostatistical structures, conditional simulations may not offer a meaningful reduction in the simulation's variance. However, the result may be considered more reliable than before, e.g., in the study case, since the values of the conditioning strength parameters around the section were lower than the mean value for the field (entire set), the peak value of *FoS* for the conditional simulation became lower than the peak value for the unconditional one;
- Incorporating the TBCOSIM into the RFEM produces an improved and efficient approach to deal with probabilistic analysis of geotechnical structures, complying with the spatial correlation structures of soil properties, which comprise them.

Acknowledgements

The authors would like to acknowledge the financial support from Coordenação de Aperfeiçoamento de Pessoal de Nível Superior (CAPES), Brazil.

Declaration of interest

The authors have no conflicts of interest to declare. All co-authors have observed and affirmed the contents of the paper and there is no financial interest to report.

Authors' contributions

Jean Lucas dos Passos Belo: conceptualization, data curation, methodology, validation, writing – original draft. Paulo Ivo Braga de Queiroz: supervision, methodology, validation, writing – review & editing. Jefferson Lins da Silva: supervision, writing – review & editing.

List of symbols

a	Spatial correlation range in the field
a_x	Horizontal correlation range in the field
a_y	Vertical correlation range in the field
BH	Borehole
c	Cohesion
C	Sill of the variogram
$C(h)$	Correlation function
COSGS	Sequential Gaussian Co-simulation
CoV	Coefficient of variation
CRF	Conditional Random Field
E	Young's modulus
FE	Finite element
FEM	Finite Element Method
FoS	Factor of safety
GSLIB	Geostatistical Software Library
h	Spatial lag between two points in the field
h_x	Horizontal lag between two points in the field
h_y	Vertical lag between two points in the field
KLE	Karhunen-Loève Expasion
LAS	Local Average Subdivision
LEM	Limit Equilibrium Method
MA	Moving Average Method
MCS	Monte Carlo simulation
MD	Matrix Decomposition Method
N	North
p	Expected order for the probability of failure
PDF	Probability Density Function
P_f	Probability of failure
RFEM	Random Finite Element Method
RFT	Random Field Theory
RVT	Regionalized Variables Theory
SGS	Sequential Gaussian Simulation

SM	Spectral Method
sph	Spherical function
sRFEM	Sophisticated Random Finite Element Method
SRM	Strength Reduction Method
TBCOSIM	Turning Bands Co-simulation
TBS	Turning Bands Simulation
x	Point in the field
Z(x)	Value of the random variable for a point in the field
Z_{cc}	Value of the random variable in the conditional random field
Z_{ci}	Value of the random variable in the unconditional random field
Z_{kc}	Value of the random variable in the kriging field based on the sample data
Z_{ki}	Value of the random variable in the kriging field based on the simulated unconditional data replacing known data
β	Reliability index
ϕ	Friction angle
γ	Unit weight
γ(h)	Simple variogram function
$\gamma_{12}(h)$	Cross-variogram function
μ	Mean
ν	Poisson's ratio
σ	Standard deviation

References

Belo, J.L.P., & Silva, J.L. (2020). Reliability analysis of a controlled stage-constructed and reinforced embankment on soft ground using 2d and 3d models. *Frontiers in Built Environment*, 5(150), http://dx.doi.org/10.3389/fbuil.2019.00150.

Belo, J.L.P., Silva, J.L., & Queiroz, P.I.B. (2022). Reliability analysis of an embankment built and reinforced on soft ground using LE and FE. *Sustainability*, 14(4), 2224. http://dx.doi.org/10.3390/su14042224.

Carr, J.R., & Myers, D.E. (1985). Cosim: a fortran iv program for coconditional simulation. *Computers & Geosciences*, 11, 675-705. http://dx.doi.org/10.1016/4830098-3004(85)90012-3.

Chilès, J., & Delfiner, P. (2012). *Geostatistics: modeling spatial uncertainty* (2nd ed.). John Wiley & Sons. https://doi.org/10.1002/9781118136188.

Deutsch, C.V., & Journel, A.G. (1997). *GSLIB: geostatistical software library and user's guide.* (2nd ed.). Oxford University Press.

Emery, X. (2008). A turning bands program for conditional co-simulation of cross-correlated gaussian random fields. *Computers & Geosciences*, 34, 1850-1862. http://dx.doi.org/10.1016/j.cageo.2007.10.007.

Emery, X., & Lantuéjoul, C. (2006). Tbsim: a computer program for conditional simulation of three-dimensional gaussian random fields via the turning bands method. *Computers & Geosciences*, 32, 1615-1628. http://dx.doi.org/10.1016/j.cageo.2006.03.001.

Fenton, G.A., & Vanmarcke, E.H. (1990). Simulation of random fields via local average subdivision. *Journal of Engineering Mechanics*, 116, 1733-1749. http://dx.doi.org/10.1061/(ASCE)0733-9399(1990)116:8(1733).

Folle, D., Costa, J., Koppe, J., & Raspa, G. (2006). Metodologies for soil heterogeneities quantification for use on geotechnical engineering. *Solos e Rochas*, 29(3), 297-310.

Griffiths, D.V., & Fenton, G.A. (1993). Seepage beneath water retaining structures founded on spatially random soil. *Geotechnique*, 43, 577-587. http://dx.doi.org/10.1680/geot.1993.43.4.577.

Griffiths, D.V., & Lane, P.A. (1999). Slope stability analysis by finite elements. *Geotechnique*, 49, 387-403. http://dx.doi.org/10.1680/geot.1999.49.3.387.

Griffiths, D.V., Huang, J., & Fenton, G.A. (2009). Influence of spatial variability on slope reliability using 2-d random fields. *Journal of Geotechnical and Geoenvironmental Engineering*, 135(10), 1367-1378.

Isaaks, E. (1990). *The application of Monte Carlo methods to the analysis of spatially correlated data* [Unpublished doctoral dissertation]. Stanford University.

Johari, A., & Fooladi, H. (2020). Comparative study of stochastic slope stability analysis based on conditional and unconditional random field. *Computers and Geotechnics*, 125, 103707. http://dx.doi.org/10.1016/j.compgeo.2020.103707.

Johari, A., & Gholampour, A. (2018). A practical approach for reliability analysis of unsaturated slope by conditional random finite element method. *Computers and Geotechnics*, 102, 79-91. http://dx.doi.org/10.1016/j.compgeo.2018.06.004.

Jurado, C.S., Breul, P., Bacconnet, C., & Benz-Navarrete, M. (2020). Probabilistic 3d modelling of shallow soil spatial variability using dynamic cone penetrometer results and a geostatistical method. *Georisk: Assessment and Management of Risk for Engineered Systems and Geohazards*, 15(2), 139-151. http://dx.doi.org/10.1080/17499518.2020.1728558.

Kim, J.M., & Sitar, N. (2013). Reliability approach to slope stability analysis with spatially correlated soil properties. *Soil and Foundation*, 53, 1-10. http://dx.doi.org/10.1016/j.sandf.2012.12.001.

Li, Y., Hicks, M., & Vardon, P. (2016). Uncertainty reduction and sampling efficiency in slope designs using 3d conditional random fields. *Computers and Geotechnics*, 79, 159-172. http://dx.doi.org/10.1016/j.compgeo.2016.05.027.

Liu, L.-L., Cheng, Y.-M., & Zhang, S.-H. (2017). Conditional random field reliability analysis of a cohesion-frictional slope. *Computers and Geotechnics*, 82, 173-186. http://dx.doi.org/10.1016/j.compgeo.2016.10.014.

Liu, Y., Li, J., Sun, S., & Yu, B. (2019). Advances in Gaussian random field generation: a review. *Computational*

Geosciences, 23, 1011-1047. http://dx.doi.org/10.1007/s10596-019-09867-y.

Matheron, G. (1973). The intrinsic random functions and their applications. *Advances in Applied Probability*, 5, 439-468. http://dx.doi.org/10.2307/1425829.

Melchers, R.E., & Beck, A.T. (2017). *structural reliability analysis and prediction*. (3rd ed.). John Wiley & Sons. https://doi.org/10.1002/9781119266105.

Monteiro, S.T., Ramos, F., & Hatherly, P. (2009). Conditional random fields for rock characterization using drill measurements. In *2009 International Conference on Machine Learning and Applications*, Miami, December 2009 (pp. 366–371). IEEE. https://doi.org/10.1109/ICMLA.2009.80.

Mrabet, Z., & Bouayed, A. (2000). Reducing uncertainty on the results of reliability analysis of earth fills using stochastic estimations. In *Second International Conference on Computer Simulation in Risk Analysis and Hazard Mitigation*, Bologna, Italy (pp. 203-214). WIT Press.

Muñoz, E., Cordão Neto, M.P., & Ochoa, A. (2018). Effects of spatial variability on slope reliability: a hypothetical case study. *Soils and Rocks*, 41(3), 381-390. http://dx.doi.org/10.28927/SR.4113381.

Paravarzar, S., Emery, X., & Madani, N. (2015). Comparing sequential gaussian and turning bands algorithms for cosimulating grades in multi-element deposits. *Comptes Rendus Geoscience*, 347, 84-93. http://dx.doi.org/10.1016/j.crte.2015.05.008.

Ren, W. (2005). *Short note on conditioning turning bands realization*. Centre for Computational Geostatistics, University of Alberta.

Sayão, A.S.F.J., Sandroni, S.S., Fontoura, S.A.B., & Ribeiro, R.C.H. (2012). Considerations on the probability of failure of mine slopes. *Soils and Rocks*, 35(1), 31-37.

Schöbi, R., & Sudret, B. (2015). Application of conditional random fields and sparse polynomial chaos expansions to geotechnical problems. In *Proceedings of the 12th International Conference on Structural Safety and Reliability* (pp. 1356-1363). Amsterdã: IOS Press.

Smith, I.M., Griffiths, D.V., & Margetts, L. (2013). *Programming the finite element method*. (5th ed.). John Wiley & Sons.

Stefanou, G., & Papadrakakis, M. (2007). Assessment of spectral representation and Karhunen-Loève expansion methods for the simulation of Gaussian stochastic fields. *Computer Methods in Applied Mechanics and Engineering*, 196, 2465-2477. http://dx.doi.org/10.1016/j.cma.2007.01.009.

Sudret, B., & Der Kiureghian, A. (2000). *Stochastic finite element methods and reliability: a state-of-the-art report* (Rep. No. UCB/SEMM-2000/08). University of California at Berkley.

Verly, G.W. (1993). Sequential gaussian cosimulation: a simulation method integrating several types of information. In A. Soares (Ed.), *Geostatistics Tróia '92* (Vol. 1, pp. 543–554). Springer. https://doi.org/10.1007/978-94-011-1739-5_42.

Yang, R., Huang, J., Griffiths, D., & Sheng, D. (2017). Probabilistic stability analysis of slopes by conditional random fields. In J. Huang, G. A. Fenton, L. M. Zhang & D. V. Griffiths (Eds.), *Geo-Risk 2017* (pp. 450-459). ASCE. https://doi.org/10.1061/9780784480717.043.

Yang, R., Huang, J., Griffiths, D., Meng, J., & Fenton, G.A. (2019). Optimal geotechnical site investigations for slope design. *Computers and Geotechnics*, 114, 103111. http://dx.doi.org/10.1016/j.compgeo.2019.103111.

Soils and Rocks
An International Journal of Geotechnical and Geoenvironmental Engineering
www.soilsandrocks.com
ISSN 1980-9743
ISSN-e 2675-5475

Typical geotechnical profiles of the main soil deposits found in the Maceio city, Alagoas, from SPT boreholes

Juciela Cristina dos Santos[1#], Roberto Quental Coutinho[2],
Juliane Andréia Figueiredo Marques[3]

Article

Keywords
Barreiras formation
Typical profile
Limestone
Sandstone
Organic clay

Abstract

This work had as objective to carry out the construction of typical soil profiles of the main existing deposits in the city of Maceio from a database of SPT boreholes, built in GIS environment. In total, 1,686 records of drilling were specialized in sediments of the Barreiras Formation, Coastal Deposits, and lagoons-river, presenting the most frequent characteristics, exemplified through representative profiles. The Barreiras Formation, which covers about 75% of the urban area of the city, presented profiles with a predominance of clayey, without water level records. The deposits lagoons-river, located in the vicinity of Mundaú lagoon, were characterized by the significant presence of soft and organic clays, sometimes peat, it can reach large thicknesses and with the water table rising in certain regions. In the coastal plain, where the highest vertical construction indices in the city are concentrated, it presented an area with a predominance of fine to medium sand, with or without silt, and a water table varying between 1,00 m and 5,00 m. The analysis also allowed for the identification and mapping of the occurrence of limestone rock, sandstone rock, soft and organic clay rocks in the coastal plain, presenting a typical profile of their occurrence, helping to understand the geotechnical behavior of these materials in the studied region.

Introduction

It is consolidated in the middle of geoinformation technologies, the conception of systematized and processed data, used as raw material for the generation of information. It is for this purpose that this article aims to contribute to the understanding of the main geotechnical aspects of existing soil deposits in Maceio, Alagoas, through the construction of typical and representative profiles, created using simple recognition boreholes (SPT), systematized through Geographic Information System.

Bastos & Zuquette (2005) mention the development of a database from surveys in several European countries, such as Italy and England, and the survey database developed by Nathanail & Rosenbaum (1998), in addition to countries like France, Scotland among others.

The British Geological Survey (BGS, 2019) also performs the construction of geological maps through a Geology viewer of Great Britain, using a *GISweg*, featuring a simple tool, aimed at the public, which has a database with well sweep, earthquake timeline and 3D Visualization Models.

Chacón et al. (2006) cites the participation of scientists from 17 countries in the production of engineering geology maps through landslide databases using geographic information systems.

In Brazil, the geotechnical databases structured by Luiz & Guitierrez (2020) in Maringá, Bastos et al. (2007) and Miranda & Bressani (2007) in Rio Grande do Sul, Mafra Júnior (2007) and Cardoso & Medeiros (2011) in Santa Catarina, Wosniak & Wendler (2002) in Paraná, Augusto Filho (2005) in Minas Gerais, among others.

One of the most consolidated works for the Northeast, concerns the preparation of soft medium and organic clays database in Recife city, made by Coutinho et al. (1996). The information's contained included parameters of tests performed in the field and laboratory, in addition to SPT probes. The application of SPT data associated with Geographic Information Systems (GIS) for the construction of geotechnical maps it has been widely used for several applications, being widespread in some areas and gaining more and more space in geotechnics.

1. Characteristics of the study area

Maceio has approximately 511 km^2 and an estimated population of 1,025,360 inhabitants (IBGE, 2020), having

#Corresponding author. E-mail address: juciela.santos@ceca.ufal.br
[1]Universidade Federal de Alagoas, Campus de Engenharias e Ciências Agrárias, Rio Largo, AL, Brasil.
[2]Universidade Federal de Pernambuco, Centro de Tecnologia e Geociências, Recife, PE, Brasil.
[3]Universidade Federal de Alagoas, Centro de Tecnologia, Maceió, AL, Brasil.

Submitted on January 6, 2022; Final Acceptance on October 10, 2022; Discussion open until February 28, 2023.
https://doi.org/10.28927/SR.2022.000122

hot and humid climate, classified as type As' according to the Koppen classification. For the purposes of this article, the studied area is limited to the urban area of the Maceió city. Figure 1 presents a location map of the studied area.

In the geological aspect, Maceió has three main deposits: Barreiras Formation sediments, Coastal sediments and Lagoon-river sediments, near the Mundaú Lagoon.

The sediments of the Barreiras Formation cover approximately 75% of the urban area of Maceio and are considered the last deposits in the Alagoas Sedimentary Basin, with an average width of 20 km, forming a package between 60 and 130 m (Santos et al., 2004). It has poorly consolidated sediments characterized by sub-horizontal layers of different granulometry, associated with fluvial processes, being considered the most expressive geological unit on the Brazilian coast. The lithology is composed of clastic sediments of continental origin, which had their deposition associated with Cenozoic events of a climatic and/or tectonic nature, with Plio-Pleistocene (Tertium-Quaternary) age, presenting itself with bright color, ranging from orange, red, purple, yellow to white (Alheiros et al., 1988).

The coastal and lagoons-river deposits of the city of Maceio, have a quaternary origin, resulting from the marine, fluvial and wind action, which created a coastal and lagoon plain with marine and lacustrine terraces, sandy ridges and old drowned estuaries that give rise to the lakes (Mendes, 2017).

These Holocene marine terraces in which the lower part of the city developed, they form a long and extensive coastal plain, with a thickness of 25 m in the districts of Ponta Verde and 49 m in the district of Ponta da Barra, reaching up to 80 m in the district of Trapiche da Barra (Santos, 2004). In the geological chart of Brazil to the millionth (2004), these coverages were mapped as Holocene marine deposits (Q2li), classified as sand with seashells, clay and silt rich in organic matter and well selected fine sand dunes.

The river lagoon sediments are in the vicinity of Mundaú lagoon, which according to (Santos, 2004) they are located from the inland delta of the Mundau river to the end of Santa Rita Island. They are constituted by marine and lacustrine terraces, with occurrence of clays, clay and silt rich in organic matter and sands with fragments of crustaceans.

To better understand of the local geology and the various geological formations that make up the soil and subsoil of the region, a simplified geological profile was built (Figure 2).

2. Materials and methods

The geotechnical characterization of the soil deposits found in the city of Maceio was carried out through the identification and location of drilling records SPT in the study area, provided by the company AGM Geotechnical LTDA, between 2007 and 2017, containing drillhole execution reports, profiles and location sketches.

The survey bulletins were systematized through the creation of a database, based on the model produced and consolidated by the Slopes, Plains and Disasters Geotechnical Group (GEGEP/UFPE), built using the database manager system (DBMS) PostgreSQL and the extension for spacial data PostGIS. The choice for this system was because it is a free tool that already has embedded tools for analysis, processing and identification of spatial data and the facility of data integration with geographic information systems.

The *software* QGIS 3.10.7 was used as a geographic information system, performing geoprocessed data analysis, building maps of the deposits found and the spatial location

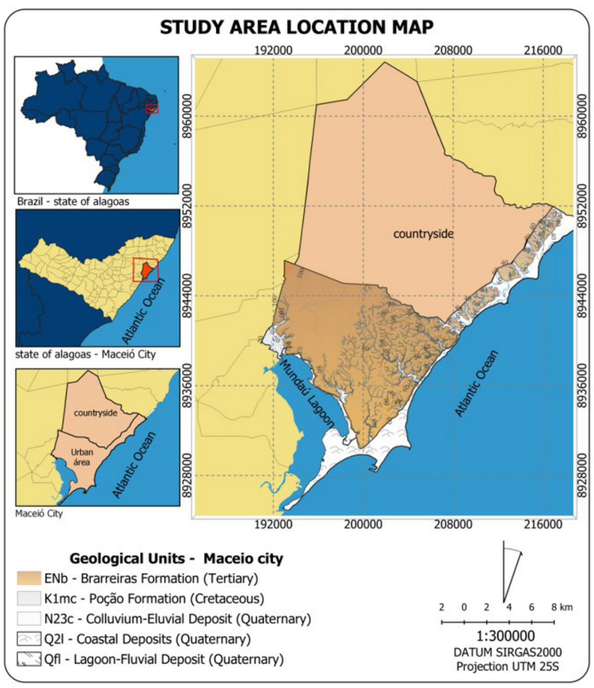

Figure 1. Study area location map.

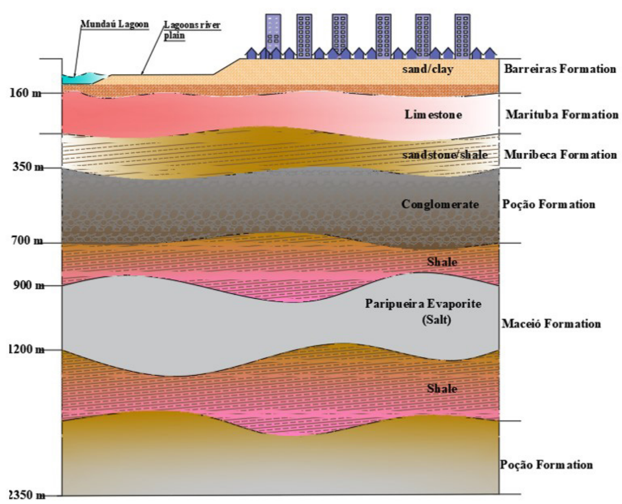

Figure 2. Simplified profile of geology in Maceio.

of drilling records, allowing the identification of the most frequent and representative soil layers of the main existing deposits in Maceio, highlighting the particularities and areas of occurrence.

3. Analysis and results

For the geotechnical characterization of the studied area, 1,686 drilling records SPT were used, distributed as shown in Figure 3.

Most of the drilling records are found under sediments from the Barreiras Formation. The high verticalization also brings several significant records in the coastal deposits, more specifically in the districts of Pajuçara, Ponta Verde and Jatiúca, however, leaving the regions of Pontal da Barra, Trapiche, Prado, Poço and Centro and most of the north coast neighborhoods uncovered. The same occurs in the lagoons-river deposits, where verticalization is less expressive.

The representative soil profiles used as an example for each type of deposit studied are spatially located and represented in Figure 4 as well as the area of occurrence of sandstone, limestone and soft and organic clays.

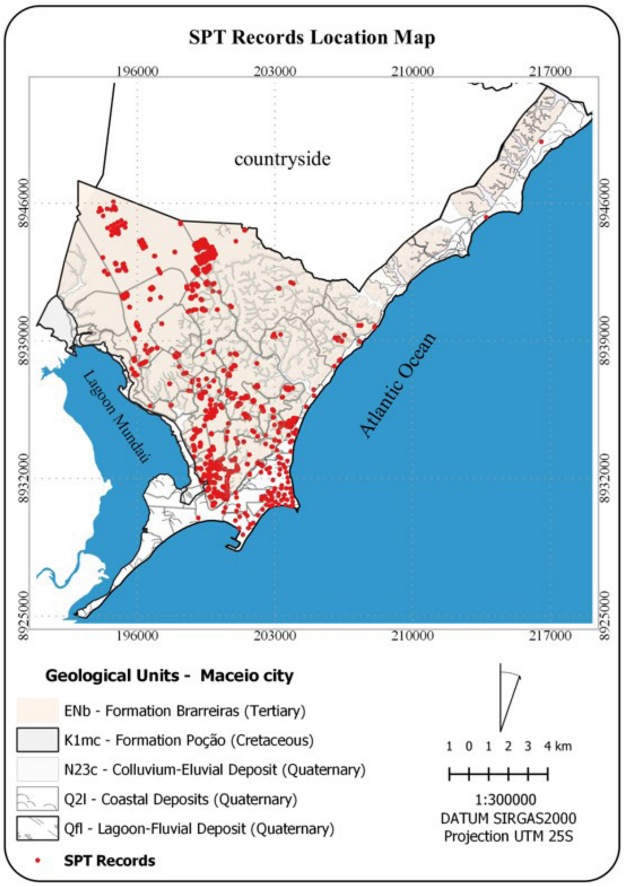

Figure 3. SPT records Location Map

3.1 Geotechnical characterization of Barreiras Formation sediments

To carry out the characterization of the sediments of the Barreiras Formation, approximately 1,500 records of drilling were used, distributed through 13 layers with depths that varied between 1.00 m and 37.00 m. Due to the degree of representativeness, the profiles were analyzed up to the 5th layer of soil. The probes were separated into four representative groups, taking into account the granulometry of the material obtained in the field:

a) Group 01: more sandy soils, composed of sands, silty sands and sandy silts;
b) Group 02: soils identified with finer granulometry, composed of clays, silty clays and clayey silts;
c) Group 03: soils identified as sands composed of clay and silt, such as clayey sands, clayey silty sands, clayey silt sand and sandy clay silts;
d) Group 04: soils identified as composite clays, such as sandy clays, silty sand clays, sandy silt clay and sandy clay silts.

It was found that the subsoil has about 55% of the SPT profiles presenting exclusively clayey layers and 43% presenting layers with intercalations between sand and clay.

The repetitions between sandy e clayey layers occur mostly with clayey predominance (81%), with only 19% having sandy predominance. This sand/clay intercalation pattern with vertical repetition may be associated with depositional cycles, common to sedimentary surface flat alluvial.

The highest incidence of occurrence is in groups with clayey predominance, with silt and sand (G02 e G04), that is, soils with finer granulometry, which together represent between 65% and 85% in all layers, with greater incidence for clays composed of sand and silt (G04). In these layers, the description of the presence of laterization and boulders (pebbles) is also frequent. Although less frequent, sandy layers

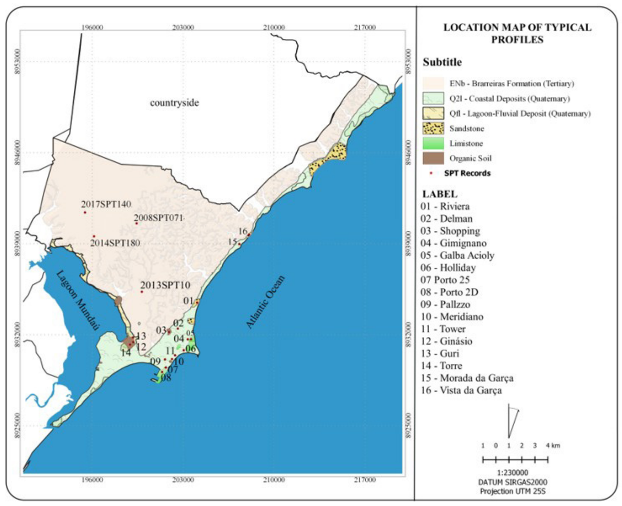

Figure 4. SPT records Location Map used as an example.

(G01 and G03) intersperse the clayey layers in depth, with a greater occurrence of sands composed of silt and clay, which represent between 15% and 35%. In these layers, laterization, boulders (pebbles) and clay nodules are also frequent.

Table 1 presents the most frequent characteristics found in the group of surveys studied, considering the particle size classification of materials.

In the analyzed SPT records, no groundwater levels were found, despite the existence of an aquifer in the Barreiras Formation in Maceió city, as its depth is greater than that reached by the studied drillings. According to Nobre et al. (2007), the underground waters of the Maceio city vary from 30 to 500 meters in thickness, passing through several geological formations, not being reached by the analyzed drillings.

Examples of representative profiles of SPT drillings inserted in the studied area are presented in Figure 5, which show two profiles with exclusively clayey layers, and Figure 6,

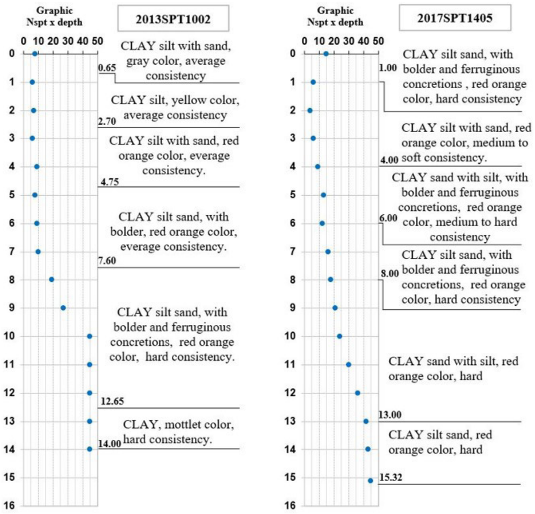

Figure 5. Example of profile with exclusively clayey layers.

Table 1. Most frequent characteristics of the soil layers of the Barreiras Formation.

Layers	Group	Occurrence	Material Classification
1st	G04	51% Clay + Sand + Silt	Gray, yellow, orange-red and variegated colours, medium consistency, occurring pebbles (pebbles).
	G02	30% Clay and Clay +Silt	Colours yellow, sometimes gray, orange-red and variegated, soft to hard with the occurrence of pebbles.
	G01	11% Sand and Sand +Silt	Gray, yellow, cream and orange-red colours, fluffy to medium compact, with gravel, pebble, and clay nodules.
	G03	8% Sand +Clay + Silt	Gray, yellow, and cream colours, fluffy to little compact, with gravel and clay nodules.
2nd	G02	59% Clay and Clay +Silt	Colours yellow, gray and orange-red, soft to hard, with little occurrence of gravel.
	G04	29% Sand +Clay + Silt	Orange-red and yellow colours, medium compact to hard, with the occurrence of gravel and rusty concretions.
	G03	10% Clay + Sand + Silt	Yellow and orange-red colours occurring gray, soft to hard, with gravel and ferruginous concretions.
	G01	3% Sand and Sand +Silt	Yellow, red-orange, cream, grey and mottled, medium compact to compact, with clay and gravel nodules.
3rd	G04	58% Clay + sand + Silt	Colours orange-red, yellow, gray and mottled, medium compact, with gravel (pebble) and ferruginous concretions.
	G02	26% Clay and Clay +Silt	Red-orange, yellow and variegated colours, medium to hard consistency, with gravel and ferruginous concretions.
	G03	13% Sand + Clay + Silt	Orange-red, yellow and gray colours, medium compact to compact, with gravel and ferruginous concretions
	G01	2% Sand and Sand +Silt	Yellow, grey, orange-red and cream, fluffy to very compact, with gravel and clay nodules occurring
4th	G04	42% Clay + Sand + Silt	Red-orange and variegated colours, occurring yellow and gray, hard to hard, occurring pebbles (pebbles) and ferruginous concretions.
	G02	32% Clay and Clay +Silt	Colours variegated, orange-red, yellow, and grey, soft to hard, with gravel and ferruginous concretions.
	G03	22% Sand +Clay + silt	Red-orange and yellow colours, medium compact to hard, with possible gravel (pebbles) and rusty concretions.
	G01	4% Sand and Sand +Silt	Yellow, gray and orange-red colours, medium compact to hard, clay nodules and little gravel may occur
5th	G04	43% Clay and Clay +Silt	Colours reddish orange variegated and yellow, hard, with gravel (pebbles) and ferruginous concretions.
	G02	41% Clay + Sand + Silt	Colours red orange, mottled and yellow, hard to hard, occurring pebbles (pebbles).
	G01	12% Sand +Clay + Silt	Red-orange and yellow colours, compact to very compact, with gravel.
	G03	4% Sand and Sand +Silt	Colours yellow and orange red, compact to very compact, with gravel.

which show two profiles with intercalation layers between sand and clay.

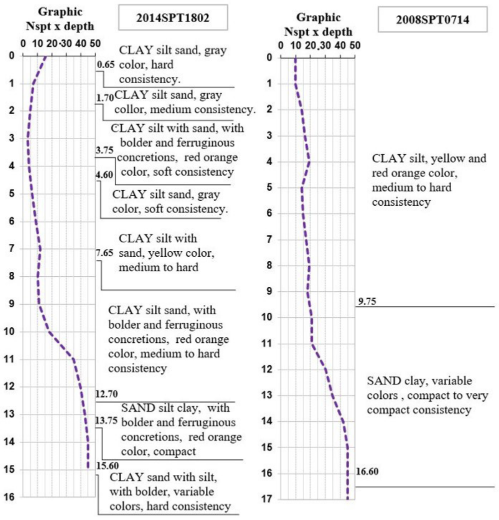

Figure 6. Example of profile with intercalation clay and sand layers.

3.2 Geotechnical characterization of coastal deposit

The drilling records located in the coastal deposits are distributed in the neighborhoods of Poço, Jaraguá, Ponta da Terra, Pajuçara, Jatiúca, Mangabeiras, Ponta Verde, Cruz das Almas, Jacarecica, Guaxuma, Garça Torta and Ipioca.

The surveys showed that the area has a water table varying at a depth between 1.00 m and 5.00 m. The most frequent soil layers are fine sand with silt and fine to medium sand, together representing a percentage of occurrence greater than 58%. The sandy silt starts from the second layer, with percentages that vary between 12% and 23%. Clays mixed with silt and sand occur less frequently, but are common in all layers, representing between 8% and 19% of the soils. In the studied area, calcareous rocks were found as an occurrence from the second layer onwards, at depths ranging from 1.00 m to 15.00 m. The most frequent soil layers and their characteristics are presented in table 2.

Representative profiles of the beach region are presented for the neighborhoods Pajuçara (Figure 7), Ponta Verde (Figure 8), and Jatiúca (Figure 9).

Table 2. Frequent features of the layers found in coastal deposits.

Layers	Class	Occurrence	medium width (m)	Material Classification		
				color	consistency	note
1st	Sandy Silt	-	2.3	Yellow, ligth gray, dark gray, brown and red orange	Fluffy, medium compact	construction waste (26%), crustacean fragments (7%), clay nodules (2%), boulder (pebbles) (6%)
	Fine Sand with Silt	49%				
	Fine to Medium Sand	30%				
	Limestone Sand	-				
	Limestone	-				
	Clay and Clay+Silt+Sand	16%				
2nd	Sandy Silt	12%	3.4	Yellow, light gray, dark gray, cream and brown.	Fluffy, medium compact	Resíduos da construção (2%), fragmento de crustáceo (7%), pedregulho (seixo) (6%)
	Fine Sand with Silt	57%				
	Fine to Medium Sand	20%				
	Limestone Sand	3%				
	Limestone	2%				
	Clay and Clay+Silt+Sand	8%				
3rd	Sandy Silt	23%	3.4	Yellow, ligth gray, dark gray, cream.	Fluffy, medium compact	Resíduos da construção (2%), fragmento de crustáceo (33%), pedregulho (seixo) (10%).
	Fine Sand with Silt	38%				
	Fine to Medium Sand	26%				
	Limestone Sand	3%				
	Limestone	2%				
	Clay and Clay+Silt+Sand	9%				
4th	Sandy Silt	20%	3.4	Yellow, ligth gray, dark gray, cream.	Fluffy, medium compact	Fragmento de crustáceo (27%), pedregulho (seixo) (13%), nódulo de argila (3%)
	Fine Sand with Silt	54%				
	Fine to Medium Sand	14%				
	Limestone Sand	4%				
	Limestone	7%				
	Clay and Clay+Silt+Sand	8%				
5th	Sandy Silt	13%	3.62	Yellow, ligth gray, dark gray, cream.	medium to very compact	Fragmento de crustáceo (13%), pedregulho (seixo) (15%), nódulo de argila (6%)
	Fine Sand with Silt	30%				
	Fine to Medium Sand	30%				
	Limestone Sand	9%				
	Limestone	2%				
	Clay and Clay+Silt+Sand	19%				

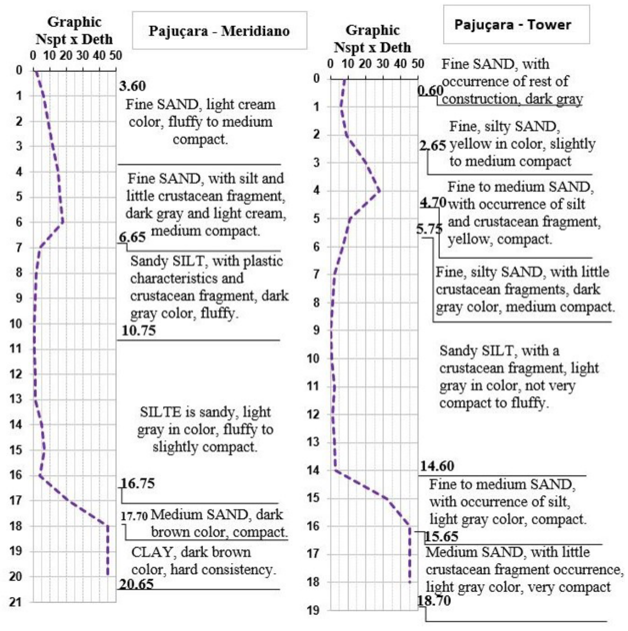

Figure 7. Example of profile located in the Pajuçara neighborhood.

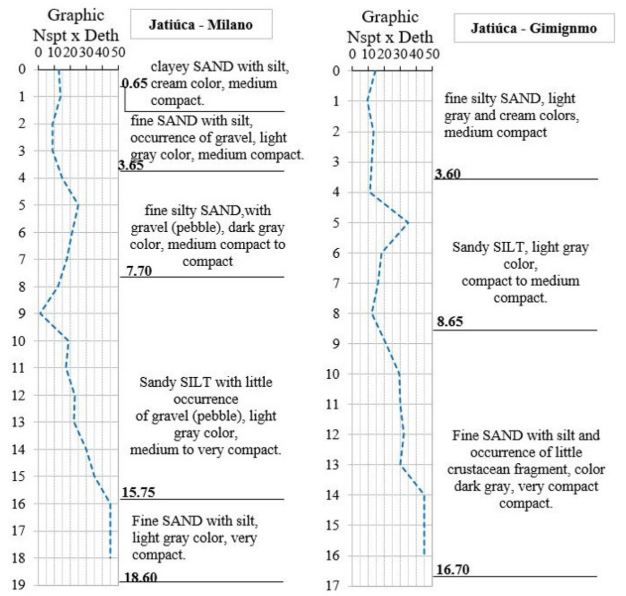

Figure 9. Example of profile located in the Jatiuca neighborhood.

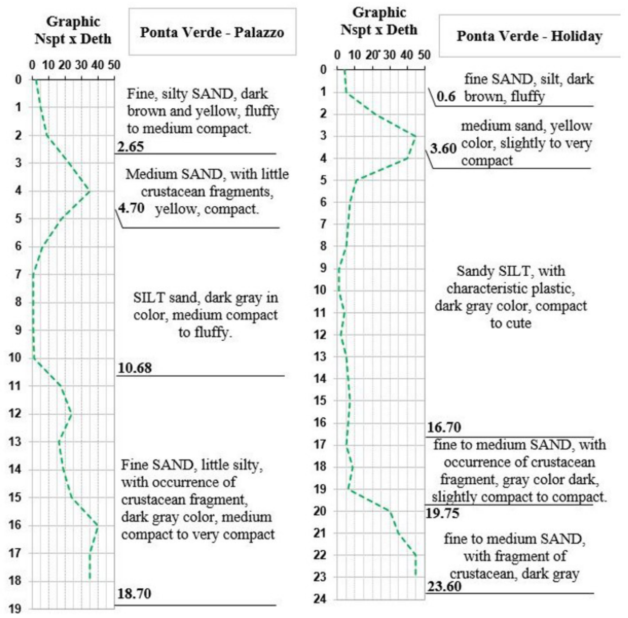

Figure 8. Example of profile located in the Ponta Verde neighborhood.

3.3 Geotechnical characterization lagoon river deposit

In Maceio, there are few records of drilling in the lagoons-river region, due to the low construction demand in the region, however, the analyzed SPT allowed the identification of 05 representative soil layers, described as per table 3.

The first layer is usually made up of fine sand, with or without the occurrence of silt, of consistency ranging from fluffy to medium compact, occurring soft clay/organic, with peat and crustacean fragments, starting near the surface (≈ 0.60 m), being able to reach large thicknesses (± 15.00 m), representing, in most cases, the second layer. The next layers represent silty sand, sandy clay and fine sand, medium compactness, and variable thickness. Marques e Marques (2005) found similar results. Figure 10 present example of profile located in lagoon river Deposit.

3.4 Limestone, sandstone, soft clay and organic deposits

A very special feature in the city of Maceio is the occurrence of limestone, sandstone and soft/organic clay deposits in the coastal region, and soft/organic clay in the lagoon region. In this article, based on studied SPT boreholes, areas of incidence of these deposits were mapped, shown in Figure 11.

3.4.1 Occurrence of limestone rocks

Limestone rocks are visible on the coast of the city of Maceio, especially at low tide, on the beaches of Pajuçara and Ponta Verde. Studies carried out by Mendes (2017) identified gray, yellow, and gray limestone deposits with bluish tones, constituting the occurrence of sedimentary limestone associated with Phanerozoic sediments from the Sergipe-Alagoas Basin.

The presence of limestone was evidenced in some of the surveys studied, occurring discontinuously in the horizontal direction, which in many situations brings the need for more detailed geotechnical studies in the area of incidence, limestone being identified in only part of the land of the same work, which can directly influence the applied foundation solutions.

Table 3. Frequent features of the layers found in Lagoon River Deposit.

Layer	W.L. (m)	Material Classification		Nspt medium
		Class	consistency	
1st	2.00	Fine Sand with or without silt	Fluffy to medium compact	1 – 10
2nd		Soft clay or Organic Soil (peat)	Very soft	0 – 1
3rd		Silt Sand, with or without clay	Medium compact to little compact	4 – 15
4th		Sand clay or Silt clay	Medium to hard	6 – 12
5th		Fine Sand with or without clay	Medium compact	15 – 18

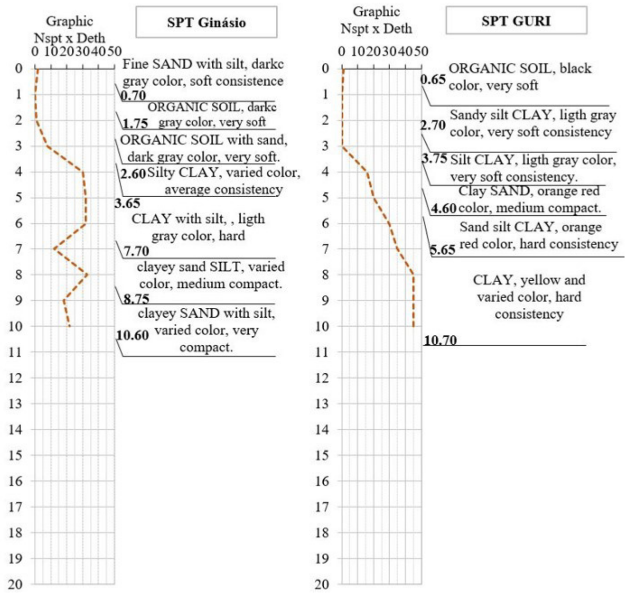

Figure 10. Example of profile located in Lagoon River Deposit.

Limestone was found more frequently in contact with soil classified as fine sand, with or without silt, and limestone, the latter with characteristics of residual soil. The analyzed boreholes tend not to exceed the limestone layer when found, as it is impenetrable to percussion.

Figure 12 shows three typical profiles of the coastal region with occurrence of limestone at a depth of approximately 5.00 m (a), an example where the drilling exceeded the limestone layer (b) and an example of occurrence of limestone rock at a depth of 10.00 m (c).

3.4.2 Occurrence of sandstone rocks

The occurrence of sandstone rocks was identified in the narrowest range of coastal sediments, more specifically in areas of the Jatiúca, Cruz das Almas, Garça Torta and Ipioca neighborhoods.

The layer where sandstone rock occurs has low strength, being penetrated through the SPT test. This characteristic may be related to the degree of weathering of the rock, requiring more detailed geotechnical studies to understand the physical properties of these materials. Figure 13 shows examples of profiles with appearance of sandstone rock.

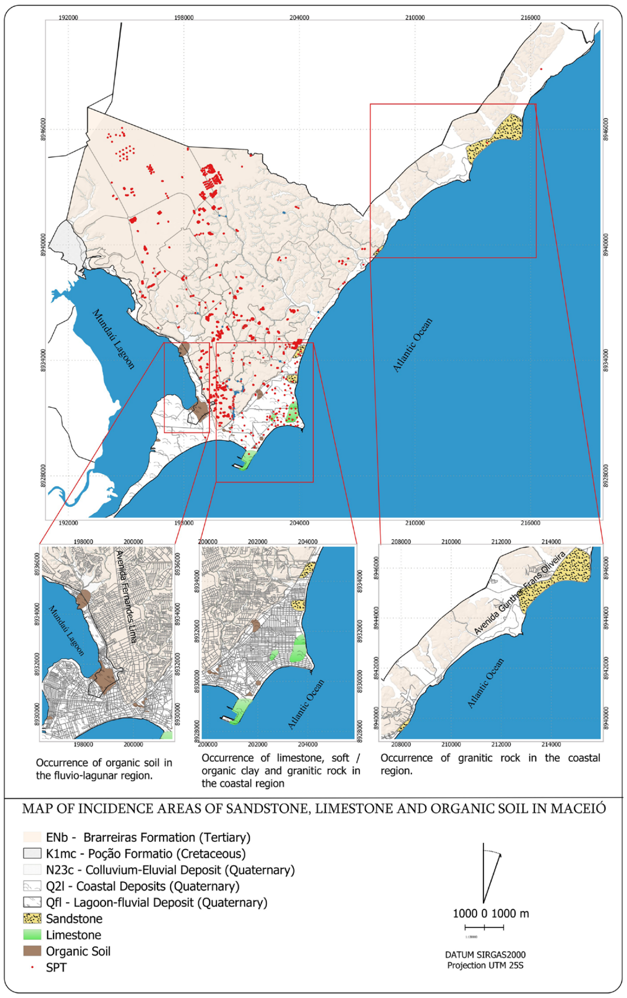

Figure 11. Map localization areas of incidence the rocks and soil.

3.4.3 Occurrence of organic soil

On the coastal plain, deposits of the organic soil were found between Dona Constança de Góes Monteiro and Comendador Gustavo Paiva avenues, located near the Maceio shopping mall, in the Mangabeiras district, near the harbor of Maceio, in the Jaraguá district, and around the Salgadinho stream in the Poço district. The layers of soft/organic clays are less thick in this region, varying between 1.00 m and 3.00 m. Figure 14 presents two examples of

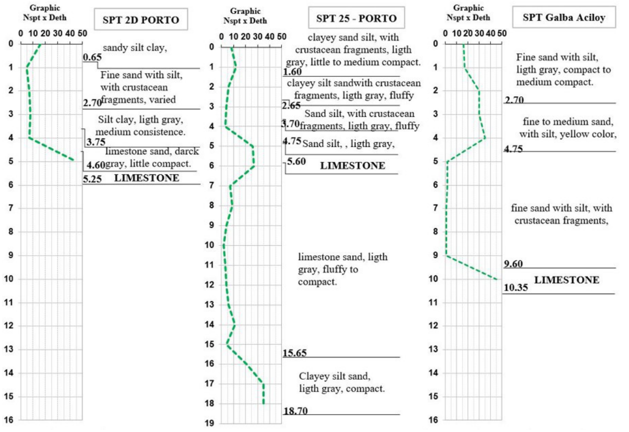

Figure 12. Example of profile with occurrence of limestone layer.

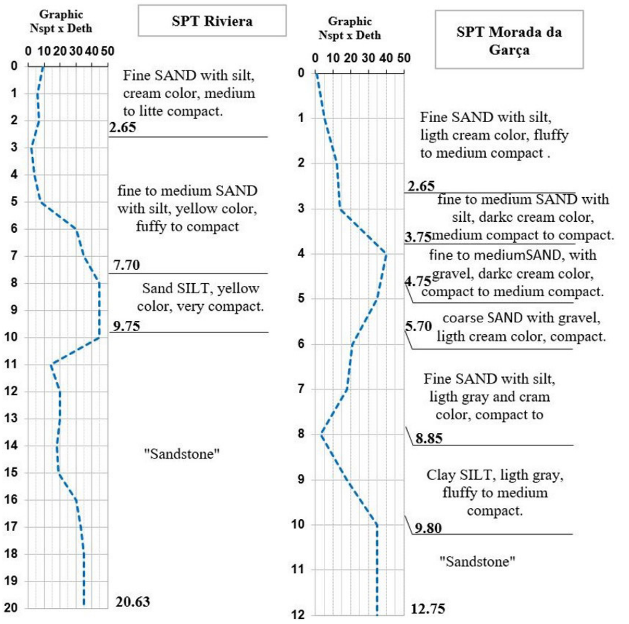

Figure 13. Example of profile with occurrence of Sandstone layer.

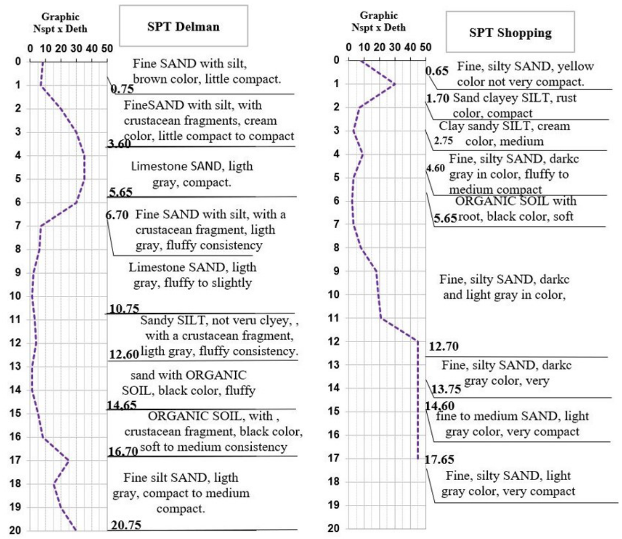

Figure 14. Example of profile with occurrence of soft clays in coastal deposits.

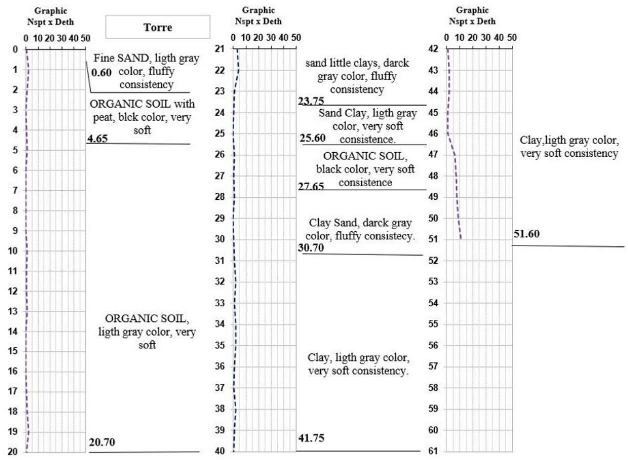

Figure 15. Example of profile with occurrence with occurrence of thick layer of soft clay.

profiles that record the occurrence of soft clays in an area covered by coastal deposits.

In the lagoons-river plain, on the banks of the Mundaú lagoon, the soft/organic clays were identified between the Levada, Bom Parto and Bebedouro neighborhoods, as well as portions in the Trapiche da Barra neighborhood, highlighting the regions along the banks of Frog e village Brejal stream, Ceasa and the production market, where the thickest layers are found, with the occurrence of peat starting at depths less than 1.00 m from the surface and reaching a thickness of 15.0 m. This region is characterized by the occurrence of anthropogenic grounding actions for the construction of dwellings, where previously there were floodplains and mangroves and outcrops of the water table. Figure 15 shows an example of a profile located in the Levada neighborhood where the soft/organic clay layer presents a significant thickness.

In this example, the layers of organic soil are already noticeable at a depth of 0.60 m, very close to the surface to a depth of 20.00 m. Another very thick layer occurs from 30.00 m onwards, presenting a clay with a very soft consistency, until reaching a depth of 51.60 m.

4. Conclusion

The design of typical and representative profiles of the main soil deposits found in Maceio constitutes an important tool to aid in the execution of engineering projects in the region.

Analyzing the drilling records arranged under the sediments of the Barreiras Formation, it was possible to identify the existence of layers with a clayey predominance (between 69% and 84%) with frequent occurrence of laterization in depth, with no water levels being registered in the analyzed profiles. The coastal deposits, in turn, have layers with a predominance of fine sand, with and without silt, and a water table ranging from 1.00-5.00 m.

The SPT records enabled the spatial location of areas where there are deposits of limestone, sandstone and soft clays, inserted in the coastal plain, in contact with layers of fine sand and/or medium sand, with or without silt, or calcic sand.

In the studied region, it was observed that Limestone has a characteristic of discontinuity in the horizontal direction, which can be evidenced only in parts of the land, with occurrences being registered at a depth of up to 15.00 m. The analyzed boreholes tend not to go beyond the Limestone layer, as it is impenetrable to percussion, however, when exceeded, a limestone layer was found, with a significant loss of resistance. It is important to emphasize the need for more detailed geotechnical investigations in areas with this type of occurrence since the existence of voids in carbonate rocks is common and may be associated with its geological process or dissolution processes.

Sandstone rocks were also identified, more commonly in parts of the city's north coast neighborhoods, with friable rock characteristics, penetration being possible through the SPT test, which may be related to the degree of weathering of the rock, requiring more detailed geotechnical studies for the knowledge of the physical properties of these materials.

Soft and organic clays also occur in the coastal plain, having a small thickness (between 1-3m), and may occur at variable depths.

In the lagoons-river deposit, the water table was found at an average depth of 2.00 m, and it may outcrop on the surface. These deposits are characterized by the occurrence of soft and organic clays from the second layer onwards, which can reach a thickness of up to 15 m. The other layers are made up of fine sands, silty sands and sandy clays of varying thickness.

Acknowledgements

To the Geotechnical Engineering Group for Slopes, Plains and Disasters (GEGEP) of the Federal University of Alagoas and to AGM geotechnical for providing the survey information.

Declaration of interest

The authors have no conflicts of interest to declare. All co-authors have observed and affirmed the contents of the paper and there is no financial interest to report.

Authors' contributions

Juciela Cristina dos Santos: conceptualization, data curation, methodology, visualization, writing – original draft. Roberto Quental Coutinho: conceptualization, methodology, supervision, validation. Juliane Andréia Figueiredo Marques: validation, review & editing.

List of symbols

BGS	British Geological Survey
DBMS	British Geological Survey
GIS	Geographic Information System
Nspt	SPT number
SPT	Standard Penetration Test
W.L.	Water Level

References

Alheiros, M., Lima Filho, M.F., Monteiro, F.A.J., & Oliveira Filho, J. (1988). Sistemas Deposicionais na Formação Barreiras no Nordeste Oriental. In *34th Congresso Brasileiro de Geologia* (pp. 753-760). Belém – PA, Sociedade Brasileira de Geologia.

Augusto Filho, O. (2005). *Implementação de banco de dados geotécnico como ferramenta adicional de gestão urbana da URBEL* (Technical Report, pp. 1-14). Universidade de São Paulo (USP).

Bastos, C. A., Miranda, T. C., Shuler, A. R., Schmitt, L. A., & Vesconcelos, S. M. (2007). Mapeamento Geotécnico da Planície Costeira Sul do Rio Grande do Sul. In *6° Simpósio Brasileiro de Cartografia Geotécnica e Geoambiental* (pp. 1-6), Uberlândia, MG.

Bastos, G., & Zuquette, L.V. (2005). Armazenamento, consulta e visualização das informações produzidas no mapeamento geotécnico. In *5° Simpósio Brasileiro de Aplicações de Informática em Geotecnia: Vol. 1* (no. 1, pp. 67-72). Belo Horizonte: EE/UFMG.

British Geological Survey – BSG. (2019). *Great Britain geology viewer*. Retrieved in September 14, 2021, from https://www.bgs.ac.uk/discoveringGeology/geologyOfBritain/viewer.html

Cardoso, S., & Medeiros, S.B. (2011). *Aplicação do modelo SHALSTAB na previsão de deslizamentos de encostas no litoral de Santa Catarina* [Monography, University of Sul of Santa Catarina – UNISUL]. University of Sul of Santa Catarina.

Chacón, J., Irigaray, C., Fernández, T., & El Hamdouni, R. (2006). Engineering geology maps: landslides and geographical information systems. *Bulletin of Engineering Geology and the Environment*, 65, 341-411. http://dx.doi.org/10.1007/s10064-006-0064-z.

Coutinho, R.Q., Monteiro, C.F.B., & Oliveira, A.T.J. (1996). Banco de dados das argilas orgânicas moles/médias do Recife - Versão 3.0. In *Simpósio Brasileiro de Informática em Geotecnia – INFOGEO* (pp. 105-116). São Paulo: Associação Brasileira de Mecânica dos Solos (ABMS).

Instituto Brasileiro de Geografia e Estatística – IBGE. (2020). *IBGE Cidades*. IBGE.

Luiz, A.M.F., & Guitierrez, N.H.M. (2020). Geostatistical data analysis of the Standard Penetration Test (SPT) conducted in Maringá-Brazil and correlations with geomorphology. *Soils and Rocks*, 43(4), 619-629.

Mafra Júnior, C.S. (2007). *Elaboração do mapa preliminar das Unidades Geotécnicas do Município de Brusque Associado a um Banco de Dados Geotécnico em ambiente SIG* [Unpublished Masters' dissertation]. University of Santa Catarina.

Marques, A.G., & Marques, J.A.F. (2005). Práticas de Fundações no Estado de Alagoas. In A.D. Gusmão, J. Gusmão Filho, J.T.R. Oliveira & G.B. Maia, (Eds.), *Geotecnia no Nordeste*. Ed Universitária da UFPE.

Mendes, V.A. (2017) *Geologia e recursos minerais do estado de Alagoas: escala 1:250.000*. CPRM -Serviço Geológico do Brasil.

Miranda, T. C., Bressani, L.A. (2007). Mapeamento das Unidades Geotécnicas e Montagem de Banco de Dados na Área Abrangida pela Obra de Duplicação da BR101 Sul, RS, Brasil. In *Congresso Luso Brasileiro de Geotecnia* (pp. 1-15), Coimbra, Portugal. ABGE.

Nathanail, C.P., & Rosenbaum, M.S. (1998). Spatial management of geotechical data for site selectio. *Engineering Geology*, 50(3-4), 347-356.

Nobre, R.C.M., Rotunno Filho, O.C., Mansur, W.J., Nobre, M.M.M., & Cosenza, C. (2007). Groundwater vulnerability and risk mapping using GIS, modeling and a fuzzy logic tool. *Journal of Contaminant Hydrology*, 94(3-4), 277-292. http://dx.doi.org/10.1016/j.jconhyd.2007.07.008.

Santos, R.C.A.L. (2004). *Evolução da Linha de Costa a Médio e Curto Prazo Associada ao Grau de Desenvolvimento Urbano e aos Aspectos Geoambientais na Planície Costeira de Maceió-Alagoas* [Doctoral thesis, University Federal of Pernambuco]. University Federal of Pernambuco. https://repositorio.ufpe.br/handle/123456789/6577

Santos, R.J.Q., Lima, R.C.A., & Ferreira Neto, J.V. (2004). A geomorfologia do tabuleiro como consequência do neotectonismo. In L.M. Araujo (Org.), *Geografia: espaço, tempo e planejamento* (pp. 255-268). EDUFAL.

Wosniak, M.T., & Wendler, M. (2002). *Banco de Dados Geotécnico da Cidade de Curitiba* [Monography]. University of Tuiuti (in Portuguese).

Soils and Rocks

An International Journal of Geotechnical and Geoenvironmental Engineering

www.soilsandrocks.com

ISSN 1980-9743
ISSN-e 2675-5475

Numerical evaluation of the influence of compaction and soil strength parameters on GRSW

Leone César Meireles[1], Mario Vicente Riccio Filho[2], Heraldo Nunes Pitanga[2], Roberto Lopes Ferraz[3], Taciano Oliveira da Silva[3], Sérgio Leandro Scher Dias Neto[3#]

Article

Keywords
Numerical modelling
Compaction
Deformations
Reinforced soils

Abstract

This paper presents a numerical evaluation, using PLAXIS 2D finite element software, of the effects of varying the distance of the heavy compaction from the face in a geosynthetic reinforced soil wall (GRSW). The main effects studied were the tensions in the reinforcements and the horizontal deformations of the face, including the influence of the type of shear strength envelope (total stresses or effective stresses) of the soil. In this study, a young gneiss residual soil (silty sand) was studied to obtain the grain size distribution, index properties and parameters of strength and deformability. This soil was considered for backfill in hypothetical sections of GRSW. The numerical results contributed to a better understanding of the GRSW behaviour, with evaluations closer to real field conditions. In the analyses carried out, when increasing the heavy compaction distance from the face, there are tendencies pointing to the reduction of the tensions in the reinforcements, displacement toward the interior of the soil mass of the points at which the maximum reinforcement tension occurs and reduction of the horizontal deformations of the face.

Introduction

In geosynthetic reinforced soil walls (GRSW), several factors influence the distribution of tensions and deformations in the reinforced soil mass, such as the wall height, stiffness and spacing of reinforcements, stiffness and slope of the face, foundation conditions, backfill soil characteristics, effect of tensions induced by compaction, application of overloads and restriction to the displacements of the base, etc. In recent decades, several authors have developed studies based on experimental and/or numerical evaluations to determine the effects of these influencing factors on the mechanical behaviour of GRSW [e.g., Bathurst & Ezzein (2016), Chen et al. (2017), Ehrlich et al. (2012), Ehrlich & Mirmoradi (2013), Hatami & Bathurst (2005), Mirmoradi et al. (2016), Mirmoradi & Ehrlich (2018a, b), Riccio et al. (2014), Saramago (2002)].

As highlighted by Mirmoradi (2015), despite the several studies carried out, the results indicate that there is a need for additional studies to better understand the effects of the influencing factors for predicting the maximum traction mobilized in the reinforcement elements (T_{max}), the main factor to be determined for adequately designing GRSW (Ehrlich & Mirmoradi, 2016) and predicting face displacements and traction in reinforcements.

Several studies present a constructive recommendation that a backfill soil strip close to the face should be compacted with less energy to reduce the horizontal tensions close to the face and, consequently, the deformations due to the construction process [e.g., Bathurst et al. (2009), Ehrlich & Mitchell (1994), Elias et al. (2001), Hatami et al. (2008), Koerner & Koerner (2018), Mirmoradi & Ehrlich (2018b), Mitchell & Villter (1987)]. Although this recommendation is widely found in the literature, this factor has rarely been considered in the developed studies, as emphasized by Mirmoradi & Ehrlich (2018a).

In the present study, aiming to contribute to understanding the mechanical behaviour of the GRSW, with approaches increasingly closer to the real field conditions, the effects of the distance of application of heavy compaction from the face of GRSW were analysed numerically in terms of tensions and deformations. From a typical section, the analyses were performed with variations in the stiffness of the reinforcements and the distances of heavy compaction application from the face (light and heavy compaction were considered). In addition, for the backfill soil, after characterization and laboratory tests,

[#] Corresponding author. E-mail address: sergio.neto@ufv.br
[1] Samarco Mineração, Belo Horizonte, MG, Brasil.
[2] Universidade Federal de Juiz de Fora, Faculdade de Engenharia, Juiz de Fora, MG, Brasil.
[3] Universidade Federal de Viçosa, Departamento de Engenharia Civil, Viçosa, MG, Brasil.

Submitted on March 6, 2022; Final Acceptance on October 4, 2022; Discussion open until February 28, 2023.
https://doi.org/10.28927/SR.2022.003022

the strength parameters in terms of total and effective stresses were considered (triaxial strength envelopes). A comparison between the results is presented, considering the position and magnitude of the maximum tension mobilized in the reinforcements (T_{max}) and the horizontal displacements of the face at the end of the construction period.

1. Material and methods

1.1. Typical analysis section

For the numerical analyses in terms of tensions and deformations, a typical hypothetical GRSW retaining structure with a typical configuration adopted in several works was considered. The studied hypothetical structure was composed of precast concrete blocks and used geogrids as a geosynthetic reinforcement element and a gravel layer for drainage, just behind the face blocks. Table 1 lists the main geometric characteristics of the analysis section shown in Figure 1.

The numerical analyses were performed using the finite element method in PLAXIS 2D (Brinkgreve & Vermeer, 2002) with consideration of the plane strain state. In Figure 2 the boundary conditions adopted can be observed, namely, the restriction of horizontal displacement on the sides of the section—on the left side only applied to the foundation—and the total restriction of displacements and rotation at the base. The typical section was discretized in triangular elements composed of 15 nodes. The overall refinement adopted for the mesh was classified as Medium and, close to the contacts with reinforcements and the face, Very Fine. The mesh has a total of 3,007 elements and 24,299 nodes.

Table 1. Main geometric characteristics of the analysis section.

Description	Value
Free height (m)	4.20
Face inlay (m)	0.40
Face inclination	1H:10V
Length of reinforcements (m)	3.50
Vertical spacing between reinforcements (m)	0.40

1.2. Material properties

The linear elastic constitutive model was used for the face blocks. The parameters were defined according to the experimental results obtained by Mohamad et al. (2007). The soil-block interface friction factor (R_{inter}) was set as 0.7 (i.e., $\mu = 0.7 \cdot \tan \phi'$), where ϕ' is the effective friction angle of the soil backfill. For the drainage layer, the work of Riccio et al. (2014) was used, in which the material is presented with the Hardening Soil constitutive model similar to the hyperbolic fit proposed by Duncan et al. (1980), which considers the variation in the elastic modulus in relation to the confining stress (σ_3), in addition to considering the effect of soil dilatancy and introducing a plastification function. In the model, the plastification surface is not fixed in the stress space but expands due to plastic deformations (Brinkgreve & Vermeer, 2002). For the drainage layer, the standard recommendation of the PLAXIS 2D software was used, with $E_{ur}^{ref} = 3E_{50}^{ref}$, in which E_{ur}^{ref} and E_{50}^{ref} are the stiffnesses of the material for the reference confining tension (p^{ref}), corresponding to 50% of the maximum deformation, respectively, in unloading and loading. In addition, the software considers the tangent modulus obtained from oedometric tests (E_{eod}^{ref}) and the exponential coefficient (m) applied in the relationship between stiffness and tension level. In the present study, the adopted value of E_{eod}^{ref} was equal to the value of E_{50}^{ref}, which is the value obtained from the triaxial tests for an effective consolidation stress of 80 kPa. The value of m was also obtained from the stress-deformation curves of

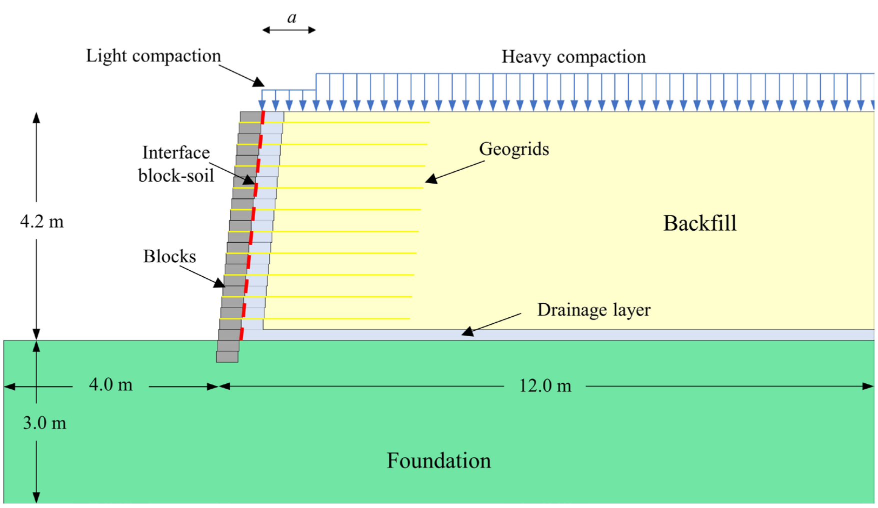

Figure 1. Analysed section with variations of the external loading.

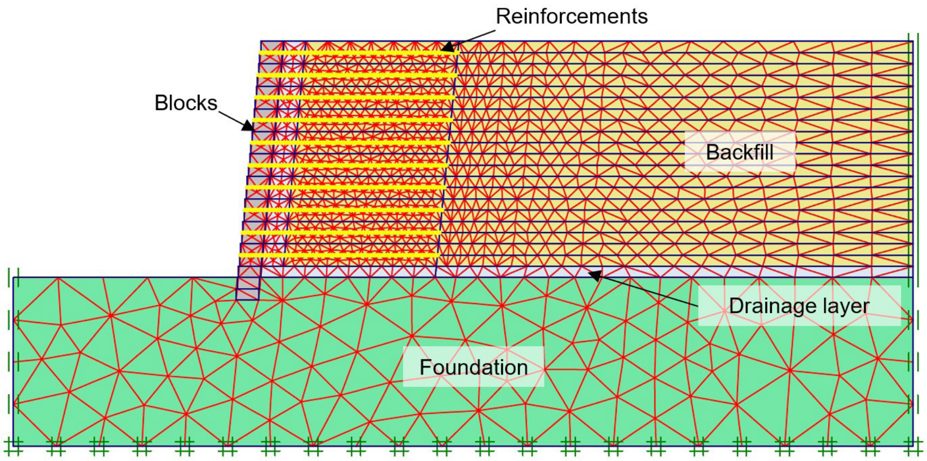

Figure 2. Numerical model and finite element mesh in PLAXIS 2D.

Table 2. Soil characteristics.

∅* ≤ 2 μm (%)	∅ ≤ 20 μm (%)	∅ ≤ 2 mm (%)	w_{opt} (%)	$\gamma_{d,max}$ (kN/m³)
10	22	100	13.8	17.43

*∅: effective diameter of soil particles.

the triaxial tests for effective consolidation stresses (σ_3) of 40, 80, 160 and 320 kPa.

The elastoplastic constitutive model, with the Mohr-Coulomb failure criterion, was considered for the foundation. The parameters of the foundation were assigned in such a way that it had a good bearing capacity and did not significantly influence the values of maximum tensile stresses acting on the reinforcements.

The backfill soil adopted in the analyses, a young gneiss residual soil, was characterized in the laboratory. On specimens moulded to a 98% degree of compaction at Normal Proctor energy, hydrostatic and undrained triaxial tests were performed in the saturated condition (CIU_{sat}), according to D4767 (ASTM, 2011), using consolidation stresses (σ_3) of 40, 80, 160 and 320 kPa. Table 2 presents the values obtained in the characterization and Normal Proctor tests for the studied soil.

The soil backfill was modelled with the Hardening Soil constitutive model, using the approach explained earlier for the drainage layer. The parameters for the hyperbolic relationship between stress and strain were defined to obtain the best fit of the hyperbole to the curves obtained in the triaxial tests.

For the test carried out with an effective consolidation stress of 320 kPa, an unloading and reloading cycle was performed. In this way, the real ratio between the reload stiffness and the initial stiffness (E_{ur}/E_i) was obtained. In general, using the real ratio (E_{ur}/E_i) is rarely considered. The parameters of the mentioned materials are listed in Table 3. As the backfill soil was submitted to loading and unloading due to compaction, determining the E_{ur}/E_i ratio is relevant.

The reinforcement elements were modelled as a linear elastic material using the hypothesis of perfect adherence with adjacent soil. Under working conditions, this hypothesis is considered acceptable, as presented by Jewell (1980) and Dyer & Milligan (1984). Geogrids were considered for the geosynthetic reinforcements, which are made up of polyester (PET) polymers whose stiffnesses are as follows: R1 = 400 kN/m, R2 = 800 kN/m and R3 = 1500 kN/m. Stiffness values were selected for 5% deformation.

1.3. Compaction

The calculation of the vertical stress induced by compaction ($\sigma_{zc,i}$) was performed using the procedure proposed by Ehrlich & Mitchell (1994). Two compaction devices were considered, namely a heavy compactor (compactor roller) and a light compactor (vibratory plate). A typical vibratory plate had a vertical induced stress measured by Saramago (2002) using accelerometers. The measurements show a vertical stress induced by the equipment of approximately 73 kPa. The compactor roller (type CA 250 PD, Dynapac), as presented by Riccio et al. (2014), presents a maximum vertical force (Q) of 378 kPa. For the calculation of $\sigma_{zc,i}$ by the procedure proposed by Ehrlich & Mitchell (1994), the friction angle of the backfill soil and characteristics of the compaction equipment were used. Stresses induced by compaction were evaluated using parameters obtained from the shear failure envelopes in terms of total and effective stresses.

The Type 2 procedure proposed by Mirmoradi & Ehrlich (2014) was adopted for compaction simulation in

Table 3. Input parameters adopted in the numerical modelling for the drainage layer, the face blocks and the foundation soil of the typical sections analysed.

Materials	Backfill soil*		Drainage layer	Blocks	Foundation
Constitutive Model	*Hardening Soil Model*		*Hardening Soil Model*	*Linear elastic*	*Elastoplastic with Mohr-Coulomb failure criterion*
Stress path	Total	Effective	-	-	-
Friction angle, ϕ (°)	60	36	40	-	35
Cohesion (kPa)	20	6	0	-	10
Dilatancy angle, ψ (º)	2	2	0	-	0
Unit weight,γ (kN/m^3)	20	19	20	25	20
E_{50}^{ref} (MPa)	9	9	40	-	-
E_{oed}^{ref} (MPa)	9	9	55	-	-
E_{ur}^{ref} (MPa)	22	22	120	-	-
Exponent modulus, *m*	0.7	0.7	0.5	-	-
Young modulus, *E* (MPa)	-	-	-	50	50
Poisson Coefficient, υ	0.3	0.3	-	0.2	0.3

*The backfill soil parameters are listed in detail in item 3.1.

the numerical analyses. In this procedure, the compaction of each layer is simulated by a single load-unload cycle, with the application of the vertical stress induced by compaction ($\sigma_{zc,i}$) at the top and bottom of the layer. The authors found that the Type 2 procedure represents, more appropriately, the efforts due to compaction.

1.4. Numerical analysis program

Table 4 shows the analysis program corresponding to the simulations carried out and the corresponding codes assigned to them. For the analysis section presented previously (Figure 1), analyses were performed in terms of effective stress (ES) and total stress (TS) for reinforced soil using three (03) types of reinforcement and four (04) distances of heavy compaction from the face (*a*). The distances considered are 0, 0.25, 0.5 and 1.0 m.

2. Results and discussions

2.1. Laboratory tests

The laboratory characterization of the backfill soil indicates that it has a unified classification, according to D2487 (ASTM, 2017), SM (Silty sand). The use of fine-grained soils for GRSW is a common practice in Brazil, an example is given in Riccio et al. (2014).

Figure 3 shows a compilation of the results of the hydrostatic and consolidated undrained triaxial tests in the saturated condition (CIU_{sat}). As can be seen in Figure 3a, the material presented an increase in its Young's modulus with increasing confining stress (σ_3), that is, the higher is the confining stress (σ_3) the higher the Young's modulus (*E*).

From the stress-strain curves, the parameters of the hyperbolic fit (Duncan et al., 1980) were optimized to obtain the best fit for determining parameters *K* and *m*. Figure 3a shows the hyperbolic fit each stress-strain curve (σ_3 = 40, 80, 160 and 320 kPa) obtained from the triaxial tests. A better fit in the initial stretches of the curves was chosen since the GRS walls have small horizontal deformations.

Figure 3b shows the envelopes for trajectories of total and effective stresses. The strength parameters, cohesion intercept (*c* or *c'*) and friction angle (ϕ or ϕ') were determined from the envelopes (solid lines) obtained from the maximum value of σ_d (deviator stress) of each experimental stress-strain curve. Thus, the effective strength parameters were *c'* = 6 kPa and ϕ' = 36°, and the total strength parameters were *c* = 60 kPa and ϕ = 20°. This difference between the parameters obtained from the total and effective stress envelopes leads to significant differences in the prediction of the tension in the reinforcements.

Figure 3c illustrates the unload-reload cycle carried out in the test with a 320 kPa effective consolidation stress. A 149.55 MPa stiffness (E_{ur}) was obtained. Since the initial stiffness (E_i) obtained was 61.7 MPa for the test with the same effective consolidation stress, the real E_{ur} / E_i ratio obtained was 2.4. It should be noted that this value is within the typical range presented by Duncan et al. (1980).

2.2. Magnitude of maximum tension in the reinforcements (T_{max})

Figure 4 presents a compilation of the results of maximum tension in the reinforcements (T_{max}) obtained in the numerical analyses that provided data to evaluate the influence of the distance of heavy compaction from the face. For a better understanding of these results, the sum of

Table 4. Data corresponding to the analyses carried out and the code for each.

Shear failure envelope	Reinforcement	*a* (cm) Distance of Heavy compaction from the face	Code
Effective stress (ES)	R1 (J = 400 kN/m)	0	ES-R1-0
		25	ES-R1-25
		50	ES-R1-50
		100	ES-R1-100
	R2 (J = 800 kN/m)	0	ES-R2-0
		25	ES-R2-25
		50	ES-R2-50
		100	ES-R2-100
	R3 (J = 1500 kN/m)	0	ES-R3-0
		25	ES-R3-25
		50	ES-R3-50
		100	ES-R3-100
Total stress (TS)	R1 (J = 400 kN/m)	0	TS-R1-0
		25	TS-R1-25
		50	TS-R1-50
		100	TS-R1-100
	R2 (J = 800 kN/m)	0	TS-R2-0
		25	TS-R2-25
		50	TS-R2-50
		100	TS-R2-100
	R3 (J = 1500 kN/m)	0	TS-R3-0
		25	TS-R3-25
		50	TS-R3-50
		100	TS-R3-100

the maximum tensions acting on the reinforcements (ΣT_{max}) and the sum of the positions at which the maximum tensions (ΣX_{max}) occur were plotted in the graphs, in which X is the distance from the point at which the maximum took place far from the back side of the face.

In general, when distancing the heavy compaction from the face, there are reductions in the maximum tensions mobilized in the reinforcements and displacement of the points at which they occur to the interior of the reinforced soil mass.

For the analyses considering effective parameters for the backfill soil (Figure 4a, b and c), average reductions of ΣT_{max} (3, 7 and 12%) were obtained when considering, respectively, the distances of heavy compaction of 0.25, 0.50 and 1.0 m from the face. On the other hand, when considering the sum of the positions of points at which maximum tensions occur (ΣX_{max}), there was, respectively, an increase in the sum of the positions where T_{max} occurs by 4, 9 and 36%; that is when increasing the distance of heavy compaction from the face, the point where T_{max} occurs moves to the interior of the soil mass.

For the analyses in which the total parameters for the backfill soil were considered (Figure 4d, e and f), there is a smaller influence of the distance of heavy compaction from the face on the comparison parameters (ΣT_{max} and ΣX_{max}). The sum of the maximal tensions in the reinforcements (ΣT_{max}) showed reductions of 1, 2 and 4% when considering, respectively, the distances of heavy compaction from of 0.25, 0.50 and 1.0 m the face. When considering the sum of the position of points where the maximum tension occurs (ΣX_{max}), the average positions move towards to the interior of the soil mass, increasing, respectively, by 1, 4 and 5%.

It is important to point out that, for the analyses considering of total parameters of the backfill soil, as already mentioned, due to the reduction in the friction angle ($\phi' = 36º$ to $\phi = 20º$), there is a reduction in the vertical stress induced by compaction, which is 80 kPa. The vertical stress induced by the light compaction applied close to the face is 73 kPa, independent of the soil friction (compaction per hand tamper, $\sigma'_{zc,i} = F/A$, F is the static equivalent weight and A is the area of the plate).

Regardless of kind of strength parameters (effective or total), the behaviour observed is the following, the higher distance of heavy compaction from the face, the lower the ΣT_{max} and the sum of the distance between the location of the T_{max} and the face increase.

Regarding the stiffness of geosynthetic reinforcements (Figure 4), in the analyses based on effective parameters (ES analyses) and in the analyses based on total parameters (TS analyses), the values of the maximum tensions in the reinforcements increase with the increase in the stiffness modulus of the geosynthetic reinforcement.

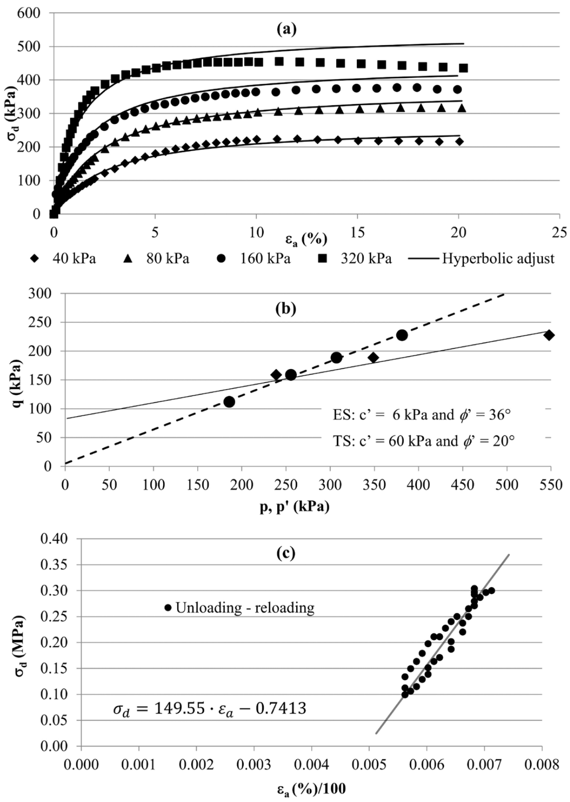

Figure 3. Results from the CIUsat triaxial tests for σ_3 equal to 320 kPa, considering the unload-reload cycle - (a) deviator stress (σ_d) versus axial strain (ε_a) curves, (b) failure envelopes in terms of total stress (TS) and effective stress (ES) and (c) unload-reload cycle.

2.3. Position of the maximum tension in the reinforcements (X_{max})

Figure 5 and Figure 6 illustrate the points at which the maximum tensions mobilized in the reinforcements (X_{max}) occur for the analyses performed with effective and total backfill soil parameters, respectively.

The stiffness variation of the reinforcements did not result in significant differences in the points at which the maximum tensions occur. For the two upper layers of the reinforcements, taking into account the effective parameters of the backfill soil, the displacement of the points of maximum tensions towards the interior of the soil mass with increasing distance of the application of heavy compaction from the face. This behaviour is associated with the fact that the vertical induced stress due compaction is much higher than the geostatic vertical stress. The vertical induced stress produce a horizontal induced stress ($\sigma'_{xp,i} = K_o \cdot \sigma'_{zc,i}$) loading the reinforcement. Thus, the location of T_{max} has a tendency to move towards the region where the compaction was applied, moving away from the proximity of the face, where there is no compaction. This displacement is shown to be important for evaluating the stability to pulling out the reinforcement element. For the analyses with the use of total parameters of the backfill soil (Figure 6), as mentioned for T_{max} results, due to the small difference between heavy and light compaction, the results are very similar.

Concerning the points of maximum tension in the reinforcements, it is emphasized that because it is a GRSW with a rigid face, there is a tendency for these points to occur close to the face (Christopher et al., 1990).

The displacement of the point of maximum tension to the interior of the soil mass implies an increase in the length of the reinforcement in the active zone of the reinforced soil and, consequently, a reduction in the length in the resistant zone, which causes reduction of the factor of safety to the pull-out of the element (Chen et al., 2017).

2.4. Horizontal displacements of the face

A comparison was made between the results obtained for the horizontal displacements (U_x) of the face, considering the analyses performed using effective and total shear strength parameters. In general, the results are consistent with reinforcement stiffness. For the analyses that consider the effective parameters for the backfill soil (Figure 7) and those considering total parameters (Figure 8), there are reductions in horizontal displacements with the use of stiffer reinforcements.

Similar to the considerations made for the magnitude of the maximum tension in the reinforcements (since there is no significant difference between the heavy and light compaction in the analyses with the use of total parameters), the horizontal displacements of the face are very close for this condition.

For the analyses using the effective parameters of the backfill soil, there is a significant difference between the analyses with heavy compaction closest to the face (a = 0 m and a = 0.25 m) and those that use heavy compaction farthest from the face (a = 0.50 m and a = 1.00 m). For the condition where a = 0.25 m and a = 0.50 m, especially for the upper layers of the reinforcements, there are smaller displacements, compared with the ones observed in the bottom layers of the GRSW. The higher the stiffness of the reinforcement leads to smaller displacements of the upper layers in the analyses with heavy compaction closest to the face (a = 0 m and a = 0.25 m).

The vertical induced stress generated by compaction, $\sigma'_{zc,i}$, and the horizontal induced stress, $\sigma'_{xp,i}$ ($\sigma'_{xp,i} = K_o \cdot \sigma'_{zc,i}$), are greater than the geostatic vertical and horizontal stresses ($\sigma'_h = K_a \cdot \sigma'_v$). So, according to Ehrlich & Mitchell (1994), the geosynthetic is submitted to a transitory high level of stress with a portion of unrecovered stress, as measured by Riccio et al. (2014).

However, this displacement is opposed to lateral pressures due to the compaction of the backfill. In this way, when carrying out the analyses with increasing distance of heavy compaction from the face, consequently with reducing the portion of reinforcements subjected to the loads of this

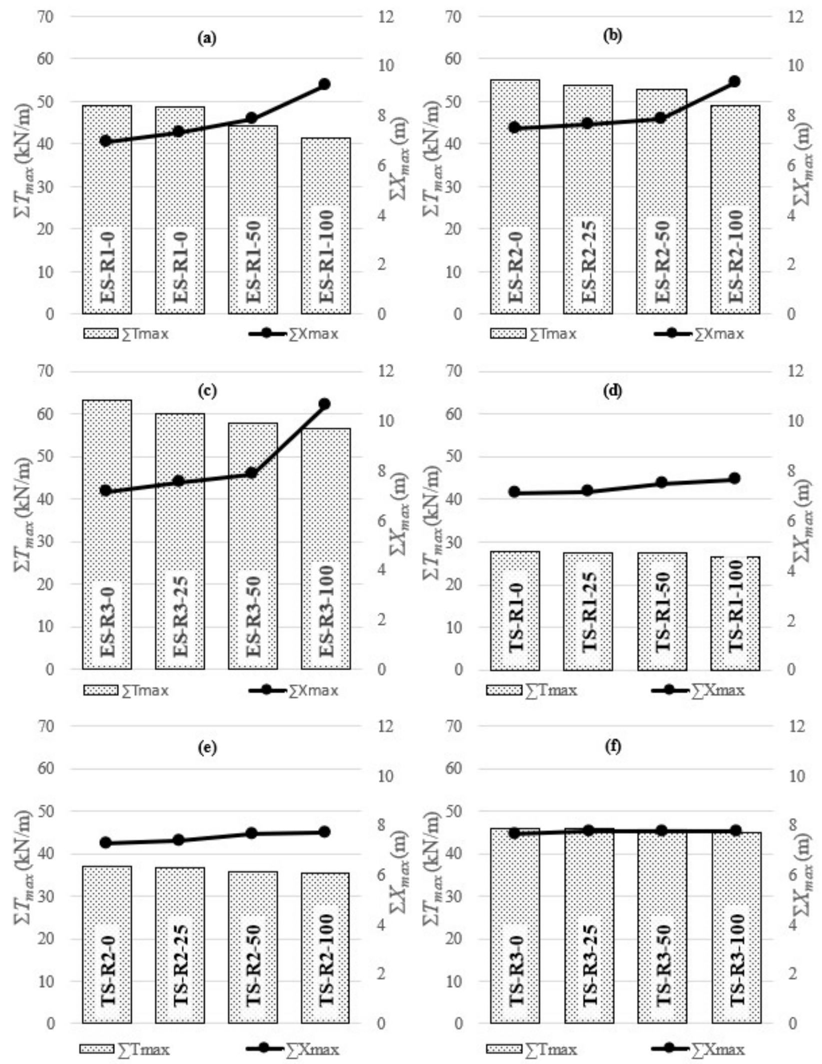

Figure 4. Influence of the stiffness modulus of the reinforcement (J) and the distance of heavy compaction from the face on the sum of the magnitude of the maximum tensions in the reinforcements (ΣT_{max}) and on the sum of the positions at which the maximum tensions in the reinforcements occur (ΣX_{max}).

compaction, there is a point where the maximum horizontal displacements occur. For the analyses performed, this maximum displacement occurred with 0.50 m distance of heavy compaction from the face.

In both analyses, the horizontal displacements of lower layers of the reinforcements are restricted by the stiffness of the foundation. In fact, according to Bathurst et al. (2009), the tensions in the reinforcements may be higher the half-height of the wall, generating larger deformations in this region. Another observation refers to the point where the maximum horizontal displacements (U_x) occur. In the analyses with the application of heavy compaction closest to the face ($a = 0$ m and $a = 0.25$ m), the points at which the maximum horizontal displacements occur are approximately half the height of the walls. In those that use heavy compaction farthest from the face ($a = 0.50$ m and $a = 1.00$ m), these points are elevated; however, these displacements are not maximum at the top of the structure.

Importantly, in executing GRSW, the analysis with the application of heavy compaction nearest to the face ($a = 0$ m and $a = 0.25$ m) is difficult to perform. Thus, the analyses that considered heavy compaction farthest from the face ($a = 0.50$ m and $a = 1.00$ m) are more consistent with the conditions found in the real works. For the latter, as can be seen in Figure 7 and Figure 8, by moving the application of heavy compaction away from the face, face displacements were reduced.

Note that the results obtained numerically for the face horizontal displacements show similarities with other results found in the literature Miyata (1996), Helwany et al. (1999), Reeves (2003), Farrag et al. (2004), Yoo & Jung (2004), Benjamim et al. (2007), Bathurst et al. (2009) and Yang et al. (2009). The pattern

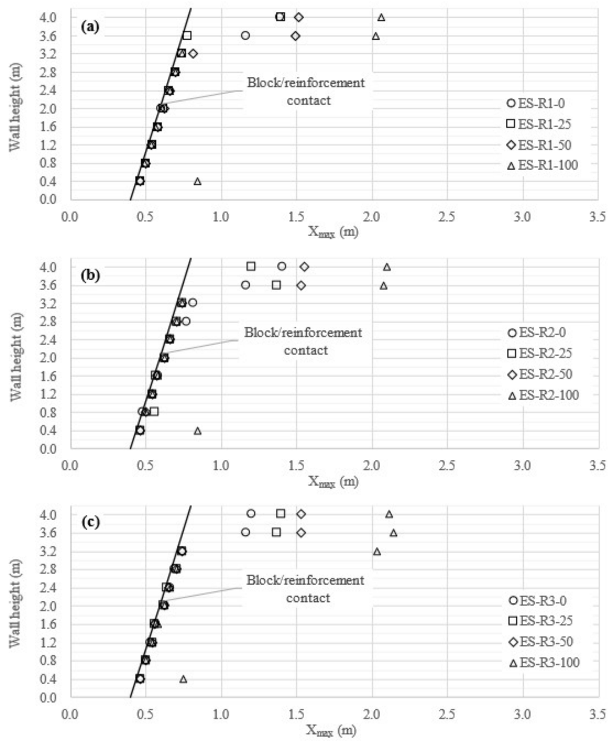

Figure 5. Positions of the maximum tensions in the reinforcements (X_{max}): numerical analyses in terms of Effective Stress (ES) when considering reinforcement stiffness (J) equal to (a) 400 kPa, (b) 800 kPa and (c) 1500 kPa.

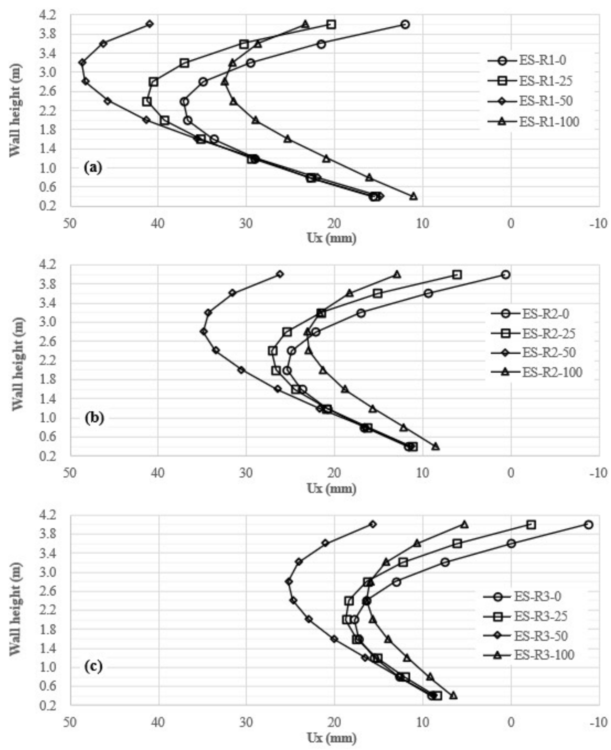

Figure 7. Horizontal displacements of the face: analyses in terms of effective stress (ES), considering the reinforcement stiffness (J) equal to (a) 400 kPa, (b) 800 kPa and (c) 1500 kPa.

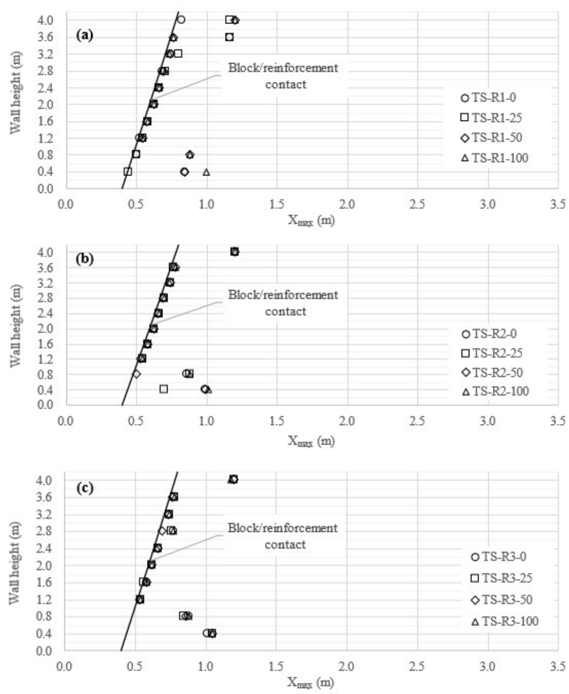

Figure 6. Positions of the maximum tensions in the reinforcements (X_{max}): numerical analyses in terms of Total Stress (TS) when considering reinforcement stiffness (J) equal to (a) 400 kPa, (b) 800 kPa and (c) 1500 kPa.

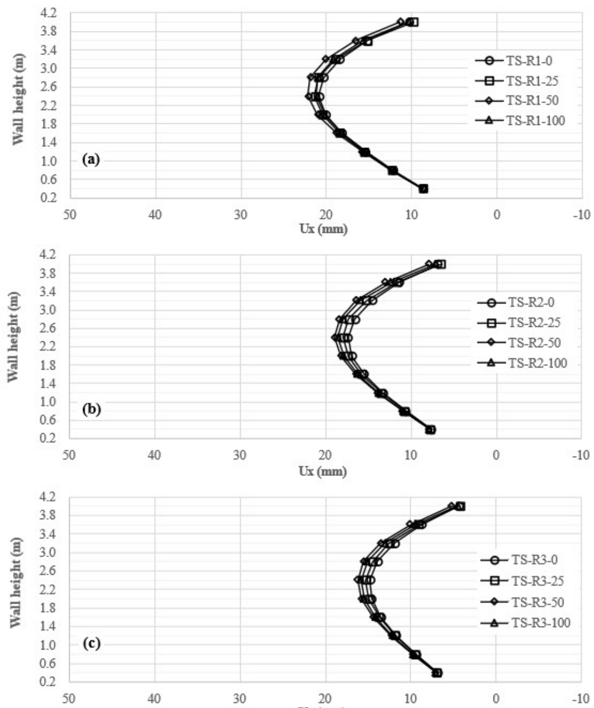

Figure 8. Horizontal displacements of the face: analyses in terms of total stress (TS), considering the reinforcement stiffness (J) equal to (a) 400 kPa, (b) 800 kPa and (c) 1500 kPa.

found for the maximum horizontal displacements of the face was also identified in the field measurements presented by Reeves (2003), with maximum deformations in the half-height portion of the GRSW. The data measured by Reeves (2003) were used by several authors to validate numerical models or design methods. The field measurements presented by Reeves (2003) were made on walls of soil reinforced with steel mesh, an enveloped face and light compaction.

Farrag et al. (2004) and Benjamim et al. (2007) also presented data on displacements of the face of reinforced soil walls built in full scale. They observed the same pattern found by Reeves (2003), i.e., maximum displacements at the half-height of the wall. However, it should be noted that in Farrag et al. (2004), although the wall was built with geogrids, as reinforcement elements, and concrete face blocks, there is no information on the type soil compaction used (light or heavy compaction). In Benjamim et al. (2007), the GRSW was built using an enveloped face, geotextiles, as reinforcement elements, and light compaction to densify the soil.

However, Riccio et al. (2014) found in an instrumented GRSW, locations of T_{max} not close to the face along the depth of the wall. The monitored GRSW had similar characteristics to the hypothetic GRSW presented in this study, but the foundation of the retaining wall monitored by Riccio et al. (2014) was a piled concrete slab.

3. Conclusions

This study presents a computational model of a GRSW using soil shear strength parameters obtained from triaxial tests. The objective was to analyse the influence of compaction in the magnitude of the tensions in the reinforcements, face horizontal deformation and position of maximum reinforcement´s tension. The main conclusions are as follows.

In general, the results show the importance of considering the compaction-induced effects. In the analyses performed, the compaction caused influence on the magnitude and position of the maximum tensions in the reinforcements and the horizontal displacements of the face were determined. It is also identified that, with increasing stiffness of the reinforcements, there is an increase in the tensions mobilized and a reduction in the horizontal displacements of the face.

When analysing the influence of using distances close to the face for applying light compaction, it was identified that, by increasing these distances, that is, by moving the heavy compaction away from the face, there is a reduction in the sum of maximum tensions in the reinforcements (ΣT_{max}) and an increase in the sum of the positions at which T_{max} (ΣX_{max}) occurs. The increase in the positions at which T_{max} occurs means greater distances of T_{max} in relation to the face with increasing distance of heavy compaction from the face, especially for the upper layers. This increasing distance of T_{max} from the face is an important aspect to analyse since it will imply a reduction of the lengths of reinforcements in the resistant zone and, consequently, reduction in the factor of safety to pull-out.

Concerning the horizontal displacements of the face, it was expected that when distancing the heavy compaction from the face, there would be reductions in the displacements of the face. This behaviour was identified in the analyses in which the light compaction was considered in the first 0.50 m and 1.00 m behind the face. However, for the analyses in which only the application of heavy compaction was considered or the application of light compaction in the first 0.25 m behind the face was considered, the face displacements were smaller, especially in the upper portion of the walls analysed. It is understood that this behaviour may be associated with some factors, such as:

- Consideration of a 0.40 m wide drainage layer behind the face. Thus, for the analyses where the distance of heavy compaction was zero or 0.25 m, heavy compaction is supported on stiffer materials;
- Reducing the vertical stress induced by compaction in the region close to the face reduces the stiffness of the materials in the region since, with the use of the Hardening Soil model, the stiffness is a function of the confining stress;
- The linear elastic behaviour of the reinforcement and the perfect adhesion of the reinforcement with the soil. In this way, a greater extension of loads referring to the heavy compaction causes greater unloading and return of the elements to the original position.

It should be noted that the analyses considering heavy compaction at the face or a distance of only 0.25 m do not adequately represent the actual conditions of the work since in practice it is difficult to perform heavy compaction at distances less than 0.50 m from the face. Thus, when considering the analyses that are more consistent with the conditions of the constructive practices, that is, distances of 0.50 m and 1.00 m, it was observed that by moving the heavy compaction away from the face, there is a reduction of the sum of maximum tensions in the reinforcements, displacement towards the interior of the soil mass of the points at which the maximum tensions occur and reduction in horizontal displacements of the face. The results indicate that, mainly for the numerical evaluation of face displacements (U_x) and position of the maximum tension in the reinforcements (X_{max}), one should avoid the application of the vertical stress induced by compaction close to the face of GRSW in compaction modelling as in the analyses using zero or 0.25 m spacing.

It is important to highlight that the results obtained are limited to the considerations adopted for the analyses, such as soil type, reinforcement elements, face, foundation conditions and loads corresponding to the stresses induced by compaction.

Acknowledgements

The authors thank CNPq (Brazilian Council of Research), FAPEMIG (Minas Gerais State Council of Research) and CAPES (Coordination for the Improvement of Higher Education Personnel).

Declaration of interest

The authors have no conflicts of interest to declare. All co-authors have observed and affirmed the contents of the paper and there is no financial interest to report.

Authors' contributions

Leone César Meireles: conceptualization, investigation, data curation, formal analysis, writing – original draft, writing – review and editing. Mario Vicente Riccio Filho: conceptualization, investigation, data curation, formal analysis, writing – review and editing. Heraldo Nunes Pitanga: conceptualization, investigation, data curation, formal analysis, writing – review and editing. Roberto Lopes Ferraz: conceptualization, investigation, data curation, formal analysis, writing – review and editing. Taciano Oliveira da Silva: conceptualization, investigation, data curation, formal analysis, writing – review and editing. Sérgio Leandro Scher Dias Neto: conceptualization, investigation, data curation, formal analysis, writing – review and editing.

List of symbols

a	heavy compaction distance from the face
c	cohesion intercept
c'	effective cohesion intercept
E	Young modulus
E_i	initial stiffness
E_{ur}	unloading/reloading stiffness
E_{50}^{ref}	stiffnesses of the material for the reference confining tension in loading
E_{eod}^{ref}	modulus obtained from oedometric test
E_{ur}^{ref}	stiffnesses of the material for the reference confining tension in unloading and reloading
J	stiffness of reinforcement
K	hyperbolic parameter
K_a	active earth pressure coefficient
K_0	coefficient of earth pressure at rest
m	exponential coefficient
p^{ref}	reference confining tension
q_c	distributed load
R_{inter}	interface friction factor
T_{max}	maximum tension in the reinforcement
U_x	horizontal displacements
X	positions at which the maximum tensions occur
Z	depth
γ	unit weight
ν	poisson Coefficient
ϕ	friction angle (°)
ϕ'	effective friction angle (°)
φ	effective diameter of soil particles
ΣT_{max}	sum of the maximum tensions acting on the reinforcements
ΣX_{max}	sum of the positions at which the maximum tensions occur
σ_3	consolidation stresses
σ'_h	effective horizontal stress
σ'_v	effective vertical stress
$\sigma_{xp,i}$	horizontal stress induced by compaction
$\sigma_{zc,i}$	vertical stress induced by compaction
ψ	dilatancy angle

References

ASTM D4767. (2011). *Standard Test Method for Consolidated Undrained Triaxial Compression Test for Cohesive Soils*. ASTM International, West Conshohocken, PA.

ASTM D2487-17. (2017). *Standard Practice for Classification of Soils for Engineering Purposes (Unified Soil Classification System)*. ASTM International, West Conshohocken, PA.

Bathurst, R.J., & Ezzein, F.M. (2016). Geogrid pullout load–strain behaviour and modelling using a transparent granular soil. *Geosynthetics International*, 23(4), 271-286. http://dx.doi.org/10.1680/jgein.15.00051.

Bathurst, R.J., Nernheim, A., Walters, D.L., Allen, T.M., Burgess, P., & Saunders, D.D. (2009). Influence of reinforcement stiffness and compaction on the performance of four geosynthetic-reinforced soil walls. *Geosynthetics International*, 16(1), 43-59. http://dx.doi.org/10.1680/gein.2009.16.1.43.

Benjamim, C.V.S., Bueno, B.S., & Zornberg, J.G. (2007). Field monitoring evaluation of geotextile-reinforced soil-retaining walls. *Geosynthetics International*, 14(2), 100-118. http://dx.doi.org/10.1680/gein.2007.14.2.100.

Brinkgreve, R., & Vermeer, P. (2002). *PLAXIS 2D: Finite Element Code for Soil and Rock Analyses - Version 8*. CRC Press.

Chen, J., Zhang, W., & Xue, J. (2017). Zoning of reinforcement forces in geosynthetic reinforced cohesionless soil slopes. *Geosynthetics International*, 24(6), 565-574. http://dx.doi.org/10.1680/jgein.17.00023.

Christopher, B.R., Gill, S.A., Giroud, J.P., Juran, I., Mitchell, J.K., Schlosser, F., & Dunnicliff, J. (1990). *Reinforced soil structures* (Vol. 1: Design and Construction Guidelines). U.S. Department of Transportation, Federal Highway Administration.

Duncan, J.M., Bryne, P., Wong, K.S., & Mabrt, P. (1980). *Strength, stress-strain and bulk modulus parameters for finite element analyses of stresses and movements in soil masses*. College of Engineering, Office of Research Services, University of California.

Dyer, M.R., & Milligan, G.W. (1984). A photoelastic investigation of the interaction of a cohesionless soil with reinforcement placed at different orientations. In *Proceedings of the International Conference on In Situ Soil and Rock Reinforcement* (pp. 257-262). Paris: ISSMFE.

Ehrlich, M., & Mirmoradi, S.H. (2013). Evaluation of the effects of facing stiffness and toe resistance on the behavior of GRS walls. *Geotextiles and Geomembranes*, 40, 28-36. http://dx.doi.org/10.1016/j.geotexmem.2013.07.012.

Ehrlich, M., & Mirmoradi, S.H. (2016). A simplified working stress design method for reinforced soil walls. *Geotechnique*, 66(10), 854-863. http://dx.doi.org/10.1680/jgeot.16.P.010.

Ehrlich, M., & Mitchell, J. K. (1994). Working stress design method for reinforced soil walls. *Journal of Geotechnical Engineering*, 120(4), 625-645. http://dx.doi.org/10.1061/(ASCE)0733-9410(1994)120:4(625).

Ehrlich, M., Mirmoradi, S.H., & Saramago, R.P. (2012). Evaluation of the effect of compaction on the behavior of geosynthetic-reinforced soil walls. *Geotextiles and Geomembranes*, 34, 108-115. http://dx.doi.org/10.1016/j.geotexmem.2012.05.005.

Elias, V., Christopher, B. R., & Berg, R. R. (2001). *Mechanically stabilized earth walls and reinforced soil slopes – design and construction guidelines* [No. FHWA-NHI-00-043]. U.S. Department of Transportation, Federal Highway Administration.

Farrag, K., Abu-Farsakh, M., & Morvant, M. (2004). Stress and strain monitoring of reinforced soil test wall. *Transportation Research Record: Journal of the Transportation Research Board*, 1868(1), 89-99. http://dx.doi.org/10.3141/1868-10.

Hatami, K., & Bathurst, R.J. (2005). Development and verification of a numerical model for the analysis of of geosynthetic-reinforced soil segmental walls under working stress conditions. *Canadian Geotechnical Journal*, 42(4), 1066-1085.

Hatami, K., Witthoeft, A.F., & Jenkins, L.M. (2008). Influence of inadequate compaction near facing on construction response of wrapped-face mechanically stabilized earth walls. *Transportation Research Record: Journal of the Transportation Research Board*, 2045(1), 85-94. http://dx.doi.org/10.3141/2045-10.

Helwany, S.M.B., Reardon, G., & Wu, J.T.H. (1999). Effects of backfill on the performance of GRS retaining walls. *Geotextiles and Geomembranes*, 17(1), 1-16. http://dx.doi.org/10.1016/S0266-1144(98)00021-1.

Jewell, R.A. (1980). *Some effects of reinforcement on the mechanical behavior of soils*. University of Cambridge.

Koerner, R.M., & Koerner, G.R. (2018). An extended data base and recommendations regarding 320 failed geosynthetic reinforced mechanically stabilized earth (MSE) walls. *Geotextiles and Geomembranes*, 46(6), 904-912. http://dx.doi.org/10.1016/j.geotexmem.2018.07.013.

Mirmoradi, S.H. (2015). *Evaluation of the behavior of reinforced soil walls under working stress conditions* [Doctoral thesis]. Federal University of Rio de Janeiro. Retrieved in October 28, 2022, from http://www.coc.ufrj.br/en/doctoral-thesis/584-2015/5336-seyedhamed-mirmoradi.

Mirmoradi, S.H., & Ehrlich, M. (2014). Modeling of the compaction-induced stresses in numerical analyses of grs walls. *International Journal of Computational Methods*, 11(2), 1342002. http://dx.doi.org/10.1142/S0219876213420024.

Mirmoradi, S.H., & Ehrlich, M. (2018a). Numerical simulation of compaction-induced stress for the analysis of RS walls under working conditions. *Geotextiles and Geomembranes*, 46(3), 354-365. http://dx.doi.org/10.1016/j.geotexmem.2018.01.006.

Mirmoradi, S.H., & Ehrlich, M. (2018b). Experimental evaluation of the effect of compaction near facing on the behavior of GRS walls. *Geotextiles and Geomembranes*, 46(5), 566-574. http://dx.doi.org/10.1016/j.geotexmem.2018.04.010.

Mirmoradi, S.H., Ehrlich, M., & Dieguez, C. (2016). Evaluation of the combined effect of toe resistance and facing inclination on the behavior of GRS walls. *Geotextiles and Geomembranes*, 44(3), 287-294. http://dx.doi.org/10.1016/j.geotexmem.2015.12.003.

Mitchell, J. K., & Villter, W. B. (1987). *Reinforcement of earth slopes and embankments*. National Academies of Sciences, Engineering, and Medicine.

Miyata, K. (1996). Walls reinforced with fiber reinforced plastic geogrids in Japan. *Geosynthetics International*, 3(1), 1-11. http://dx.doi.org/10.1680/gein.3.0050.

Mohamad, G., Lourenço, P.B., & Roman, H.R. (2007). Mechanics of hollow concrete block masonry prisms under compression: review and prospects. *Cement and Concrete Composites*, 29(3), 181-192. http://dx.doi.org/10.1016/j.cemconcomp.2006.11.003.

Reeves, J.W. (2003). *Performance of a full-scale wrapped face welded wire mesh reinforced soil retaining wall* [Master thesis]. Royal Military College of Canada (RMC).

Riccio, M., Ehrlich, M., & Dias, D. (2014). Field monitoring and analyses of the response of a block-faced geogrid wall using fine-grained tropical soils. *Geotextiles and Geomembranes*, 42(2), 127-138. http://dx.doi.org/10.1016/j.geotexmem.2014.01.006.

Saramago, R. P. (2002). *Study of the influence of compaction on the behavior of reinforced soil walls using physical models* [Doctoral thesis]. Federal University of Rio de Janeiro. (in Portuguese). Retrieved in October 28, 2022, from http://www.coc.ufrj.br/pt/teses-de-doutorado/146-2002/926-robson-palhas-saramago

Yang, G., Zhang, B., Lv, P., & Zhou, Q. (2009). Behaviour of geogrid reinforced soil retaining wall with concrete-rigid facing. *Geotextiles and Geomembranes*, 27(5), 350-356. http://dx.doi.org/10.1016/j.geotexmem.2009.03.001.

Yoo, C., & Jung, H.-S. (2004). Measured behavior of a geosynthetic-reinforced segmental retaining wall in a tiered configuration. *Geotextiles and Geomembranes*, 22(5), 359-376. http://dx.doi.org/10.1016/S0266-1144(03)00064-5.

Soils and Rocks

An International Journal of Geotechnical and Geoenvironmental Engineering

www.soilsandrocks.com

ISSN 1980-9743
ISSN-e 2675-5475

Microstructural characterization of a 3D-printed soil

Alessio Ferrari[1,2], Marco Rosone[1], Silvia La Rosa[1], Giovanni Sapienza[1]

Article

Keywords
3D-printing
Soil additive manufacturing
Soil extrusion
Soil fabric

Abstract

Transversal applications of 3D-printing (or Additive Manufacturing) have been recently implemented in the field of Geomechanics. In a 3D-printing process, the printed volume is obtained from successive layering of adjacent soil filaments. In this work, the fabric of an as-printed soil has been carried out by combining Mercury Intrusion Porosimetry (*MIP*) tests and Scanning Electron Microscope (*SEM*) observations, with the aim to highlight how the particle arrangements and the orientation and shape of pores are linked to the printing operation. The microstructural analyses showed that macropores are the result of the relative position of the filaments and their initial distortion in quasi-undrained conditions. Particle arrangement within the soil filament is strongly anisotropic, due to the rotative movement of the soil in the extruder.

1. Introduction

The fields of application of 3D-printing (or Additive Manufacturing) are constantly growing, including uses in Geomechanics. 3D-printing of polymeric materials has been used to manufacture synthetic porous samples aiming at mimicking characteristics of soils and rocks (Ju et al., 2014; Dal Ferro & Morari, 2015; Bourke et al, 2016; Gomez at al., 2019). On the other hand, soils have been also used as printing materials, for artistic scopes, for the preparation of samples for laboratory testing (Hanaor et al., 2015; Matsumura & Mizutani, 2015; Mansoori et al., 2018; Pua et al., 2018; Pua & Caicedo, 2020), or even for the construction of structures and infrastructures (Khoshnevis, 2004; Perrot et al., 2018).

In a printing process, the soil exits from the printer as filaments along prescribed paths; the result is a volume consisting of successive layers of adjacent soil filaments. The fabric of the printed soil is then the result of the initial microstructural characteristics of the filament, of the relative position of the adjacent filaments, and of all possible hydro-mechanical loads happening in the process (e.g increase of total stress as the layers overlap, or variations in water content due to exposure to hygroscopic conditions).

There is strong evidence on the fundamental role of the fabric of clayey soils on their hydro-mechanical response (e.g. Romero & Simms, 2008; Muñoz-Castelblanco et al., 2012; Cordão Neto et al., 2018; Ferrari et al., 2022). This link seems highly relevant for a 3D-printed soil, in which the fabric can be seen as a controlled result of the printing process. In this regard, this note presents the results of a microstructural investigation carried out on 3D-printed soil samples prepared with a commercial 3D-printer, specifically adapted to be used with a fine soil. The different microstructural peculiarities of the as-printed samples are identified and discussed thanks to the combined use of Scanning Electron Microscope (*SEM*) and Mercury Intrusion Porosimetry (*MIP*).

2. Material and methods

A commercial clayey soil used for artistic purposes was used as printing material; the geotechnical characteristics are listed in Table 1. Starting from the as-received condition, the soil was accurately mixed with distilled water to reach a consistency index *CI* close to 0.5 (corresponding target water content $w = 0.32$), which ensured adequate workability and limited the occlusion of air bubbles in the soil during the printing process.

A *Delta-WASP2040-Clay-Printer* has been used to prepare the samples. The printing system (Figure 1a) includes a 3-liter air-tight tank, in which an air-pressurized ram moves the soil toward the extruder; this latter holds an endless screw connected to a stepper motor. The rotation of the screw forces the extrusion of the soil filament through the nozzle. In this work a nozzle with a diameter of $d_n = 1.4$ mm was used. The air pressure in the tank was set to 600 kPa and maintained constant during the whole printing process. The printing velocity has been set equal to 180 mm/min.

The printer was programmed to print samples with a base of 75 mm x 75 mm and a height of 25 mm, obtained by the superposition of horizontal layers. As shown in Figure 1b,

#Corresponding author. E-mail address: marco.rosone@unipa.it
[1]University of Palermo, Department of Engineering, Palermo, Italy.
[2]Ecole Polytechnique Fédérale de Lausanne, Laboratory of Soil Mechanics, Lausanne, Switzerland.

Submitted on May 28, 2022; Final Acceptance on October 7, 2022; Discussions open until February 28, 2023.
https://doi.org/10.28927/SR.2022.005422

Table 1. Main geotechnical properties of the printed soil (specific gravity Gs, liquid limit LL, plastic limit PL, clay fraction fclay, silt fraction fsilt, sand fraction fsand).

Gs (-)	*LL* (-)	*PL* (-)	f_{clay} (%)	f_{silt} (%)	f_{sand} (%)
2.77	0.45	0.21	52	46	2

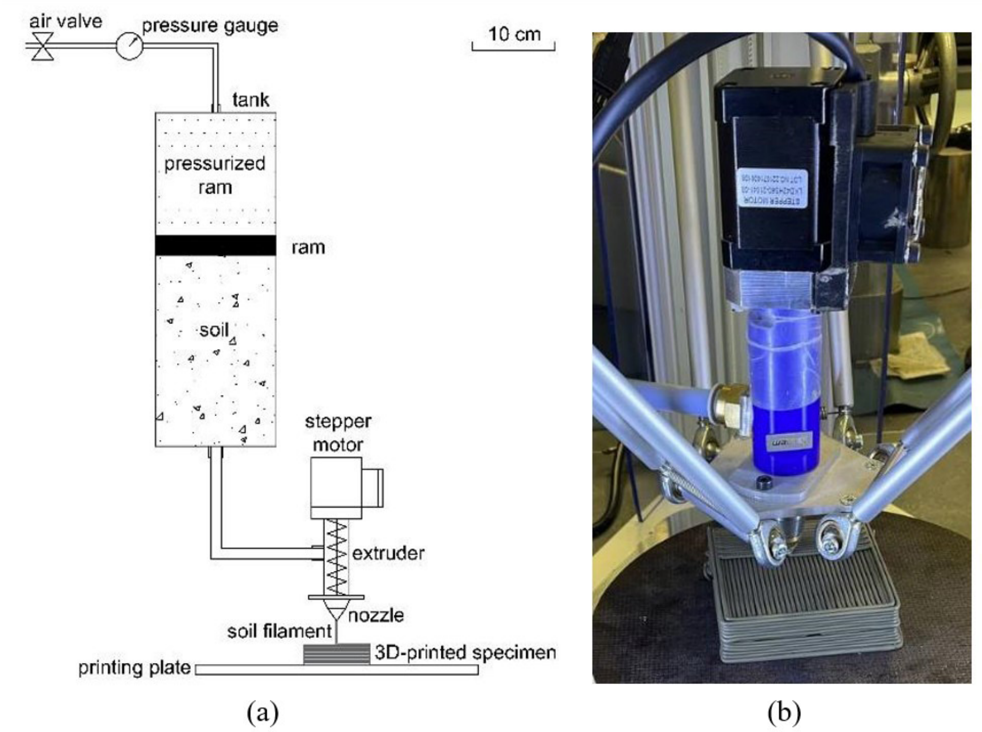

Figure 1. Schematic layout of the 3D soil printer (a) and photo of a sample being printed (b).

each layer was confined with two parallel filaments printed along the perimeter, while the internal part was filled with adjacent filaments extruded along the same direction; in each subsequent layer, the extruding direction was changed by 90 degrees.

Three samples were prepared to assess the repeatability of the printing procedure in terms of final sample characteristics (water content and void ratio). Cubical specimens of around 1 cm^3 were cut from the central part of two printed samples and used for the microstructural investigation.

Scanning Electron Microscope (*SEM*) observations and Mercury Intrusion Porosimetry (*MIP*) tests were carried out on the printed specimens after they were freeze-dried. This operation was done by submerging the specimens in liquid nitrogen (thus creating amorphous ice and avoiding the water volume to increase due to crystallization) and by subsequent sublimation in quasi-vacuum (P = 0.06 mbar) and under low temperature (T = -52°C).

A *Quanta-200-FEG* SEM was used for the observations in high-vacuum mode on golden-coated specimens. *MIP* tests were performed using a porosimeter (*Pascal 140–440 series, Thermo Scientific*) attaining a maximum intrusion pressure of 400 MPa, corresponding to an entrance pore diameter of about 4 nm. An extrusion stage was also performed after the mercury intrusion.

3. Fabric of the printed samples

Water contents of the printed samples were found in a narrow range with an average value of 0.30, slightly lower than the preparation water content, as a probable consequence of a partial consolidation induced by the stress applied through the row, and some drying due to the exposure to atmosphere (measured total suction of as-printed samples was about 0.3 MPa). In spite of some variability in as-printed void ratio (e = 1.07 ± 0.07), the applied 3D-printing procedure was considered adequate to produce samples with similar characteristics. The average degree of saturation was 0.73.

To observe the fabric of the 3D-printed samples, the external surface (top and lateral) and the vertical cross-section of the extracted specimens were observed at *SEM* (Figure 2).

The top surface of the specimen and its cross section are framed at 60X of magnification in Figure 2a and 2b, respectively. In particular, Figure 2a shows a zone of the top surface, where an inversion of the printing direction occurred. At this magnification, the soil filaments appear

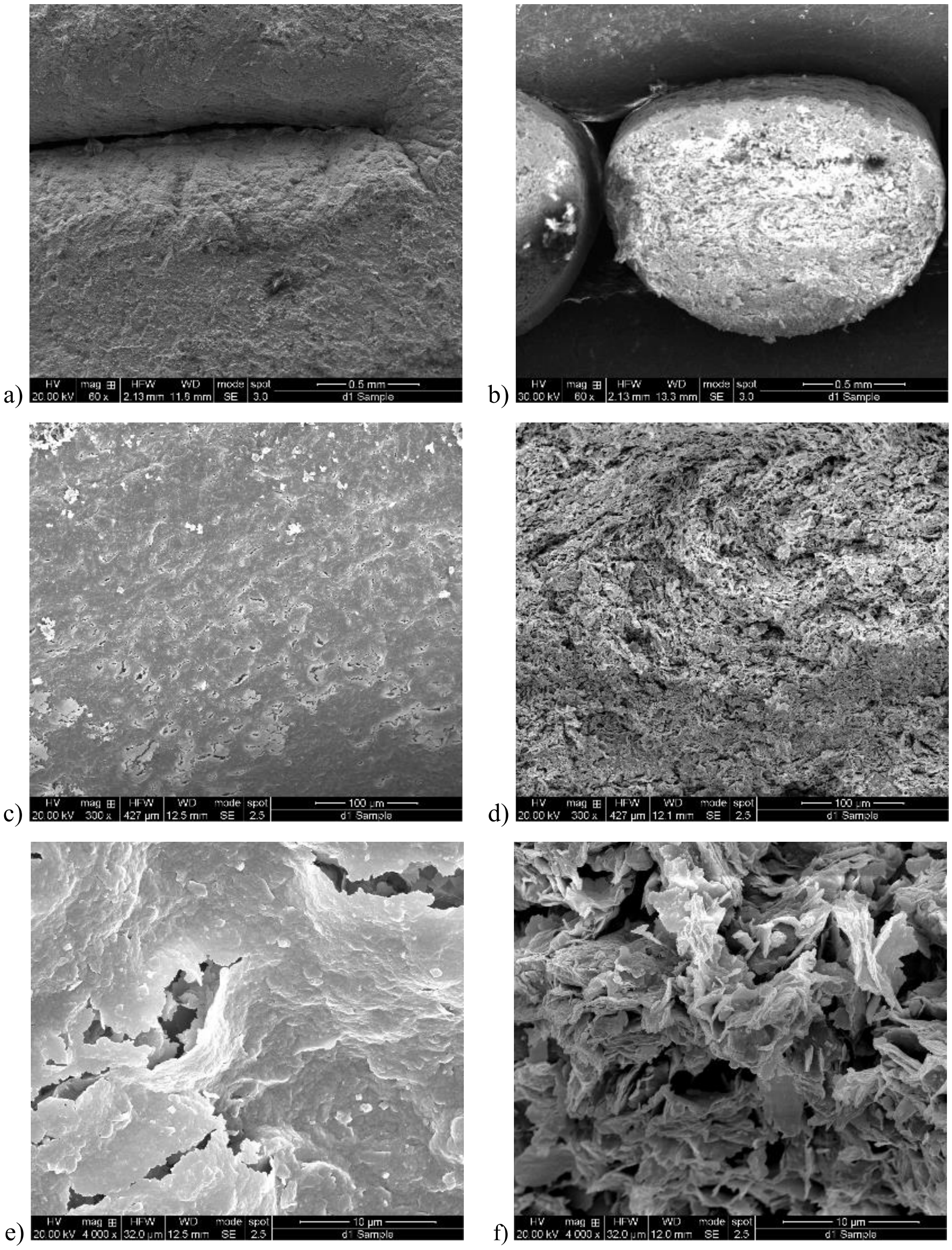

Figure 2. SEM photomicrographs of the 3D-printed soil: external surface (top in a, lateral in c and e) and vertical cross section (b, d and f). Magnifications are 60X (a, b), 300X (c, d) and 4000X (e, f).

homogeneous. Figure 2b shows the result of the superposition of the filaments: a certain ovalization in the cross-section of the filament can be detected, as a probable result of the weight of the above layers. Interestingly, the area of the cross section of the filament coincides with the area of the circle having the diameter of the nozzle (d_n = 1.4 mm), suggesting that the deposition of the filament occurs in undrained conditions, without volume change. As a consequence of this ovalization, a good contact is observed when two filaments overlap, while an inflection is produced in the void space among adjacent filaments. Voids between the soil filaments have an average equivalent diameter of 150 μm and they represent the macropores (inter-filament pores) of the 3D-printed soil.

At 300X, the external surface of the filament (Figure 2c) shows a smooth and compact particle arrangement, with iso-oriented clay particles and few pores 0.3÷1.5 μm wide and 3÷30 μm long. On the microphotograph of the cross-section of the filament at 300X (Figure 2d), a spiral trend of the particles orientation can be observed, as a result of the rotative movement of the screw in the extruder. Pores having a maximum diameter of about 30 μm as well as pores 1-2 μm wide and 10÷70 μm long can be identified at the contacts between the clay aggregates (Figure 2d).

In the last microphotographs, taken with a 4000X magnification, different arrangements of the clayey particles are visible. Particles on the lateral surface (Figure 2e) are iso-oriented and arranged with face-to-face packing; the arrangement of the particles in the inner part of the filament (Figure 2f) is more complex showing aggregated structures with both face-to-face and edge-to-face contacts. At this magnification, inter-aggregate pores, having a dimension of few microns, and intra-aggregates pores of smaller dimensions (lower than 0.5 μm) are visible. It is worth to observe that where the clayey particles are packed with face-to-face contacts the intra-aggregates pores are smaller.

The results of MIP tests performed on two different specimens are reported in Figure 3a in terms of the intruded/extruded void ratio *(*e_i*,* the ratio of the void volume intruded by mercury ($V_{v,i}$) to the volume of soil particles (V_s)) and in Figure 3b in terms of the Pore Side Density *PSD* ($PSD = -\Delta e_i/\Delta(logd)$) as a function of the computed pore diameter d. The total void ratios intruded during the MIP tests (e_i = 0.838 and 0.898) were lower than the mean void ratio measured on the 3D-printed samples (e = 1.07).

This difference is believed to be the result of the pores larger than 120 μm which are filled with mercury before the injection starts, and which are not detected with the technique. This maximum detectable pore diameter well corresponds to the average diameter of the inter-filament pores (150 μm). The intruded void ratio is then attributed to the pores within the filaments only. The corresponding microstructural or intra-filament void ratio (e^m, ratio of the volume of intra-filament pores to the volume of the solid phase) is then quantified in the range of e^m = 0.838÷0.898. The lower bound of macropores, which corresponds to the gaps left by the printing process between the filament, is set to 120 μm (Figure 3).

On the other hand, an analytical evaluation for the macrostructural or inter-filament void ratio (e^M, ratio of the volume of inter-filament pores to the volume of the solid phase) based on geometrical considerations allows to compute a value e^M = 0.274. The sum of the microstructural and macrostructural void ratios is in good agreement with the average void ratio of the 3D-printed samples (Figure 3a, right axis).

The main modal diameter of pores (d = 1 μm, Figure 3b) corresponds both to the pores observed along the external surface of soil filament and to the pores between clayey aggregates observed in the cross-section. According to the procedure proposed by Delage & Lefebvre (1984) intra-assemblage porosity results in a reversible behaviour during the intrusion/extrusion phases, while mercury is trapped by capillary effects in the bigger pores once the applied pressure is removed (Figure 3a). This criterion applied to the two

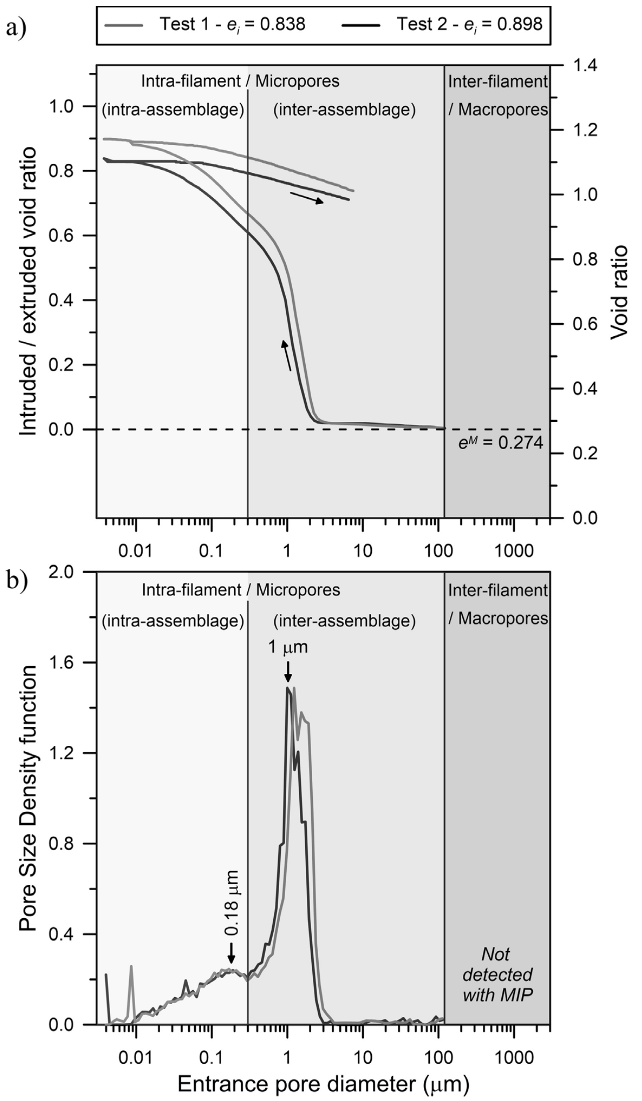

Figure 3. Void ratio (a) and Pore Size Density (b) as a function of the Entrance Pore Diameter from MIP tests.

tests performed could provide the upper bound value of the intra-assemblage as d = 0.127 μm. These micropores include the porosity between clayey particles stacked in face-to-face disposition. However, the criterion based on intrusion and extrusion curves could underestimate the limit value (Yuan et al., 2020). In fact, a secondary peak of *PSD* can be identified in the same range of micropores (d = 0.18 μm). This class of micropores corresponds to the intra-assemblage pores located between particles stacked in face-to-edge disposition (Figure 3f). Then, on the base of *PSD* evolution (Figure 3b) a more consistent upper limit for the intra-assemblage pores domain can be identified at d = 0.3 μm.

4. Conclusion

The note explored the fabric of a 3D-printed clayey soil, highlighting how the particle arrangements and size, orientation and shape of pores are strongly linked to the printing operation. In particular, it was observed that the macropores are the result of the relative position of the filaments and their initial distortion in quasi-undrained conditions. Particle arrangement within the soil filament is strongly anisotropic due to the rotative movement of the soil in the extruder. Moreover, intra-assemblage pores, located in between the clayey assemblages, and intra-assemblage pores, as the results of different particle contacts (both face-to-face and edge-to-face contacts), characterize the microporosity in the intra-filament soil structure.

It is believed that these observations could pose the basis for engineering the creation of fabric-controlled samples; this capability could serve multiple purposes, such as the production of samples with precise hydro-mechanical characteristics, e.g. permeability and water retention properties.

Declaration of interest

The authors have no conflicts of interest to declare. All co-authors have observed and affirmed the contents of the paper and there is no financial interest to report.

Authors' contributions

Alessio Ferrari: conceptualization, funding acquisition, methodology, supervision, writing, validation. Marco Rosone: conceptualization, methodology, data analysis, writing – original draft. Silvia La Rosa: investigation, formal analysis, writing. Giovanni Sapienza: investigation.

List of symbols

CI consistency index;
d entrance pore diameter in MIP test;
d_n diameter of the nozzle;
e void ratio;
e_i intruded/extruded void ratio in MIP test;
e^m ratio of the volume of intra-filament pores to the volume of the solid phase;
e^M ratio of the volume of inter-filament pores to the volume of the solid phase;
f_{clay} clay fraction;
f_{sand} silt fraction;
f_{silt} silt fraction;
G_s specific gravity;
LL liquid limit;
MIP Mercury Intrusion Porosimetry;
P absolute pressure;
PL plastic limit,
PSD Pore Size Density function from *MIP* test;
SEM Scanning Electron Microscope
T temperature;
V_s volume of soil particles;
$V_{v,i}$ void volume intruded by mercury in *MIP* test;
w water content.

References

Bourke, M.C., Viles, H.A., Nicoli, J., Lyew-Ayee, P., Ghent, R., & Holmlund, J. (2016). Innovative applications of laser scanning and rapid prototype printing to rock breakdown experiments. *Earth Surface Processes and Landforms*, 33, 1614-1621.

Cordão Neto, M.P., Hernandez, O., Reinaledo, R.L., Borges, C., & Caicedo, B. (2018). Study of the relationship between the hydromechanical soil behavior and microstructure of a structured soil. *Earth Sciences Research Journal*, 22(2), 91-101.

Dal Ferro, N., & Morari, F. (2015). From real soils to 3D-printed soils: reproduction of complex pore network at the real size in a silty-loam soil. *Soil Science Society of America Journal*, 79(4), 1008-1017.

Delage, P., & Lefebvre, G. (1984). Study of the structure of a sensitive champlain clay and of its evolution during consolidation. *Canadian Geotechnical Journal*, 21, 21-23.

Ferrari, A., Bosch, J.A., Baryla, P., & Rosone, M. (2022). Volume change response and fabric evolution of granular MX80 bentonite along different hydro-mechanical stress paths. *Acta Geotechnica*, 17, 3719-3730. http://dx.doi.org/10.1007/s11440-022-01481-0.

Gomez, J.S., Chalaturnyk, R.J., & Zambrano-Narvaez, G. (2019). Experimental investigation of the mechanical behavior and permeability of 3D printed sandstone analogues under triaxial conditions. *Transport in Porous Media*, 129, 541-557.

Hanaor, D.A.H., Gan, Y., Revay, M., Airey, D.W., & Einav, I. (2015). 3D printable geomaterials. *Geotechnique*, 66(4), 323-332.

Ju, Y., Xie, H., Zheng, Z., Lu, J., Mao, L., Gao, F., & Peng, R. (2014). Visualization of the complex structure and stress field inside rock by means of 3D printing technology. *Chinese Science Bulletin*, 59(36), 5354-5365.

Khoshnevis, B. (2004). Automated construction by contour crafting – related robotics and information technology. *Automation in Construction*, 13, 5-19.

Mansoori, M., Kalantar, N., & Palmer, W. (2018). Handmade by machine: a study on layered paste deposition methods in 3D printing geometric sculptures. In *Proceedings of the Conference Fabrication and Sculpting Event (FASE) 2018*, Instituto Superior Técnico, Lisbon, Portugal, June 6-8.

Matsumura, S., & Mizutani, T. (2015). 3D printing of soil structure for evaluation of mechanical behavior. Acta Stereologica. In *Proceeding of the 14th International Congress for Stereology and Image Analysis*, Liège, Belgium, July 6-10.

Muñoz-Castelblanco, J.A., Pereira, J.M., Delage, P., & Cui, Y.J. (2012). The water retention properties of a natural unsaturated loess from northern France. *Géotechnique*, 62(2), 95-106.

Perrot, A., Rangeard, D., & Courteille, E. (2018). 3D printing of earth-based materials: processing aspects. *Construction & Building Materials*, 17, 670-676.

Pua, L.M., & Caicedo, B. (2020). Reproducing the inherent variability of soils using a three-dimensional printer. *International Journal of Physical Modelling in Geotechnics*, 21(6), 295-313.

Pua, L.M., Caicedo, B., Castillo, D., & Caro, S. (2018). Development of a 3D clay printer for the preparation of heterogeneous models. In A. McNamara, S. Divall, R. Goodey, N. Taylor, S. Stallebrass & J. Panchal (Eds.), *Physical modelling in geotechnics* (pp. 155-160). CRC Press.

Romero, E., & Simms, P.H. (2008). Microstructure investigation in unsaturated soils: a review with special attention to contribution of mercury intrusion porosimetry and environmental scanning electron microscopy. *Geotechnical and Geological Engineering*, 26, 705-727.

Yuan, S., Liu, X., Romero, E., Delage, P., & Buzzi, O. (2020). Discussion on the separation of macropores and micropores in a compacted expansive clay. *Géotechnique Letters*, 10(3), 454-460.

Soils and Rocks
An International Journal of Geotechnical and Geoenvironmental Engineering
www.soilsandrocks.com
ISSN 1980-9743
ISSN-e 2675-5475

Geomechanical parameters in the active zone of an unsaturated tropical soil site via laboratory tests

Jeferson Brito Fernandes[1], Alfredo Lopes Saab[1], Breno Padovezi Rocha[2#], Roger Augusto Rodrigues[1], Paulo César Lodi[1], Heraldo Luiz Giacheti[1]

Article

Keywords
Unsaturated soil
Suction
Triaxial compression test
Bender elements
Oedometer test

Abstract

The seasonal variability of geotechnical parameters in the unsaturated zone is typically neglected in the design of geotechnical works. In most of the geotechnical projects the parameters are determined only for the saturated condition. Although it is known that this condition is the most critical to soil strength and deformability, this conservative approach may neglect a possible important contribution of the unsaturated condition, resulting in an increase in the cost of the geotechnical solution. This paper presents and discusses the site characterization of the active zone of an unsaturated sandy soil profile under different suction conditions. Laboratory tests with controlled suction (retention curves, triaxial compression with bender elements and oedometer tests) were carried out on undisturbed samples collected from 1.0 to 5.0 m depth. The results show that strength and deformability parameters are strongly affected by soil suction and are less influenced by confinement stress up to 5.0 m depth. All the investigated subsoil profile shows a collapsible behavior, more pronounced closer to the ground surface and under the effect of higher suction values. The findings highlight the importance of incorporating the suction influence in the site investigation, parameter determination, and geotechnical design for more economical, reliable, and environmentally sustainable solutions.

1. Introduction

Urban growth contributes to an increase in regional temperatures, alters the rainfall regime, and causes local extreme events and natural disasters. Southeastern Brazil is one of the regions where there is a greater tendency for precipitation increase, while in the Northeast there is drought. It is important to advance the understanding of the geomechanical behavior of soils in tropical and subtropical climatic environments by studying key aspects that are not yet well understood, such as the impact of the unsaturated state on the laboratory and in situ determination of the geomechanical properties of these soils (Vilar & Rodrigues, 2011; Zhang et al., 2014; Zhang, 2016). This aspect is also important in the design of infrastructure works with emphasis on the seasonal variability that may occur (Fernandes, 2016; Dong et al., 2018; Silva et al., 2019).

The behavior of unsaturated soils depends on the moisture content and consequently on the soil suction. Changes in the moisture content and suction in an unsaturated soil can occur due to climate variations (Blight, 2003; Cui et al., 2005). It is important to know the soil properties through direct in situ or laboratory measurements in the geotechnical design practice. The time of year when a particular unsaturated soil site is investigated can have a strong influence mainly on the in-situ test data (Giacheti et al., 2019; Rocha et al., 2021).

The depth of the subsoil to which changes in moisture content take place is referred to as the active zone. The active zone is generally defined as the region of fluctuation in moisture content of an unsaturated soil, which can change seasonally due to climatic variations (Fredlund, 2006). Significant soil deformation or movement can occur due to variations in soil moisture/energy in this zone. It is important to note that varying soil suction affects the behavior of collapsible and expansive unsaturated soils. Lightweight structures such as highways and railroads (Sánchez et al., 2014) or small buildings are often subject to severe damage due to wetting of a collapsible or expansive soil. Abrupt and significant settlements in geotechnical structures are common in collapsible soils after flooding (Jennings & Knight, 1975; Vilar & Rodrigues, 2011). Cut slopes (Tsiampousi et al., 2017) and infinite slopes (Ray et al., 2010; Zhang et al., 2014) are

#Corresponding author. E-mail address: breno.rocha@ifsp.edu.br.
[1] Universidade Estadual Paulista "Júlio de Mesquita Filho", Faculdade de Engenharia, Departamento de Engenharia Civil e Ambiental, Bauru, SP, Brasil.
[2] Instituto Federal de São Paulo, Ilha Solteira, SP, Brasil.

Submitted on January 9, 2022; Final Acceptance on October 4, 2022; Discussion open until February 28, 2023.
https://doi.org/10.28927/SR.2022.000422

prone to rupture or may experience irreversible movement due to changes in negative soil and water pressures. Therefore, seasonal variability can lead to complex and often costly assessment of unsaturated soil properties, from a practical point of view. However, even today, geotechnical designs rely almost exclusively on data obtained through short-term site investigation programs.

The conventional laboratory tests, i.e., those that are performed without any soil suction control, generally do not adequately consider the transient condition of moisture content. Modern laboratory testing options are available (Delage et al., 2008) to consider the suction influence on soil behavior. It is important to recognize the significant progress that suction control has brought to the understanding of unsaturated soils, especially Hilf's (1956) axis translation technique.

Some researchers in recent decades have proposed ways to interpret laboratory test data on unsaturated soils. It has been usual to consider two independent stress state variables (suction and net stress) over a wide suction range (Fredlund & Morgenstern, 1977; Toll, 1990). It can range from 0 to 500 kPa for most geotechnical engineering problems, according to (Khalili & Khabbaz, 1998; Vanapalli et al., 1996). Fredlund et al. (1978) and Ho & Fredlund (1982) extended the Mohr-Coulomb criterion for unsaturated soils using state variables by defining failure surfaces assumed as planar and represented by friction angles ϕ' and ϕ^{B}.

Escario & Sáez (1986) found the non-linearity of ϕ^{B} from the interpretation of experimental data and it prompted some researchers to propose empirical models to represent the total cohesion intercept (e.g., Vanapalli et al., 1996; Vilar, 2006). The failure envelopes of unsaturated soils can be determined in laboratory via triaxial compression tests with controlled suction (Fredlund et al., 1978; Khalili & Khabbaz, 1998; Vanapalli et al., 1996; Zhang, 2016). The drainage conditions in the consolidation and shear phase can be different depending on the type of triaxial test performed.

Modern triaxial compression testing devices allow to use equipment for the direct measurement of load and displacement of soil specimens within the triaxial cells. Bender elements have also been used to measure shear wave velocities (V_s) with deformations in the order of 10^{-4} to $10^{-6\%}$. Therefore, theory of elasticity is valid to determine the maximum shear modulus (G_0):

$$G_0 = \rho \, .Vs^2 \tag{1}$$

G_0 is a reference geotechnical parameter to be considered in the site characterization for geotechnical design (Jamiolkowski, 2012; Rocha et al., 2022). The triaxial compression test system equipped with bender elements allow to verify the quality of specimen (Ferreira et al., 2011). It also allows determining the variation of G_0 with the confining net stress, void ratio, soil suction, and over consolidation ratio (Dong et al., 2018; Dong & Lu, 2016; Georgetti, 2014; Hardin & Blandford, 1989; Hoyos et al., 2015; Leong & Cheng, 2016; Nyunt et al., 2011).

The compressibility parameters are also important in a proper site characterization program, especially for foundation settlements prediction (Skempton & Jones, 1944; Lambe & Whitman, 1976). The compressibility of unsaturated soils, mainly the collapsible ones, is more complex and difficult to predict since suction changes can induce significant variation in compressibility parameters such as the over consolidation stress and the compression index.

Jennings & Knight (1975) proposed the use of single and double oedometer tests since many unsaturated soils present collapsible behavior. Sun et al. (2007) conducted suction-controlled tests on a compacted clay to study the influence of different dry unit weight and suction values on the collapse behavior for both isotropic and anisotropic stress states. Vilar & Rodrigues (2011) carried out suction-controlled tests on an undisturbed clayey sand to study the soil collapsibility with the gradual reduction of suction upon vertical stresses.

The main research goal in the recent years has been to understand the behavior of unsaturated soils extending the concepts of the Critical States Soil Mechanics (Alonso et al., 1990). Research has been based on experimental data in which the axis translation technique is used mainly as a tool to understand the hydraulic and mechanical behavior of unsaturated soils. So, controlled suction laboratory tests are essential to understand the unsaturated soil behavior and its seasonal variability in the active zone of the soil profile.

This paper presents and discusses the characterization via laboratory tests of the active zone of an unsaturated tropical sandy soil profile under different suction conditions. The main contribution is to highlight the importance of incorporating the suction influence on determining soil parameters and considering it in the geotechnical engineering design as well as to expand the database of geotechnical parameters in a typical unsaturated tropical soil.

2. Materials and methods

2.1 Study site

The study site is the experimental research area (Lat.: S 22º05' to S 22º26'; Long.: W 49º00'to W 49º16') from the São Paulo State University, in Bauru, São Paulo, Brazil. The geology consists predominantly of sediments from Bauru Group (Marília and Adamantina Formations), covering the volcanic rocks of Serra Geral Formation that outcrop towards the Valley of the Tietê River. De Mio (2005) describes these soils as being formed mainly by deposits of colluvial origin submitted to tropical weathering process, resulting in porous and collapsible soils.

Figure 1 shows some index properties and grain size distribution (with and without dispersant) up to 6 m depth. The soil is classified as clayey sand and the grain size distribution is relatively uniform. The dry unit weight (γ_d) and unit weight of solids (γ_s = 26.8 kN/m³) are practically

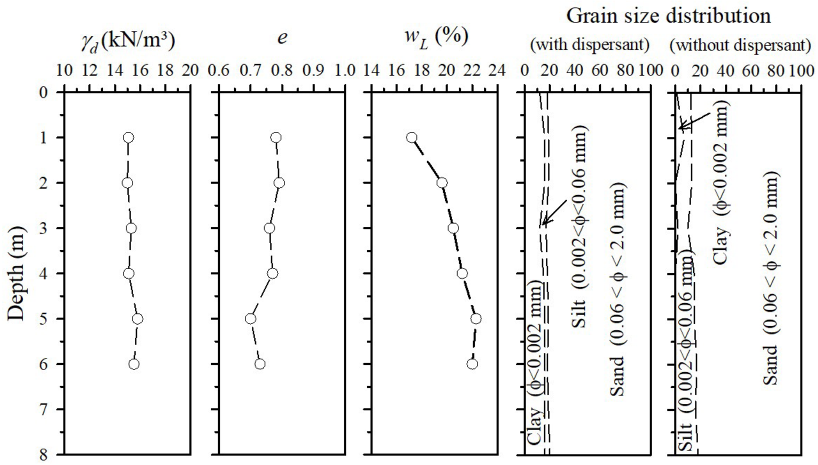

Figure 1. Grain size distribution and index properties [adapted from Giacheti et al. (2019)].

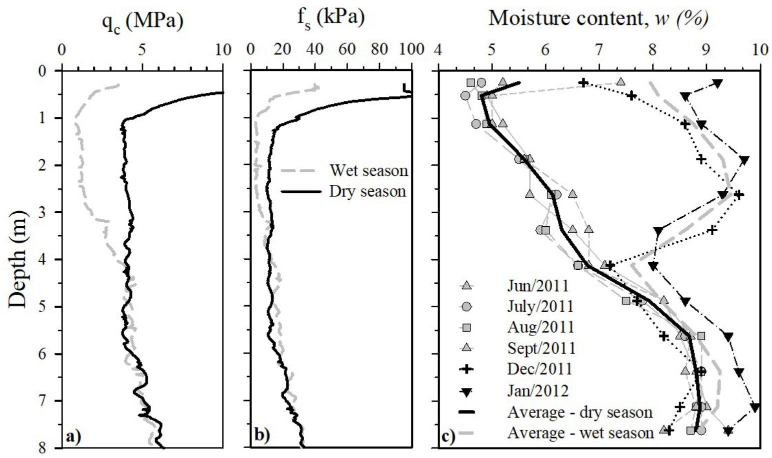

Figure 2. Wet and dry seasons profiles: (a) and (b) average CPT data; (c) moisture content data [adapted from Giacheti et al. (2019)].

constant with depth. The void ratio (*e*) at 1.0 m depth is equal to 0.78 and it is also almost constant up to 4 m depth and drops to about 0.70 at 5 and 6 m depth. The liquid limit at 1.0 m depth (w_L) is 17% and tends to increase with depth. The fine portion of the soil is non-plastic (plastic limit - w_P, cannot be determined) and has iron and aluminum oxides, hydroxides, and kaolinite. It is classified as SM Group soil in the Unified Soil Classification System (ASTM, 2017).

The study site has a tropical climate with well-defined wet and dry seasons. The Cone and the Piezocone Penetration Tests (CPT and CPTu) can be used as a high profiling resolution technique to assess site stratigraphy and variability (De Mio & Giacheti, 2007). Giacheti et al. (2019) investigated the seasonal influence on the study site based on CPT campaigns carried out in different season of the year. The tests were carried out in a wooded area with some *Caesalpinia peltophoroides Benth*, commonly referred as "*Sibipirunas*". The trees are likely to have a system of lateral roots and one large tap root and affected the seasonal variability.

The role of suction on soil behavior can be observed in Figure 2a, 2b since the seasonal variation has significantly influenced the CPT data up to about 4 to 5 m depth. The monitoring of the moisture content profiles (Figure 2c) indicates that a high variation occurs closer to the ground surface, and it decreases with depth.

2.2 Laboratory tests

Soil blocks were retrieved from exploratory sampling pits to get disturbed and undisturbed samples following ABNT (1986). Laboratory tests for soil characterization (physical indexes, grain size distribution and Atterberg limits) were carried out every meter interval up to 5 m depth. Soil water retention curves were determined under drying trajectory by using the filter paper technique, suction plate, and pressure plate tests. The specimens were obtained from quasi-static driving of beveled PVC rings (53 mm in diameter and 12 mm high) on undisturbed samples collected at 1.0, 3.0 and 5.0 m depth. The specimens were saturated with distilled and de-aerated water. The filter paper *Whatman* nº 42 and the calibration of Chandler & Gutierrez (1986) and Chandler et al. (1992) were used to determine the experimental data points by the filter paper method following the procedures suggested by Marinho & Oliveira (2006). The equation proposed by van Genuchten (1980) was used to adjust experimental datapoints obtained by different methods.

Soil shear strength was determined through saturated and unsaturated consolidated drained triaxial compression tests (CD type) with an axial strain rate of 0.05%/min to endure dissipation of the excess pore water pressure during all tests. Specimens 50 mm in diameter by 100 mm in height were carved from undisturbed soil samples collected at 1.5, 3.0, and 5.0 m depth by an exploratory sample pit. The experimental test program was designed to ensure the integrity of specimens, as well as the quality of the collected samples. The soil suction values were 0, 50, 200, and 400 kPa and the net normal stresses were 50, 100 and 200 kPa. The saturation (zero suction) was achieved applying back pressure up to a pore-pressure coefficient B ≥ 0.95. Table 1 presents the index properties of the samples before and after saturated and unsaturated triaxial tests.

The suction values were installed in the unsaturated specimens and maintained through Hilf (1956) axis-translation technique by means of a 500 kPa air entry value porous plate. The pore-air pressure was elevated above atmospheric pressure such that pore-water pressure becomes positive (Hilf, 1956; Fredlund, 2006). The failure envelopes Fredlund et al. (1978) were determined for each investigated depth to obtain friction angle and the cohesion intercept (Vilar, 2006).

The maximum shear modulus (G_0) was determined in a triaxial chamber equipped with bender elements. The specimens were carved from the undisturbed samples collected at 1.5, 3.0, and 5.0 m depths. The suction levels were 0, 50, 200 and 400 kPa and isotropic state stresses were 25, 50, 100 and 200 kPa. The shear wave velocity (V_s) was determined by the first time of arrival method, after the specimen consolidation (Fernandes, 2016). The G_0 variations as a function of soil suction and net normal stress were determined for each tested depth.

Table 1. Index properties for the soil samples before and after the triaxial tests.

Depth (m)	Net normal stress (kPa)	Index properties	Soil suction, s (kPa)							
			0		50		200		400	
			Before	After	Before	After	Before	After	Before	After
1.5	50	e	0.689	0.584	0.710	0.599	0.761	0.705	0.788	0.759
		w (%)	5.10	20.12	6.05	7.00	5.94	6.17	5.65	5.69
		γ_d (kN/m^3)	15.96	17.02	15.77	16.86	15.31	15.82	15.08	15.32
	100	e	0.717	0.579	0.749	0.574	0.769	0.668	0.776	0.714
		w (%)	5.82	18.24	5.64	7.05	5.94	6.12	5.79	5.65
		γ_d (kN/m^3)	15.70	17.07	15.41	17.13	15.24	16.16	15.18	15.73
	200	e	0.703	0.409	0.711	0.532	0.781	0.628	0.807	0.608
		w (%)	5.71	19.36	5.90	7.15	5.42	6.07	5.92	*
		γ_d (kN/m^3)	15.83	18.09	15.76	17.61	15.14	16.56	14.92	16.76
3.0	50	e	0.814	0.665	0.742	0.690	0.741	0.706	0.726	0.709
		w (%)	8.35	*	8.31	*	7.88	6.97	7.25	6.43
		γ_d (kN/m^3)	14.79	16.11	15.40	15.88	15.41	15.73	15.54	15.70
	100	e	0.740	0.566	0.748	0.641	0.734	0.665	0.770	0.703
		w (%)	8.08	*	8.29	*	8.62	6.59	8.64	6.55
		γ_d (kN/m^3)	15.42	17.13	15.35	16.35	15.47	16.12	15.16	15.76
	200	e	0.753	0.534	0.745	0.653	0.733	0.605	0.791	0.608
		w (%)	8.61	*	7.85	*	7.61	6.31	9.19	7.07
		γ_d (kN/m^3)	15.31	17.49	15.38	16.24	15.48	16.72	14.98	16.68
5.0	50	e	0.717	0.605	0.674	0.654	0.688	0.671	0.702	0.678
		w (%)	10.23	*	10.27	7.93	9.12	7.78	9.84	7.23
		γ_d (kN/m^3)	15.67	16.76	16.07	16.26	15.94	16.10	15.80	16.03
	100	e	0.684	0.532	0.697	0.598	0.692	0.646	0.697	0.663
		w (%)	10.54	*	10.22	8.10	8.93	7.11	9.01	7.15
		γ_d (kN/m^3)	15.97	17.55	15.85	16.83	15.90	16.34	15.85	16.18
	200	e	0.712	0.537	0.707	0.621	0.704	0.602	0.686	0.607
		w (%)	10.31	*	10.05	8.25	9.98	7.18	9.86	6.98
		γ_d (kN/m^3)	15.71	17.50	15.76	16.59	15.79	16.79	15.95	16.74

*Not determined.

Conventional and controlled-suction oedometer tests were performed using oedometer-type chambers like the one developed by Escario & Sáez (1986). The compressibility parameters for the undisturbed soil samples collected at 1.0, 2.0, 3.0, 4.0 and 5.0 m depth were determined under different suction values (0, 50, 100, 200 and 400 kPa).

The specimens were retrieved from a quasi-static driving of a metal ring of 70 mm diameter and 25 mm high. They were inundated with distillated and deaired water and installed on high air-entry porous plate at the base of the oedometer-type chambers. The specimens were subjected to air pressure inside the chamber, which allowed the imposition of suction through axis-translation technique of Hilf (1956). A total of 25 confined compression curves were determined for 5 different soil suction values (0, 50, 100, 200 and 400 kPa) and for each test depth (from 1.0 to 5.0 m). Table 2 presents the index properties of the samples before and after oedometer tests.

3. Analysis and results

3.1 Soil water retention curve

Figure 3 shows the experimental data, in terms of gravimetric moisture content (w) and soil suction (s), as well as the best curves fitted for 1.0, 3.0 and 5.0 m depth samples. All the curves are typical of sandy soils with low water retention (Fredlund & Xing, 1994). They are bimodal with four zones: a boundary effect zone, two transition zones and a residual zone (Vanapalli et al., 1996). The boundary effect zone is short, from 0 to 2 kPa in which the soil is saturated by capillarity. The transition zones start from the point of the first air entry value (AEV), about 2 kPa, ending at the residual moisture, around 2%. As the suction increases the moisture decreases significantly in the transition zones. Values of soil suction higher than the first air entry value (about 2 kPa) and lower than the second air entry value (about 1 MPa), indicate that the macropores and soil micropores are respectively unsaturated and saturated. The water in the micropores begins to drain significantly for suction values between the second air entry value and the residual moisture content. A large variation on suction causes a little change in moisture content in the residual zone. The soil pores are occupied mainly by air and the liquid phase is discontinuous in this zone.

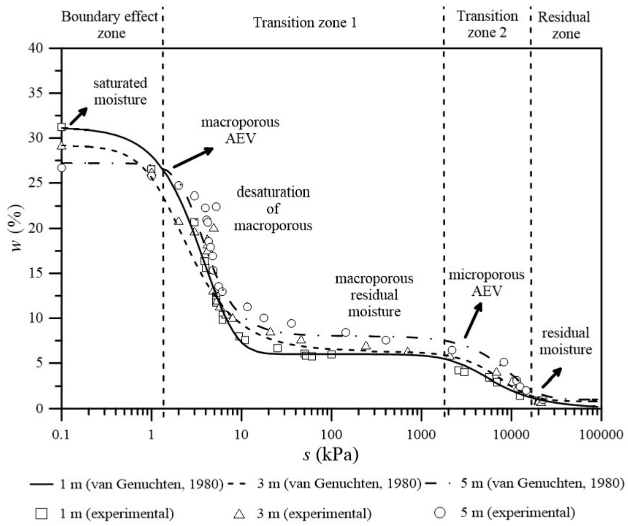

Figure 3. Soil water retention curves for the collect soil samples.

Table 2. Index properties for the soil samples before and after the oedometer tests.

Depth (m)	Index properties	Soil suction, s (kPa)									
		0		50		100		200		400	
		Before	After	Before	After	Before	After	Before	After	Before	After
1.0	e	0.849	0.477	0.856	0.554	0.853	0.544	0.841	0.587	0.811	0.612
	w (%)	8.06	18.21	7.87	7.16	7.87	6.89	7.89	6.15	8.15	5.94
	γ_d (kN/m^3)	14.58	18.25	14.53	17.35	14.55	17.46	14.64	16.99	14.89	16.72
2.0	e	0.871	0.500	0.889	0.569	0.959	0.586	0.907	0.619	0.806	0.610
	w (%)	9.3	19.35	9.30	8.27	9.53	7.83	9.65	7.28	9.65	7.19
	γ_d (kN/m^3)	14.60	17.89	14.24	17.18	13.73	17.00	14.11	16.65	14.89	16.75
3.0	e	0.838	0.500	0.776	0.523	0.769	0.528	0.663	0.519	0.744	0.545
	w (%)	7.57	19.9	9.07	8.46	9.07	7.34	9.11	7.05	9.11	6.95
	γ_d (kN/m^3)	14.60	17.89	15.11	17.62	15.17	17.56	16.13	17.66	15.39	17.37
4.0	e	0.816	0.497	0.827	0.544	0.794	0.551	0.732	0.560	0.791	0.607
	w (%)	8.74	21.04	9.10	8.48	9.10	8.21	8.76	7.33	8.76	7.16
	γ_d (kN/m^3)	14.81	17.97	14.72	17.42	14.99	17.34	15.53	17.24	15.02	16.74
5.0	e	0.765	0.496	0.703	0.504	0.718	0.542	0.730	0.555	0.737	0.565
	w (%)	10.25	18.36	10.30	9.19	10.11	8.19	10.15	7.79	9.83	7.61
	γ_d (kN/m^3)	15.24	18.02	15.80	17.93	15.66	17.48	15.55	17.34	15.49	17.23

3.2 Shear strength

Figures 4 show the triaxial compression tests data in terms of the variation of deviatoric stress *versus* axial strain and variation of volumetric strain *versus* axial strain.

There is no clear peak stress in the curves independently of the test depth and soil suction (Figure 4). After reaching a certain stress value, the strain increases almost continuously with no increase in stress. It shows a contractive behavior during shearing, as can be seen in the volumetric strain *versus* axial strain curves (Figure 4).

The interpretation of the data presented in Figure 4 indicates a slight increase of soil rigidity with increasing depth and soil suction, as can be seen in Figure 5 in terms of the secant

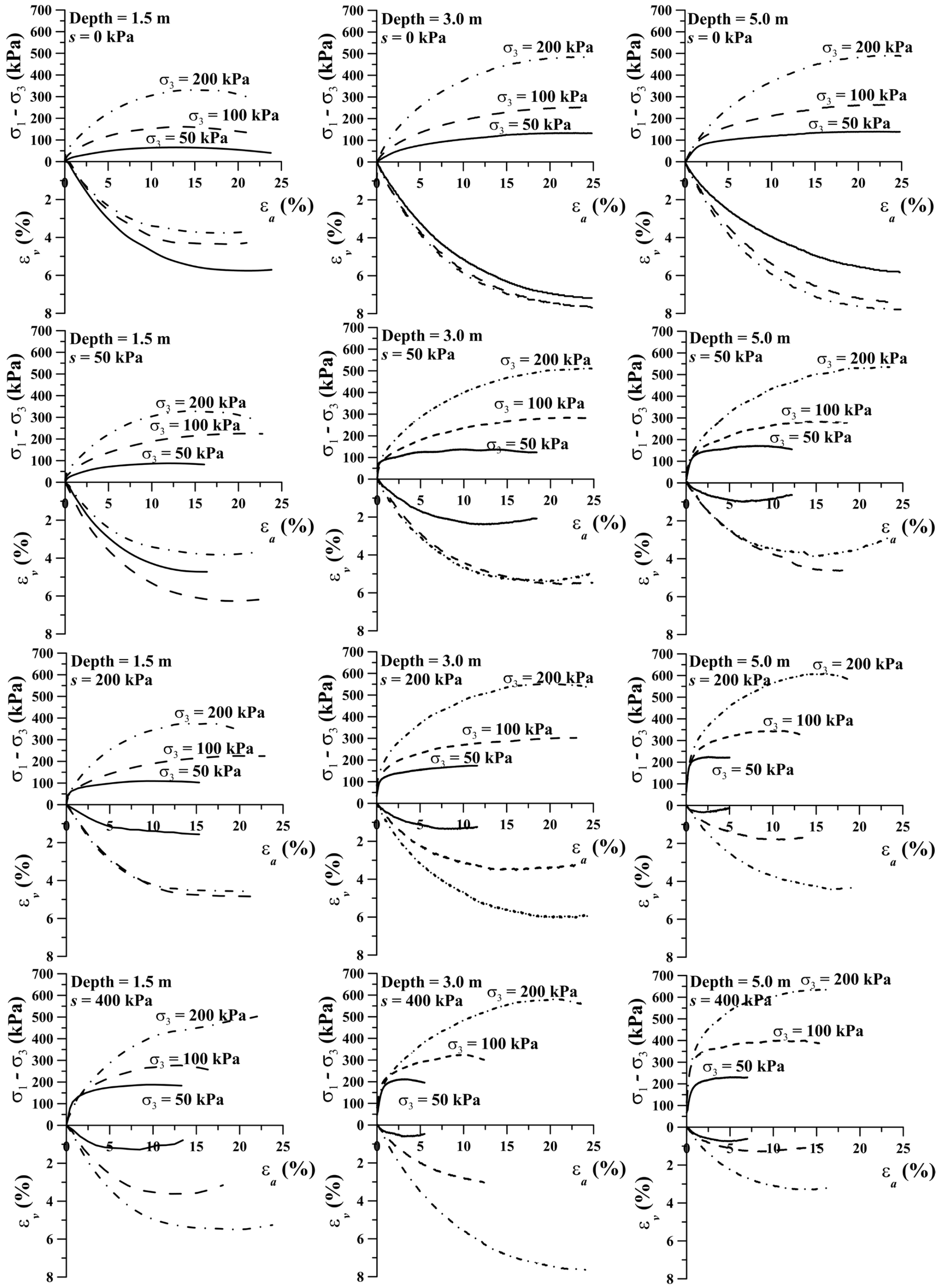

Figure 4. Variation of deviatoric stress *versus* axial strain and variation of volumetric strain *versus* axial strain for the triaxial compression tests. Data for different depths and soil suctions.

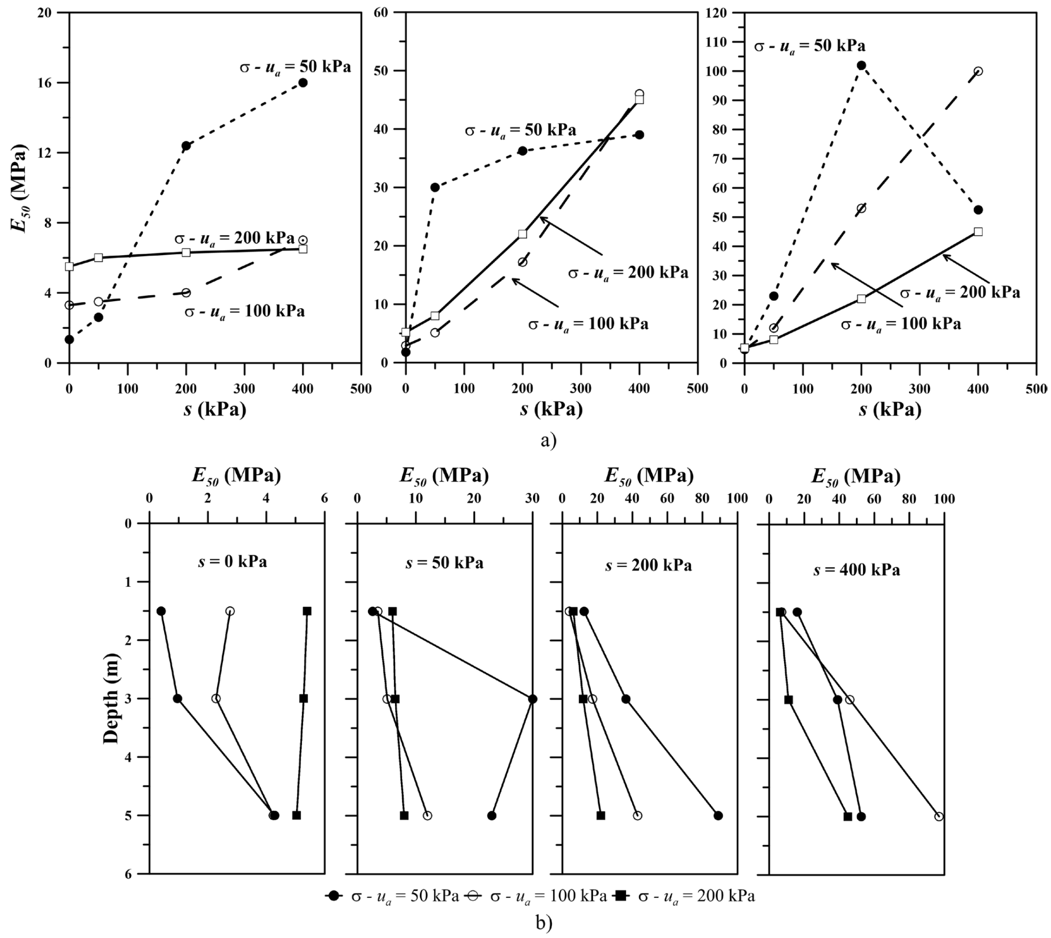

Figure 5. Variation of secant modulus (E_{50}) with (a) soil suction and (b) depth.

modulus in drained triaxial testing at 50 percent strength (E_{50}). Such behavior is mainly related to the increase of the over consolidation stress with depth and soil suction, which is going to be presented and discussed later, based on the confined compression test data.

The Mohr-Coulomb failure envelopes from Figure 6 were defined after the interpretation of the deviatoric stress curves versus axial strain for the three different depths. They were defined after the interpretation of the deviatoric stress curves *versus* axial strain for the three different sample depths (Figure 4). The maximum deviatoric stress $(\sigma_1 - \sigma_3)_{max}$ was used as the failure criterion. The envelopes were drawn by fitting a straight-line tangent to the three Mohr failure circles drawn from the interpretation of the data from each series of tests, depending on the test depth and soil suction.

The failure envelopes indicate that there are differences between saturated and unsaturated soils mainly in terms of the cohesion intercepts (Figure 7). The soil from 1.5 m depth has a cohesion intercept that varies from 0 to 16 kPa while the soil at the 5 m depth varies from 5.3 to 28.7 kPa. It can also be seen in this figure that the inclinations of shear strength failure envelope for 3 and 5 m depth samples are approximately equal regardless of the suction values. This means that the internal friction angle of the soil shows little changes with suction to higher depths. It is interesting to point out that grain size distribution of these soils is almost the same along depth (Figure 1).

The friction angle varies little with suction and the cohesion intercept increases hyperbolically with suction. The hyperbolic fit Equation 2 is shown in Figure 7, which led to coefficients of determination (R^2) close to the unit. Table 3 shows the values of constants a and b from the hyperbolic equation representative for each tested depth. Such behavior was observed by (Escario & Sáez, 1986; Röhm & Vilar, 1995; Vilar, 2006).

$$\tau = c' + (\sigma - \mathrm{u_a}).\ \mathrm{tg}\ \Phi' + s.\frac{1}{a + b.\mathrm{s}} \qquad (2)$$

3.3 Maximum shear modulus

The G_0 values determined in the laboratory using bender elements is presented in Figure 8. It can be seen in this figure that G_0 tends to increase linearly with net confining stress

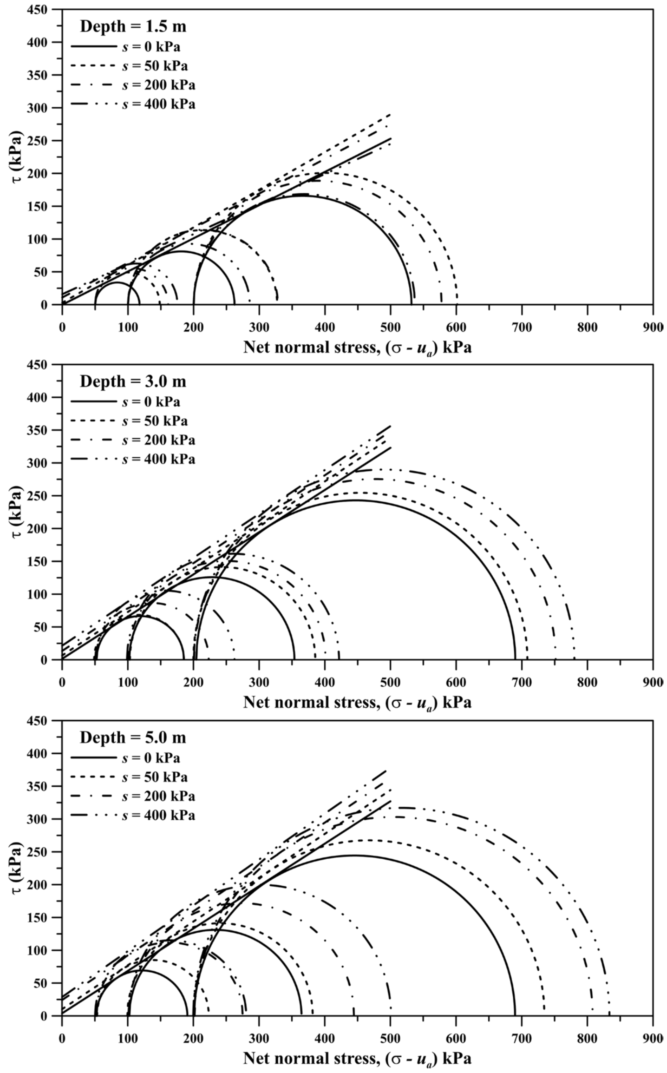

Figure 6. CD controlled suction triaxial compression test failure envelopes for different sample depth and soil suction values.

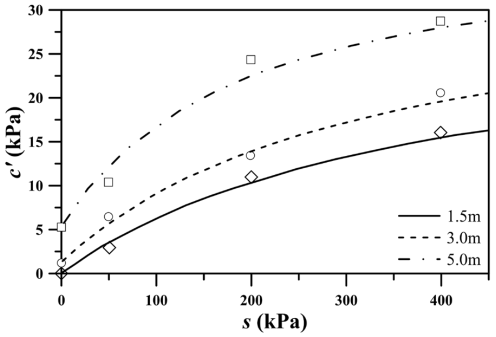

Figure 7. Cohesion intercept *versus* soil suction for different test depth and the hyperbolic fit.

Table 3. Values of *c'* and ϕ', fitting parameters (*a* and *b*) and coefficient of determination (R^2).

Depth (m)	*c'* (kPa)	ϕ'(°)	*a*	*b*	R^2
1.5	0.0	26.8	12.5	0.032	1.00
3.0	1.2	32.6	9.5	0.029	0.99
5.0	5.3	32.4	5.6	0.029	0.98

and nonlinearly with soil suction for the three tested depths. The same behavior (i.e., nonlinearity between G_0 and soil suction and linearity between G_0 and net confining stress) was also observed for unsaturated reconstituted sands by Nyunt et al. (2011) using, however, different equations to represent these behaviors. To better represent the influence of net stress and soil suction on soil stiffness, Equation 3 and Equation 4 were respectively used to fit the experimental data.

$$G_0 = f + g.\left(\sigma - u_a\right) \tag{3}$$

$$G_0 = G_{0,sat} + \frac{s}{m + \left(n\ .s\right)} \tag{4}$$

Where G_0 is the maximum shear modulus at the saturated condition, $(\sigma - u_a)$ is the net confining stress, s is the soil suction, and f, g, m, and n are the fitting parameters.

Table 4 shows the fitting parameters for G_0 and net confining stress and Table 5 the fitting parameters for G_0 and soil suction for the 1.5 m depth sample.

Table 4. Values of the fitting parameters for the sample collected at 1.5 m depth to represent the variation of G_0 with net stress.

$u_a - u_w$ (kPa)	f	g	R^2
0	40.7	0.5502	0.99
50	64.0	0.5413	0.99
200	70.5	0.5979	0.99
400	74.4	0.6055	0.99

Table 5. Values of the fitting parameters for the sample collected at 1.5 m depth to represent the variation of G_0 with soil suction.

$\sigma - u_a$ (kPa)	m	n	R^2
25	0.8068	0.0294	0.99
50	0.7279	0.0226	1.00
100	1.3801	0.0238	0.99
200	1.0835	0.0194	0.99

Figure 8 also shows an increase of G_0 with the test depth (i.e., net confining stress) and that G_0 increased at a faster rate with soil suction, up to approximately 50 kPa In general, G_0 tend to increase with soil suction and net confining stress. Such behavior is attributed to an increase in soil stiffness (higher rigidity of soil skeleton) due to either soil suction or confining pressure (Leong et al., 2006; Mancuso et al., 2002; Takkabutr, 2006).

3.4 Compressibility

Figure 9 shows the confined compression curves determined by the oedometer tests carried out with constant suction value for all the test depths. The data interpretation shows an increase on stiffness with increasing suction. It can also be seen in this figure that over consolidation

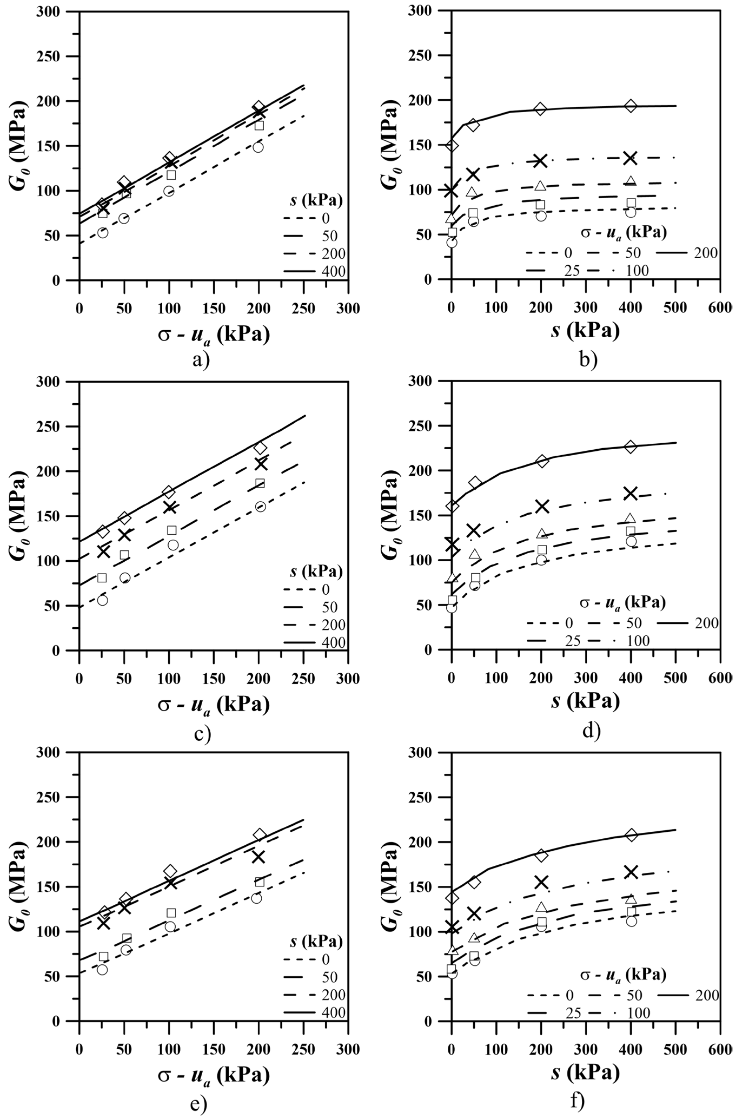

Figure 8. Variation of maximum shear modulus with net stress (a, c, and e) and soil suction (b, d, and f) as well as the fitting equations for samples collected at 1.5, 3.0 and 5.0 m depth.

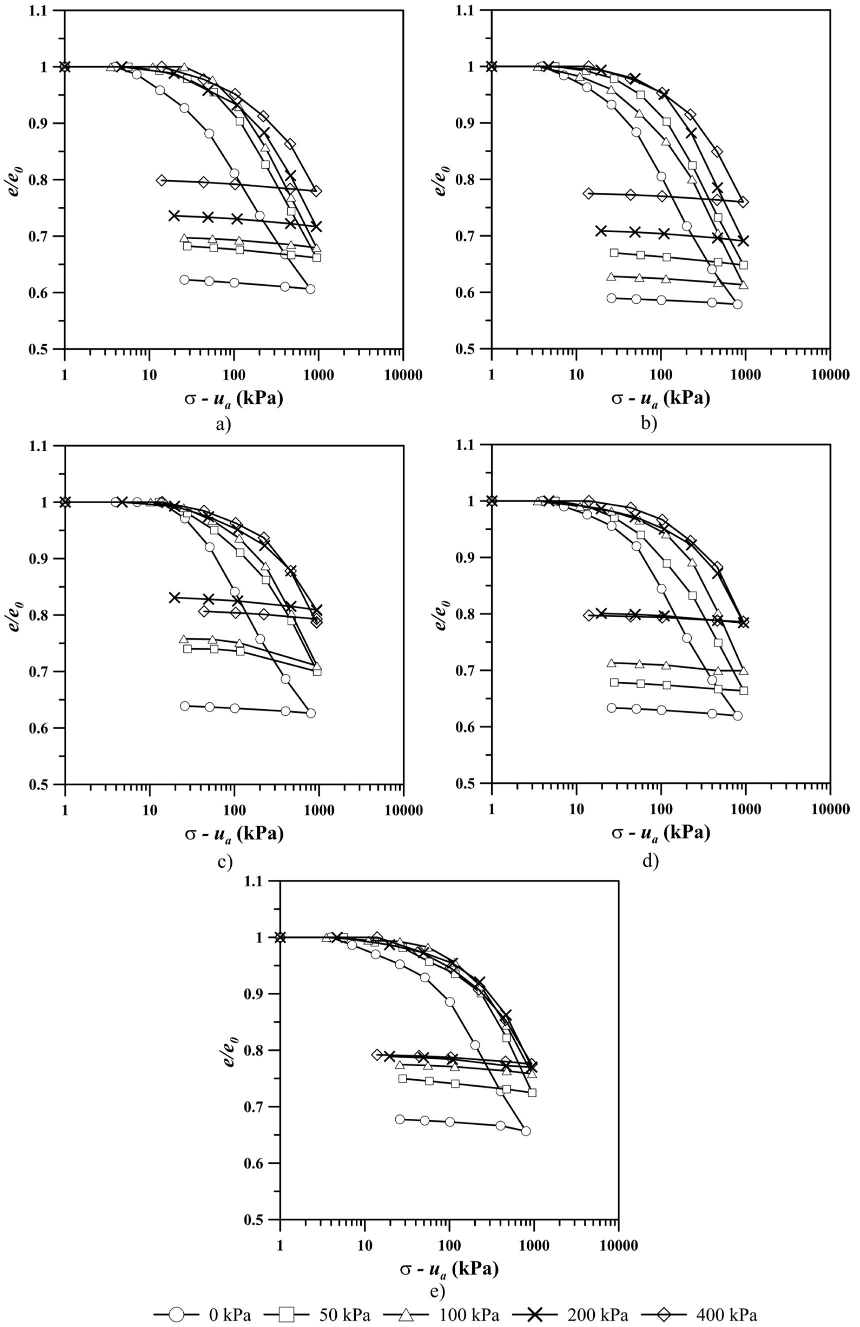

Figure 9. Controlled suction oedometer test data determined for soil samples collected at (a) 1.0; (b) 2.0; (c) 3.0; (d) 4.0; and (e) 5.0 m depth.

stress (σ_p) and the slope of the virgin compression line, represented by the compression index (C_c), vary with soil suction. For instance, over consolidation stress increases from 30 kPa to 176 kPa by varying suction from 0 to 400 kPa for the 1.0 m test depth.

The collapse potential (*CP*) can be indirectly estimated quantifying the discontinuity between the saturated and unsaturated curves from Figure 9, in a similar way to the double tests proposed by Jennings & Knight (1975). There is a higher collapse potential (*CP*) for the higher suction values, which decreases with increasing depth (Figure 10). Therefore, *CP* is higher closer to the ground surface and for higher suction values.

Figure 11 shows an increase in the soil stiffness, represented by the oedometric modulus (M_d), with increasing suction. It is also possible to observe in this figure that M_d values are relatively low up to about a net vertical stress equal 200 kPa and increase after that value. Soil that undergoes to a volume reduction due to collapse gets denser, which leads to an increase in the oedometric modulus with net vertical stress.

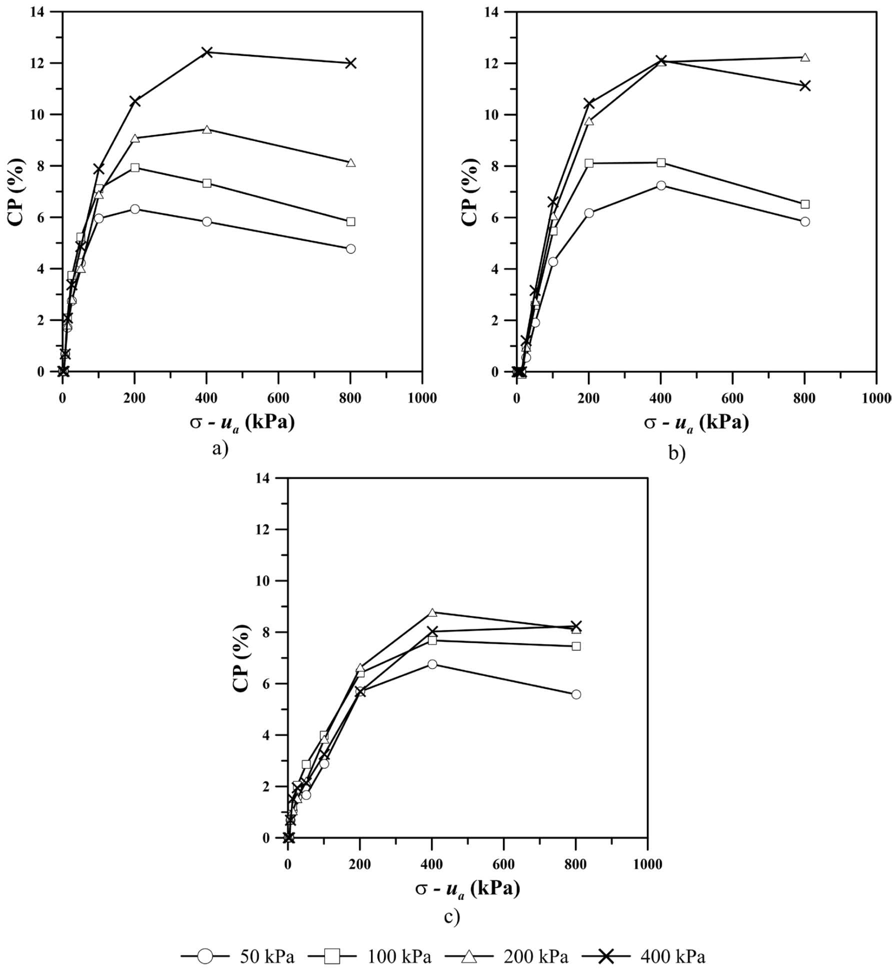

Figure 10. Collapse potential *versus* soil suction (50, 100, 200 and 400 kPa) for the different test depths: (a) 1.0; (b) 3.0; and (c) 5.0 m.

4. The variation of geotechnical parameters with depth

Shear strength parameters (c, ϕ), compressibility parameters (σ_p, C_c), maximum shear modulus (G_0) and collapse potential (CP) and their variation with soil suction along depth are summarized in Figure 12.

It can be observed from Figure 12 that the variation of the friction angle with suction is more pronounced for the 1.5 m depth than for 3.0 and 5.0 m depths. It can also be noted in this figure that the ϕ angle is practically the same for 3.0 and 5.0 m depths and higher than the 1.5 m depth. This figure also shows that the cohesion intercept increases with suction and with depth.

The over consolidation stress (σ_p) for the saturated condition is low and has little variation with depth, between 25 and 50 kPa (Figure 12). On the other hand, the σ_p increases with suction and with depth. The slope of the virgin compression line (C_c) also varies with suction, but practically does not vary with depth. This figure also shows that the collapse potential (CP) increases with soil suction and decreases with depth. The magnitude of collapsible behavior is higher in the upper portion of the soil profile, and it increases with suction. In addition, the maximum shear modulus (G_0) increases with soil suction and with depth. It is important to mention that the values of G_0 and CP were determined from the estimated effective stress (σ'_v) for the tested depths considering the unit weight of the studied soil.

Figure 12 also shows that the lower shear strength and the lower soil stiffness occurs at the 1.5 m depth, and these parameters slightly increase with depth for both the low and to the high suction values. It is also possible to observe that soil suction has a higher influence on cohesion intercept (c) and on the over consolidation stress (σ_p) than in friction angle (ϕ) and in compression index (C_c).

Soil suction has greater influence on the geotechnical parameters in the active zone of the studied soil profile (Figure 12) than the physical index properties (grain size distribution, consistency limits, unit weight of solids and void ratio). The presented data highlight the importance of understanding the suction influence on the behavior of the active zone of the studied soil profile. Such aspect is important for shallow foundations design since variability caused by suction is more relevant than spatial variability at the study site.

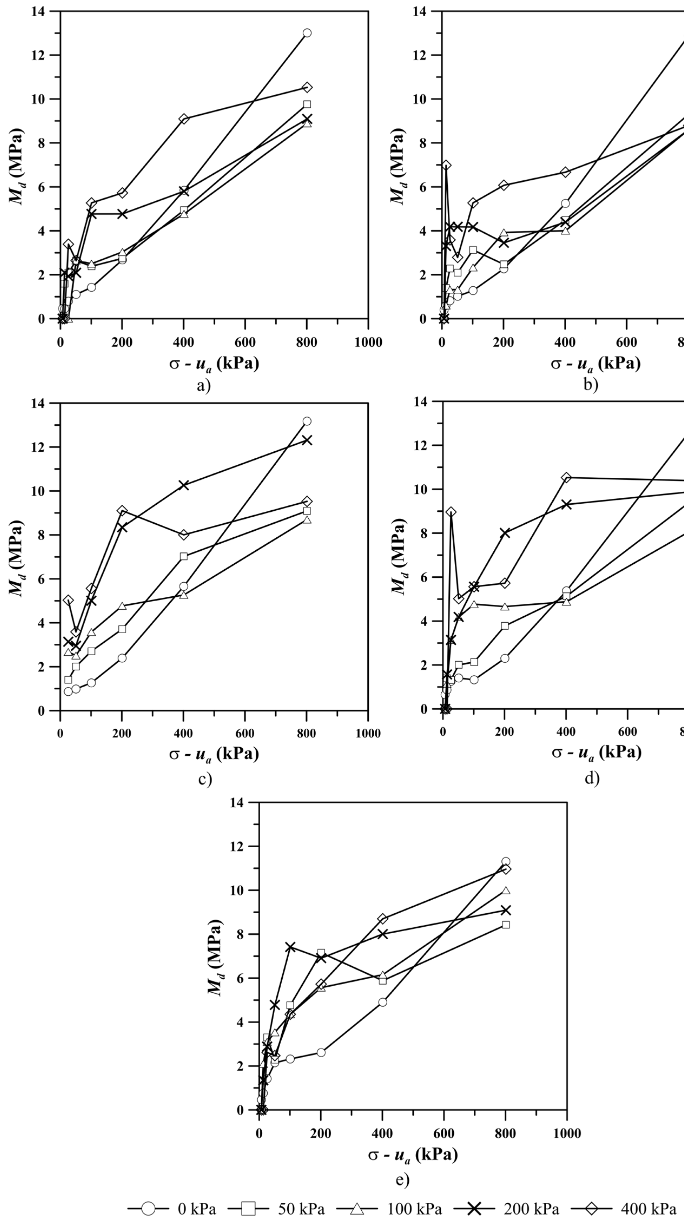

Figure 11. Oedometric modulus (M_d) *versus* the vertical stress at constant suction value for soil samples collected at (a) 1.0; (b) 2.0; (c) 3.0; (d) 4.0; and (e) 5.0 m depth.

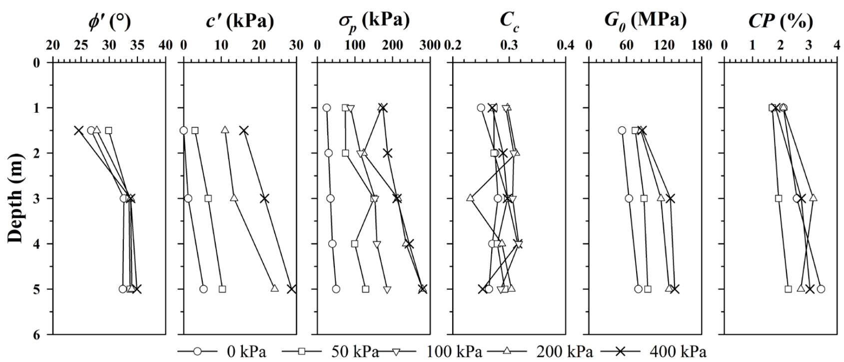

Figure 12. Variation of cohesion intercept, internal friction angle, over consolidation stress, compression index, maximum shear modulus and collapse potential with suction along depth for the study site.

5. Conclusions

- Characterization tests, index properties, retention curves and the mechanical parameters determined along depth indicate that the profile is fairly homogeneous up to 5.0 m depth;
- Water retention curves showed a typical behavior of porous sandy soil, with low air entry value and accented desaturation curve. The bimodal format is due to the existence of two air entry values: the first because of the presence of macropores and the second because of the drainage of micropores of the soil aggregate fraction;
- There is little influence of depth on that soil shear strength up to 5.0 m depth. The higher contribution on strength parameters is due to soil suction, which increases the intercept cohesion with lower influence of the internal friction angle;
- Compressibility parameters, mainly the σ_p, are also more affect by suction than the depth. The increase on soil suction caused an increase in over consolidation stress (σ_p) and changes in soil compression index (C_c). The constrained modulus (M_d) increases with increasing depth and soil suction;
- The G_0 values tends to increase linearly with net confining stress and nonlinearly with soil suction for the three tested depths. The greater variation of G_0 with suction was observed at 3.0 and 5.0 m depth samples;
- The soil has collapsible behavior with important collapse potential mainly under effect of higher suction values and closer to the ground surface;
- The geomechanical parameters of the studied soil are strongly influenced by suction and less influenced by depth and it must be incorporated to the practical design. In general, the presented test data show that the geotechnical parameters are more sensitive to soil suction than to the increase on depth in the active zone of the soil profile.

Acknowledgements

The authors thank the São Paulo Research Foundation, FAPESP (Grant 2017/23174-5), the National Council for Scientific and Technological Development, CNPq (Grant 436478/2018-8) and the Coordination for the Improvement of Higher Education Personnel, CAPES, for supporting their research.

Declaration of interest

The authors have no conflicts of interest to declare. All co-authors have observed and affirmed the contents of the paper and there is no financial interest to report.

Authors' contributions

Jeferson Brito Fernandes: Conceptualization, Data curation, Visualization, Writing – original draft. Alfredo Lopes Saab: Conceptualization, Data curation, Methodology, Supervision, Validation, Writing – original draft. Breno Padovezi Rocha: Formal Analysis, Investigation, Methodology, Writing – review & editing. Paulo César Lodi: Experimental supervision, Validation, Writing – review & editing. Roger Augusto Rodrigues: Conceptualization, Experimental supervision, Methodology, Writing – review. Heraldo Luiz Giacheti: Conceptualization, Methodology, Supervision, Funding acquisition, Project administration, Writing – review.

List of symbols

AEV	air entry value
a	fitting parameter
b	fitting parameter
B	pore-pressure coefficient
c	cohesion intercept
c'	effective cohesion intercept
C_c	compression index
CD	consolidated drained triaxial compression tests
CP	collapse potential
CPT	cone penetration test
CPTu	piezocone penetration test
E	void ratio
E_{50}	secant modulus in drained triaxial testing at 50 percent strength
f	fitting parameter
f_s	sleeve friction
g	fitting parameter
G_0	maximum shear modulus
$G_{0,sat}$	maximum shear modulus at the saturated condition
m	fitting parameter
M_d	oedometric modulus
n	fitting parameter
q_c	cone resistance
s	soil suction value
SM	silty sands
R^2	coefficient of determination
V_s	shear wave velocity
w	gravimetric moisture content
w_L	liquid limit
w_P	plastic limit
γ_d	dry unit weight
γ_s	unit weight of solids
ρ	soil bulk density
σ_p	over consolidation stress
σ'_v	effective stress
$\sigma - u_a$	net confining stress
$(\sigma_1 - \sigma_3)_{max}$	maximum deviatoric stress
t	shear stress
ϕ'	friction angle
ϕ^b	friction angle with respect to matric suction

References

ABNT NBR 9604. (1986). *Solo - Abertura de Poço e Trincheira de Inspeção em Solo, com Retirada de Amostras Deformadas e Indeformadas.* ABNT - Associação Brasileira de Normas Técnicas, Rio de Janeiro, RJ.

Alonso, E.E., Gens, A., & Josa, A. (1990). A constitutive model for partially saturated soils. *Geotechnique*, *40*(3), 405-430. http://dx.doi.org/10.1680/geot.1990.40.3.405.

ASTM D2487-17. (2017). *Standard Practice for Classification of Soils for Engineering Purposes (Unified Soil Classification System).* ASTM International, West Conshohocken, PA.

Blight, G.E. (2003). The vadose zone soil-water balance and transpiration rates of vegetation. *Geotechnique*, *53*(1), 55-64. http://dx.doi.org/10.1680/geot.2003.53.1.55.

Chandler, R.J., & Gutierrez, C.I. (1986). The filter-paper method of suction measurement. *Geotechnique*, *36*(2), 265-268. http://dx.doi.org/10.1680/geot.1986.36.2.265.

Chandler, R.J., Crilly, M.S., & Montgomery-Smith, G. (1992). OA low-cost method of assessing clay desiccation for low-rise-buildings. *Proceedings of the Institution of Civil Engineers. Civil Engineering*, 92(2), 82-89. http://dx.doi.org/10.1680/icien.1992.18771.

Cui, Y.J., Lu, Y.F., Delage, P., & Riffard, M. (2005). Field simulation of *in situ* water content and temperature changes due to ground–atmospheric interactions. *Geotechnique*, *55*(7), 557-567. http://dx.doi.org/10.1680/geot.2005.55.7.557.

De Mio, G. (2005). *Geological conditioning aspects for piezocone test interpretation for stratigraphical identification in geotechnical and geo-environmental site investigation* [Doctoral thesis, University of São Paulo]. University of São Paulo's repository (in Portuguese). Retrieved in January 9, 2022, from https://teses.usp.br/teses/disponiveis/18/18132/tde-27042006-170324/pt-br.php

De Mio, G., & Giacheti, H.L. (2007). The use of piezocone tests for high-resolution stratigraphy of Quaternary sediment sequences in the Brazilian coast. *Anais da Academia Brasileira de Ciências*, *79*(1), 153-170. http://dx.doi.org/10.1590/S0001-37652007000100017.

Delage, P., Romero, E., & Tarantino, A. (July 2-4, 2008). Recent developments in the techniques of controlling and measuring suction in unsaturated soils. In *1st European Conference on Unsaturated Soils* (pp.33-52). Durham: Glasgow Universities.

Dong, Y., & Lu, N. (2016). Correlation between small-strain shear modulus and suction stress in capillary regime under zero total stress conditions. *Journal of Geotechnical and Geoenvironmental Engineering*, *142*(11), 04016056. http://dx.doi.org/10.1061/(ASCE)GT.1943-5606.0001531.

Dong, Y., Lu, N., & McCartney, J.S. (2018). Scaling shear modulus from small to finite strain for unsaturated soils. *Journal of Geotechnical and Geoenvironmental Engineering*, 144(2), 04017110. http://dx.doi.org/10.1061/(ASCE)GT.1943-5606.0001819.

Escario, V., & Sáez, J. (1986). The shear strength of partly saturated soils. *Geotechnique*, *36*(3), 453-456. http://dx.doi.org/10.1680/geot.1986.36.3.453.

Fernandes, J.B. (2016). *Shear strength and stiffness of an unsaturated soil by triaxial tests* [Master's dissertation, São Paulo State University]. São Paulo State University's repository (in Portuguese). Retrieved in January 9, 2022, from https://repositorio.unesp.br/handle/11449/143473

Ferreira, C., Fonseca, A.V., & Nash, D.F.T. (2011). Shear wave velocities for sample quality assessment on a residual soil. *Soil and Foundation*, *51*(4), 683-692. http://dx.doi.org/10.3208/sandf.51.683.

Fredlund, D.G. (2006). Unsaturated soil mechanics in engineering practice. *Journal of Geotechnical and Geoenvironmental Engineering*, *132*(3), 286-321. http://dx.doi.org/10.1061/(ASCE)1090-0241(2006)132:3(286).

Fredlund, D.G., & Morgenstern, N.R. (1977). Stress state variables for unsaturated soils. *Journal of the Geotechnical Engineering Division*, *103*(5), 447-466. http://dx.doi.org/10.1061/AJGEB6.0000423.

Fredlund, D.G., & Xing, A. (1994). Equations for the soil-water characteristic curve. *Canadian Geotechnical Journal*, *31*(4), 521-532. http://dx.doi.org/10.1139/t94-061.

Fredlund, D.G., Morgenstern, N.R., & Widger, R.A. (1978). The shear strength of unsaturated soils. *Canadian Geotechnical Journal*, *15*(3), 313-321. http://dx.doi.org/10.1139/t78-029.

Georgetti, G.B. (2014). *Stiffness and strength of a lateritic unsaturated soil* [Doctoral thesis, University of São Paulo]. University of São Paulo's repository (in Portuguese). Retrieved in January 9, 2022, from https://teses.usp.br/teses/disponiveis/18/18132/tde-20032015-103943/en.php

Giacheti, H.L., Bezerra, R.C., Rocha, B.P., & Rodrigues, R.A. (2019). Seasonal influence on cone penetration test: an unsaturated soil site example. *Journal of Rock Mechanics and Geotechnical Engineering*, *11*(2), 361-368. http://dx.doi.org/10.1016/j.jrmge.2018.10.005.

Hardin, B.O., & Blandford, G.E. (1989). Elasticity of particulate materials. *Journal of Geotechnical Engineering*, *115*(6), 788-805. http://dx.doi.org/10.1061/(ASCE)0733-9410(1989)115:6(788).

Hilf, J.W. (1956). *An investigation of pore-water pressure in compacted cohesive soils* [Doctoral thesis, University of Colorado]. United State Department of the Interior Bureau of Reclamation, Design and Construction Division, Denver, CO, USA.

Ho, D.Y.F., & Fredlund, D.G. (January, 11-15, 1982). Increase in shear strength due to suction for two Hong Kong soils. In *ASCE Geotechnical Engineering Division Specialty Conference* (pp. 263-295). New York: American Society of Civil Engineers.

Hoyos, L.R., Suescún-Florez, E.A., & Puppala, A.J. (2015). Stiffness of intermediate unsaturated soil from simultaneous suction-controlled resonant column and bender element testing. *Engineering Geology*, *188*, 10-28. http://dx.doi.org/10.1016/j.enggeo.2015.01.014.

Jamiolkowski, M. (2012). Role of geophysical testing in geotechnical site characterization. *Soils and Rocks*, *35*(2), 117-137.

Jennings, J.E., & Knight, K. (1975). A guide to construction on or with materials exhibiting additional settlement due to collapse of grain structure. In *6th Regional Conference for Africa on Soil Mechanics and Foundation Engineering* (pp. 99-105). Netherlands: A. A. Balkema.

Khalili, N., & Khabbaz, M.H. (1998). A unique relationship for χ for the determination of the shear strength of unsaturated soils. *Geotechnique*, *48*(5), 681-687. http://dx.doi.org/10.1680/geot.1998.48.5.681.

Lambe, T.W., & Whitman, R.V. (1976). *Soil mechanics*. Chichester: John Wiley & Sons.

Leong, E.C., & Cheng, Z.Y. (2016). Effects of confining pressure and degree of saturation on wave velocities of soils. *International Journal of Geomechanics*, *16*(6), http://dx.doi.org/10.1061/(ASCE)GM.1943-5622.0000727.

Leong, E.C., Cahyadi, J., & Rahardjo, H. (2006). Stiffness of a compacted residual soil. In *Unsaturated Soils 2006* (pp. 1169-1180). Reston. American Society of Civil Engineers. https://doi.org/10.1061/40802(189)95.

Mancuso, C., Vassallo, R., & D'Onofrio, A. (2002). Small strain behavior of a silty sand in controlled-suction resonant column - torsional shear tests. *Canadian Geotechnical Journal*, *39*(1), 22-31. http://dx.doi.org/10.1139/t01-076.

Marinho, F., & Oliveira, O. (2006). The filter paper method revisited. *Geotechnical Testing Journal*, *29*(3), 14125. http://dx.doi.org/10.1520/GTJ14125.

Nyunt, T.T., Leong, E.C., & Rahardjo, H. (2011). Strength and small-strain stiffness characteristics of unsaturated sand. *Geotechnical Testing Journal*, *34*(5), 103589. http://dx.doi.org/10.1520/GTJ103589.

Ray, R.L., Jacobs, J.M., & Alba, P. (2010). Impacts of unsaturated zone soil moisture and groundwater table on slope instability. *Journal of Geotechnical and Geoenvironmental Engineering*, *136*(10), 1448-1458. http://dx.doi.org/10.1061/(ASCE)GT.1943-5606.0000357.

Rocha, B.P., Rodrigues, A.R.C., Rodrigues, R.A., & Giacheti, H.L. (2022). Using a seismic dilatometer to identify collapsible soils. *International Journal of Civil Engineering*, *20*, 857-867. http://dx.doi.org/10.1007/s40999-021-00687-9.

Rocha, B.P., Rodrigues, R.A., & Giacheti, H.L. (2021). The flat dilatometer test in an unsaturated tropical soil site. *Geotechnical and Geological Engineering*, *39*(8), 5957-5969. http://dx.doi.org/10.1007/s10706-021-01849-1.

Röhm, S.A., & Vilar, O.M. (September 6-8, 1995). Shear strength of an unsaturated sandy soil. In *Proceedings of the First International Conference on Unsaturated Soils* (pp. 189-193). Netherlands: A. A. Balkema.

Sánchez, M., Wang, D., Briaud, J.L., & Douglas, C. (2014). Typical geomechanical problems associated with railroads on shrink-swell soils. *Transportation Geotechnics*, *1*(4), 257-274. http://dx.doi.org/10.1016/j.trgeo.2014.07.002.

Silva, N.M., Rocha, B.P., & Giacheti, H.L. (2019). Prediction of load-settlement curves by the DMT in an unsaturated tropical soil site. *Soils and Rocks*, *42*(3), 351-361. http://dx.doi.org/10.28927/SR.423351.

Skempton, A.W., & Jones, O.T. (1944). Notes on the compressibility of clays. *Quarterly Journal of the Geological Society*, *100*(1-4), 119-135. http://dx.doi.org/10.1144/GSL.JGS.1944.100.01-04.08.

Sun, D., Sheng, D., & Xu, Y. (2007). Collapse behaviour of unsaturated compacted soil with different initial densities. *Canadian Geotechnical Journal*, *44*(6), 673-686. http://dx.doi.org/10.1139/t07-023.

Takkabutr, P. (2006). *Experimental investigations on small-strain stiffness properties of partially saturated soils via resonant column and bender element testing* (Doctoral thesis). University of Texas at Arlington.

Toll, D.G. (1990). A framework for unsaturated soil behaviour. *Geotechnique*, *40*(1), 31-44. http://dx.doi.org/10.1680/geot.1990.40.1.31.

Tsiampousi, A., Zdravkovic, L., & Potts, D.M. (2017). Numerical study of the effect of soil–atmosphere interaction on the stability and serviceability of cut slopes in London clay. *Canadian Geotechnical Journal*, *54*(3), 405-418. http://dx.doi.org/10.1139/cgj-2016-0319.

van Genuchten, M. (1980). A Closed-form equation for predicting the hydraulic conductivity of unsaturated soils. *Soil Science Society of America Journal*, *44*(5), 892-898. http://dx.doi.org/10.2136/sssaj1980.03615995004400050002x.

Vanapalli, S.K., Fredlund, D.G., Pufahl, D.E., & Clifton, A.W. (1996). Model for the prediction of shear strength with respect to soil suction. *Canadian Geotechnical Journal*, *33*(3), 379-392. http://dx.doi.org/10.1139/t96-060.

Vilar, O.M. (2006). A simplified procedure to estimate the shear strength envelope of unsaturated soils. *Canadian Geotechnical Journal*, *43*(10), 1088-1095. http://dx.doi.org/10.1139/t06-055.

Vilar, O.M., & Rodrigues, R.A. (2011). Collapse behavior of soil in a Brazilian region affected by a rising water table. *Canadian Geotechnical Journal*, *48*(2), 226-233. http://dx.doi.org/10.1139/T10-065.

Zhang, J., Huang, H.W., Zhang, L.M., Zhu, H.H., & Shi, B. (2014). Probabilistic prediction of rainfall-induced slope failure using a mechanics-based model. *Engineering Geology*, *168*, 129-140. http://dx.doi.org/10.1016/j.enggeo.2013.11.005.

Zhang, X. (2016). Limitations of suction-controlled triaxial tests in the characterization of unsaturated soils. *International Journal for Numerical and Analytical Methods in Geomechanics*, *40*(2), 269-296. http://dx.doi.org/10.1002/nag.2401.

Soils and Rocks

An International Journal of Geotechnical and Geoenvironmental Engineering

www.soilsandrocks.com

ISSN 1980-9743
ISSN-e 2675-5475

Study of the behavior of an instrumented soil nail wall in Salvador-Brazil

André Luiz Delmondes Filho[1#], Erinaldo Hilário Cavalcante[2], Carlos Rezende Cardoso Júnior[2], Demóstenes de Araújo Cavalcanti Júnior[2]

Article

Keywords
Soil nailing
Numerical modeling
Displacement monitoring
Instrumentation

Abstract

This paper aims to analyze the behavior of a soil-nailed excavation located in Salvador, Bahia, Brazil. Numerical stress-strain modeling was conducted, using finite element method. The horizontal displacement profiles obtained for the wall face in the numerical analysis presented a good correlation compared to field instrumentation monitoring with inclinometers. The results showed that the magnitude of the maximum numerical and experimental displacements was lower than the simplified models recommended by international manuals and technical literature. However, the monitoring data was compatible with other cases of instrumented nailed excavations in silt-sandy soil in the city of Salvador. Numerical models also adequately represented the distribution of tensile forces in nails. The maximum tensile forces observed numerically were smaller than those calculated using analytical methods. It was emphasized that the results of field monitoring and numerical models correspond to a stage immediately after the end of the retaining structure execution, not considering the evolution of deformations in long term.

1. Introduction

Soil nailing is a widely used technique to stabilize cut slopes in Brazil. In the Brazilian practice of soil nailing design, the stability analysis is normally based on limit equilibrium methods, i.e., in obtaining a safety factor for the evaluated sliding surfaces. However, this methodology does not predict the deformations in the reinforced soil mass and, consequently, does not accurately represent the behavior of the structure, whereas the stress redistribution in nails is not considered.

In addition to theoretical analysis in the design phase, soil nail performance evaluation has proved to be of fundamental importance, using instrumentation and field tests, both during the construction and utilization phases. This routine is also included in the recent Brazilian standard NBR 16920-2 (ABNT, 2021). By this framework, this work aims to analyze the behavior of a soil-nailed excavation using numerical analysis, based on the interpretation of monitoring data and other tests performed, for a case study in Salvador, Bahia, Brazil.

2. Background on soil nail wall displacements and internal forces

In the initial context, several instrumentation programs performed in nailed structures had contributed to the definition of displacements magnitude in nailed soil walls and reported that horizontal displacements at the top of the excavation present values between 0.1 and 0.5% of its height (H), at the end of the construction phase (e.g. Clouterre, 1991; Gaessler & Gudehus, 1981; Mitchell & Villet, 1987). Based on these results, some international manuals (e.g. Clouterre, 1991; Lazarte et al., 2015) propose simplified formulas for maximum horizontal displacement on the top of the wall, equal 0.002H to 0.003H, depending on sandy or clayey soils, respectively.

According to Yuan et al. (2019b), the main simplified models for wall displacement prediction only take wall height and soil type into account, disregarding wall geometry, nail length, spacing and inclination angle, and external surcharge loading influence. Furthermore, the effect of time on displacement magnitude is also not considered. Data from monitored structures indicate that displacements in nailed soils tend to increase post-construction, especially in the first six months, depending on the type of soil, and may increase up to 15% in long term (Lazarte et al., 2015).

Over the last decades, numerical methods have been one of the main tools for predicting deformations in nailed soil masses, especially using the finite element method (FEM), both 2D and 3D analysis. The numerical tools are capable of simulating constructive phases and incorporating constitutive models, which reproduce the structure behavior with certain

#Corresponding author. E-mail address: delmondes@usp.br
[1]Universidade de São Paulo, Escola Politécnica, São Paulo, São Paulo, SP, Brasil.
[2]Universidade Federal de Sergipe, Departamento de Engenharia Civil, São Cristóvão, SE, Brasil.

Submitted on October 25, 2021; Final Acceptance on September 5, 2022; Discussions open until February 28, 2023.
https://doi.org/10.28927/SR.2022.076221

fidelity, in static, seismic, or dynamic conditions (e.g. Garzón-Roca et al., 2019; Gerscovich et al., 2005; Lima, 2002; Razavi & Hajialilue Bonab, 2017; Sharma & Ramkrishnan, 2020). Recently, some studies have applied statistical approaches and machine learning techniques, including artificial neural network (ANN) for nailed wall displacement prediction (e.g. Liu et al., 2021; Yuan et al., 2019b).

Regarding soil nail monitoring, the investigation conducted by Saré (2007) showed that instrumentation with inclinometers is efficient both for obtaining point displacements and for assessing the global displacement of the soil mass. The comparison between the data obtained by the field monitoring and the results of the numerical analysis was satisfactory regarding the prediction of the retaining structure displacements and the loads acting in the nails. Other technologies also successfully applied for soil nail monitoring include Brillouin distributed optical fiber sensors (DOFS), Fiber Bragg grating (FBG) sensors, and unmanned aerial vehicles (UAV) (Esmaeili et al., 2019; Hong et al., 2017; Hu et al., 2018).

The geometric line with the maximum axial tensile force in the nails could define a potential rupture surface, which separates the soil mass into two zones: the active zone and the passive zone (Ehrlich, 2003). In the nailed excavations instrumented and monitored by Clouterre (1991), the distance between the face of the retaining wall and the line of maximum tension in the nails presented values between 0.3 and 0.5 times the excavation height (H). Lazarte et al. (2015) indicate that this value can be between 0.3H and 0.4H for the upper nails and between 0.15H and 0.20H for the lower ones (Figure 1).

Some approaches and formulations have been proposed to estimate the maximum tensile force (T_{max}) acting in the nails, as a function of the active earth pressure coefficient (K_a), the soil unit weight (γ), the excavation height (H), and the horizontal (S_h) and vertical (S_v) spacing between nails

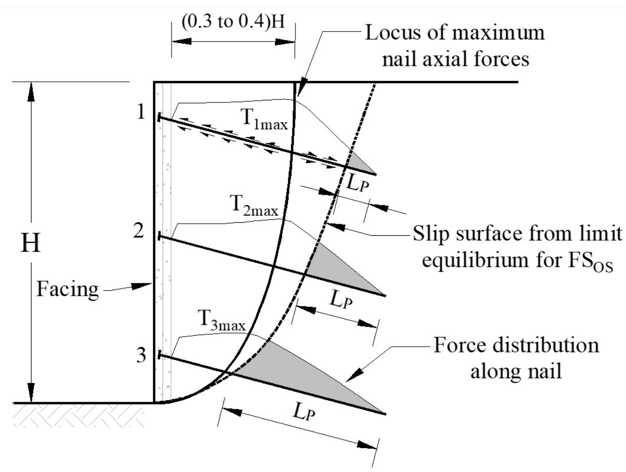

Figure 1. Position of the potential rupture surface and locus of maximum nail axial forces (Lazarte et al., 2015).

(Briaud & Lim, 1997; Lazarte, 2011; Lazarte et al., 2015; Lin et al., 2017; Lin & Bathurst, 2018; Yuan et al., 2019a). Briaud & Lim (1997) propose Equations 1 and 2 for the upper nail line and the lower ones, respectively. Lazarte et al. (2015) provided expressions 3 and 4, for nails located at the upper two-thirds and the lower third of the excavation, respectively.

$$T_{\max} = 0.65 \times K_a \times \gamma \times H \times S_v \times S_h \tag{1}$$

$$T_{\max} = 0.33 \times K_a \times \gamma \times H \times S_v \times S_h \tag{2}$$

$$T_{\max} = 0.75 \times K_a \times \gamma \times H \times S_v \times S_h \tag{3}$$

$$T_{\max} = 0.38 \times K_a \times \gamma \times H \times S_v \times S_h \tag{4}$$

3. Case study of a nailed wall in Salvador, Brazil

3.1. Project description, geotechnical characterization and field instrumentation

The soil-nailed wall under study is part of a residential project in Salvador, Bahia, Brazil. The necessary data for this work were obtained from the company responsible for the retaining system design. Figure 2 shows two photographic records of the structure during its construction phase.

The retaining structure presents heights between 7.7 and 14.8 meters. The project used different configurations for nail length: 6.0 and 12.0 m (e.g. sections E 2+10.00 and E 4+0.00) and 6.0, 9.0, and 12.0 m (e.g. E 3+10.00). Nails were composed of steel bars of 20 mm in diameter, type CA-50, and drilling hole diameter equal to 75 mm. The excavated site is composed, basically, of interleaved layers of sandy silt and clay silt with sand, as illustrated in the geotechnical cross-view in Figure 3.

The field instrumentation of the nailed excavation included inclinometers for monitoring horizontal displacements in the nailed wall. Four inclinometers were inserted at different stations according to Table 1 and the soil nailed wall was monitored until the end of the construction phase. The location of the inclinometers is illustrated in Figure 4. A qualitative analysis of the monitoring data was conducted and verified a good profile of Inclinometer 1, which was defined as the reference values for the present study.

Table 1. Summary of installed inclinometers for the soil nailed wall case.

Inclinometer N°	Location/Station	Depth (m)
1	E 2+10,00	22.5
2	E 5+10,00	22.5
3	E 8+0,00	15.5
4	E 7+0,00	21.5

(a) (b)

Figure 2. Construction of the soil-nailed wall. Top view (a) and front view (b), during shotcrete application stage.

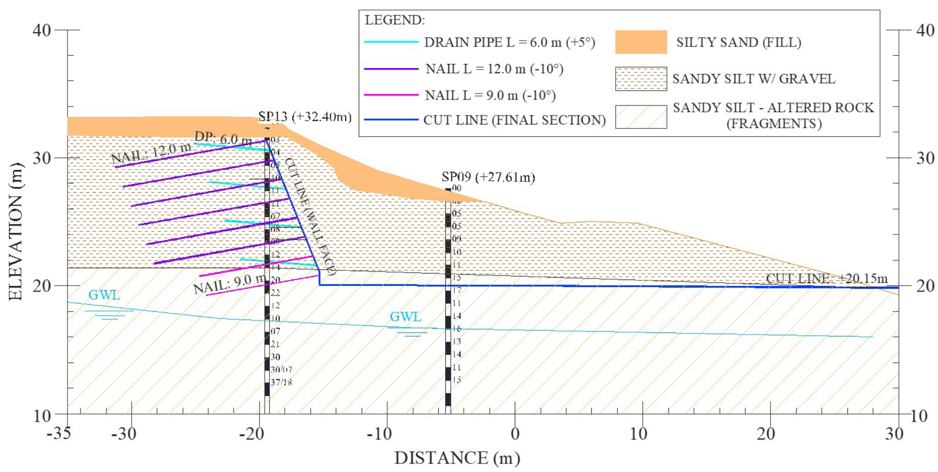

Figure 3. Geotechnical cross-view – Section E 3+10.00.

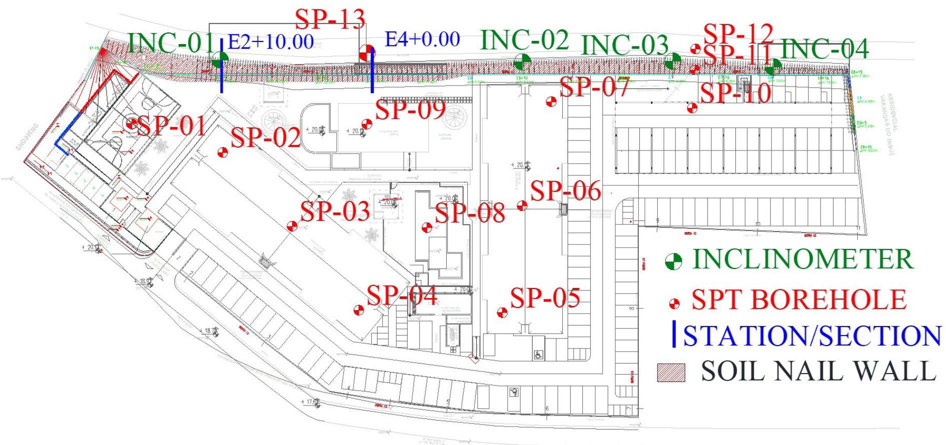

Figure 4. Location of reference sections, inclinometers, and Standard Penetration Tests performed on-site.

3.2. Numerical modeling procedure

The numerical analysis was conducted using the finite element method software SIGMA/W, as a module GeoStudio 2012 geotechnical package. Two cross-sections were analyzed, E 2+10.00 and E 4+0.00. As presented in Table 1, section E 2+10.00 was instrumented with an inclinometer and monitored until the end of the construction phase. Thus, the analysis of this section was conducted to calibrate the soil deformability parameters, comparing the displacements obtained in the numerical model with the ones obtained by the field monitoring.

Geometry inserted for analysis of section E 2+10.00 in the initial condition (*InSitu*) is presented in Figure 5a. The sub-horizontal lines represent the nails, while the vertical one reproduces the inclinometer installed in the section. To simplify the model, only two layers of soil were adopted (see legend). On the right side of the reinforced area, the division of layers aims to represent the excavation stages. The sequential steps of excavation and insertion of the nails were reproduced in the model, for each reinforcement level, to represent the stress changes in the soil. The final condition of the analysis is illustrated in Figure 5b.

The finite element mesh was generated using quadrilateral and triangular elements with a global dimension equal to 0.50 m, a value suggested by Corte (2017), who also performed numerical and stability simulations in nailed soil using the GeoStudio software. The mesh of the model in section E 4+0.00 was composed of 4949 elements, totaling 5050 nodes. This unstructured quadrilateral and triangular mixed mesh is recommended for general cases in excavation analysis (GEO-SLOPE, 2013). The geometry inserted for the model of section E 4+0.00 in the final condition of excavation is presented in Figure 6.

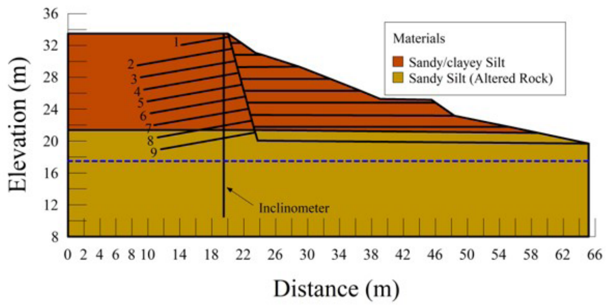

(a) Initial condition

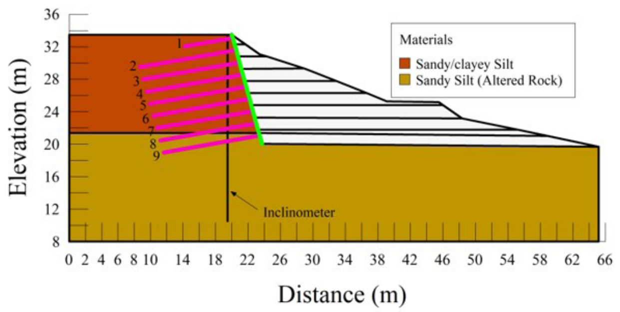

(b) Final condition

Figure 5. Model of section E 2+10.00, in initial (a) and final (b) conditions.

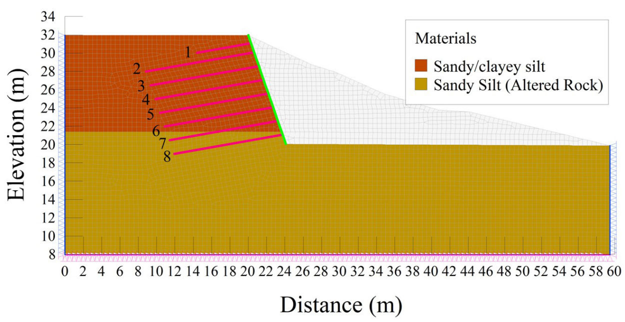

Figure 6. Final model of E 4+0.00 section, including mesh and boundary conditions.

The pink and green lines in the models correspond, respectively, to the nails and the shotcrete facing, inserted in the model as beam elements. Nails were modeled with a design inclination equal to 10° and lengths of 6.0 and 12.0 m (according to the design of each section), for both analyzed sections. Connection between nail heads and shotcrete face was modeled as rigid. The necessary input data for the beam elements are cross-sectional area, moment of inertia, and Young's modulus.

Geometric parameters were calculated according to the design specifications. The model used the nails' equivalent moment of inertia, considering the horizontal spacing, for an adequate representation of the elements bending stiffness. The Young's modulus (E_{beam}) applied to the beam elements was calculated according to the weighted average of steel and concrete areas (in the case of the nails, the grout material). This procedure was used in the numerical simulations performed by Gerscovich et al. (2005) and by Singh & Babu (2010). A synthesis of the geometric and elastic parameters applied in beam elements of the nails and the coating (wall face) is presented in Table 2, as input data in the software.

Soil was represented by the elastic-plastic model with Mohr-Coulomb rupture criteria, for which, in addition to the unit weight (γ), five other parameters are needed: Young's modulus (E_{soil}), internal friction angle (ϕ), cohesion (c), dilatancy angle (ψ) and Poisson's ratio (ν). The Young's modulus of the soil layers was obtained by adjusting the displacements of the model with those monitored in the field, for the instrumented section E 2+10.00. The values of 35 and 48 MPa for the upper and lower layers, respectively, were those that led to the best approximation between the displacements of the numerical model and those measured by the inclinometer. The shear strength parameters were obtained from direct shear tests, except the dilatancy angle, which was adopted null, following the recommendations of the SIGMA/W manual (GEO-SLOPE, 2013). The analyses carried out by Pereira (2016) also followed this recommendation. Poisson's ratio was adopted 0.25, according to the suggested range of values

Table 2. Elastic and geometric parameters of the beam elements used in numerical models.

Element	Young's modulus (GPa)	Area (cm^2)	Inertia (cm^4)
Nail	34.4	44.2	155.3
Wall face	24.1	800	4266.7

for sandy soils in Jia (2018). Table 3 presents a synthesis of the soil parameters applied in the analyses for both sections.

4. Analysis results and discussion

4.1. Wall displacements

A map of horizontal displacements in the entire model analyzed for section E 2+10.00 is shown in Figure 7. The horizontal displacements on the nailed soil wall face range from 2.5 to 4.5 mm, with greater values at the top of the retaining structure. For section E 4+0.00, the same map is shown in Figure 8. For this section, horizontal displacements on the face of the nailed soil range from 1.5 to 3.0 mm, with higher values also in the vicinity of the retainer's top.

The horizontal displacement profile on the excavation face of section E 2+10.00 is illustrated in Figure 9a, for all excavation phases. Reinforcing what was seen in Figure 7, in the curves, the maximum displacement equal to 4.7 mm is found at the top of the structure. However, in the lower third of the excavation, displacements reaching values of 4.0 mm are observed. The significant displacement values in the lower third of the excavation can be simply associated with the efforts resulting from lateral earth pressure, which is higher in that area. Another aspect that calls attention is the evolution of displacements with the advance of the excavation phases. For this section, in the last three stages, the maximum displacement at the top has increased by 88%, going from 2.5 mm (end of Step 6) to 4.7 mm (Step 9, final). Also, for section E 2+10.00, Figure 9b shows the curves of the horizontal displacements obtained by the numerical model for the vertical line, inserted to represent the inclinometer

Table 3. Elastic and geometric parameters of the beam elements.

Soil description	γ (kN/m^3)	E_{soil} (MPa)	Φ (°)	c (kPa)	ψ (°)	ν
Sandy/silty clay	16.7	35	28.7	16.5	0	0.25
Sandy silt (altered rock)	17.0	48	24.5	25.0	0	0.25

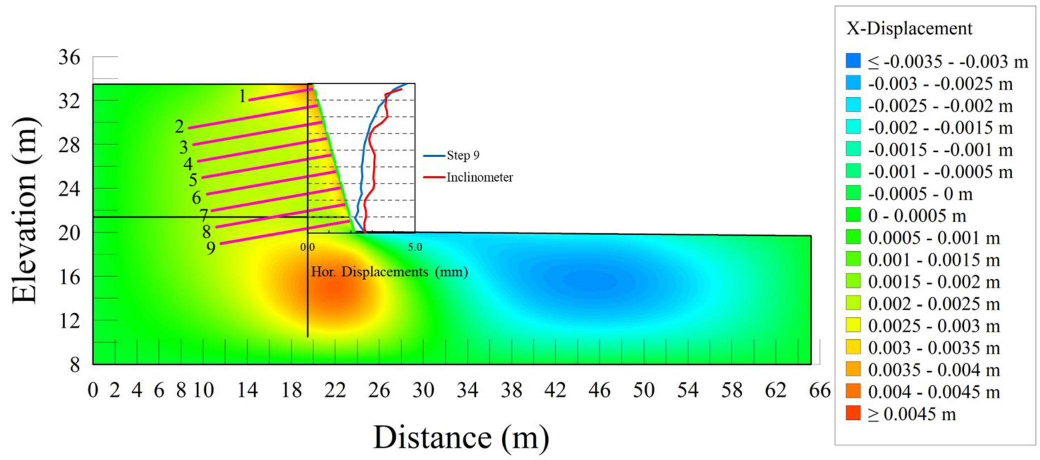

Figure 7. Section E 2+10.00. Horizontal displacements (in X) – Final step.

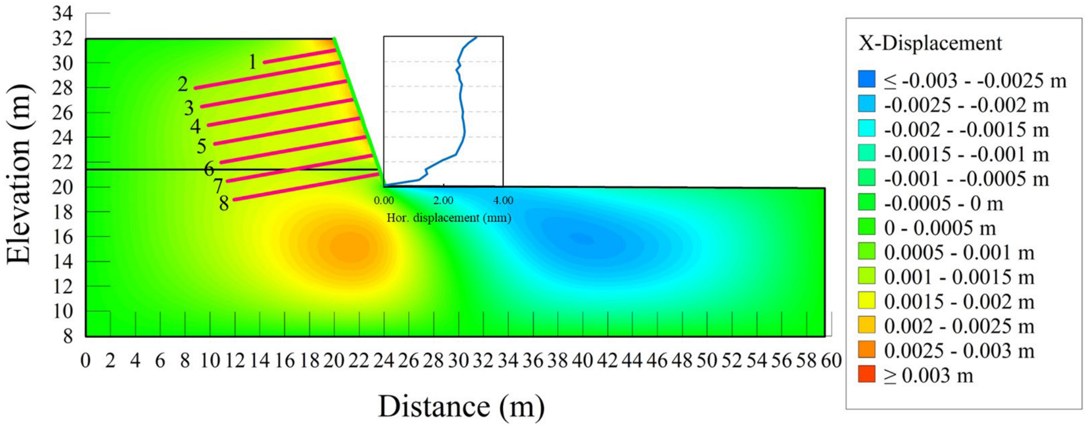

Figure 8. Section E 4+0.00. Horizontal displacements (in X) – Final step.

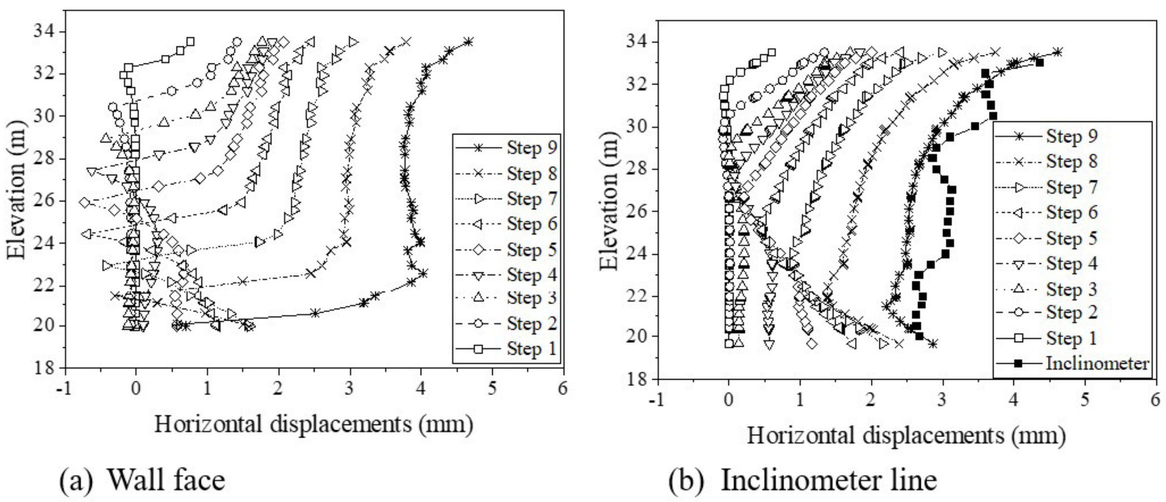

Figure 9. Horizontal displacement profiles (in X) for section E 2+10.00. (a) Wall face; (b) Inclinometer line.

installed in the field, as well as the horizontal displacements obtained by the real inclinometer. The figure shows a good correlation between the results obtained from the numerical analysis and the values obtained from the readings performed with the inclinometer, with the excavation completed, for the adopted elastic parameters.

The horizontal displacement profile on the excavation face of section E 4+0.00 is illustrated in Figure 10, for all excavation phases. Again, in the curves, the maximum displacements were found at the top, reaching 3.1 mm in the final stage. In the lower half of the excavation, for the final step, maximum displacements of 2.7 mm are observed. As in the analysis of section E 2+10.00, it can be reiterated the evolution of displacements with the advance of excavation phases. In the last three phases, the displacements at the top more than doubled in value, increasing from 1.4 mm (end of Step 5) to 3.1 mm (Step 8, final).

Analyzing the results of the two modeled sections, the displacement profiles showed similar behavior, with maximum horizontal displacements at the top. However, considerable displacements were also found in the bottom half of the excavation. This behavior has been discussed in some studies, such as Cardoso & Carreto (1989), Barley (1992), Shiu et al. (1997), and Lima (2002), who report the influence of the excavation face inclination on the horizontal displacement profile, since the analytical predictions more widespread by the technical literature are valid for vertical excavations (90°), differently from the model of this research. In some cases, for smaller slopes, maximum displacements even tend to be located below the top.

Regarding the magnitude of horizontal displacements, for both analyzed sections, the maximum values are in the order of 0.03% of the excavation height. This result is considerably smaller than the predictions made by international literature. However, a study of the behavior of nailed excavations performed in Salvador, Brazil, by

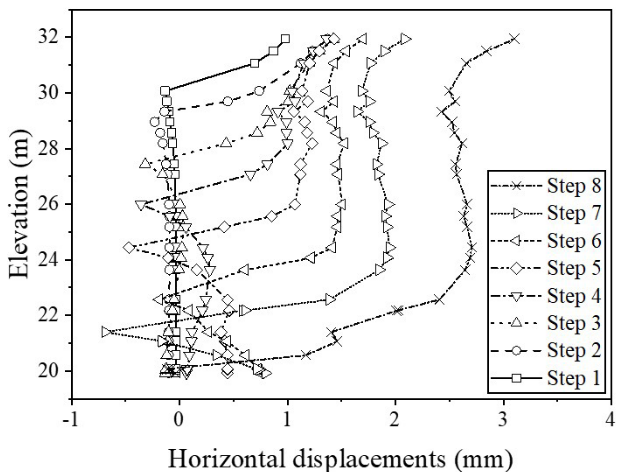

Figure 10. Horizontal displacement profile (in X) for section E 4+0.00.

Décourt et al. (2003), also showed results much smaller than the analytical predictions. The maximum displacements obtained by the authors, also in silty-sandy soil, were in the order of 0.07% of the excavation height. In this context, it should be noted that both the results of field monitoring and those obtained from numerical models correspond to a stage immediately after the end of the retaining structure execution, not considering the evolution of the deformations over time, that is, in the long term.

4.2. Axial load distribution on nails

The distribution of the axial tensile load along the nails length (L_{nail}) for section E 2+10.00, referring to the end of the construction, is shown in Figure 11a. The graph is presented in a way that the nail length axis starts on the right, corresponding to the face of the wall (head of the nails), in order to represent

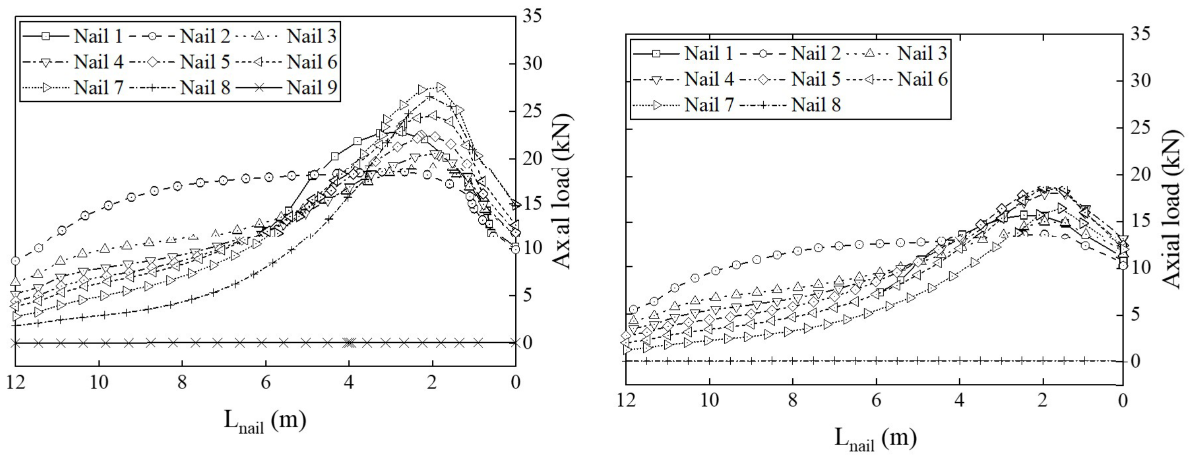

(a) Section E 2+10.00 (b) Section E 4+0.00

Figure 11. Distribution of axial tensile load along the nails length after the excavation is completed. (a) Section E 2+10.00; (b) Section E 4+0.00.

the position of the reinforcements in the models. For this section, the maximum forces in the nails varied between 18 kN (nail 2) and 28 kN (nail 7). It is noteworthy that the loads obtained for the lower nail line (nail 9) were practically null. Figure 11b shows the distribution of the axial tensile load along the nails' length in section E 4+0.00, referring to the end of the execution. For this section, the maximum forces in the nails varied between 14 kN (nail 2) and 18 kN (nail 6). Similarly, to section E 2+10.00, the loads obtained for the lowest nail line (nail 8) were practically null.

For both sections, a similar distribution of tensile force is observed, in which the maximum loads are located at a distance from the wall face that corresponds to values of 0.14H and 0.17H. Predictions made by Clouterre (1991) indicate that the maximum load line can be placed at a distance of 0.30H to 0.50H. In Lazarte et al. (2015) this value varies between 0.30H and 0.40H, for nails closer to the top, and between 0.15H and 0.20H for the lower nail lines. Regarding the maximum tensile forces, the values obtained in the two num

erical analyses are considerably smaller than those predicted using the methodologies proposed by Briaud & Lim (1997) and by Lazarte et al. (2015), which provide values from 50 to 130 kN, considering the different positions of the nails. However, it is significant that both proposals cited do not consider the effect of cohesion, and do not represent well the soil under study. If cohesion were considered mathematically in the distribution of the active earth pressure acting on the nails, perhaps the authors' proposals would approximate the results obtained in the numerical analyses. Similar observations are presented by Santos (2019) and Ehrlich et al. (2021).

The relation between the tensile force close to the wall face (nail head) and the maximum tensile force in the nails presented an average value of 0.54 and 0.68 for the sections E 2+10.00 and E 4+0.00, respectively, approaching Clouterre's analytical predictions (Clouterre, 1991). It's also possible to observe relatively small load values at the end of the nails, except for nail 2, positioned in the higher portion of the excavation, which was possibly influenced by the shorter nail 1 (first line), as discussed in Razavi & Hajialilue Bonab (2017).

5. Conclusions

This paper presented the analysis of the behavior of a soil-nailed excavation carried out in the city of Salvador, Bahia, Brazil. Some constraints on the retaining structure behavior were evaluated, related to deformations and stress on the nails:

- The horizontal displacement profiles from the numerical models and the inclinometer monitoring showed very similar behavior. The displacements observed in numerical models for two sections analyzed in this work were equivalent, with maximum horizontal displacements at the top, but with significant values in the lower portion of the excavation;
- Regarding the magnitude of the horizontal displacements, the maximum values obtained were of the order of 0.03% of the excavation height (H), therefore, smaller than the predictions of the international literature (0.002H to 0.003H) but compatible with other cases of instrumented nailed excavations in silt-sandy soil in the city of Salvador, as detailed in Décourt et al. (2003);
- The distribution of tensile forces in the nails was compatible with the analytical calculations, in which the maximum forces are located behind the face of the wall. However, the magnitude of the maximum

tensile forces was considerably smaller than the estimated by international manuals models. The relationship between the tensile force close to the face and the maximum tensile force in the nails, on the other hand, approached Clouterre's analytical predictions (Clouterre, 1991).

Acknowledgements

The authors acknowledge the Universidade Federal de Sergipe and GEOTEC Consultoria e Serviços Ltda. for the technical support given to this research, and the Brazilian agency Coordenação de Aperfeiçoamento de Pessoal de Nível Superior (CAPES) for the financial support provided to the first author during this study.

Declaration of interest

The authors have no conflicts of interest to declare.

Authors' contributions

André Luiz Delmondes Filho: conceptualization, data curation, formal analysis, methodology, visualization, writing – original draft. Erinaldo Hilário Cavalcante: conceptualization, methodology, project administration, resources, supervision, validation. Carlos Rezende Cardoso Júnior: conceptualization, investigation, methodology, resources, supervision. Demóstenes de Araújo Cavalcanti Júnior: conceptualization, investigation, resources.

List of symbols

c Soil cohesion
E_{beam} Young's modulus of beam elements (numerical analysis)
E_{soil} Young's modulus of soil
H Excavation depth
K_a Active earth pressure coefficient
L_{nail} Nail length
T_{max} Maximum tensile force acting in the nails
S_h Horizontal spacing between nails
S_v Vertical spacing between nails
γ Soil unit weight
ϕ internal friction angle of soil
ν Poisson's ratio of soil
ψ Dilatancy angle

References

ABNT 16920-2. (2021). *Walls and Slopes in Reinforced Soils - Part 2: Soil Nail*. ABNT - Associação Brasileira de Normas Técnicas, Rio de Janeiro, RJ (in Portuguese).

Barley, D.A. (1992). Soil nailing - case histories and developments. In: *Proceedings of the ICE Conference on Retaining Structures*, Cambridge.

Briaud, J.-L., & Lim, Y. (1997). Soil-nailed wall under piled bridge abutment: simulation and guidelines. *Journal of Geotechnical and Geoenvironmental Engineering*, 123(11), 1043-1050. http://dx.doi.org/10.1061/(ASCE)1090-0241(1997)123:11(1043).

Cardoso, A.S., & Carreto, A.P. (1989). Performance and analysis of a nailed excavation. In: *Proceedings of the 12th International Conference on Soil Mechanics and Foundation Engineering* (pp. 1233–1236). Rio de Janeiro. Publications Committee of XII ICSMFE.

Clouterre. (1991). *Recommendations CLOUTERRE 1991. Soil Nailing Recommendations-1991 for Designing, Calculating, Constructing and Inspecting Earth Support Systems Using Soil Nailing*. U.S. Department of Transportation, Federal Highway Administration.

Corte, F.H. (2017). *Containment analysis in nailed soil in the city of São Bernardo do Campo/SP* [Master's dissertation, Universidade Estadual de Campinas]. Universidade Estadual de Campinas' repository (in Portuguese). https://doi.org/10.47749/T/UNICAMP.2017.989014.

Décourt, L., de Campos, L.E.P., & Menezes, M.S.S. (2003). Projeto e comportamento de escavações estabilizadas com solo grampeado em Salvador. In *Solo grampeado - Projeto, execução, instrumentação e comportamento - Workshop* (pp. 105-120). São Paulo, SP: ABMS.

Ehrlich, M. (2003). Solos grampeados - Comportamento e procedimentos de análise. In *Solo grampeado - Projeto, execução, instrumentação e comportamento - Workshop* (pp. 127-137). São Paulo, SP: ABMS.

Ehrlich, M., Rosa, C. A. B., & Mirmoradi, S. H. (2021). Effect of construction and design factors on the behaviour of nailed-soil structures. *Proceedings of the Institution of Civil Engineers - Geotechnical Engineering*, 1-13. https://doi.org/10.1680/jgeen.20.00139.

Esmaeili, F., Ebadi, H., Saadatseresht, M., & Kalantary, F. (2019). Application of UAV photogrammetry in displacement measurement of the soil nail walls using local features and CPDA method. *ISPRS International Journal of Geo-Information*, 8(1), 25. http://dx.doi.org/10.3390/ijgi8010025.

Gaessler, G., & Gudehus, G. (1981). Soil Nailing - Some Aspects of a New Technique. In: *Proceedings of the 10th International Conference on Soil Mechanics and Foundation Engineering*, Stockholm. (Vol. 3, pp. 665-670), Publications Committee of X ICSMFE.

Garzón-Roca, J., Capa, V., Torrijo, F.J., & Company, J. (2019). Designing soil-nailed walls using the amherst wall considering problematic issues during execution and service life. *International Journal of Geomechanics*, 19(7), 05019006. http://dx.doi.org/10.1061/(ASCE)GM.1943-5622.0001453.

GEO-SLOPE. (2013). *Stress-deformation modeling with SIGMA/W - an engineering methodology*. GEO-SLOPE International Ltd.

Gerscovich, D.M.S., Sieira, A.C.C.F., Lima, A.P., & Sayão, A.S.F.J. (2005). Técnicas de modelagem numérica de escavações de taludes em solo grampeado. In: *Proceedings of the IV Conferencia Brasileira sobre Estabilidade de Encostas*, (pp. 671-680). Salvador.

Hong, C.Y., Zhang, Y.F., Li, G.W., Zhang, M.X., & Liu, Z.X. (2017). Recent progress of using Brillouin distributed fiber optic sensors for geotechnical health monitoring. *Sensors and Actuators. A, Physical*, 258, 131-145. http://dx.doi.org/10.1016/j.sna.2017.03.017.

Hu, Y., Hong, C., Zhang, Y., & Li, G. (2018). A monitoring and warning system for expressway slopes using FBG sensing technology. *International Journal of Distributed Sensor Networks*, 14(5), 155014771877622. http://dx.doi.org/10.1177/1550147718776228.

Jia, J. (2018). Soil dynamics and foundation modeling. In J. Jia (Ed.), *Soil dynamics and foundation modeling: offshore and earthquake engineering*. Springer. https://doi.org/10.1007/978-3-319-40358-8.

Lazarte, C.A. (2011). *Proposed specifications for LRFD Soil-Nailing design and construction* (NCHRP Report 701). National Cooperative Highway Research Program.

Lazarte, C.A., Robinson, H., Gómez, J.E., Baxter, A., Cadden, A., & Berg, R. (2015). Soil nail walls reference manual. In National Highway Institute. *Geotechnical Engineering Circular No. 7* (FHWA-NHI-14-007). U.S. Department of Transportation, Federal Highway Administration.

Lima, A.P. (2002). *Deformability and stability of slopes supported by soil nailing* [Master's dissertation, Pontifícia Universidade Católica do Rio de Janeiro - PUC-Rio]. PUC-Rio's repository (in Portuguese). https://doi.org/10.17771/PUCRio.acad.3335.

Lin, P., & Bathurst, R.J. (2018). Reliability-based internal limit state analysis and design of soil nails using different load and resistance models. *Journal of Geotechnical and Geoenvironmental Engineering*, 144(5), 04018022. http://dx.doi.org/10.1061/(asce)gt.1943-5606.0001862.

Lin, P., Bathurst, R.J., & Liu, J. (2017). Statistical evaluation of the FHWA simplified method and modifications for predicting soil nail loads. *Journal of Geotechnical and Geoenvironmental Engineering*, 143(3), 04016107. http://dx.doi.org/10.1061/(asce)gt.1943-5606.0001614.

Liu, D., Lin, P., Zhao, C., & Qiu, J. (2021). Mapping horizontal displacement of soil nail walls using machine learning approaches. *Acta Geotechnica*, 16(12), 4027-4044. http://dx.doi.org/10.1007/s11440-021-01345-z.

Mitchell, J.K., & Villet, W.C.B. (1987). *Reinforcement of earth slopes and embankments* (NCHRP Report 290). National Cooperative Highway Research Program.

Pereira, A.B. (2016). *Estudos numéricos do comportamento tensão-deformação de estruturas em solo grampeado* [Master's dissertation, Universidade Federal de Ouro Preto]. Universidade Federal de Ouro Preto's repository (in Portuguese). http://www.repositorio.ufop.br/handle/123456789/6532

Razavi, S.K., & Hajialilue Bonab, M. (2017). Study of soil nailed wall under service loading condition. *Proceedings of the Institution of Civil Engineers - Geotechnical Engineering*, 170(2), 161-174. http://dx.doi.org/10.1680/jgeen.16.00006.

Santos, C.A.B.R. (2019). *Numerical analysis of the behavior of soil nailing excavations: case study and influence of design and execution conditioners* [Master's dissertation, Universidade Federal do Rio de Janeiro]. UFRJ's repository (in Portuguese).

Saré, A.R. (2007). *Behavior of an instrumented soil nailed excavation on a residual soil* [Doctoral thesis, Pontifícia Universidade Católica do Rio de Janeiro - PUC-Rio]. PUC-Rio's repository (in Portuguese). https://doi.org/10.17771/PUCRio.acad.11686.

Sharma, A., & Ramkrishnan, R. (2020). Parametric optimization and multi-regression analysis for soil nailing using numerical approaches. *Geotechnical and Geological Engineering*, 38(4), 3505-3523. http://dx.doi.org/10.1007/s10706-020-01230-8.

Shiu, Y.K., Yung, P.C.Y., & Wong, C.K. (1997). Design, construction and performance of a soil nailed excavation in Hong Kong. In *Proceedings of the 14th International Conference on Soil Mechanics and Foundation Engineering* (pp. 1339-1342). Hamburg. Publications Committee of XIV ICSMFE.

Singh, V.P., & Babu, G.L.S. (2010). 2D numerical simulations of soil nail walls. *Geotechnical and Geological Engineering*, 28(4), 299-309. http://dx.doi.org/10.1007/s10706-009-9292-x.

Yuan, J., Lin, P., Huang, R., & Que, Y. (2019a). Statistical evaluation and calibration of two methods for predicting nail loads of soil nail walls in China. *Computers and Geotechnics*, 108, 269-279. http://dx.doi.org/10.1016/j.compgeo.2018.12.028.

Yuan, J., Lin, P., Mei, G., & Hu, Y. (2019b). Statistical prediction of deformations of soil nail walls. *Computers and Geotechnics*, 115, 103168. http://dx.doi.org/10.1016/j.compgeo.2019.103168.

Soils and Rocks
An International Journal of Geotechnical and Geoenvironmental Engineering
www.soilsandrocks.com
ISSN 1980-9743
ISSN-e 2675-5475

Determination of the size of rock fragments using RVM, GPR, and MPMR

Pradeep Thangavel[1#], Pijush Samui[1]

Article

Keywords
Blasting
GPR
MPMR
RVM
Rock fragmentation

Abstract

For predicting the size of rock fragments during drilling and blasting operations, this article uses GPR, RVM, and MPMR. The current analysis makes use of a blast data set generated in a prior investigation. In this study, a portion of the blast data was utilized to train a model to determine the mean particle size arising from blast fragmentation for each of the similarity groups generated. The particle size was modeled as a function of seven different variables. The dataset contains information about the bench height and drilled burden ratio (H / B), spacing to burden ratio (S / B), burden to hole diameter ratio (B / D), stemming to burden ratio (T / B), powder factor (P_f), modulus of elasticity (E), and in-situ block size (X_B) are the input and output is X_{50}. By comparing forecasts with actual mean particle size values and predictions based on one of the most widely used fragmentation estimation techniques in the blasted literature, the capacity of the generated models may be established. The statistical parameters, actual vs predicted curve, Taylor diagram, error bar, and developed discrepancy ratio are used to analysis the performance of models. A comparative study has been carried out between the developed RVM, GPR, and MPMR. The results show the developed models have the capability for prediction of X_{50}. From these comparisons, the MPMR has the highest value with a high degree of precision and robustness in the size of rock fragments X_{50}.

1. Introduction

Rock mass is a heterogeneous material, and in blasting and drilling, the heterogeneity of the rock generates size distribution of fragmented rocks. The total economics of mine workings are heavily reliant on the estimation of blasted rock mass fragmentation. The cost of loading, transport, crushing, and milling operations can all be reduced dramatically by using blasting as a major fragmentation method. Blast fragmentation is primarily determined by the blast design as well as the qualities of the rock mass (Jug et al., 2017; Mohamed et al., 2019). Direct and indirect approaches are used to quantify the size distribution of shattered rock following blasting. In the direct procedure, the only methodology is fragment sieving analysis. Despite being the most accurate approach among others, it is not practicable due to its high cost and time requirements. As a result, observational, empirical, and digital approaches have been created as indirect methods. Researchers can use a range of existing tools and models to predict and process blasting findings, one of which is machine learning techniques, which is possibly the most extensively used way to estimate fragmentation after blasting. There are different empirical models available for the determination of the size distribution of rock fragments in the literature (Kuznetsov, 1973; Aler et al., 1996; Ozkahraman, 2006; Jethro et al., 2016). However, the available methods are not so reliable (Shi et al., 2012).

Singh et al. (2019) use dataset from forty open space bench explosion in the four open Indian mines to track blast-induced rock disintegration as a function of explosion parameters such as spacing, powder feature, hole size, weight, stemming depth, and hole bench height. Tao et al. (2020) investigated blast-induced rock fragmentation using a combination of analytical modelling, finite element simulation, and image recognition. They used sequential alterations in the model geometry to investigate the major impact of rock fragility and effective dimensions on fragment size distribution, demonstrating that the effect of fracture toughness on fragmentation is included in the effect of material size. The deep CNN was utilised by Yang et al. (2021) to automatically categorise rock fragment images taken by a timed capture camera. Bamford et al. (2021) discuss the implications of using deep learning models for the fragmentation of rock assessment. Using an end-to-end deep learning technique, convolution neural network architecture was trained to predict mean sizes of blasted rock fragments straight from a 2D image. His research examines the DNN model's accuracy and effectiveness as a tool for automated and rapid rock fragmentation analysis. Researchers have tried different numerical and Artificial Intelligence (AI)

[#]Corresponding author. E-mail address: tpradeep1125@gmail.com
[1]National Institute of Technology Patna, Department of Civil Engineering, Patna, Bihar, India.

Submitted on July 23, 2022; Final Acceptance on October 11, 2022; Discussion open until February 28, 2023.
https://doi.org/10.28927/SR.2022.008122

techniques for the determination of the size distribution of rock fragments (Zhang & Goh, 2013; Zhang et al., 2019, 2020a, b, c; Kumar et al., 2021; Li et al., 2022).

Relevance vector machine (RVM) is a type of soft computing method that combines the concepts of Markov property, automated relevance determination (ARD), Bayesian principle, and maximum probability into a probabilistic Bayesian learning framework (Kong et al., 2019). The functional forms of RVM and SVM are identical. The much more significant benefit of RVM over SVM is its ability to make probabilistic predictions. RVM's high sparseness also allows it to reduce the number of kernel functions utilized in computing, making it particularly suitable for online monitoring. SVM kernel functions must satisfy Mercer's criterion, which asserts that the related kernel matrix of a symmetric function is semi-positive. SVM kernel functions must satisfy Mercer's criterion, which asserts that the related kernel matrix of a symmetric function is semi-positive. RVM, on the other hand, has the advantage of being able to use any kernel function without having to satisfy Mercer's criterion (Samui, 2012; Li et al., 2017; Biswas et al., 2019; Kardani et al., 2021; Pradeep et al., 2021). In the domain of machine learning, GPR, a nonparametric Bayesian method fo regression, is causing a stir. GPR has various advantages, including the capacity to work with limited datasets and provide uncertainty measures on predictions (Chalupka et al., 2013; Caywood et al., 2017; Baiz et al., 2020). The minimax probability machine classification technique underpins MPMR, which is a regression method. There were no assumptions made in this model about the numerical distribution of the data. It is based on the probabilistic framework. It is been used brilliantly in a variety of engineering sectors (Strohmann & Grudic, 2003; Samui & Kim, 2017; Kumar et al., 2020).

For the purpose of determining the mean particle size X_{50} resulting from rock blast fragmentation, this article uses RVM, GPR, and MPMR. The dataset contains information about the ratio of bench height to drilled burden $/B$, ratio of stemming to burden (T / B), ratio of spacing to burden (S / B), ratio of burden to hole diameter (B / D), modulus of elasticity (E), powder factor (P_f), in-situ block size (X_B) are inputs and outputs are (X_{50}) in the database. The models are trained by using data of 70% and tested by 30% data. These models are performing under MATLAB software. The predicted mean size of rock (X_{50}) from models results is compared with actual data for analysis of the capacity of the model. For the comparative purpose statistical parameters, actual vs predicted curve, Taylor diagram, error bar, and DDR criteria are used in this article.

2. Details of data

The blast database created by Hudaverdi et al. (2011) (Kulatilake et al., 2010; Hudaverdi et al., 2011; Shi et al., 2012) is covered in this section. To create the blast database, data from previous blasts in various regions of the world. There are quarries in Istanbul, as well as mines in Spain called Enusa and Reocin. The Murgul Copper Mine in northeastern Turkey, with Mrica Quarry in Indonesia, Soma Basin in western Turkey, the Dongri–Buzurg mine in Central India, and the Akdaglar and Ozmert Quarries in northern Istanbul (Kulatilake et al., 2010). The ratio of bench height to drilled burden (H / B) , ratio of stemming to burden (T / B), ratio of spacing to burden (S / B), ratio of burden to hole diameter (B / D), modulus of elasticity (E), powder factor (P_f), in-situ block size (X_B) are inputs and outputs are X_{50} in the database. Figure 1 shows the scatter plot matrix for the original data set. Table 1 shows the statistical analysis of the input variables used to develop the models to predict fragmentation. The term "normalization" in statistics refers to the scaling down of a data collection so that the normalized data falls between 0 and 1. Such normalization approaches make it possible to compare matching normalized values from two or more separate data sets in a way that eliminates the impact of scale differences. To put it another way, a data set with large values may readily be compared to a data set with lower values. The data is split into two groups. A training dataset is necessary for the model to be trained. 70% of data sets are considered for training in this study. A testing dataset is necessary in order to estimate model performance. The remaining 30% is used as the testing data set in this study. The normalization equation is shown in Equation 1.

$$x_{Normalized} = \frac{\left(x_{Actual} - x_{mini}\right)}{\left(x_{maxi} - x_{mini}\right)} \tag{1}$$

3. Developed model details

3.1 Relevance Vector Machine (RVM)

RVM is introduced by Tipping (2000). It is constructed based on the Bayesian concept. In RVM, the Equation 2 represents the input and output relation.

$$t = \Phi w + \varepsilon \tag{2}$$

This article uses $H/B, S/B, B/D, T/B, P_f, E, and\ X_B$ as inputs of RVM. The output is X_{50}.

Table 1. Statistical analysis of the input parameters used to create models to predict fragmentation.

	S / B	H / B	B / D	T / B	P_f	X_B	E
Minimum	1	1.3	18	0.5	0.2	0.02	9.5
Maximum	1.7	6.8	39.5	4.7	1.3	2.3	60
Mean	1.2	3.3	27.4	1.3	0.5	1.1	29.5
Std deviation	0.1	1.6	4.8	0.7	0.2	0.5	17.9

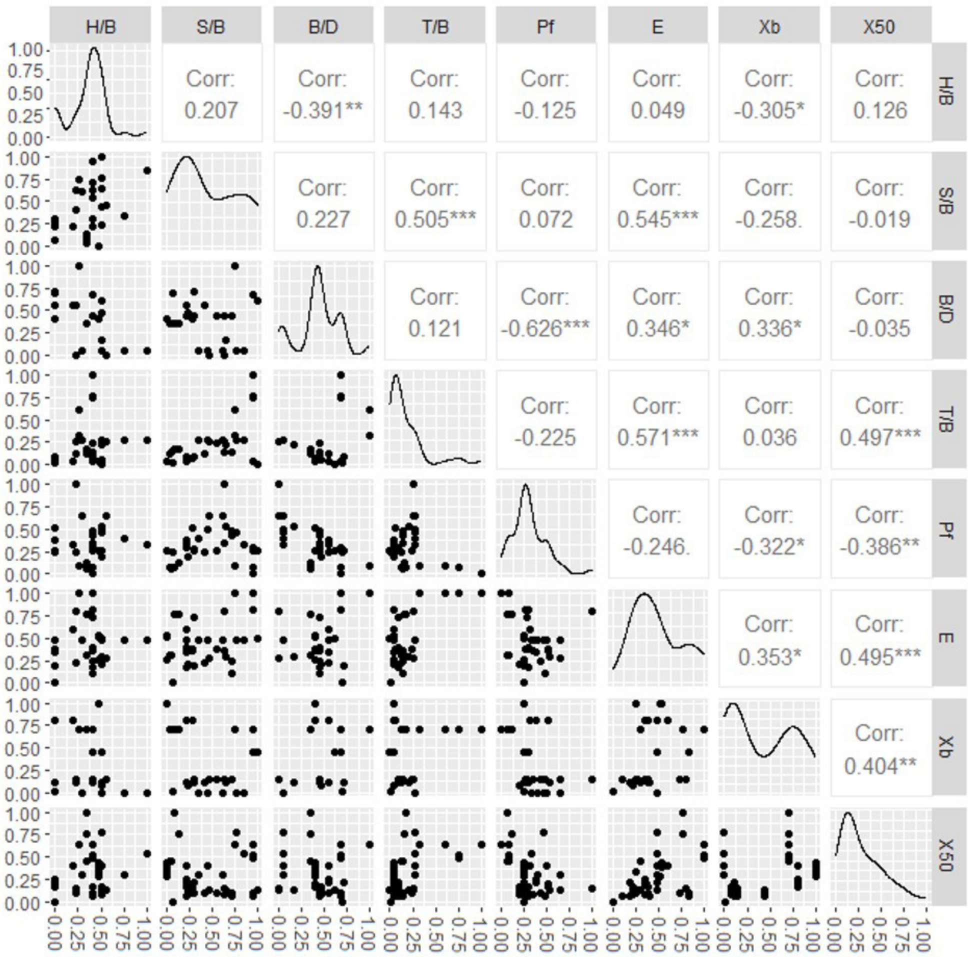

Figure 1. Correlation and scatter plot of data.

So, $x = \left[H/B, S/B, B/D, T/B, P_f, E, X_B\right]$ and $y = \left[X_{50}\right]$

Where $\Phi = \left[\phi(x_1), \dots, \phi(x_N)\right]$ and $\phi(x_n) = \left[K(x_n, x_1), K(x_n, x_2), \dots, K(x_n, x_M)\right]^T$, $K(x_n, x_1)$ is kernel function. ε follows the Gaussian distribution having mean zero and σ^2 variance. The likelihood of the complete dataset is given below:

$$p\left(\frac{t}{w}, \sigma^2\right) = \left(2\pi\sigma^2\right)^{-\frac{N}{2}} \exp\left\{-\frac{1}{2\sigma^2 t - \Phi w^2}\right\} \tag{3}$$

The value of t can be determined by maximizing the above Equation 2. The maximization of Equation 2 can cause overfitting. Over the weights, automated relevance detection (ARD) prior is set to prevent overfitting.

$$p(w|\alpha) = \prod_{i=0}^{N} N\left(w_i | 0, \alpha_i^{-1}\right) \tag{4}$$

Where the hyperparameter vector that specifies how far each weight can depart from zero. According to Bayes' rule, the combination of likelihood and prior is given by:

$$p\left(\frac{w}{t}, \alpha, \sigma^2\right) = \frac{p\left(\frac{t}{w}, \sigma^2\right) p\left(\frac{w}{\alpha}\right)}{p\left(\frac{t}{\alpha}, \sigma^2\right)} \tag{5}$$

The posterior covariance (Σ) and mean (μ) are given below:

$$\Sigma = \left(A + \alpha^{-2}\Phi^T\Phi\right)^{-1} \tag{6}$$

$$\mu = \sigma^{-2} \sum \Phi^T t \tag{7}$$

Where $A = diag(\alpha)$

The details of RVM is given by Tipping (2000). Radial basis function $(x, x_i) = \exp\left\{-\frac{(x_i - x)(x_i - x)^T}{2\sigma^2}\right\}$, where the kernel function is the width of the radial basis function σ.

3.2 Gaussian Process Regression (GPR)

For output (y) prediction, the GPR model use the following model

$$y_i = f(x_i) + \varepsilon$$

In this article, GPR uses the same inputs and output as used by the RVM.

$$\text{So, } x = \left[\frac{H}{B}, \frac{S}{B}, \frac{B}{D}, \frac{T}{B}, P_f, E, X_B\right] \text{ and } y = [X_{50}]$$

The spreading of output (y_{N+1}) for a novel input vector (x_{N+1}) is represented by

$$\begin{pmatrix} y \\ y_{N+1} \end{pmatrix} \sim N(0, K_{N+1}) \tag{8}$$

The expression of K_{N+1} is given below:

$$K_{N+1} = \begin{bmatrix} [K] & [K(x_{N+1})] \\ [K(x_{N+1})^T] & [k(x_{N+1})] \end{bmatrix} \tag{9}$$

Where $K(x_{N+1})$ is the $N \times 1$ vector which covariances lies between training and the testing input, and $K(x_{N+1})$represent the auto covariance of the test input.

The distribution of y_{N+1} is Gaussian. The mean and variance of y_{N+1} are given below:

$$\mu = K(x_{N+1})^T K^{-1} y \tag{10}$$

$$\sigma^2 = k(x_{N+1}) - K(x_{N+1})^T K^{-1} K(x_{N+1}) \tag{11}$$

The GPR model uses the same training dataset, testing dataset, kernel function, and normalization technique as used by the RVM model. The program of GPR has been developed by MATLAB.

3.3 Minimax Probability Machine Regression (MPMR)

MPMR is developed by Lanckriet et al. (2003). In MPMR, the relation between input(x) and output(y) is given by the following equation.

$$y = \sum_{i=1}^{N} \beta_i K(x_i, x) + b \tag{12}$$

Where $K(x_i, x)$ is kernel function, β_i and b are output from the MPMR algorithm.

In this article, MPMR uses the same inputs and output as used by the RVM and GPR.

$$\text{So, } x = \left[\frac{\mathrm{H}}{\mathrm{B}}, \frac{\mathrm{S}}{\mathrm{B}}, \frac{\mathrm{B}}{\mathrm{D}}, \frac{\mathrm{T}}{\mathrm{B}}, \mathrm{P_f}, \mathrm{E}, \mathrm{X_B}\right] \text{ and } y = [X_{50}]$$

MPMR is developed by constructing dichotomy classifier [24]. All of the regression data $+\varepsilon$ is shifted into one data set along the output. The second dataset is created by relocating all of the regression data $-\varepsilon$ down the output line. The regression surface is the categorization border between these two classes.

Both the RVM and the MPMR models employ the identical training dataset, testing dataset, kernel function, and normalization technique. The program of MPMR has been constructed using MATLAB.

3.4 Evaluation of models

The model's accuracy was explained using a variety of statistical methodologies. The parameters are determination coefficient (R^2), Nash-Sutcliffe efficiency (NS), Root mean square error ($RMSE$), Weighted mean absolute percentage error ($WMAPE$), Variance Account Factor (VAF), Performance index (PI) (Wong, 1985), Willmott's Index of agreement (WI) (Willmott, 1984), Mean absolute error (MAE) (Chai & Draxler, 2014), Mean Bias Error (MBE), Expanded uncertainty (U_{95}) (Behar et al., 2015), and t-statistic ($t\,stat$) (Stone, 1994).

$$R^2 = \frac{\sum_{i=1}^{N}(d_i - d_{mean})^2 - \sum_{i=1}^{N}(d_i - y_i)^2}{\sum_{i=1}^{N}(d_i - d_{mean})^2} \tag{13}$$

$$WMAPE = \frac{\sum_{i=1}^{n}\left|\frac{d_i - y_i}{d_i}\right| \times d_i}{\sum_{i=1}^{n} d_i} \tag{14}$$

$$NS = 1 - \frac{\sum_{i=1}^{n}(d_i - y_i)^2}{\sum_{i=1}^{n}(d_i - d_{mean})^2} \tag{15}$$

$$RMSE = \sqrt{\frac{1}{N}\sum_{i=1}^{N}(d_i - y_i)^2} \tag{16}$$

$$VAF = \left(1 - \frac{var(d_i - y_i)}{var(d_i)}\right) \times 100 \tag{17}$$

$$PI = adj.R^2 + (0.01 \times VAF) - RMSE \tag{18}$$

$$WI = 1 - \left[\frac{\sum_{i=1}^{N} (d_i - y_i)^2}{\sum_{i=1}^{N} \left\{ |y_i - d_{mean}| + |d_i - d_{mean}| \right\}^2} \right] \quad (19)$$

$$MAE = \frac{1}{N} \sum_{i=1}^{N} |(y_i - d_i)| \quad (20)$$

$$MBE = \frac{1}{N} \sum_{i=1}^{N} (y_i - d_i) \quad (21)$$

$$U_{95} = 1.96 \left(SD^2 + RMSE^2 \right)^{\frac{1}{2}} \quad (22)$$

$$t\,stat = \sqrt{\frac{(N-1) MBE^2}{RMSE^2 - MBE^2}} \quad (23)$$

4. Results and discussion

4.1 Parameter and evaluation of models

The models are trained by using training data set under adjusting model parameters by trial and error method. The achievement of RVM model depends on the right selection of value of σ. The design value of σ has been determined using the trial and error method. The developed RVM model gives greatest performance shown in Table 1. The value of w has been represented in Figure 2. In Figure 2 it is clearly shown that 22 training datasets have non-zero w. So, number of relevance vector is 22. Figures 3-5 demonstrate the performance of training dataset and testing dataset. This article uses Determination coefficient (R^2) to asses the performance of the developed RVM, GPR and MPMR models. For a good model, the value of R^2 should be close to one. Figures 3-5 show that the value of R for both the training and testing datasets is close to one. For the prediction of X_{50}, the constructed RVM yields the following equation (Equation 24).

$$\varepsilon \mathrm{x} = \sum_{i=1}^{90} w_i \exp \left\{ -\frac{(x_i - x)(x_i - x)^T}{0.08} \right\} \quad (24)$$

For GPR model the design values of error ε and kernel function σ have been considered by the approach of trial and error method. Therefore, the developed GPR proves his ability for prediction of X_{50}. Similarly for MPMR, Figure 5 illustrates the performance of training and testing for the MPMR model. It is also clear from figure that the value of R^2 is close to one for training as well as testing datasets. The model tuning parameters are shows in the Table 2.

Table 2. Model tuning parameter.

	RVM	GPR	MPMR
ε	-	0.001	0.004
σ	0.2	0.5	0.7

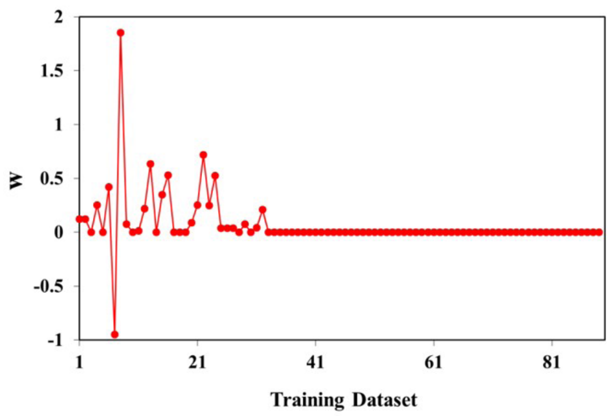

Figure 2. Weights Vs number of data for RVM.

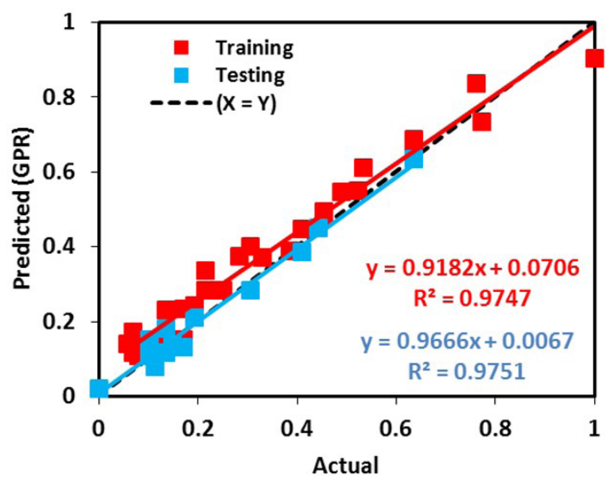

Figure 3. Actual Vs predicted plot for GPR.

For the training and testing datasets, a scatter plot is created showing actual against predicted values. Scatter plot measure the prediction capacity of the developed models using the target value and actual value. The point on the line $(y = x)$ denotes the predictive model's perfect prediction value. Similarly, a point close to the line denotes a model forecast that is accurate. Figures 3-5, depicts a graphical depiction of the actual and anticipated value performance for the training datasets and testing datasets. According to this graph, all three models are the best, especially RVM achieving $R^2 = 0.99$ in the training and testing stages of the model.

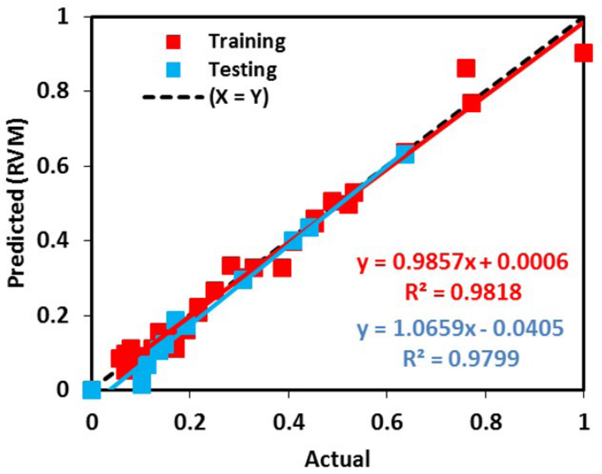

Figure 4. Actual Vs predicted plot for RVM.

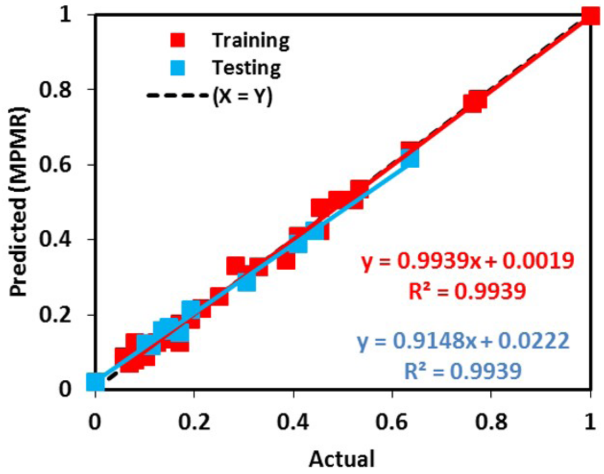

Figure 5. Actual Vs predicted plot for MPMR.

4.2 Statistical parameter

Table 3 shows the statistical parameters of the proposed models. In the rock sample, all of the models achieve above a 95% level of correlation. In every case of a rock sample, the models outperformed the humans. To account for the higher efficiency of the models, RMSE, MAE, and MBE should be near to 0, R^2 should be close to 1, and VAF should be close to 100. As a result, the improved fit of all of the models is confirmed. The degree of error in model predictions is measured by WI, which runs from 0 to 1. Its values near 1 are the most advantageous for good models. The model with the greater value is superior. All models have the best value based on the limits and range of parameters in these tables. MPMR values are best then RVM better than GPR. More detail of parameters are referred in Kardani et al. (2021).

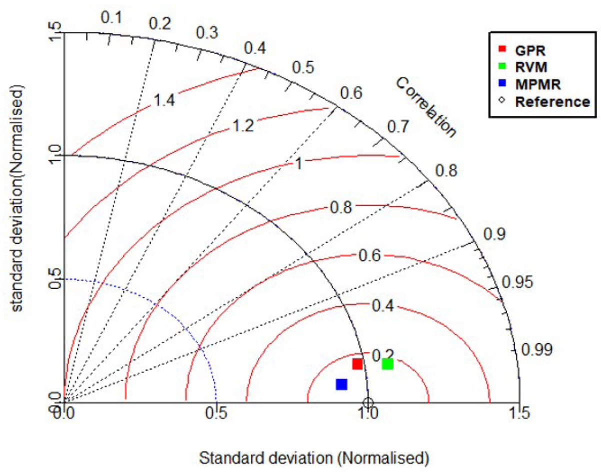

Figure 6. Taylor diagram for the dataset (training).

4.3 Taylor diagram

The mathematical diagrams are used to show which of various model's accuracy in single 2D, Taylor created this figure in 1994 (Taylor, 2001) to make comparing different models easier. The Pearson correlation coefficient, the root-mean-square error (RMSE), and the standard deviation are used to assess the degree of correspondence between the modeled and observed behavior in terms of three statistics. This diagram (Figures 6-7) is presented in this article using the GPR, MPMR, and RVM models. All models are performing well in the training and testing stages. When compared to GPR and MPMR, RVM is the best.

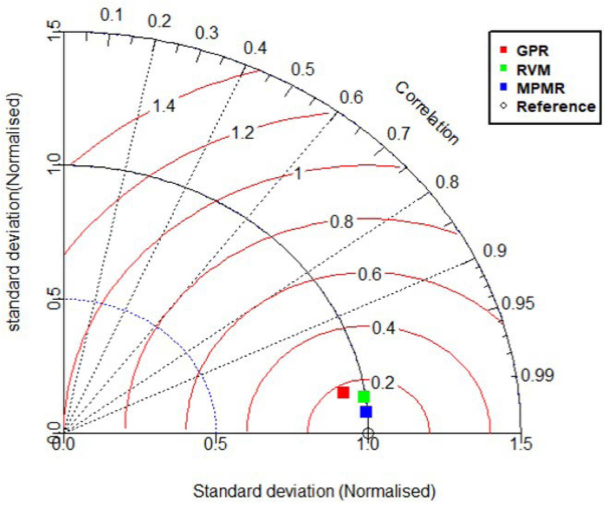

Figure 7. Taylor diagram for the dataset (testing).

4.4 Error bars

This section studies the error of predicted data in each model for the purposes of comparison of the model. The error bar diagrams are used to display the error level in models. Maximum, mean, and minimum values are also shown in Figures 8-10. In the GPR model has been described most of the values are negative and the range of -0.1 to 0.1. In RVM error values are in the range of -0.1 to 0.1 and the maximum, mean, and minimum values are also better than GPR. MPMR error values are comparatively best because the range of -0.06 to 0.06 and other maximum, mean and minimum values also. Therefore, the solution of this study MPMR has been the robust model.

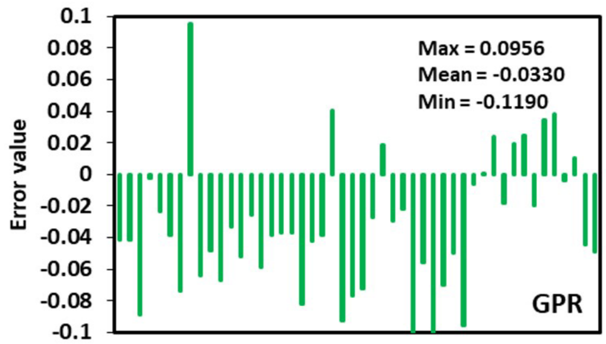

Figure 8. Error bars for GPR model.

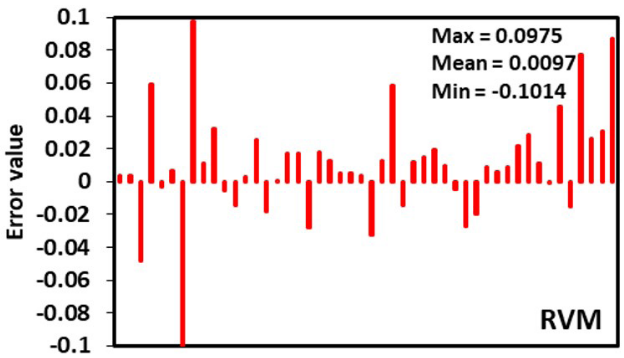

Figure 9. Error bars for RVM model.

4.5 DDR criterion

Developed discrepancy ratio also used in this paper and it was proposed by Noori et al. (2010). Evaluation have been dependent on MSE and R^2. DDR values were obtained by Equation 25. The standard error indexes a mean error value but does not provide information about the error distribution. As a result, the model's efficiency during the development phase must be assessed through the use of the dataset. Figures 11-12 shows the DDR results obtained for

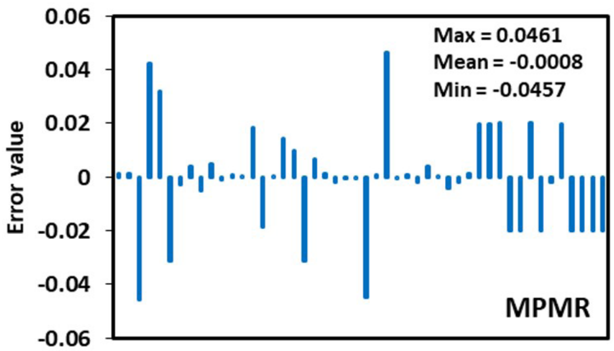

Figure 10. Error bars for MPMR model.

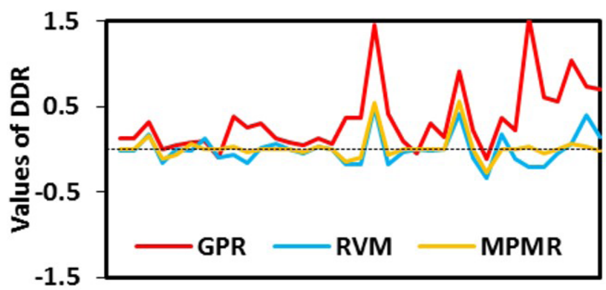

Figure 11. DDR values for train data.

Table 3. Evaluated statistical parameter values.

Parameters	GPR		RVM		MPMR		Ideal value
	Train	Test	Train	Test	Train	Test	
R^2	0.9747	0.9751	0.9818	0.9799	0.9939	0.9939	1
WMAPE	0.1780	0.0941	0.0714	0.1265	0.0356	0.0765	0
NS	0.9350	0.9720	0.9816	0.9409	0.9939	0.9863	1
RMSE	0.0609	0.0274	0.0324	0.0398	0.0186	0.0192	0
VAF	97.1459	97.2211	98.1804	97.0058	99.3929	98.6462	100
PI	1.8787	1.8684	1.9265	1.8837	1.9677	1.9477	2
MAPE	35.5901	15.2365	12.2803	24.2228	6.9645	10.3958	0
WI	0.9826	0.9929	0.9953	0.9867	0.9985	0.9963	1
MAE	0.0544	0.0227	0.0218	0.0305	0.0109	0.0185	0
MBE	0.0456	-0.0025	-0.0038	-0.0280	0.0000	0.0018	0
U95	0.2335	0.1717	0.2433	0.1934	0.2423	0.1580	0
t-sta	6.5916	0.3017	0.6848	3.2728	0.0023	0.3185	Smaller value

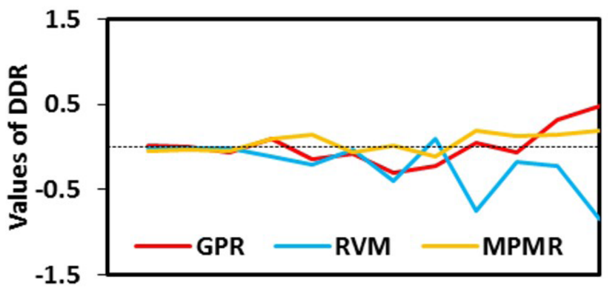

Figure 12. DDR values for test data.

all three models in the both (train and test) stages. The DDR figures shows the less deviation models (i.e.) MPMR curve nearly equal to zero line. When compared to the efficiency of other models based on DDR index, it reveals that the MPMR model is best.

$$DDR = \left(\frac{Estimated\ value}{Actual\ value}\right) - 1 \quad (25)$$

5. Conclusion

The machine learning methods were developed for predicting the rock fragmentation X_{50} due to drilling and blasting operations by using GPR, SVM, and MPMR models. A predicted all models were developed using factors such as blast design parameters, explosive parameters, modulus of elasticity, and in-situ block size. The developed models were trained using 90 training data and performance was tested by 13 testing data. The models were successfully demonstrated for predicting the rock fragmentation X_{50}. The performances were evaluated by using statistical parameter, Actual vs, predicted curve, Taylor diagram, Error bar diagram , and developed discrepancy ratio. All statistical parameter values of models were attained result within the ideal limit. Actual vs predicted show the accuracy of predicted value. Taylor diagram deals with three parameters like correlation, standard deviation, and RMSE in single 2D graph. In this diagram, the MPMR model behaved admirably. Error value also used to compared the models, MPMR have been reached very lesser range of error (-0.06 to 0.06). DDR values also showed nearer to the 0, in the case of MPMR. From this evaluation study, all models were performed well especially for MPMR has been performed best than other two models. The MPMR has been attained best accuracy of predicted value, $R^2 = 0.99$ in training and testing. Hence, the MPMR has been chosen as a robust model for predicting of rock fragmentation X_{50}. Expanding the blast databases that will be used to build the fragmentation prediction models outlined in this paper, as well as analyzing additional rock attributes of the rock mass that will be exposed to blasting if such information is available, could be part of future work.

Declaration of interest

The authors confirm that this research work content has no conflict of interest.

Authors' contributions

Pradeep Thangavel: conceptualization, developing models, visualization, and writing – original draft. Pijush Samui: conceptualization, data curation, methodology, and supervision.

List of symbols

x_{Actual}	actual data set
x_{Mini}	dataset's minimum value
x_{max}	dataset's maximum value
w	weight vector
ε	noise vector
N	number of datasets
α	hyperparameter vector
d_i	observed i^{th} value
y_i	predicted i^{th}
d_{mean}	average of the observed value
SD	standard deviation
K_{N+1}	covariance matrix

References

Aler, J., Mouza, J., & Arnould, M. (1996). Measurement of the fragmentation efficiency of rock mass blasting and its mining applications. *International Journal of Rock Mechanics and Mining Sciences & Geomechanics Abstracts*, *33*, 125-139. http://dx.doi.org/10.1016/0148-9062(95)00054-2.

Baiz, A.A., Ahmadi, H., Shariatmadari, F., & Torshizi, M.A.K. (2020). A Gaussian process regression model to predict energy contents of corn for poultry. *Poultry Science*, *99*, 5838-5843. http://dx.doi.org/10.1016/j.psj.2020.07.044.

Bamford, T., Esmaeili, K., & Schoellig, A.P. (2021). A deep learning approach for rock fragmentation analysis. *International Journal of Rock Mechanics and Mining Sciences*, *145*, 104839. http://dx.doi.org/10.1016/j.ijrmms.2021.104839.

Behar, O., Khellaf, A., & Mohammedi, K. (2015). Comparison of solar radiation models and their validation under Algerian climate - the case of direct irradiance. *Energy Conversion and Management*, *98*, 236-251. http://dx.doi.org/10.1016/j.enconman.2015.03.067.

Biswas, R., Samui, P., & Rai, B. (2019). Determination of compressive strength using relevance vector machine and emotional neural network. *Asian Journal of Civil Engineering*, *20*, 1109-1118. http://dx.doi.org/10.1007/s42107-019-00171-9.

Caywood, M.S., Roberts, D.M., Colombe, J.B., Greenwald, H.S., & Weiland, M.Z. (2017). Gaussian process regression for predictive but interpretable machine learning models: an example of predicting mental workload across tasks. *Frontiers in Human Neuroscience*, *10*, 1-19. http://dx.doi.org/10.3389/fnhum.2016.00647.

Chai, T., & Draxler, R.R. (2014). Root mean square error (RMSE) or mean absolute error (MAE)? Arguments against avoiding RMSE in the literature. *Geoscientific Model Development*, *7*, 1247-1250. http://dx.doi.org/10.5194/gmd-7-1247-2014.

Chalupka, K., Williams, C.K.I., & Murray, I. (2013). A framework for evaluating approximation methods for Gaussian process regression. *Journal of Machine Learning Research*, *14*, 333-350.

Hudaverdi, T., Kulatilake, P.H.S.W., & Kuzu, C. (2011). Prediction of blast fragmentation using multivariate analysis procedures. *International Journal for Numerical and Analytical Methods in Geomechanics*, *35*(12), 1318-1333.

Jethro, M.A., Ajayi, O.D., & Elijah, O.P. (2016). Rock fragmentation prediction using Kuz-Ram Model. *Journal of Environment and Earth Science*, *6*, 110-115.

Jug, J., Strelec, S., Gazdek, M., & Kavur, B. (2017). Fragment size distribution of blasted rock mass. *IOP Conference Series. Earth and Environmental Science*, *95*, 042013. http://dx.doi.org/10.1088/1755-1315/95/4/042013.

Kardani, N., Pradeep, T., Samui, P., Kim, D., & Zhou, A. (2021). Smart phase behavior modeling of asphaltene precipitation using advanced computational frameworks: ENN, GMDH, and MPMR. *Petroleum Science and Technology*, *39*(19-20), 804-825. http://dx.doi.org/10.1080/10916466.2021.1974882.

Kong, D., Chen, Y., Li, N., Duan, C., Lu, L., & Chen, D. (2019). Relevance vector machine for tool wear prediction. *Mechanical Systems and Signal Processing*, *127*, 573-594. http://dx.doi.org/10.1016/j.ymssp.2019.03.023.

Kulatilake, P.H.S.W., Qiong, W., Hudaverdi, T., & Kuzu, C. (2010). Mean particle size prediction in rock blast fragmentation using neural networks. *Engineering Geology*, *114*, 298-311. http://dx.doi.org/10.1016/j.enggeo.2010.05.008.

Kumar, M., Samui, P., Kumar, D., & Zhang, W. (2021). Reliability analysis of settlement of pile group. *Innovative Infrastructure Solutions*, *6*, 24. http://dx.doi.org/10.1007/s41062-020-00382-z.

Kumar, S., Rai, B., Biswas, R., Samui, P., & Kim, D. (2020). Prediction of rapid chloride permeability of self-compacting concrete using Multivariate Adaptive Regression Spline and Minimax Probability Machine Regression. *Journal of Building Engineering*, *32*, 101490. http://dx.doi.org/10.1016/j.jobe.2020.101490.

Kuznetsov, V.M. (1973). The mean diameter of the fragments formed by blasting rock. *Soviet Mining Science*, *9*, 144-148. http://dx.doi.org/10.1007/BF02506177.

Lanckriet, G.R.G., Ghaoui, L., Bhattacharyya, C., & Jordan, M.I. (2003). A robust minimax approach to classification. *Journal of Machine Learning Research*, *3*, 555-582. http://dx.doi.org/10.1162/153244303321897726.

Li, N., Nguyen, H., Rostami, J., Zhang, W., Bui, X., & Pradhan, B. (2022). Predicting rock displacement in underground mines using improved machine learning-based models. *Measurement*, *188*, 110552. http://dx.doi.org/10.1016/j.measurement.2021.110552.

Li, S., Zhao, H., & Ru, Z. (2017). Relevance vector machine-based response surface for slope reliability analysis. *International Journal for Numerical and Analytical Methods in Geomechanics*, *41*, 1332-1346. http://dx.doi.org/10.1002/nag.2683.

Mohamed, F., Riadh, B., Abderazzak, S., Radouane, N., Mohamed, S., & Ibsa, T. (2019). Distribution analysis of rock fragments size based on the digital image processing and the Kuz-Ram model Cas of Jebel Medjounes Quarry. *Aspects in Mining & Mineral Science*, *2*, 325-329. http://dx.doi.org/10.31031/amms.2019.02.000545.

Noori, R., Khakpour, A., Omidvar, B., & Farokhnia, A. (2010). Comparison of ANN and principal component analysis-multivariate linear regression models for predicting the river flow based on developed discrepancy ratio statistic. *Expert Systems with Applications*, *37*, 5856-5862. http://dx.doi.org/10.1016/j.eswa.2010.02.020.

Ozkahraman, H.T. (2006). Fragmentation assessment and design of blast pattern at Goltas limestone quarry, Turkey. *International Journal of Rock Mechanics and Mining Sciences*, *43*, 628-633. http://dx.doi.org/10.1016/j.ijrmms.2005.09.004.

Pradeep, T., Bardhan, A., & Samui, P. (2021). Prediction of rock strain using soft computing framework. *Innovative Infrastructure Solutions*, *7*, 37. http://dx.doi.org/10.1007/s41062-021-00631-9.

Samui, P. (2012). Application of relevance vector machine for prediction of ultimate capacity of driven piles in cohesionless soils. *Geotechnical and Geological Engineering*, *30*, 1261-1270. http://dx.doi.org/10.1007/s10706-012-9539-9.

Samui, P., & Kim, D. (2017). Minimax probability machine regression and extreme learning machine applied to compression index of marine clay. *Indian Journal of Geo-Marine Sciences*, *46*(11), 2350-2356.

Shi, X.Z., Zhou, J., Wu, B.B., Dan, H., & Wei, W. (2012). Support vector machines approach to mean particle size of rock fragmentation due to bench blasting prediction. *Transactions of Nonferrous Metals Society of China*, *22*(2), 432-441. http://dx.doi.org/10.1016/S1003-6326(11)61195-3.

Singh, B.K., Mondal, D., Shahid, M., Saxena, A., & Roy, P.N.S. (2019). Application of digital image analysis for monitoring the behavior of factors that control the rock fragmentation in opencast bench blasting: a case study conducted over four opencast coal mines of the Talcher

Coalfields, India. *Journal of Sustainable Mining*, *18*, 247-256. http://dx.doi.org/10.1016/j.jsm.2019.08.003.

Stone, R.J. (1994). A nonparametric statistical procedure for ranking the overall performance of solar radiation models at multiple locations. *Energy*, *19*, 765-769. http://dx.doi.org/10.1016/0360-5442(94)90014-0.

Strohmann, T., & Grudic, G.Z. (2003). A formulation for minimax probability machine regression. *Advances in Neural Information Processing Systems*, *15*, 1-8.

Tao, J., Yang, X.G., Li, H.T., Zhou, J.W., Qi, S.C., & Lu, G.D. (2020). Numerical investigation of blast-induced rock fragmentation. *Computers and Geotechnics*, *128*, 103846. http://dx.doi.org/10.1016/j.compgeo.2020.103846.

Taylor, K.E. (2001). Summarizing multiple aspects of model performance in a single diagram. *Journal of Geophysical Research, D, Atmospheres*, *106*(D7), 7183-7192.

Tipping, M.E. (2000). The relevance vector machine. *Advances in Neural Information Processing Systems*, *12*, 652-658.

Willmott, C.J. (1984). On the evaluation of model performance in physical geography. In G.L. Gaile & C.J. Willmott (Eds.), *Spatial statistics and models* (pp. 443-460). Dordrecht: Springer. https://doi.org/10.1007/978-94-017-3048-8_23.

Wong F.S. (1985). Slope reliability and response surface method. *Journal of Geotechnical Engineering*, *111*, 32-53.

Yang, Z., He, B., Liu, Y., Wang, D., & Zhu, G. (2021). Classification of rock fragments produced by tunnel boring machine using convolutional neural networks. *Automation in Construction*, *125*, 103612. http://dx.doi.org/10.1016/j.autcon.2021.103612.

Zhang, W., Zhang, R., Wang, W., Zhange, F., & Goh, A.T.C. (2019). A multivariate adaptive regression splines model for determining horizontal wall deflection envelope for braced excavations in clays. *Tunnelling and Underground Space Technology*, *84*, 461-471. http://dx.doi.org/10.1016/j.tust.2018.11.046.

Zhang, W., Zhang, R., Wu, C., Goh, A.T.C., & Wang, L. (2020a). Assessment of basal heave stability for braced excavations in anisotropic clay using extreme gradient boosting and random forest regression. *Underground Space*, *7*(2), 233-241. http://dx.doi.org/10.1016/j.undsp.2020.03.001.

Zhang, W., Zhang, R., Wu, C., Goh, A.T.C., Lacasse, S., Liu, Z., & Liu, H. (2020b). State-of-the-art review of soft computing applications in underground excavations. *Geoscience Frontiers*, *11*, 1095-1106. http://dx.doi.org/10.1016/j.gsf.2019.12.003.

Zhang, W.G., & Goh, A.T.C. (2013). Multivariate adaptive regression splines for analysis of geotechnical engineering systems. *Computers and Geotechnics*, *48*, 82-95. http://dx.doi.org/10.1016/j.compgeo.2012.09.016.

Zhang, W.G., Li, H.R., Wu, C.Z., Li, Y.Q., Liu, Z.Q., & Liu, H.L. (2020c). Soft computing approach for prediction of surface settlement induced by earth pressure balance shield tunneling. *Underground Space*, *6*(4), 353-363. http://dx.doi.org/10.1016/j.undsp.2019.12.003.

Soils and Rocks
An International Journal of Geotechnical and Geoenvironmental Engineering
www.soilsandrocks.com
ISSN 1980-9743
ISSN-e 2675-5475

Development of neuro-fuzzy models for predicting shear behavior of rock joints

Silvrano Adonias Dantas Neto[1#], Matheus Cavalcante Albino[1], Ana Raquel Sena Leite[1], Ammanda Aragão Abreu[1]

Article

Keywords
Rock discontinuities
Shear strength
Dilation
Neuro-fuzzy technique

Abstract

The purpose of this article is to present predictive models of dilation and shear stress of rock discontinuities by applying the neuro-fuzzy technique, which uses a) the high capacity of artificial neural networks (ANN) to understand and to model complex multivariate phenomena, and b) the concepts of fuzzy sets theory to consider the variability of the input parameters in the proposed models' responses. To develop the proposed models, experimental results were obtained from large-scale direct shear tests performed on different types of rock discontinuities and boundary conditions. The input variables of the proposed neuro-fuzzy models are the normal boundary stiffness, the ratio of fill thickness to asperity height, the initial normal stress, the joint roughness coefficient, the uniaxial compressive strength of the intact rock, the basic friction angle of the intact rock, the friction angle of the infill, and the shear displacement. The proposed models for dilation and shear stress provided results that fitted satisfactorily the experimental data, and the analyses of their performances indicated that they can represent the influence of the input variables on the shear behavior parameters of the rock discontinuities. The results from the neuro-fuzzy systems developed are also closer to the experimental data than those estimated by using traditional analytical methodologies existing in Rock Mechanics. This occurs because once considering the uncertainty of the input data, a more representative shear behavior prediction can be made by the neuro-fuzzy models.

1. Introduction

The discontinuities present in the rock masses are one of the main factors influencing their mechanical behavior. Distinct studies have aimed to estimate the shear behavior of the rock discontinuities, to provide parameters to analyze and design projects in Rock Mechanics realistically.

Several analytical models have been developed to represent the shear behavior of rock discontinuities. Some works worth mentioning are Barton (1973), Barton & Choubey (1977), Barton & Bandis (1990), Skinas et al. (1990), Papaliangas et al. (1993), Indraratna & Haque (2000), Indraratna et al. (2005, 2008, 2010, 2013), and Oliveira & Indraratna (2010). However, application of such analytical models is limited because they do not consider some key-factors governing the shear behavior of the rock discontinuities, such as the normal boundary stiffness imposed by the surrounding rock mass and the presence of infill material, or due to the difficulty in obtaining some of their parameters. Due to these limitations, other analysis methodologies have been used in Rock Mechanics, such as the intelligent systems that use the artificial neural networks (ANN), the fuzzy logic, and the neuro-fuzzy techniques to predict the shear behavior of the rock discontinuities (Dantas Neto et al., 2017; Leite et al., 2019a, b).

Besides the studies with the use of ANN have shown its excellent performance for predicting the shear behavior of rock discontinuities, some of the highlighted disadvantages, which can be also attributed to the analytical models, regards their deterministic character, i.e., the fact that they cannot consider the influence of the variability and uncertainties inherent to the input variables in their predictions. Thus, some systems which are developed based on the concepts of the fuzzy sets theory, or fuzzy logic, present themselves as an alternative for the development of predictive models that may consider the variability and uncertainties of the input variables in the models' responses without requiring a widespread field or laboratory investigation.

The fuzzy logic proposed by Zadeh (1965) is like a tool designed to address subjective problems, involving imprecise and vague data, in addition to being able to use prior knowledge on such studied phenomena. Using the

[#]Corresponding author. E-mail address: silvrano@ufc.br
[1]Universidade Federal do Ceará, Departamento de Engenharia Hidráulica e Ambiental, Fortaleza, CE, Brasil.
Submitted on March 11, 2022; Final Acceptance on September 23, 2022; Discussion open until February 28, 2023
https://doi.org/10.28927/SR.2022.003322

potential of fuzzy logic, several studies have been done on Rock Mechanics to predict some rock mass and intact rock properties, such as Kayabasi et al. (2003), Sonmez et al. (2003), and Harrison & Hudson (2010). However, results presented by Matos et al. (2019a, b) indicate that the fuzzy logic has proven somewhat satisfactory for predicting the peak shear strength of the rock discontinuities but has not provided results that help to properly represent its variation with the shear displacement imposed on the unfilled discontinuities.

Therefore, to use the high learning potential inherent in the ANN and the capacity of the fuzzy sets in considering the variability or uncertainties of the input parameters in the predictive model responses, Jang (1993) proposes a neuro-fuzzy controller called ANFIS (Adaptive-Network-based Fuzzy Inference System), which is based on the construction of a set of fuzzy inference rules from appropriate membership functions, creating adjusted in-out patterns. In Rock Mechanics, some of the developed neuro-fuzzy systems were proposed by Gokceoglu et al. (2004), Singh & Singh (2006), Noorani et al. (2010), Jalalifar et al. (2011), and Yesiloglu-Gultekin et al. (2013) for modeling some properties of the rock masses and the intact rocks.

Matos (2018) and Matos et al. (2019a, b) proposed fuzzy and neuro-fuzzy models that provide predictions of the shear behavior of unfilled rock discontinuities. Although they supply satisfactory results, these models do not consider the effect of the infill material, which is one of the main factors influencing the shear behavior of rock discontinuities (Papaliangas et al., 1993; Haque, 1999; Indraratna et al., 2010, 2013; Oliveira & Indraratna, 2010; Shrivastava & Rao, 2018).

In this context, the objective of this article is to present predictive models of dilation and shear stress of the rock discontinuities based on neuro-fuzzy techniques, which use the high capacity of the artificial neural networks in representing complex and multivariate phenomena, and the concepts inherent in the fuzzy sets, allowing for consideration of the variability or uncertainties of the input data in the responses of the proposed systems.

2. Modeling in rock mechanics with intelligent systems

As an alternative to existing analytical models (Barton, 1973; Barton & Choubey, 1977; Barton & Bandis, 1990; Skinas et al., 1990; Indraratna et al., 2005, 2008, 2010, 2013, 2014, 2015; Oliveira & Indraratna, 2010; etc.), and to facilitate the prediction process of shear behavior of the rock discontinuities under different boundary conditions, intelligent systems using artificial neural networks, fuzzy logic, and neuro-fuzzy techniques have been increasingly applied in Rock Mechanics (Jalalifar et al., 2011; Ocak & Seker, 2012; Yesiloglu-Gultekin et al., 2013; Dantas Neto et al., 2017; Sadrossadat et al., 2018; Matos, 2018; Matos et al., 2019a, b; Leite et al., 2019a, b). The choice of these systems is usually based on several factors which consider the high capacity of understanding and modeling multivariate and non-linear complex problems.

2.1 Fuzzy logic

Zadeh (1965) introduced the concept of fuzzy sets, the role of which is to represent human knowledge on a determined phenomenon, or problem, by treating the information vaguely and imprecisely. According to the author, fuzzy sets are represented by membership functions, in which they associate each element of the set to the respective degree of membership, whose value is between 0 and 1. Unlike the deterministic approach, in which a single value is attributed to a certain input variable in a model, the fuzzy set theory attributes to it a set of possible values within a given membership level (Zadeh, 1965; Jang et al., 1997).

The basic structure of a fuzzy inference system consists of three conceptual components: a set of rules, representing the relations between the fuzzy sets; a database, which defines all membership functions used in the fuzzy rules; and a reasoning process, that executes the inference procedure over the fuzzy rules, producing a response or output. There are different types of fuzzy inference systems, the best-known being those proposed by Mamdani (1974), Tsukamoto (1979), and Takagi & Sugeno (1983).

Harrison & Hudson (2010) states that mathematics present in fuzzy logic can be a proper tool to solve Rock Mechanics problems, bearing in mind that it allows consideration of the uncertainties present in the rock masses and their structures. Using fuzzy logic features, some studies such as those presented by Sonmez et al. (2003), Kayabasi et al. (2003) have used the logic fuzzy to predict properties in the rock masses.

Based on a fuzzy inference system of the Mamdani (1974) type, Sonmez et al. (2003) estimated several parameters necessary for characterizing rock mass using the Geological Strength Index (GSI). The authors concluded that the fuzzy sets provide a more practical way of working with cases in which the data are limited and uncertain.

Kayabasi et al. (2003) estimated the rock mass deformation modulus based on simple regressions, multiple regressions, and a Mamdani (1974) fuzzy inference system. The authors' results show that the predictions made by the fuzzy system were more reliable compared to the experimental data.

Matos (2018) and Matos et al. (2019a, b) used the Mamdani (1974) and Takagi & Sugeno (1983) type fuzzy models for predicting the shear behavior of unfilled rock discontinuities. Based on the authors' results, it was found that first-order Takagi & Sugeno (1983) models were those that performed best in dilation and shear stress estimations, comparing the output data of these systems with the experimental data used. Besides, their results have shown good performance only to predict the peak shear stress.

According to the aforementioned works, it is possible to observe the difficulty of choosing the suitable membership functions for each input variable considered in any modeled phenomenon remains the main limitation of fuzzy logic systems. Besides, the higher the number of input variables the higher the computational effort necessary to perform the inference procedures during the modeling process.

2.2 Artificial Neural Networks (ANN)

Haykin (2008) defines an artificial neural network as a mechanism formed by processors distributed in parallel layers, consisting of processing units that are called artificial neurons, having the natural tendency to store knowledge and make it available for use. One of the main types of ANN used in engineering is the multilayer perceptron, which is a feed-forward neural network formed typically of three types of layers: the input layer, whose main function is to receive the external "stimulus"; the hidden layers, responsible for extracting more complex statistics from the modeled mechanism; and the output layer, which provides the results of the modeled phenomenon by the ANN (Haykin, 2008).

An artificial neural network is trained by alterations in their synaptic weights and biases, using a specific learning algorithm and the knowledge about the existing modeled phenomenon in a set of experimental data containing known input-output patterns. After the training phase, the performance of the neuronal model is checked at a phase called testing, using a set of input-output values that was not presented to the network during the alteration of synaptic weights and biases. In general, in the process of defining a neuronal model, various architectures are trained and tested until identifying a configuration that has the best performance in predicting the responses during the training phase, and which demonstrates a satisfactory capacity to generalize knowledge of the phenomenon modeled by the neuronal network during testing (Haykin, 2008; Dantas Neto et al., 2017).

The functionalities and high learning capacity of the ANN have led to the development of various studies in Rock Mechanics, for example, by Sonmez et al. (2016), Dehghan et al. (2010), Ocak & Seker (2012), Dantas Neto et al. (2016, 2017), Leite et al. (2019a, b) and others.

Dehghan et al. (2010) used regressions and neuronal models to predict the uniaxial compressive strength and the elastic modulus in samples of the rock mass. The authors concluded that the results of the models developed with ANN were closer to the experimental data used, emphasizing the capacity of those systems to represent the nonlinear aspects of the phenomena studied.

Dantas Neto et al. (2016, 2017) produced a model that uses ANN to predict dilation and shear stress found in unfilled discontinuities. Considering the main factor influencing the shear behavior of rock discontinuities, the model gave satisfactory results when compared to the experimental data used in their development, as well as allowing the user faster and more practical calculations of the estimations.

Dantas Neto et al. (2017) and Leite et al. (2019a, b) also proposed predicting models for the shear behavior of unfilled and infilled rock discontinuities under constant normal stiffness (CNS) and constant normal loading (CNL) conditions with multilayer perceptrons. It can be observed that these neuronal models have provided results closer to the experimental data than the estimations obtained from applying different analytical models used by the authors, showing the capacity of the ANN to predict the shear behavior of rock discontinuities.

2.3 Neuro-fuzzy systems

Jang et al. (1997) mention that the modeling process of a neuro-fuzzy problem is based on two segments: the artificial neural network, which recognizes patterns to adapt to the change in their medium, and the fuzzy inference system, which allows the incorporation of human knowledge and perform a role of inference and decision-making about a specific problem. Jang (1993) proposed a class of ANN that are functionally equivalent to a fuzzy inference system known as the Adaptive Network-based Fuzzy Inference System (ANFIS). Figure 1 illustrates an ANFIS model made up of two fuzzy inference rules, based on the concepts of the fuzzy inference system of the Takagi & Sugeno (1983) type for representing a specific phenomenon.

Jang (1993) differentiates each layer shown in Figure 1 according to its functions. The nodes in Layer 1 are not adaptable and the values of its nodes are defined according to Equation 1, where x and y are the input in the nodes, and A_i, or B_i, are the fuzzy sets associated with the nodes. In this example, "i" depicts the value of 1 and 2 in virtue of the number of fuzzy inference rules and sets used. Each output ($O_{1,i}$) of Layer 1 is the value of the degree of membership obtained from x and y, calculated by any preestablished membership function.

$$O_{1,i} = \mu_{A_i(x)} \; ou \; O_{1,i} = \mu_{B_i(y)}, \; i = 1,2 \tag{1}$$

Layer 2 is made up of fixed nodes, which function is to calculate the product of the input signals, according to

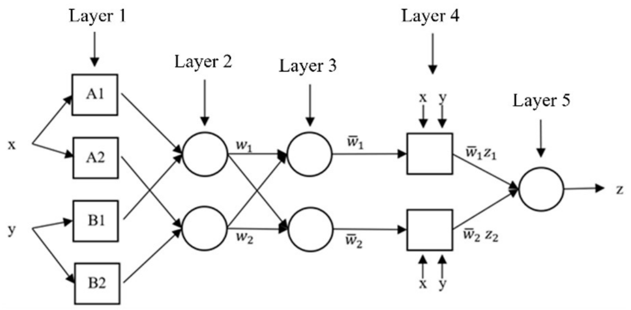

Figure 1. Diagram of an ANFIS neuro-fuzzy model (Jang, 1993).

Equation 2. Each output of this layer represents the weight of its fuzzy inference rule.

$$O_{2,i} = w_i = \mu_{A_i(x)} \cdot \mu_{B_i(y)},\ i = 1,2 \quad (2)$$

The nodes in Layer 3 are also fixed and they calculate the ratio between the weight of each fuzzy rule and the sum of the weights of all fuzzy rules according to Equation 3.

$$O_{3,i} = \overline{w}_i = \frac{w_i}{w_1 + w_2},\ i = 1,2 \quad (3)$$

Layer 4 contains adaptable nodes that have outputs computed according to Equation 4, in which $\overline{w}_i$ is the output from Layer 3 and p_i, q_i, and r_i are referred to as consequent parameters.

$$O_{4,i} = \overline{w}_i z_i = \overline{w}_i \left(p_i x + q_i y + r_i \right) \quad (4)$$

Finally, Layer 5 is characterized by a single fixed node, whose function is to calculate the output (z) of the neuro-fuzzy system by summing all its input signals together, according to Equation 5.

$$O_{5,i} = z = \sum_i \overline{w}_i z_i \quad (5)$$

Jang (1993) points out that when the premise parameters are fixed, the output (z) of the neuro-fuzzy system can be expressed through a linear combination of the consequent parameters, as presented in Equation 6.

$$z = (\overline{w}_1 x) p_1 + (\overline{w}_1 y) q_1 + (\overline{w}_1) r_1 + (\overline{w}_2 x) p_2 + (\overline{w}_2 y) q_2 + (\overline{w}_2) r_2 \quad (6)$$

The linear combination represented in Equation 6 allows the hybrid learning process proposed by Jang (1993). This process consists of two phases: the forward phase, when the outputs proceed to Layer 4, the consequent parameters being calculated by the least-squares method; and the backward phase when the error sign is defined by the difference between the output calculated by the ANFIS system and the experimental data spreads through the system and the premise parameters are calculated by the gradient descent method (Jang, 1993; Jang et al., 1997). Thus, the ANFIS neuro-fuzzy system tends to move closer to the desired response pattern, comprising the problem under analysis with the modification of the parameters inherent to the membership functions, which result in the development of optimized fuzzy sets.

In the training process of the ANFIS neuro-fuzzy systems, an initial structure is required with fuzzy sets and established membership functions. Jang et al. (1997) point to various methodologies that can be used in developing these initial structures, such as the grid partitioning method and the subtractive clustering technique. The grid partitioning method is based on dividing the input variables domain in equally spaced sizes from membership functions of the same format. In the case of the subtractive clustering method proposed by Chiu (1994), the clustering centers are created according to the distribution of the input data in the variable domains based on the concept of data density, which creates the number of membership functions necessary to represent the problem under analysis.

Neuro-fuzzy systems have been used in several Rock Mechanics applications, such as those presented by Gokceoglu et al. (2004), Singh & Singh (2006), Noorani et al. (2010), Jalalifar et al. (2011), Yesiloglu-Gultekin et al. (2013), Sadrossadat et al. (2018), Matos (2018).

Gokceoglu et al. (2004) used a neuro-fuzzy model to estimate the rock mass deformation modulus. From the study, it was noticeable that the results from the developed neuro-fuzzy system were closer to the experimental data than the predictions made by the empirical models used by the authors.

Singh & Singh (2006), in turn, developed neuro-fuzzy models and ANN to predict the Poisson's ratio and Young's modulus of intact rocks. The authors used as input variables in their models the property of intact rock, as the uniaxial compressive strength and tensile strength. Comparing the results from the developed models, the neuro-fuzzy system provided estimations closer to the experimental data.

Matos (2018) used ANFIS systems to predict the shear behavior of unfilled rock discontinuities submitted to CNS and CNL conditions. The models gave satisfactory results when compared to the experimental data used in their development. Despite the results, the neuro-fuzzy systems developed by these authors do not consider the presence of the fill material in the shear behavior of rock discontinuities restricting their use only to certain field situations.

3. Development of neuro-fuzzy models

3.1 Experimental data

Experimental data were obtained from 116 large-scale direct shear tests undertaken by Benmokrane & Ballivy (1989), Skinas et al. (1990), Papaliangas et al. (1993), Haque (1999), Indraratna & Haque (2000), Oliveira et al. (2009), Indraratna et al. (2010), Mehrishal et al. (2016) and Shrivastava & Rao (2018). This survey results in a set of data with 2098 input-output patterns to be used in developing and evaluating the neuro-fuzzy models for predicting dilation and shear stress of rock discontinuities. Different conditions for the rock discontinuities can be observed for the data available in the used dataset in terms of uniaxial compressive strength (soft to hard rocks), roughness profile (slightly to very rough), external boundary conditions (CNL and CNS), condition of infill (unfilled and infilled rock discontinuities), which show the wide variety of situations considered in the experimental data used in developing the proposed models. In direct shear tests carried out on CNL condition, the normal stress is constant during shearing, while in CNS conditions

3.2 Defining the input and output variables

The input variables of the neuro-fuzzy models were defined to take into consideration the main factors governing the shear behavior of rock discontinuities represented by the dilation (δ_v), in mm, and shear stress (τ_s), in MPa, during the shear process. They are:

- Normal boundary stiffness (k_n), in kPa/mm;
- Ratio of thickness of the infill material (t) to asperity height of the discontinuity (a) - t/a ratio;
- Initial normal stress (σ_{no}), in MPa;
- Joint roughness coefficient (*JRC*);
- Uniaxial compressive strength of intact rock (σ_c), in MPa;
- Basic friction angle of intact rock (ϕ_b), in degrees;
- Friction angle of infill material (ϕ_{infill}), in degrees;
- Shear displacement (δ_h), in mm.

The maximum and minimum values of the collected experimental data for the defined input and output variables are presented in Table 1. These values must be considered as the limits to which the models can be applied since they were used to establish the membership functions of the variables involved and to define the fuzzy inference rules.

3.3 Training of neuro-fuzzy models

The ANFIS models developed are based on the principles of the fuzzy inference systems of Takagi & Sugeno (1983) and the hybrid learning proposed by Jang (1993). The ANFIS systems for predicting the parameters that define the shear behavior of rock discontinuities were modeled first by neuro-fuzzy model training, in which 80% of the experimental data was randomly chosen from the available experimental. The remaining data (20%) were used later in the test phase of the developed models.

Concerning the initial structure, input variables, and membership functions adopted, different configurations were tested for the following neuro-fuzzy models:

- Model 1: created by the grid partitioning method, presenting two (2) Gaussian membership functions for the eight input variables;
- Model 2: created by the grid partitioning method, presenting three (3) Gaussian membership functions for the input variable *t/a*, and two (2) Gaussian membership functions for the remaining variables;
- Model 3: created by the grid partitioning method, presenting three (3) Gaussian membership functions for the input variables *t/a* and δ_h, and two (2) Gaussian membership functions for the remaining variables;
- Model 4: created by the grid partitioning method, presenting three (3) Gaussian membership functions for input variables *t/a*, δ_h, k_n and σ_c, and two (2) Gaussian membership functions for the remaining variables;
- Model 5: created by the subtractive clustering method, in which the number of Gaussian membership functions is obtained for each model itself;
- Model 6: variable ϕ_b is not considered as an input variable in the model, the initial structure is created using the grid partitioning method, presenting two (2) Gaussian membership functions for all remaining input variables;
- Model 7: variable ϕ_b is not considered as an input variable in the model, the initial structure is considered using the grid partitioning method, presenting three (3) Gaussian membership functions for the input variables *t/a* and δ_h, and two (2) Gaussian membership functions for the remaining input variables;
- Model 8: variables ϕ_b and ϕ_{infill} are not considered as input variables in the model, the initial structure is created using the grid partitioning method, presenting two (2) Gaussian membership functions for the other input variables;
- Model 9: variables ϕ_b and ϕ_{infill} are not considered as input variables in the model, the initial structure is created using the grid partitioning method, presenting three (3) Gaussian membership functions for the input variables *t/a* and δ_h, and two (2) Gaussian membership functions for the remaining variables.

Table 2 summarizes the main configurations established for the different neuro-fuzzy models evaluated in this paper

Table 1. Maximum and minimum values of the models' variables.

Input variables								Output variables	
k_n	t/a	σ_{n0}	JRC	σ_c	ϕ_b	ϕ_{fill}	δ_h	δ_v	τ
kPa/mm		MPa		MPa	degrees	degrees	mm	mm	MPa
0	0	0.05	2	3.5	30	0	0.02	-2.43	0.02
7515	2	46.5	20	150	37.5	35.5	26	4.97	6.68

Table 2. Configuration of studied neuro-fuzzy models.

Model	Initial structure method	Membership funcion	Number of membership functions for the considered input variables							
			K_n	t/a	σ_{no}	JRC	σ_c	ϕ_b	ϕ_{fill}	δ_h
1	Grid partitioning	Gaussian	2	2	2	2	2	2	2	2
2	Grid partitioning	Gaussian	2	3	2	2	2	2	2	2
3	Grid partitioning	Gaussian	2	3	2	2	2	2	2	3
4	Grid partitioning	Gaussian	3	3	2	2	3	2	2	3
5	Subtractive clustering	Gaussian	variable	variable	variable	variable	variable	variable	variable	variable
6	Grid partitioning	Gaussian	2	2	2	2	2	-	2	2
7	Grid partitioning	Gaussian	2	3	2	2	2	-	2	3
8	Grid partitioning	Gaussian	2	2	2	2	2	-	-	2
9	Grid partitioning	Gaussian	2	3	2	2	2	-	-	3

in an attempt to find out the model which presents the best performance in the shear behavior of the rock discontinuities. The grid partitioning method was used in all ANFIS models tested except for Model 5, in which the subtractive clustering partitioning was used to evaluate the performance of the ANFIS model when its training process is influenced by the distribution of the input data, as described in section 2.3. In this case, the number of membership functions is created according to the distribution of the input data values used in the modeling and not arbitrarily chosen by the expert. Then, it was tested whether the definition of the number of membership functions according to the distribution of available input data could improve the performance of the ANFIS models rather than the use of grid partitioning method.

With definition of such structures, one of the aims is to assess the influence of the input variables in the performance of the proposed neuro-fuzzy models. The choice of Gaussian membership functions in establishing the fuzzy sets representing the input variables was based on the satisfactory results from the various studies that adopted this function (Singh & Singh, 2006; Jalalifar et al., 2011).

The software used to develop ANFIS neuro-fuzzy models was MATLAB (Jalalifar et al., 2011; Yesiloglu-Gultekin et al., 2013). At the training phase, the different ANFIS models were developed by comparing the results obtained for each output variable (dilation or shear stress) with the experimental data, so that the parameters were created to form the membership functions and fuzzy inference rules to obtain the best performing neuro-fuzzy system possible.

3.4 Criteria for model selection and model validation

The selection criterion of the ANFIS systems was based on the comparison between the predictions made by the tested models and the experimental data used during the test phase by using the coefficient of determination (R^2). The neuro-fuzzy models that had R^2 values in the test phase higher than 0.95 were considered apt to be assessed at a later stage called the validation phase.

The validation phase consisted of predicting the shear stress and dilation of hypothetical rock discontinuities similar to the methodology used by Dantas Neto et al. (2017) to validate ANN models for predicting the shear behavior of unfilled rock discontinuities. This procedure allows checking whether the neuro-fuzzy models can represent satisfactorily the influence of the input variables on shear behavior of such discontinuities (Indraratna et al., 2014, 2015; Oliveira et al., 2009; Barton, 2013, 2016; Naghadehi, 2015; Shrivastava et al., 2011).

4. Results and discussions

4.1 ANFIS model training and testing

Tables 2-4 provide the values of the coefficients of determination (R^2) obtained during the training and testing phases of the neuro-fuzzy systems developed for predicting the dilation (D) and shear stress (S), respectively, for the different tested models. According to them, it is noticeable that the models showing the best performances are *D1*, *D2*, *D3*, and *D4* for predicting dilation, and *S1*, *S2*, *S3*, and *S4* for shear stress of rock discontinuities. The high R^2 values obtained in the training and testing phases express the excellent performance of the ANFIS models for predicting shear stress and dilation under CNL and CNS condition in rock discontinuities for a variety of conditions in terms of infill and roughness. Such results can be attributed to the consideration of uncertainties in the values of the input variables in the response of neuro-fuzzy models making them able to satisfactorily represent the phenomenon studied

Furthermore, it is found that the systems which did not consider all input variables, such as models *D6*, *D7*, *D8*, *D9*, *S6*, *S7*, *S8*, and *S9*, had inferior performances when compared to the models which use all input variables. This shows how important is to consider all the parameters governing the shear behavior of the rock discontinuities in the development of the proposed neuro-fuzzy models.

Table 3. Results in the training and test phases of the dilation prediction systems.

Model	Input variables	Initial structure	Membership functions	R^2 test	R^2 training
D1	8	Grid partitioning	2	0.99	0.99
D2	8	Grid partitioning	2, except *t/a* (3)	0.99	0.99
D3	8	Grid partitioning	2, except *t/a* and δ_h (3)	0.98	0.99
D4	8	Grid partitioning	2, except *t/a*, δ_h, k_n and σ_c (3)	0.98	0.99
D5	8	Subtractive clustering	14	0.92	0.90
D6	7	Grid partitioning	2	0.00	0.01
D7	7	Grid partitioning	2, except *t/a* and δ_h (3)	0.14	0.25
D8	6	Grid partitioning	2	0.00	0.01
D9	6	Grid partitioning	2, except *t/a* and δ_h (3)	0.01	0.02

Table 4. Results obtained in the training and test phases of the shear stress prediction systems.

Model	Input variables	Initial structure	Membership functions	R^2 test	R^2 training
S1	8	Grid partitioning	2	0.96	0.97
S2	8	Grid partitioning	2, except *t/a* (3)	0.96	0.97
S3	8	Grid partitioning	2, except *t/a* and δ_h (3)	0.97	0.98
S4	8	Grid partitioning	2, except *t/a*, δ_h, k_n and σ_c (3)	0.95	0.98
S5	8	Subtractive clustering	14	0.92	0.93
S6	7	Grid partitioning	2	0.10	0.28
S7	7	Grid partitioning	2, except *t/a* and δ_h (3)	0.37	0.50
S8	6	Grid partitioning	2	0.00	0.00
S9	6	Grid partitioning	2, except *t/a* and δ_h (3)	0.04	0.06

About the method used in the initial structure of the ANFIS systems, it is worth mentioning that models *D5* and *S5*, developed from the subtractive clustering technique, presented lower R^2 values than those obtained in the training and testing phases by models *D1*, *D2*, *D3*, *D4*, *S1*, *S2*, S3 and *S4*, which used the grid partitioning technique. This shows that by dividing the domain of input variables by the membership functions in equal sizes, it proved more efficient in predicting the shear behavior of rock discontinuities.

According to the results given in Tables 2-4, it is found that the increase in the number of membership functions did not correspond necessarily to an improvement in the performance of the ANFIS models. This can be confirmed by comparing the R^2 values obtained in the test phase in the *D2* and *D4*, and *S2* and *S4* systems, when there was a drop in the coefficients of determination even with the increase in the number of membership functions for more input variables.

4.2 Validation of neuro-fuzzy models

Neuro-fuzzy models used in the validation phase were *D1*, *D2*, *D3*, and *D4* to predict dilation, and *S1*, *S2*, *S3*, and *S4*, to predict the shear stress.

The hypothetical rock discontinuities used to validate the neuro-fuzzy models have the same characteristics considered by Dantas Neto et al. (2017) and Leite et al. (2019a, b). Therefore, for the hypothetical unfilled rock discontinuities the following parameters were considered: *JRC* = 5; σ_c = 12 MPa e ϕ_b = 37.5°. For hypothetical infilled discontinuities, it was considered that the shear strength of the infill material is characterized by a friction angle (ϕ_{infill}) of 35.5°.

The models with the best results in predicting the shear behavior of the hypothetical discontinuities were the ANFIS *D1* and *S2* systems, as shown in Figures 2-5 and in Figures 6-9 for dilation and shear stress results, respectively.

According to the results presented between Figure 2 and Figure 5, it is observed that the ANFIS *D1* model can satisfactorily represent the drop in dilation in the hypothetical rock discontinuity with the increase in normal boundary stiffness (k_n), initial normal stress (σ_{no}), and the *t/a* ratio. In addition, higher dilation values have been obtained with the increased roughness in the discontinuity, represented by the *JRC* value. Such results can be considered satisfactory to the extent that they express the trends seen in different studies (Indraratna & Haque, 2000; Indraratna et al., 2005, 2008, 2010, 2013, 2014, 2015; Oliveira et al., 2009; Oliveira & Indraratna, 2010; Barton, 2013, 2016; Naghadehi, 2015; Shrivastava et al., 2011; Shrivastava & Rao, 2018).

Figures 6-9 show the results obtained with the *S2* neuro-fuzzy model considering the input variables of the hypothetical rock discontinuities. These results show that the *S2* model is capable to express the increase of shear stress values with the normal boundary stiffness (Figure 6), initial normal stress (Figure 7), and roughness (Figure 9). It is also possible to observe its ability to represent the drop in shear stress with the increase in *t/a* ratio (Figure 8), and also due to the asperity

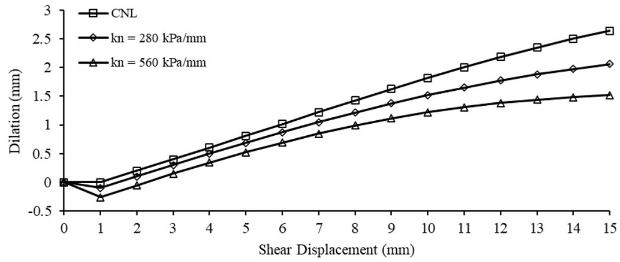

Figure 2. Effect of normal boundary stiffness on the dilation (σ_{no} = 0.5 MPa).

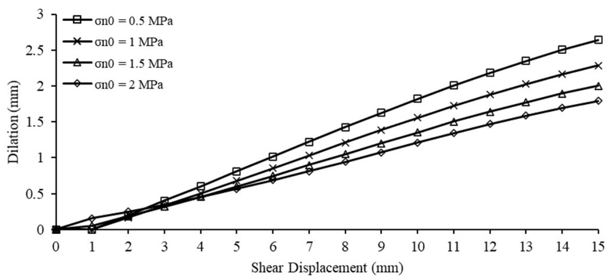

Figure 3. Effect of initial normal stress on the dilation (k_n = 0 kPa/mm).

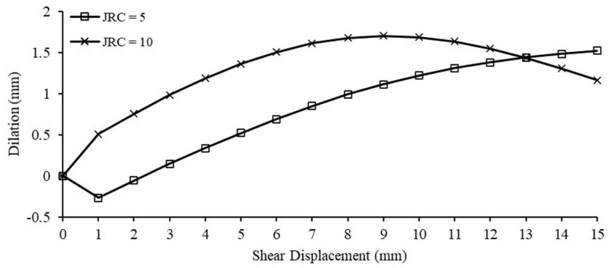

Figure 4. Effect of join|t roughness on the dilation (k_n = 560 kPa/mm and σ_{no} = 0.5 MPa).

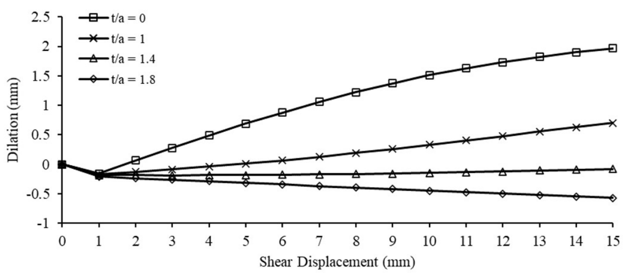

Figure 5. Effect of infill on the dilation (k_n = 425 kPa/mm and σ_{n0} = 0.3 MPa).

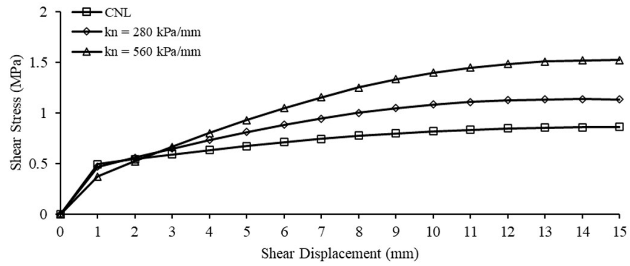

Figure 6. Effect of normal boundary stiffness on the shear stress (σ_{no} = 0.5 MPa).

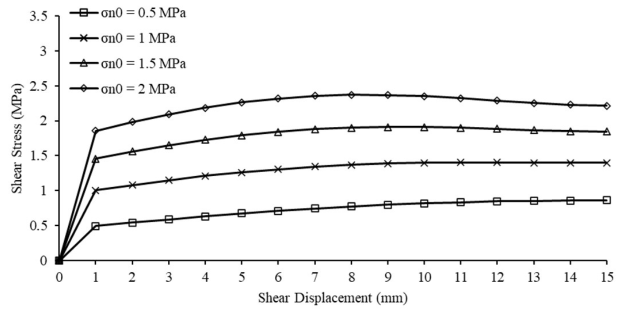

Figure 7. Effect of initial normal stress on the shear stress (k_n = 0 kPa/mm).

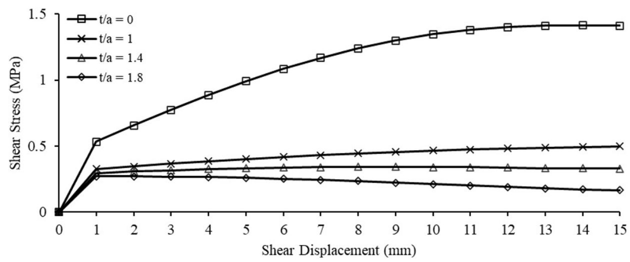

Figure 8. Effect of infill on the shear stress (k_n = 425 kPa/mm and σ_{n0} = 0.6 MPa).

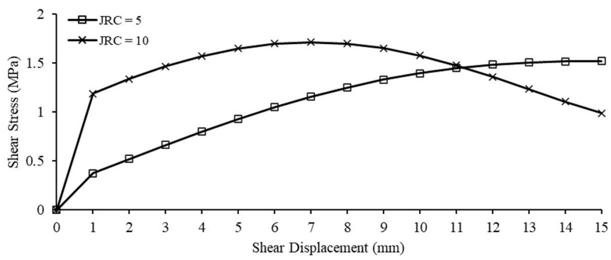

Figure 9. Effect of joint roughness on the shear stress (k_n = 560 kPa/mm and σ_{no} = 0.5 MPa).

damage occurring in rock discontinuities with high *JRC* values under CNS condition (Figure 9), similarly to what is expected when analyzing the influence of the input variables on the shear stress (Skinas et al., 1990; Papaliangas et al., 1993; Indraratna et al., 2015; Shrivastava & Rao, 2018).

5.3 Neuro-fuzzy models for predicting shear behavior of rock discontinuities

As shown and discussed previously, the neuro-fuzzy models referred to as *D1* and *S2* presented the best performances regarding the tests on experimental and hypothetical discontinuities, and were, therefore, chosen to predict the dilation and shear stress, respectively. It is worth mentioning the large number of the 2098 input-output patterns used in the concept and analysis of such models which consider different boundary conditions referring to the rock discontinuities, being developed from the grid partitioning technique using 80% of the experimental data for the training phase, and 20% for the testing phase.

Model *D1* consists of two (2) Gaussian membership functions for the eight (8) input variables that represent the main governing factors of the shear behavior of rock discontinuities, thereby creating 256 fuzzy inference rules. In the case of system *S2*, it presents 384 fuzzy inference rules, referring to the three (3) Gaussian membership functions for the *t/a* variable and two (2) Gaussian membership functions for the remaining input variables. In this context, dilation and shear stress are calculated by the respective fuzzy inference rules used in the models, when attributing input data that are within the intervals comprised by the established membership functions.

Figures 10-11 show the comparison of results obtained by applying the proposed *D1* and *S2* ANFIS models, those from the neuronal model proposed by Dantas Neto et al. (2017) to predict the dilation and shear stress, respectively, and the experimental data presented by Papaliangas et al. (1993) for an unfilled soft rock discontinuity under CNL condition, and σ_{no} = 0.05 MPa, *JRC* = 12, σ_c = 3.5 MPa and ϕ_b = 30°.

Figure 10 shows that both the ANFIS model (*D1*) and the neuronal model proposed by Dantas Neto et al. (2017) satisfactorily represented the variation of dilation with shear displacement. However, the results presented in Figure 11 show that the shear stress estimations provided by the ANFIS *S2* system were closer to the experimental data than those calculated by the ANN proposed by Dantas Neto et al. (2017). Its main limitation is the fact that it failed to represent the variation of shear stress with shear displacement in very soft rock discontinuities and submitted to low initial normal stress values, as already commented by the Dantas Neto et al. (2017).

Figures 12-13 show the comparison between the predictions from the proposed ANFIS systems, the neuronal model developed by Dantas Neto et al. (2017), and the experimental data presented by Benmokrane & Ballivy (1989), referring to unfilled hard rock discontinuity with the following characteristics and boundary conditions: σ_{no} = 1 MPa; *JRC* = 14; σ_c = 90 MPa; ϕ_b = 35°; and k_n = 315 kPa/mm (CNS condition). According to these results, both *D1* and *S2* ANFIS models fitted satisfactorily the experimental data regarding the variation in dilation (Figure 12) and shear stress (Figure 13) with the shear displacement, expressing the good performance of those neuro-fuzzy models in also estimating the shear behavior of hard rock discontinuities.

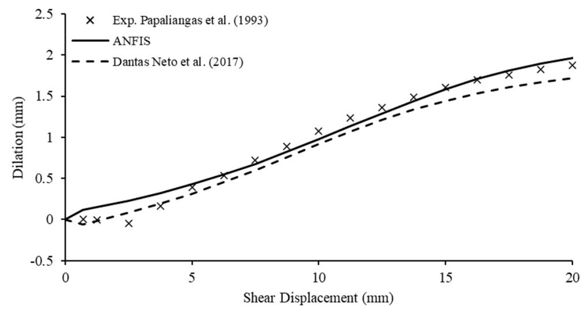

Figure 10. Comparison of experimental data for dilation of soft rocks and results from the *D1* ANFIS model and the ANN model proposed by Dantas Neto et al. (2017).

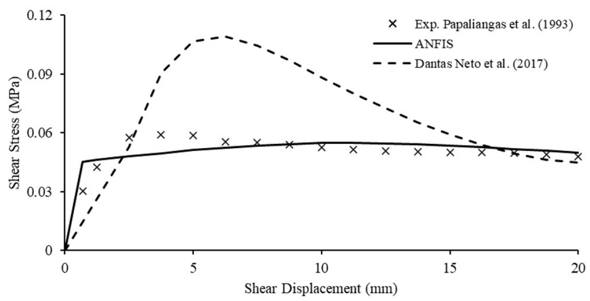

Figure 11. Comparison of experimental data for shear stress of soft rocks and results from the *S2* ANFIS model and the ANN model proposed by Dantas Neto et al. (2017).

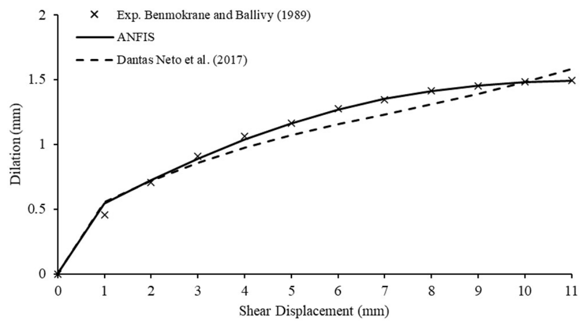

Figure 12. Comparison of experimental data for dilation of hard rocks and results from the *D1* ANFIS model and the ANN model proposed by Dantas Neto et al. (2017).

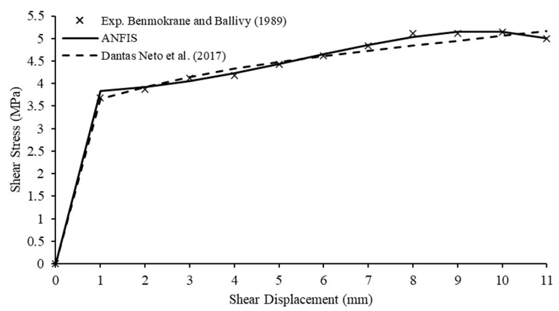

Figure 13. Comparison of experimental data for shear stress of hard rocks and results from the *S2* ANFIS model and the ANN model proposed by Dantas Neto et al. (2017).

5. Conclusions

Assessing the various neuro-fuzzy models developed in this study for the predictions of dilation and shear stress in filled and unfilled rock discontinuities, the *D1* and *S2* systems presented the best performances considering the tests and analyses made in experimental and hypothetical rock discontinuities. Such systems were designed based on the grid partitioning technique, which presented better results than the subtractive clustering technique, with 80% of the experimental data used for the training phase, the remaining 20% being used for the testing phase.

The input variables used in the developed neuro-fuzzy systems were the normal boundary stiffness (k_n), in kPa/mm; the ratio between the infill thickness and height of asperity (*t/a*); initial normal stress (σ_{no}), in MPa; joint roughness coefficient (*JRC*); uniaxial compressive strength of intact rock (σ_c), in MPa; basic friction angle of intact rock (ϕ_b), in degrees; friction angle of fill material (ϕ_{infill}), in degrees, and shear displacement (δ_h), in mm. Hence, the aim was to use the main governing factors of the shear behavior of the filled and unfilled rock discontinuities,

The model for predicting dilation (*D1*) consists of two (2) Gaussian membership functions for all input variables corresponding to a total of 256 fuzzy inference rules. Its coefficients of determination (R^2) were 0.99 in both training and testing phases indicating a satisfactory correlation between the experimental data and results obtained by the proposed neuro-fuzzy system. The neuro-fuzzy system developed for predicting the shear stress of rock discontinuities (*S2*) presents coefficients of determination of 0.97 and 0.96 in the training and testing phases, respectively, which also show the proximity between the estimations and the experimental data.

Using *D1* and *S2* ANFIS models to estimate dilation and the shear stress considering several characteristics of hypothetical infilled and unfilled rock discontinuities, it was possible to notice that the ANFIS systems satisfactorily represented the influence of the input variables on their shear behavior. This highlights the ability of neuro-fuzzy models to model multivariate, non-linear, and complex problems when compared to frequently used analytical models, and to consider the variability, or uncertainties, of the input values in the models' response.

Despite the functions of the neuro-fuzzy models in estimating the shear behavior of the infilled and unfilled rock discontinuities, the use of these systems is conditioned and limited to the intervals attributed to their input variables during the modeling process. Moreover, these models did not yet consider other key factors that influence the shear behavior of the rock discontinuities, such as the drainage condition, saturation degree, cohesion of the fill material, and weathering in the rock discontinuity walls.

Lastly, the developed neuro-fuzzy systems are not meant to substitute tests that still need to be performed on samples from rock masses. Here, the ANFIS models appear as a potential tool for the preliminary estimation of the shear behavior of rock discontinuities, by attributing values to the input variables used, providing rapid responses to help toward the design's assessment.

Acknowledgements

The authors thank Funcap (Fundação Cearense de Apoio ao Desenvolvimento Científico e Tecnológico) and Capes (Coordenação de Aperfeiçoamento de Pessoal de Nível Superior)/Proex (Pró-reitoria de Extensão Universitária e Cultura) for their financial support to the Post-Graduate Civil Engineering Program of the Federal University of Ceará, and to the Federal University of Ceará for the license of software MATLAB.

Declaration of interest

The authors have no conflicts of interest to declare. All co-authors have observed and affirmed the contents of the paper and there is no financial interest to report.

Authors' contributions

Silvrano Adonias Dantas Neto: conceptualization, supervision, data analysis, writing – review. Matheus Cavalcante Albino: data curation, methodology, modeling, writing – original draft. Ana Raquel Sena Leite: investigation, methodology. Ammanda Aragão Abreu: data analysis, format revision, writing – editing.

List of symbols

a asperity height of the discontinuity
i depicts the value of 1 and 2 in virtue of the number of fuzzy inference rules and sets used
k_n normal boundary stiffness
p_i consequent parameter
q_i consequent parameter
r_i consequent parameter
T thickness of the infill material
t/a relation between t and a
$\overline{w}_i$ output from Layer 3
x input in the nodes
y input in the nodes
z output of the neuro-fuzzy system
A_i fuzzy set associated with the nodes
B_i fuzzy set associated with the nodes
D designation for ANFIS model for dilation
$D1$ designation for ANFIS model 1 for dilation
$D2$ designation for ANFIS model 2 for dilation
$D3$ designation for ANFIS model 3 for dilation
$D4$ designation for ANFIS model 4 for dilation
$D5$ designation for ANFIS model 5 for dilation

D6 designation for ANFIS model 6 for dilation
D7 designation for ANFIS model 7 for dilation
D8 designation for ANFIS model 8 for dilation
D9 designation for ANFIS model 9 for dilation
JRC joint roughness coefficient
$_{1,}$ value of the degree of membership obtained from x and y
R^2 coefficient of determination
S designation for ANFIS model for shear stress
S1 designation for ANFIS model 1 for shear stress
S2 designation for ANFIS model 2 for shear stress
S3 designation for ANFIS model 3 for shear stress
S4 designation for ANFIS model 4 for shear stress
S5 designation for ANFIS model 5 for shear stress
S6 designation for ANFIS model 6 for shear stress
S7 designation for ANFIS model 7 for shear stress
S8 designation for ANFIS model 8 for shear stress
S9 designation for ANFIS model 9 for shear stress
δ_h shear displacement
δ_v dilation
ϕ_b basic friction angle of intact rock
ϕ_{infill} friction angle of infill material
σ_{no} initial normal stress
σ_c uniaxial compressive strength of intact rock
τ_s shear stress

References

Barton, N.R. (1973). A review of a new shear-strength criterion for rock joints. *Engineering Geology*, *7*(4), 287-332. http://dx.doi.org/10.1016/0013-7952(73)90013-6.

Barton, N.R. (2013). Shear strength criteria for rock, rock joints, rockfill and rock masses: problems and some solutions. *Journal of Rock Mechanics and Geotechnical Engineering*, *5*(4), 249-261. http://dx.doi.org/10.1016/j.jrmge.2013.05.008.

Barton, N.R. (2016). Non-linear shear strength for rock, rock joints, rockfill and interfaces. *Innovative Infrastructure Solutions*, *1*(1), 1-30. http://dx.doi.org/10.1007/s41062-016-0011-1.

Barton, N.R., & Bandis, S.C. (June 4-6, 1990). Review of predictive capabilities of JRC-JCS model in engineering practice. In N. Barton & O. Stephansson (Eds.), *Proceedings of the International Symposium on Rock Joints* (pp. 603-610). Rotterdam, Holland: A.A. Balkema.

Barton, N.R., & Choubey, V. (1977). The shear strength of rock joints in theory and practice. *Rock Mechanics and Rock Engineering*, *10*(1-2), 1-54. http://dx.doi.org/10.1007/BF01261801.

Benmokrane, B., & Ballivy, G. (June 19-22, 1989). Laboratory study of shear behaviour of rock joints under constant normal stiffness conditions. In A.W. Khair (Ed.), *Proceedings of the 30th U.S. Symposium on Rock Mechanics (Rock Mechanics as a Guide for Efficient Utilization of Natural Resources)* (pp. 899-906). Rotterdam, Holland: A.A. Balkema.

Chiu, S.L. (1994). Fuzzy model identification based on cluster estimation. *Journal of Intelligent & Fuzzy Systems*, *2*, 267-278. http://dx.doi.org/10.3233/IFS-1994-2306.

Dantas Neto, S.A., Indraratna, B., & Oliveira, D.A.F. (October 19-22, 2016). Prediction of the shear behaviour of clean joints in soft rocks using perceptron. In Sociedade Brasileira de Mecânica das Rochas (Ed.), *ISRM VII Brazilian Symposium on Rock Mechanics - SBMR 2016* (pp. 1817-1831). São Paulo, Brazil: SBMR/ABMS. https://doi.org/10.20906/CPS/SBMR-02-0025.

Dantas Neto, S.A., Indraratna, B., Oliveira, D.A.F., & Assis, A.P. (2017). Modelling the shear behaviour of clean rock joints using artificial neural networks. *Rock Mechanics and Rock Engineering*, *50*, 1817-1831. http://dx.doi.org/10.1007/s00603-017-1197-z.

Dehghan, S., Sattari, G., Chelgani, C.S., & Aliabadi, M.A. (2010). Prediction of uniaxial compressive strength and modulus of elasticity for Travertine samples using regression and artificial neural networks. *Mining Science and Technology*, *20*(1), 41-46. http://dx.doi.org/10.1016/S1674-5264(09)60158-7.

Gokceoglu, C., Yesilnacar, E., Sonmez, H., & Kayabasi, A. (2004). A neuro-fuzzy model for modulus of deformation of jointed rock masses. *Computers and Geotechnics*, *31*(5), 375-383. http://dx.doi.org/10.1016/j.compgeo.2004.05.001.

Haque, A. (1999). *Shear behaviour of soft rock joints under constant normal stiffness* [PhD dissertation]. University of Wollongong. Retrieved in September 23, 2022, from https://ro.uow.edu.au/theses/1266/

Harrison, J.P., & Hudson, J.A. (2010). Incorporating parameter variability in rock mechanics analyses: fuzzy mathematics applied to underground rock spalling. *Rock Mechanics and Rock Engineering*, *43*, 219-224. http://dx.doi.org/10.1007/s00603-009-0034-4.

Haykin, S. (2008). *Neural networks and learning machines* (3rd ed.). New York: Pearson.

Indraratna, B., & Haque, A. (2000). *Shear behaviour of rock joints*. Rotterdam: Balkema.

Indraratna, B., Jayanathan, M., & Brown, E.T. (2008). Shear strength model for overconsolidated clay-infilled idealised rock joints. *Geotechnique*, *58*(1), 55-65. http://dx.doi.org/10.1680/geot.2008.58.1.55.

Indraratna, B., Oliveira, D.A.F., & Brown, E.T. (2010). A shear-displacement criterion for soil-infilled rock joints. *Geotechnique*, *60*(8), 623-633. http://dx.doi.org/10.1680/geot.8.P.094.

Indraratna, B., Premadasa, W.N., & Brown, E.T. (2013). Shear behaviour of rock joints with unsaturated infill. *Geotechnique*, *63*(15), 1356-1360. http://dx.doi.org/10.1680/geot.12.P.065.

Indraratna, B., Premadasa, W.N., Brown, E.T., Gens, A., & Heitor, A. (2014). Shear strength of rock joints influenced by compacted infill. *International Journal of Rock

Mechanics and Mining Sciences, *70*, 296-307. http://dx.doi.org/10.1016/j.ijrmms.2014.04.019.

Indraratna, B., Thirukumaran, S., Brown, E.T., & Zhu, S. (2015). Modelling the shear behaviour of rock joints with asperity damage under constant normal stiffness. *Rock Mechanics and Rock Engineering*, *48*, 179-195. http://dx.doi.org/10.1007/s00603-014-0556-2.

Indraratna, B., Welideniya, S., & Brown, E.T. (2005). A shear strength model for idealised infilled joints under constant normal stiffness. *Geotechnique*, *55*(3), 215-226. http://dx.doi.org/10.1680/geot.2005.55.3.215.

Jalalifar, H., Mojedifar, S., Sahebi, A.A., & Nezamabadi-Pour, H. (2011). Application of the adaptive neuro-fuzzy inference system for prediction of a rock engineering classification system. *Computers and Geotechnics*, *38*(6), 783-790. http://dx.doi.org/10.1016/j.compgeo.2011.04.005.

Jang, J.S.R. (1993). ANFIS: adaptive-network-based fuzzy inference systems. *IEEE Transactions on Systems, Man, and Cybernetics*, *23*(3), 665-685. http://dx.doi.org/10.1109/21.256541.

Jang, J.S.R., Sun, C.T., & Mizutani, E. (1997). *Neuro-fuzzy and soft computing: a computational approach to learning and machine intelligence*. Englewood Cliffs: Prentice Hall.

Kayabasi, A., Gokceoglu, C., & Ercanoglu, M. (2003). Estimating the deformation modulus of rock masses: a comparative study. *International Journal of Rock Mechanics and Mining Sciences*, *40*, 55-63. http://dx.doi.org/10.1016/S1365-1609(02)00112-0.

Leite, A.R.S., Dantas Neto, S.A., & Albino, M.C. (November 11-14, 2019a). Modelo de rede neural artificial para previsão do comportamento cisalhante de descontinuidades rochosas. In D.N. Maciel (Org.), *XL Ibero-Latin American Congress on Computational Methods in Engineering (CILAMCE)* (pp. 1-13). Belo Horizonte, Brazil: ABMEC.

Leite, A.R.S., Dantas Neto, S.A., Polemis Junior, K., & Oliveira, C.M.O. (September 13-18, 2019b). Study on the shear behaviour of rock joints using different models of artificial neural networks. In S.A.B. Fontoura (Org.), *International Congress on Rock Mechanics and Rock Engineering* (pp. 2707-2714). Salzburg, Austria: ISRM.

Mamdani, E.H. (1974). Applications of fuzzy algorithms for control of simple dynamic plant. *Proceedings of the IEEE*, *121*(12), 1585-1588. http://dx.doi.org/10.1049/piee.1974.0328.

Matos, Y.M.P. (2018). *Desenvolvimento de modelos de previsão do comportamento cisalhante em descontinuidades sem preenchimento de maciços rochosos utilizando técnicas fuzzy e neuro-fuzzy* [Master's dissertation, Federal University of Ceará]. University of Ceará's repository (in Portuguese). http://www.repositorio.ufc.br/handle/riufc/30223.

Matos, Y.M.P., Dantas Neto, S.A., & Barreto, G.A. (2019a). A Takagi-Sugeno fuzzy model for predicting the clean rock joints shear strength. *REM - International Engineering Journal*, *72*(2), 193-198. http://dx.doi.org/10.1590/0370-44672018720083.

Matos, Y.M.P., Dantas Neto, S.A., & Barreto, G.A. (2019b). Predicting the shear strength of unfilled rock joints with the first-order Takagi-Sugeno fuzzy approach. *Soils and Rocks*, *42*(1), 21-29. http://dx.doi.org/10.28927/SR.421021.

Mehrishal, S., Sharifzadeh, M., Shahriar, K., & Song, J.J. (2016). An experimental study on normal stress and shear rate dependency of basic friction coefficient in dry and wet limestone joints. *Rock Mechanics and Rock Engineering*, *49*(12), 4607-4629. http://dx.doi.org/10.1007/s00603-016-1073-2.

Naghadehi, M.Z. (2015). Laboratory study of the shear behaviour of natural rough rock joints infilled by different soils. *Periodica Polytechnica. Civil Engineering*, *59*(3), 413-421. http://dx.doi.org/10.3311/PPci.7928.

Noorani, R., Kordi, H., & Ghazvinian, A.H. (June 15-18, 2010). An adaptive neuro-fuzzy inference system for uniaxial compressive strength of rocks. In J. Zhao (Org.), *Regional Symposium of the International Society for Rock Mechanics (ISRM) – EUROCK 2010* (pp. 327-331). Cavtat, Croatia: CRC Press.

Ocak, I., & Seker, S.E. (2012). Estimation of elastic modulus of intact rocks by artificial neural network. *Rock Mechanics and Rock Engineering*, *45*, 1047-1054. http://dx.doi.org/10.1007/s00603-012-0236-z.

Oliveira, D.A.F., & Indraratna, B. (2010). Comparison between models of rock discontinuity strength and deformation. *Journal of Geotechnical and Geoenvironmental Engineering*, *136*(6), 864-874. http://dx.doi.org/10.1061/%28ASCE%29GT.1943-5606.0000284.

Oliveira, D.A.F., Indraratna, B., & Nemcik, J. (2009). Critical review on shear strength models for soil-infilled joints. *Geomechanics and Geoengineering*, *4*(3), 237-244. http://dx.doi.org/10.1080/17486020903128564.

Papaliangas, T., Hencher, S.R., Lumsden, A.C., & Manolopoulou, S. (1993). The effect of frictional fill thickness on the shear strength of rock joints. *International Journal of Rock Mechanics and Mining Sciences and Geomathics*, *30*(2), 81-91. http://dx.doi.org/10.1016/0148-9062(93)90702-F.

Sadrossadat, E., Ghorbani, B., Oskooei, R., & Kaboutari, M. (2018). Use of adaptive neuro-fuzzy inference system and gene expression programming methods for estimation of the bearing capacity of rock foundations. *Engineering Computations*, *35*(5), 2078-2106. http://dx.doi.org/10.1108/EC-07-2017-0258.

Shrivastava, A.K., & Rao, K.S. (2018). Physical modeling of shear behavior of infilled rock joints under CNL and CNS boundary conditions. *Rock Mechanics and Rock Engineering*, *51*(1), 101-118. http://dx.doi.org/10.1007/s00603-017-1318-8.

Shrivastava, A.K., Rao, K.S., & Rathod, G.W. (December 15-17, 2011). Shear behaviour of infill joint under CNS boundary condition. In D.K. Sahoo, T.G.S. Kumar, B.M. Abraham & B.T. Jose (Eds.), *Proceedings of the Golden*

Jubilee: Indian Geotechnical Conference (pp. 981-984). Kochi, India: Indian Geotechnical Society.

Singh, V., & Singh, T.N. (June 17-21, 2006). A neuro-fuzzy approach for prediction of Poisson's ratio and Young's modulus of shale and sandstone. In D.P. Yale (Ed.), *41st U.S. Symposium on Rock Mechanics (Golden Rocks 2006)* (pp. 1-7). Alexandria: United States: ARMA.

Skinas, C.A., Bandis, S.C., & Demiris, C.A. (June 4-6, 1990). Experimental investigations and modelling of rock joint behaviour under constant stiffness. In N. Barton & O. Stephansson (Eds.), *Proceedings of the International Symposium on Rock Joints* (pp. 301-307). Rotterdam, Holland: A.A. Balkema.

Sonmez, H., Ercanoglu, M., Kalender, A., Dagdelenler, G., & Tunusluogly, R. (2016). Predicting uniaxial compressive strength and deformation modulus of volcanic bimrocks considering engineering dimension. *International Journal of Rock Mechanics and Mining Sciences*, *86*, 91-103. http://dx.doi.org/10.1016/j.ijrmms.2016.03.022.

Sonmez, H., Gokceoglu, C., & Ulusay, R. (2003). An application of fuzzy sets to the Geological Strength Index (GSI) system used in rock engineering. *Engineering Applications of Artificial Intelligence*, *16*(3), 251-269. http://dx.doi.org/10.1016/S0952-1976(03)00002-2.

Takagi, T., & Sugeno, M. (1983). Derivation of fuzzy control rules from human operator's control action. *IFAC Proceedings Volumes*, 16(13), 55-60. https://doi.org/10.1016/S1474-6670(17)62005-6.

Tsukamoto, Y. (1979). An approach to fuzzy reasoning method. In M.M. Gupta, R.K. Ragade & R.R. Yager (Eds.), *Advances in fuzzy set theory and applications* (pp. 137-149). Amsterdam: North-Holland Publishing Company.

Yesiloglu-Gultekin, N., Sezer, E.A., Gokceoglu, C., & Bayhan, H. (2013). An application of adaptive neuro fuzzy inference system for estimating the uniaxial compressive strength of certain granitic rocks from their mineral contents. *Expert Systems with Applications*, *40*(3), 921-928. http://dx.doi.org/10.1016/j.eswa.2012.05.048.

Zadeh, L.A. (1965). Fuzzy Sets. *Information and Control*, *8*, 338-353.

CASE STUDIES

Soils and Rocks
An International Journal of Geotechnical and Geoenvironmental Engineering
www.soilsandrocks.com
ISSN 1980-9743
ISSN-e 2675-5475

Stability analysis of a slope and runout analysis movement of the mobilized-mass volume

Bianca Cristine De Toni Riselo[1#], Larissa de Brum Passini[1],
Alessander Christopher Morales Kormann[1]

Case Study

Keywords
Landslides
Serra do Mar
Deterministic
Probabilistic
Material point method

Abstract

This research aims to present a deterministic and probabilistic analysis of the stability in 2D/3D of a road slope, located in the state of São Paulo, Brazil, in the Serra Pelada region, incorporating scenarios with and without surface suction and water level, and predict the movement of the mobilized-mass volume. The results of the stability analysis showed the variability of the safety factor, the probability of failure, and the mobilized-mass volume, in the twenty-six simulated scenarios. The results of the runout analysis of the mobilized-mass volume indicated that any possible landslide would interdict, at least, two of the three lanes of traffic, equivalent to 59.7% of the lanes. Therefore, it can be concluded that a 2D and 3D stability analysis combined with the material point method to predict the post-failure soil displacement provides a better understanding of all processes involved in a landslide, which helps to establish more adequate and effective mitigation and remedial measures for each situation. Finally, in conclusion, the studied slope, with a maximum failure probability of 1.24%, is safe in terms of its overall stability for all twenty-six simulated scenarios.

1. Introduction

Landslides are mass movements that occur in Brazil and elsewhere, and can cause damage, affecting the population and region and generating economic losses. Often these landslides are caused when mobilized stresses exceed the soil or rock strength, either by changing slope geometric factors or by triggering factors such as climatic factors, overloads, slope mass removal, and reduction of soil strength parameters.

According to Fernandes et al. (2001), the slopes's morphological parameters stand out among the landslide factors because they control the balance of forces on the slope and the hydrological dynamics of the soils. As well as the loss of suction, which is also a possible cause of instability, since there is an increase in moisture in the material due to the progress of the infiltration front in the ground (Fredlund, 1987).

The slope stability analysis is of great importance since it guarantees more physical safety of the slope itself and of the elements that might be impacted by a possible landslide. Moreover, predicting the movement of the mobilized-mass volume, after the failure, is very useful to evaluate the risk of catastrophes or to establish mitigation measures more adequate for that slope (Troncone et al., 2019).

According to Wang et al. (2018), the behavior of a landslide can be divided into two stages: failure and post-failure. The failure stage is characterized by presenting a continuous shear surface, generating little movement of soil mass. The post-failure stage is represented by its rapid formation of plastic deformations and the kinematics of the unstable soil mass until its break.

As a way of studying the two failure stages, foremost one must understand the models involved in each of the stages. A mathematical model, such as the limit equilibrium method (LEM), is the most known method of simulating the first failure stage, which focuses on the calculation of the safety factor employing material-strength theories. As to model the landslide post-failure with good precision, it is necessary a numerical model capable of simulating large deformations and distortions, such as the material point method (MPM), which uses constitutive models based on the continuum mechanics (Toro-Rojas et al., 2021).

The limit equilibrium method (LEM) is used in the stability analysis of slopes and has the objective of evaluating the possibility of the occurrence of a landslide (Gerscovich, 2016). The LEM includes the method of slices that divides the soil above the potential-failure surface in a series of slices to calculate each one's equilibrium. Among the methodologies that employ the method of slices, there are examples such

[#]Corresponding author. E-mail address: bihdetoni@hotmail.com
[1]Universidade Federal do Paraná, Programa de Pós-Graduação em Engenharia Civil, Curitiba, PR, Brasil.

Submitted on April 15, 2022; Final Acceptance on October 4, 2022; Discussion open until February 28, 2023.
https://doi.org/10.28927/SR.2022.003822

as Janbu, Spencer, Simplified Bishop, and Morgenstern-Price, which are widely used to calculate the safety factor (Liu et al., 2019). Also, this method is well-known for being a statically undetermined problem and is solved by considering the distribution of the internal forces (Liu et al., 2015). Furthermore, in the limit equilibrium method, various potential-failure surfaces are generated, by optimization or trial-and-error techniques, so then one may find the critical failure surface that corresponds to the minimal safety factor (Reale et al., 2015).

The stability analysis can be done following two approaches: deterministic and probabilistic. The deterministic stability analysis considers only the average value of the soil strength parameters and calculates only one safety factor (SF) for the problem (Tonus, 2009). This SF, in a given failure surface, is determined by the ratio of the shear strength over the mobilized shear stress, considering the equilibrium of the forces and/or moments acting on the failure surface (Liu et al., 2019). Research points out that the stability of a slope cannot be completely evaluated only by the deterministic safety factor since some slopes with high SF still fail (Chen et al., 2020).

The probabilistic stability analysis stems from the variation of the geotechnical parameters of the soil (average and standard deviation), quantitatively considering the various origins of uncertainties and determining the probability of failure and the reliability rate of the results (Wang et al., 2020). In such analysis, one must select an appropriate probabilistic method, such as the first order reliability method (FORM), the second order reliability method (SORM), the point estimative method (PEMs), or the Monte-Carlo simulation (MCS) (Ahmadabadi & Poisel, 2015). MCS is an easy implementation tool that determines the probability of failure with a desired precision, even though it is time-consuming due to the high computational effort (Fang et al., 2020).

The material point method (MPM) has been used to model various types of geotechnical problems, such as mass movements. Toro-Rojas et al. (2021) studied the effect of a landslide in the failure and post-failure stages by the analysis of the strength parameters and deformation of a slope. Conte et al. (2019) and Conte et al. (2020) demonstrated the MPM's capacity to evaluate landslides and their behavior post-failure. Bhandari et al. (2016) utilized the MPM to simulate a progressive failure of a slope caused by an earthquake, and Li et al. (2016) simulated and analyzed the post-failure process of the landslide in Wangjiayan, China.

The numerical methods are divided into two main categories: Lagrangian and Eulerian methods. The MPM combines the performance of the two methodologies, in which one continuum is discretized by a set of subdomains with information (velocity, acceleration, density, displacement, external loads, material parameters, etc.), which are concentrated on a Lagrangian point, called a material point. A computational mesh (Eulerian mesh) overlays the continuum and covers all the issue's domain, while being usually maintained fixed with time and not bound to material information. In the nodes of this mesh, equilibrium equations are resolved, and in the material points, constitutive equations and mass conservation equations are established (Conte et al., 2020).

At the beginning of each time step, the data is transferred from the material points to the mesh nodes, so then the nodal accelerations are obtained, and the acceleration, velocity, and dislocation points are determined in the stipulated time. Lastly, the position of the material points is updated on the Eulerian mesh for the later time step (Conte et al., 2020).

In light of all this context, this article seeks to analyze the stability in 2D and 3D of a road embankment, located in the state of São Paulo, Brazil, in the Serra Pelada region, via deterministic and probabilistic approaches, embodying scenarios with and without superficial suction and variation of the water levels, and predicting, in case of failure, the movement of the mobilized-mass volume.

2. Case study: data and information from the location and methodology adopted

This section of the article presents the materials and methods employed, divided into a description of the field of study, input parameters, stability analysis, and runout analysis of the movement of the mobilized-mass volume. Figure 1 represents the flowchart of the activities conducted in order to develop the analysis of stability and prediction of mass movement of the slope under study.

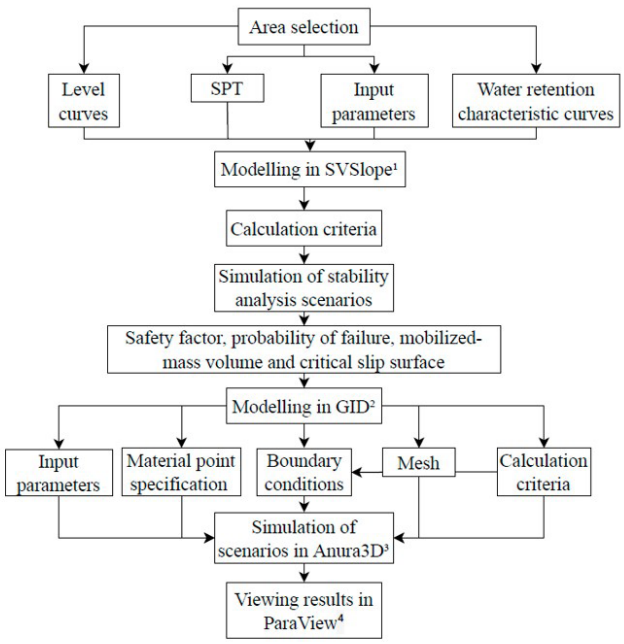

Figure 1. Flowchart of the applied method. [1]Slope stability analysis software. [2]Universal numerical simulation processor. [3]Software for numerical modeling of large strains using the material point method (MPM). [4]Open-source multiple-platform application for interactive, scientific visualization.

Beginning with the selection of the field of study, it was then determined the basic data to perform the stability analysis, such as level curves, Standard Penetration Test (SPT) results, soil parameters (cohesive intercept and friction angle, natural unit weight, Poisson's ratio, modulus of elasticity, suction) and soil-water characteristic curves.

Thereafter, the slope was modeled on the software SVSlope, the calculation criteria were indicated in it, and the stipulated scenarios of stability analysis were simulated, resulting in the safety factors, probability of failure, mobilized-mass volume, and critical slip surface.

With the results of the stability analysis, the slope was modeled in another software, GID, followed by the insertion of the slope's materials, calculation criteria, and modeling data such as the specification of the material point, boundary conditions of the model, and mesh. Finally, the scenarios of mass movement prediction were simulated on Anura3D, and the results were visualized on ParaView.

2.1 Description of the study area

The slope serving as the case study is located in the Régis Bittencourt highway, stretch of Serra do Mar, at Serra Pelada, in the state of São Paulo, Brazil, at km 551 + 600 (South Lane) (Figure 2).

In Figure 2d it is possible to notice that the slope is near the road's traffic, which contains three lanes and drainage ditches at their ends. The traffic lanes are 3.6 m wide, and the drainage ditches up until the beginning of the traffic lanes are 0.8 m wide.

The Régis Bittencourt highway poses economic importance in the Brazilian highway network since it is part of the Mercosul route and is also the main road corridor that connects important economic poles from the country's Southeast (São Paulo) and South (Paraná) (Batista, 2019). Thus, the evaluation of possible instabilities on slopes along the highway is of great relevance.

According to APRB (2019), the region of Serra Pelada, specifically the Régis Bittencourt road, presents a history of instability, with records from 2010 to 2019, amounting to 93 registered occurrences of landslides, the last nine taking place at Serra Pelada. Besides that, Batista (2019) appointed, in his study, the region in question as the most critical in his analysis of economic risks performed all around Serra Pelada.

The geological formation at Serra Pelada, according to CPRM (2013), is characterized by Amphibolitic Gneiss. The geological-geotechnical profile of the slope was defined, based on geotechnical investigations of the Standard Penetration Test (SPT) executed near the slope, as being three layers of soil: 1.5 m of superficial colluvium layer, 4.5 m of residual soil formed by sand silt, and the remaining is composed by a weathered rock (saprolite). The water level was considered in a few simulated scenarios, that being at two different depths, 6.5 m and 7.5 m below the surface. The 7.5 m depth was defined based on the data of the geotechnical investigation of the SPT that indicated a water level with a depth of less than 7.0 m, and the depth of 6.5 m was selected to comprehend the influence of the variation in the position of the water level in the results.

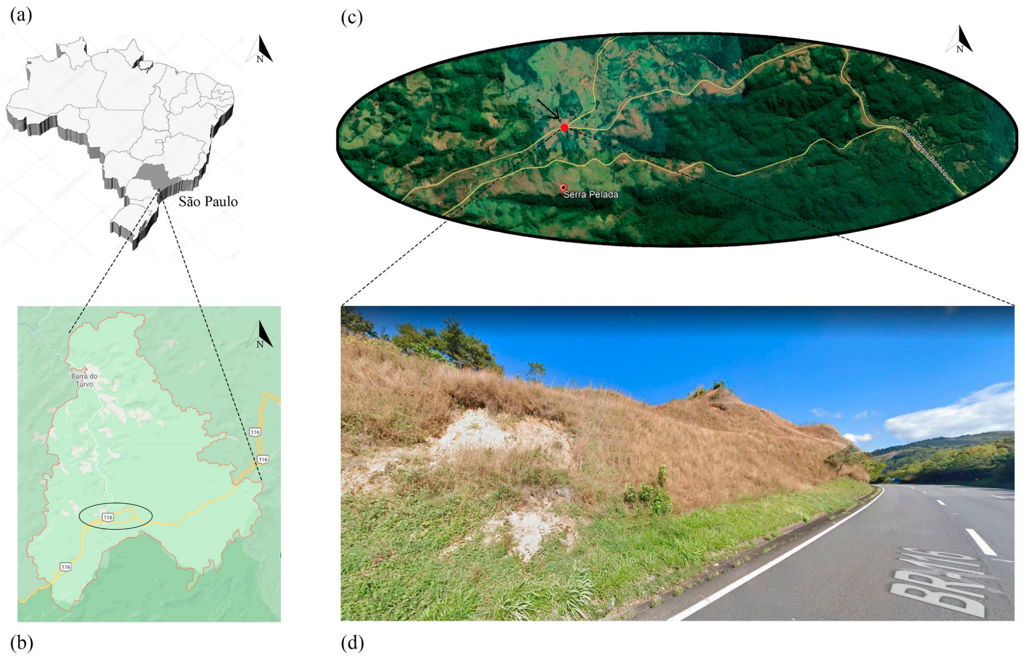

Figure 2. Study area location: (a) Brazil-São Paulo, (b) city of Barra do Turvo-SP, (c) Serra Pelada – highway BR-116 – slope point, and (d) front view of the slope in study.

2.2 Input parameters

The input parameters used in the simulations of stability and mass movement prediction were the strength parameters of soil, such as cohesive intercept (c') and friction angle (ϕ›), natural unit weight of the soil (γ_{nat}), Poisson's ratio, modulus of elasticity, suction, and the characteristic curves of water retention. Table 1 shows, for the colluvial, residual soils, and saprolite, the value intervals of the cohesive intercept and friction angle, and the average value of these parameters, besides the natural unit weight of the soil, Poisson ratio, and modulus of elasticity. The minimum value of the parameters is the value of the residual strength parameters, and the maximum value is the value of the peak strength parameters.

The shear strength parameters of the soil were determined based on the data by Trevizolli (2018). The author obtained these results by saturated direct shear tests implemented in three intact samples, in three levels of normal stress (50, 100, and 200 kPa), performed on a near slope, at km 552 + 000 (North Lane).

In the deterministic stability analyses, the average values of the geotechnical parameters, natural unit weight of the soil, internal friction angle, and cohesive intercept were considered. And in the probability analyses, in addition to the average values of the geotechnical parameters, the minimum, and maximum values were considered (Table 1), for the colluvial and residual soils. For each variable of the probabilistic data, the statistical normal distribution was considered, and truncation was not adopted, that is, the extreme values of the data intervals were determined in the direct shear test.

The suction was incorporated, in some of the stability analysis scenarios, in the first 3 m deep, 1.5 m in colluvial soil and 1.5 m in residual soil. According to Trevizolli (2018), it was adopted the interval of 20 to 120 kPa for the total suction on the surface of the soil, varying in each simulation at intervals of 20 kPa by 20 kPa. This parameter was incorporated in the surface soil decreasing with depth, that is, with maximum value at the top and null at the end of the first 3 m deep.

Finally, the characteristic curves of water retention were grounded on the compilation of experimental points of Trevizolli (2018), obtained by the filter paper method, presenting a curve in a bi-modal format for the colluvial soil and a curve in a tri-modal format for the residual soil. The residual water content levels indicated by the curves were 20% for the residual soil and 30% for the colluvial soil. The porosity, which corresponds to the volume of voids that can be filled by water when the soil is saturated, was 44% for residual soil and 52% for colluvial soil.

2.3 Stability analysis of a road slope

The slope was modeled in 2D and 3D (Figure 3), and stability analyses (deterministic and probabilistic) were performed in the two dimensions in the software SVSlope by SoilVision. The determination of the safety factor was calculated based on Morgenstern-Price's limit equilibrium method, and the probabilistic method used was Monte Carlo's with 5000 iterations.

In the slope modeling on the software, it was used the Mohr-Coulomb criteria for the strength parameters of the three

Table 1. Input parameters of colluvial soil, residual soil, and saprolite (Riselo, 2021).

Material	Colluvial soil				
Parameter	γ_{nat} (kN /m^3)	Poisson's ratio	Modulus of elasticity (kPa)	ϕ' (º)	c' (kPa)
Average value	16	0.4	3000	23.5	11.4
Minimum value	-	-	-	17.8	4.7
Maximum value	-	-	-	30	16.8
Standard deviation	-	-	-	6.5	6.7
Coefficient of variation	-	-	-	27.5	58.7
Material	Residual soil				
Parameter	γ_{nat} (kN/m^3)	Poisson's ratio	Modulus of elasticity (kPa)	ϕ› (º)	c' (kPa)
Average value	18	0.3	10000	26	7.8
Minimum value	-	-	-	21.8	5.1
Maximum value	-	-	-	30.2	10.4
Standard deviation	-	-	-	4.2	2.7
Coefficient of variation	-	-	-	16.2	34.2
Material	Saprolite				
Parameter	γ_{nat} (kN/m^3)	Poisson's ratio	Modulus of elasticity (kPa)	ϕ› (º)	c' (kPa)
Average value	17	0.3	15000	39	10.4
Minimum value	-	-	-	-	-
Maximum value	-	-	-	-	-

Note: kN: KiloNewton; kPa: KiloPascal.

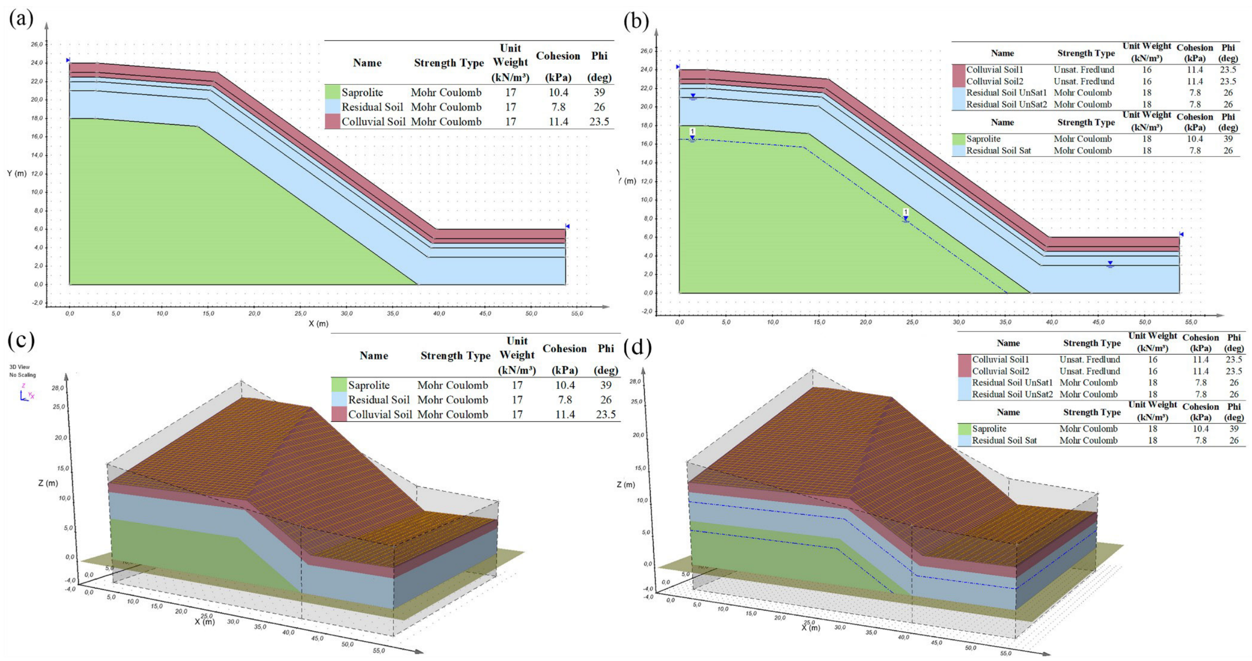

Figure 3. Slope modeling: (a) 2D without water level, (b) 2D with the water level, (c) 3D without water level, and (d) 3D with the water level.

soils. However, in the simulations that were modeled with the incorporation of the water level and superficial suction, the first 3 m of depth was considered non-saturated, thus, for these soils was adopted the respective water retention curves.

The failure surface was defined as non-circular for all simulations and the research method of this surface was the Cuckoo Search, since it was one of the only available methods for the 2D analysis as well as the 3D analysis. This way 50 nests, 350 iterations, and 500 number of vertices were considered in the method.

In the analysis, it was determined the critical failure surface, that is, the software determined the position of the failure surface that presented the lowest safety factor for the determined situation (Bentley, 2019). In total, 52 scenarios were simulated, half 2D and half 3D. From the 26 scenarios from both 2D and 3D models, only in two of them the superficial suction and water level were not considered. In the remaining scenarios, twelve simulations were performed with the water level depth at 6.5 m deep and twelve simulations were performed with the water level depth at 7.5 m deep. The deterministic analysis counts as one simulation and the probabilistic analysis counts as another simulation, even though in some cases they both obtained the same result.

The results obtained with this method were safety factor, probability of failure, and quantification of movement of the mobilized-mass volume. In addition to these numerical data, it was also possible to obtain the critical failure surface of each simulation, a necessary piece of information to perform the runout analysis of the mobilized-mass volume.

2.4 Runout analysis of the mobilized-mass volume in the hypothetical rupture

The runout analysis of the mobilized-mass volume indicates the reach, in meters, of this volume after a possible landslide on the slope, based on the material point method (MPM). In this method, a continuum is discretized by a set of subdomains that concentrate its mass, whose value is fixed to guarantee mass conservation, at a material point (Lagrangian point), which also contains information on soil properties. The movement of these material points defines the deformation state of the considered continuum (Conte et al., 2020).

The interaction between the particles is performed at the nodes of a stationary background computational mesh (Eulerian mesh), which remains constant during the calculation, eliminating the distortion problem. Also, this mesh is superimposed on the continuum and covers the entire domain, remaining fixed over time and not linked to material information (Toro-Rojas et al., 2021).

In MPM, the relationship between material points and mesh nodes is done by linear interpolation shape functions. The nodal accelerations at a given time are unknown to the problem and are calculated by solving the governing equations (equilibrium, constitutive, and mass conservation equations) in the computational mesh. After determining the nodal accelerations, an explicit scheme is used to evaluate the displacement and velocity of the material points in the analyzed time, which are updated in the Eulerian grid for the next time step (Conte et al., 2019). Due to the method using constitutive models of continuum mechanics, the elastoplastic model with the Mohr-Coulomb failure criterion was used on the slope.

The choice to use the MPM was due to the numerical method being able to simulate large distortions and deformations, indicated to follow the movement of a simulated body, such as the slope failure, and post-failure stage. In addition, the software that runs the MPM is freely available for research and studies, further favouring the choice of method.

The runout analysis was performed on the software GID with the Anura3D's plugin, being that the first software performs the pre-processing and the generation of the mesh, and the plugin generates the input files for the software Anura3D. With the position of the critical failure surface of each simulation and its respective mobilized-mass volume, the slope in the study was modeled on GID in 2D, with the three layers of soil. On Anura3D's plugin, the materials were incorporated into the model, according to Table 1, considering the soil shear strength parameters (natural unit weight, friction angle, and cohesive intercept) and the deformability parameters (Poisson ratio and modulus of elasticity). Also, it was established the boundary conditions on the model in directions "x" and "y", the number of material points of each cell, and the calculation criteria, such as the number of steps of calculation and time stage of the calculation. After incorporating and defining the data, the two input files for the software Anura3D, GOM and CPS files, were generated in text format.

With the files generated, the analyses were calculated on the software Anura3D by Windows' Command Prompt. On average, the time of analysis was 5 h and 30 min, using a notebook with an Intel i5 9300H processor, 16GB of RAM, and a 4GB NVIDIA GTX 1650 video card (Mobile). The analyses were performed in three scenarios derived from the 2D stability analyses.

Anura3D is a software used for modeling and numeric simulation of soil-water-structure interaction and great deformations, that utilizes the material point method (MPM). This software is being developed by Anura3D MPM Research Community (Anura3D, 2021).

The software allows the choice of different constitutive models for the material model solid, such as rigid body, linear elasticity, Mohr-Coulomb, and external material model. The external model option makes it possible to load other constitutive models implemented in the FORTRAN language, but the simulation must be performed only if the subroutines are compiled and referenced in DLL (Dynamic Link Library) format (Anura3D, 2021). The Mohr-Coulomb constitutive model was chosen because in the stability analysis, performed in another software (SVSlope), this model was used, keeping the same line of reasoning as it is the same slope. Other papers on the same topic that used Anura3D, employed and indicated the use of the Mohr-Coulomb model, obtaining good results. Also, as MPM uses constitutive models based on continuum mechanics and due to the complexity and little knowledge of FORTRAN language, among the available codes of models compatible with the software, the Mohr-Coulomb model was the one that best applied to the slope context.

The Mohr-Coulomb equation results in a linear shear strength envelope, which is the result of a set composed of at least 3 tests under different normal stresses to the failure plane (Trevizolli, 2018). The real envelope of shear resistance is not linear, so the Mohr-Coulomb equation is valid only for the tested stress range. Thus, the stress level of the test must be compatible with the stress level that the slope will receive throughout its useful life for the equation to be valid. Therefore, in runout analysis of soil slopes, the use of the Mohr-Coulomb constitutive model might be limited.

Based on the studies by Toro-Rojas et al. (2021) and the time of analysis, the number of elements on the mesh was defined as 46213 (0.2 m × 0.2 m), and the number of material points in each cell was defined as 6. Among these two parameters, the number of elements on the mesh is the one that has the most influence on the results of the runout analysis of the movement of the mobilized-mass volume, being more important than the number of material points.

In the first load stage, only gravity was applied to initiate the stresses. Then, in the second stage some, boundary conditions were removed, and the fragility of the failure surface was indicated. Lastly, in the third stage, the boundary conditions were returned to evaluate the mass movement on the slope over time. In total, 50 calculation steps were defined, one in the first load stage, one in the second load stage, and 48 in the third load stage.

The visualization of the results from Anura3D was done on the software ParaView, following the recommendation of the manual (Anura3D, 2021), which enabled the visualization of the displacement of the soil in the slope in 2D, during the 50 calculation stages.

3. Results and discussions

This section contemplates the results obtained with the application of the methodology, presenting the results of the stability analysis and the runout analysis of the movement of the mobilized-mass volume.

3.1 Stability analysis of a road slope

The results of the stability analyses are presented in Table 2 and Table 3. Table 2 shows the results of the simulations without considering surface suction nor water level, and Table 3 presents the results of the simulations that considered the surface suction and the two positions of the water level, at 6.5 m and 7.5 m deep. The volume result (m^3/m) is considered in the cross-section for 1 m of slope extension, and the volume result (m^3) is the total for the 37 m extension of the slope.

Table 2. SVSlope results with no surface suction and no water level (Riselo, 2021).

Analyse	Probability of Failure (%)	Safety Factor (SF)		Volume (m^3/m)		Volume (m^3)	
		Det.	Prob.	Det.	Prob.	Det.	Prob.
2D	1.24	1.21	1.19	111.70	86.59	4132.9	3203.83
3D	0.64	1.27	1.23	26.45	38.97	978.6	1442

Table 3. SVSlope results with surface suction and water level (Riselo, 2021).

WATER LEVEL AT 6.5 METERS								
Analyse	Suction (kPa)	Probability of Failure (%)	Safety Factor (SF)		Volume (m^3/m)		Volume (m^3)	
			Det.	Prob.	Det.	Prob.	Det.	Prob.
2D	20	0.28	1.25		159.9		5916.3	
	40	0.04	1.29					
	60	0.02	1.33					
	80	< 0.0002	1.36					
	100	< 0.0002	1.38					
	120	< 0.0002	1.39					
3D	20	< 0.0002	1.44		40.89		1513	
	40		1.46		35.3		1306	
	60		1.52		31.81		1177	
	80		1.68		49.59		1835	
	100		1.77		41.78		1546	
	120		1.85		58.05		2148	
WATER LEVEL AT 7.5 METERS								
Analyse	Suction (kPa)	Probability of Failure (%)	Safety Factor (SF)		Volume (m^3/m)		Volume (m^3)	
			Det.	Prob.	Det.	Prob.	Det.	Prob.
2D	20	0.28	1.25		159.9		5916.3	
	40	0.04	1.29					
	60	0.02	1.33					
	80	< 0.0002	1.36					
	100	< 0.0002	1.38					
	120	< 0.0002	1.39					
3D	20	< 0.0002	1.36		36.57		1353	
	40		1.53		47.05		1741	
	60		1.54		42.3		1565	
	80		1.61		23.43		867	
	100		1.65		48.05		1778	
	120		1.71		51.38		1901	

Among the 26 simulated scenarios, the one that presented the higher probability of failure was the first one, a 2D analysis with no surface suction nor water level, obtaining a value of 1.24%. The minimum safety factor required for a landslide of the slope is 1.3, according to the Brazilian standard ABNT NBR 11682 (ABNT, 2009), which depends on the consequences of failure, considering the level of security against material and environmental damages as low and the level of security against damages to human lives as medium. It is worth mentioning that this highway might face high consequences in case of failure. It is noticeable that the increase in surface suction in the analyzed slope provided an increase in the safety factor, guaranteeing greater safety to the slope.

It is important to assess both results, SF and probability of failure, since a low safety factor does not always indicate a failure in the slope, such as this slope, which in all simulated scenarios was considered stable. Assis (2020) points out that it is preferable to have an approximated probabilistic result than a precise deterministic result that is certainly wrong, which corroborates the importance of the probability of failure to analyze the problem.

The results of the deterministic analysis were different from the results of the probabilistic analysis only for the scenarios with no suction nor water level. Besides that, the deterministic analysis presented a more optimistic scenario due to the safety factor being higher.

The mobilized-mass volumes, for the scenarios without suction and water level, presented on Table 2, do not possess a behavior pattern. This difference in values is due to the critical surface failure considered for each analysis being different, mainly in the 3D geometry of the failure zone.

Also, due to the slope geometry, the intermediate stress (σ_2) acting on the 3D slope, which was disregarded in the 2D analysis, contributes to this difference in volumes.

The mobilized-mass volumes in the scenarios with surface suction and water level, presented in Table 3, were the same in the 2D, for both water levels, and different in the 3D. In 2D the critical surface failure was the same for all the simulations, while in 3D, for each scenario, it was found a different surface. Troncone et al. (2014), in their study, indicate that the analysis in 2D does not take into account the entire failure process, differently from the 3D analysis, which is able to evaluate all of the extension of the failure, becoming a more realistic simulation.

The difference in values of 2D and 3D is evident in the results in Table 3. The distinction in values is due to the possibility of considering all the possible landslides in the three dimensions, and also the consideration of the intermediate stress (σ_2) acting on the 3D slope, contributing to greater safety in the context

Firincioglu & Ercanoglu (2021) reported in their study that the tridimensional analyses of limit equilibrium provide a more realistic approach to the stability problems of slopes, corroborating the result found in this analysis.

Lastly, the proximity of the results with the two water level positions was observed, being the same in the 2D. In the 3D the value difference was small, having most safety factors a little higher at 6.5 m deep and volumes mobilized without behavior pattern.

Figure 4 exemplifies the deterministic analyses made in the software SVSlope and the results obtained in 2D and 3D.

3.2 Runout analysis of the mobilized-mass volume in the hypothetical rupture

The results of the runout analysis of mass movement are presented in Table 4. In this table the three simulated scenarios are listed, initially identifying the input parameters, such as mobilized-mass volume, and the results the total distance and percentage of traffic lanes intercepted.

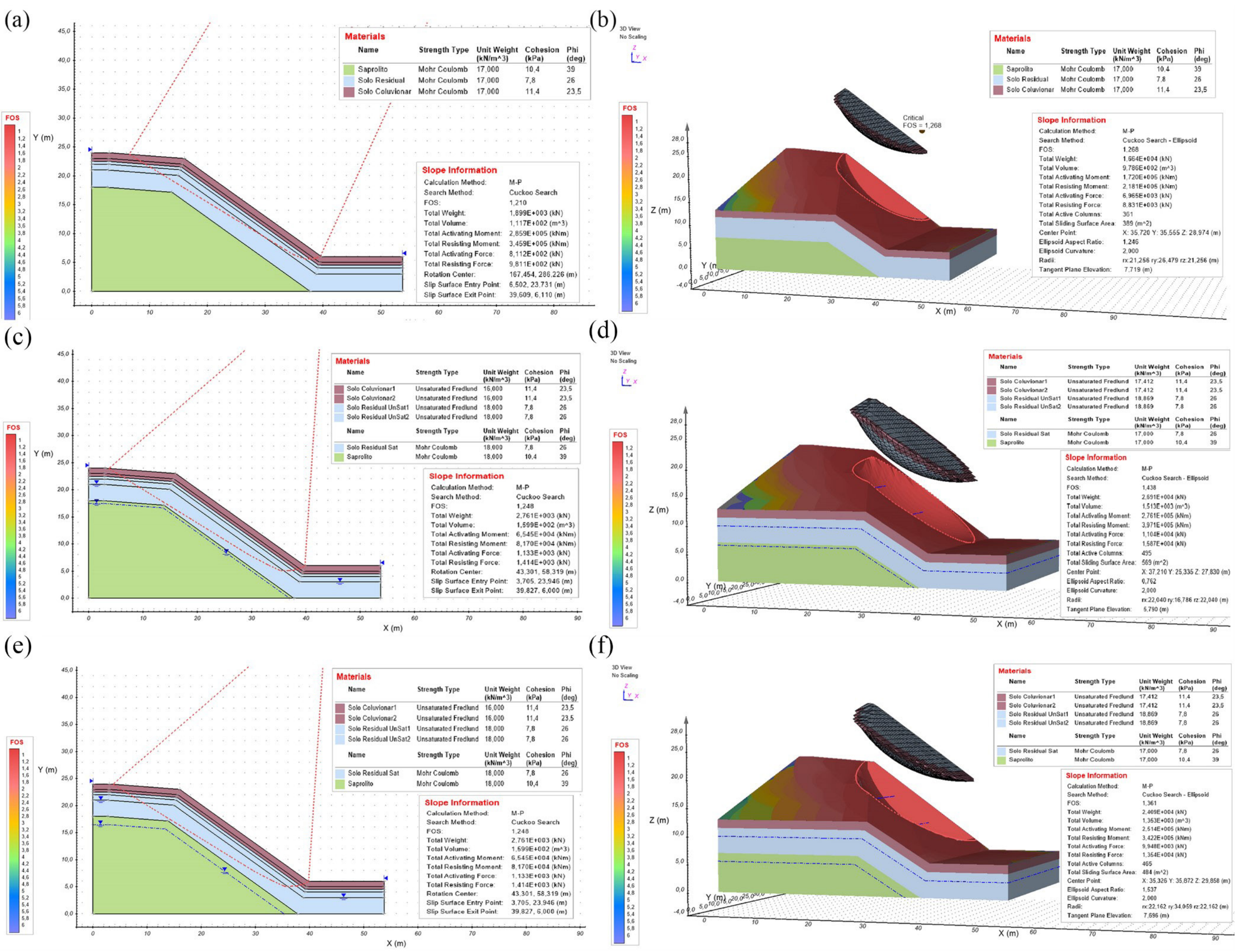

Figure 4. Deterministic analysis in SVSlope: (a) with no surface suction and no water level 2D, (b) 3D, (c) with 20 kPa surface suction and water level at 6.5 m depth 2D, (d) 3D, (e) with 20 kPa surface suction and water level at 7.5 m depth 2D and (f) 3D.

Table 4. Anura3D results of mass movement prediction.

Inputs				Outputs	
Simulation	Surface suction and water level	Stability analysis type	Mobilized-mass volume (m^3/m)	Distance covered (m)	Percentage of traffic lanes intercepted (%)
1	Not	Deterministic	111.70	8.62	72.4
2	Not	Probabilistic	86.59	7.25	59.7
3	Yes	Deterministic/ Probabilistic	159.9	10.41	89

Simulation 1 refers to the 2D deterministic analysis without surface suction and water level (line 1 – Table 2). Simulation 2 regards the 2D probabilistic analysis without surface suction and water level (line 1 – Table 2). Lastly, simulation 3 reflects all of the deterministic and probabilistic analyses with surface suction and water level (lines 1 to 6 and lines 13 to 18 – Table 3). The choice of these simulations is due to the fact that they are scenarios that presented different volumes. The selection of only the 2D analyses was due to the modeling of the software GID permitting the manual definition of the failure surface.

It is noticeable that the higher the mobilized-mass volume, more lanes are affected, as in simulation 3, which reached 89% of the traffic lanes, that is, practically all three lanes (Table 4).

Analyzing the three simulations, simulation 1 (2D deterministic analysis – with no surface suction and water level – Table 2) presented a total displacement of 8.62 m, affecting 3 traffic lanes, with an interception of up to 0.62 m of the third lane, leaving practically only the last lane free for traffic passage. Simulation 2 (2D probabilistic analysis – with no surface suction and no water level – Table 2) had 7.25 m of distance covered, affecting two traffic lanes, with a displacement of up to 2.85 m on to the second lane, also leaving only the last lane of traffic free. Simulation 3 (2D deterministic/probabilistic analysis – with surface suction and water level – Table 3) presented a displacement of 10.41 m, affecting the three traffic lanes, intercepting up to 2.41 m of the third lane, obstructing practically the whole traffic lanes.

The development of the failure surface indicates the beginning of the movement of the unstable soil mass of the slope, which moves towards the foot of the slope and later towards the traffic lanes. The displacement of the material point is what defines the kinematics of the landslide. Thus, over time, this displacement increases until the moment when the material points are in equilibrium, defining the final post-failure profile of the landslide and the total displacement distance. This distance is determined between the endpoint of the failure surface on the slope before the landslide and the endpoint of the material displaced after failure.

The displacement obtained with the analysis is typical of a post-failure rotational landslide, with distance values that increase until the slips become stable. Therefore, the mobilized soil mass accelerates until it reaches a maximum speed and then decelerates until it stops.

The methodology used was able, based on the material point method (MPM), to predict the displacement of the mobilized-mass volume. Furthermore, the MPM was able to simulate the landslide process, from the beginning of the failure to its progression in time, being able to solve failure simulations on slopes with different geometries of the failure surface. Thus, this methodology is applicable to assessing risks of traffic interruptions, based on the analysis of landslides in practical cases of slopes located close to highways. However, the choice of the constitutive model of the materials significantly influences the results of failure ranges, therefore, it is recommended the judicious choice of the model within the software. Also, the computational effort of the simulations is very high, so it is worth a previous analysis of the mesh size and the number of material points of each cell to be used in the MPM, so that the time and data processing are adequate for the desired accuracy.

Finally, a focus on the utilization of the software Anura3D to predict the movement of the mobilized-mass volume of a landslide, since it presented satisfactory results. Conte et al. (2019) and Conte et al. (2020) also used this software to assess the post-failure stage of two distinct landslides in south Italy, obtaining results consistent with those in the field. Both authors used the Mohr-Coulomb constitutive equation, obtaining a total displacement of 28 m in the sand and clayey silt, in the first paper, and a total displacement of 350 m in silty sand and clayey silt, in the second paper. That being, the utilization of the material point method (MPM), by the software Anura3D, provides reliable and applicable results to landslide problems on slopes.

Toro-Rojas et al. (2021) reported in their study that the utilization of the MPM to analyze a process of post-failure of a landslide on a slope is efficient, corroborating the result achieved in this analysis. Also, Troncone et al. (2019), concluded that the use of the MPM to simulate a landslide in all its stages and determine the distance of displacement of the slope's material is effective. Both authors used the Mohr-Coulomb constitutive equation, obtaining a runout distance of 2.5 m, in the first paper, and a runout distance of 1.7 m in a purely frictional soil, in the second paper.

Figure 5 exemplifies the 2D results visualized on ParaView, after the 50 steps of the calculation, for simulations 1 (a),

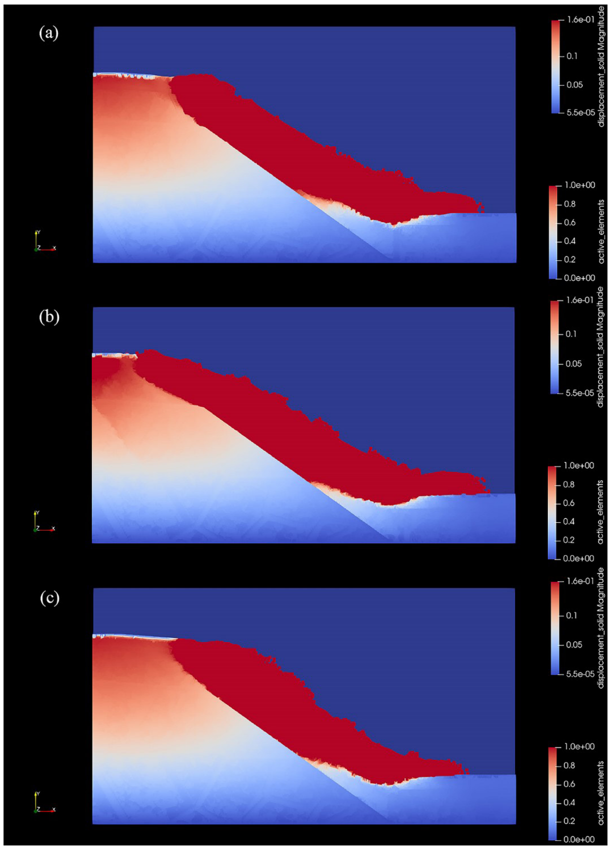

Figure 5. Mass movement prediction results in ParaView from simulations: (a) 1, (b) 2, and (c) 3.

2 (b), and 3 (c). The part in red refers to the mobile area of the slope, that is, the area above the critical failure surface.

4. Conclusions

According to the results of this study, it finds that the probabilistic analysis (applying Monte Carlo) provides a result that is more complete, since it produces, aside from the safety factor, the probability of failure of the slope. Then, even though in some scenarios the calculated safety factor, in a deterministic approach (applying Morgenstern-Price), was lower than the minimal safety factor, the probability of failure indicated a maximum value of 1,24%. According to the USACE classification (USACE, 1999), this probability value indicates a level of expected performance below average.

The incorporation of the surface suction on the unsaturated soils, by the characteristic curves of water retention, interfered in the results of safety factor (deterministic) and probability of failure. Regarding the mobilized-mass volume, no relation could be established, since it did not present a behavior pattern. It was obtained the highest quantity of volume, 159.90 m^3/m, in the 2D deterministic and probabilistic analyses with surface suction.

The results of the numeric simulation also showed that the 3D analysis presented more optimistic results when compared to the 2D analysis. The tridimensional analysis on small slopes is affected by the effect of the intermediate stress, so the results in 3D, when compared to the two-dimensional analysis, are more reliable and accurate to reality.

Regarding the shifting in the position of the consideration of water level in the slope, it was obtained a proximity to the results. The small difference in values is due to the water level being positioned in a fracturing material (saprolite), which obstructs the water flow to the shallower grounds. It is also due to the critical failure surface not reaching both water levels in the analyses, creating similar results.

The material point method (MPM), considering the Mohr-Coulomb constitutive model, utilized in this study was efficient to analyze the proposed simulations regarding the distance covered by the mobilized-mass volume, especially when compared with results obtained in other papers that used the same method. With the MPM it is possible to predict the displacement of this volume and assess the risks of traffic interruptions in practical cases of slopes close to highways.

For this study, any landslide that may come to occur, coming from this slope, will intercept at least two traffic lanes, which equals 59.7% of the existing lanes, damaging the vehicle flow and putting the safety of the highway and users at risk.

Therefore, in front of the whole study, it is concluded that the analyzed slope is safe regarding its global stability for failure. For application in other places, the best constitutive equation must be analyzed and, preferably, the parameters required by the equation must be validated by retro-analysis of known similar failures, tests, and/or bibliographic references. Furthermore, the results obtained in this article may be used as input data for future studies, such as the evaluation of the economic risk of a possible landslide and others points of this road.

Acknowledgements

The authors would like to thank the Graduate Program in Civil Engineering at the Federal University of Paraná, the support of the Technological Development Resources – RDT, of the Concessionaire Arteris S.A., under the control of the National Agency of Ground Transportation – ANTT, for making possible the accomplishment of this research project.

Declaration of interest

The authors have no conflicts of interest to declare. All co-authors have observed and affirmed the contents of the paper and there is no financial interest to report.

Authors' contributions

Bianca Riselo: conceptualization, data curation, methodology, software, formal analysis, writing – original draft preparation. Larissa Passini: supervision, validation, writing – reviewing, and editing. Alessander Kormann: supervision.

References

ABNT NBR 11682. (2009). *Estabilidade de encostas*. ABNT – Associação Brasileira de Normas Técnicas, Rio de Janeiro, RJ (in Portuguese).

Ahmadabadi, M., & Poisel, R. (2015). Assessment of the application of point estimate methods in the probabilistic stability analysis of slopes. *Computers and Geotechnics*, *69*, 540-550. http://dx.doi.org/10.1016/j.compgeo.2015.06.016.

Anura3D. (2021). *Anura3D MPM software: tutorial manual*. Anura3D MPM Research Community. Retrieved in October 31, 2022, from https://www.gidhome.com/archive/GiD_Convention/2018/courses/Module_Anura3D/TutorialManual_2017.2.pdf

Assis, A.P. (2020). Risk management for geotechnical structures: consolidating theory into practice. *Soils and Rocks*, *43*(3), 311-336. http://dx.doi.org/10.28927/SR.433311.

Autopista Régis Bittencourt – APRB. (2019). *Gestão de segurança dos taludes rodoviários da rodovia Régis Bittencourt, trecho da Serra do Mar PR-SP: estudos probabilísticos e monitoramento geológico-geotécnico para mensuração de riscos através de critérios econômicos*. APRB. Retrieved in October 31, 2022, from https://portal.antt.gov.br/documents/20122/0/Gest%C3%A3o+da+Seguran%C3%A7a+de+Taludes+Rodovi%C3%A1rios+da+Rodovia+R%C3%A9gis+Bittencourt%2C+Trecho+da+Serra+do+Mar+PR-SP+%282%29.pdf/37419216-30e8-e9d3-463b-56552bcecdc0?t=1650986489652

Batista, E.F. (2019). *Metodologias de mensuração econômica e avaliação da vulnerabilidade com aplicação em trechos da rodovia Régis Bittencourt, São Paulo-SP* [Master's dissertation, Federal University of Paraná]. Federal University of Paraná's repository (in Portuguese).

Bentley Systems Team. (2019). *SVOffice 5 help manual – 5/15/2019*. Saskatoon: SoilVision Systems Ltd.

Bhandari, T., Hamad, F., Moormann, C., Sharma, K.G., & Westrich, B. (2016). Numerical modelling of seismic failure using MPM. *Computers and Geotechnics*, *75*, 126-134. http://dx.doi.org/10.1016/j.compgeo.2016.01.017.

Chen, F., Zhang, R., Wang, Y., Liu, H., Böhlke, T., & Zhang, W. (2020). Probabilistic stability analyses of slope reinforced with piles in spatially variable soils. *International Journal of Approximate Reasoning*, *122*, 66-79. http://dx.doi.org/10.1016/j.ijar.2020.04.006.

Companhia de Pesquisa de Recursos Minerais – CPRM. (2013). Retrieved in October 4, 2022, from http://www.cprm.gov.br/publique/media/geologia_basica/pgb/mapa_eldorado_paulista.pdf

Conte, E., Pugliese, L., & Troncone, A. (2019). Post-failure stage simulation of a landslide using the material point method. *Engineering Geology*, *253*, 149-159. http://dx.doi.org/10.1016/j.enggeo.2019.03.006.

Conte, E., Pugliese, L., & Troncone, A. (2020). Post-failure analysis of the Maierato landslide using the material point method. *Engineering Geology*, *277*, 105788. http://dx.doi.org/10.1016/j.enggeo.2020.105788.

Fang, H., Chen, Y.F., Hou, Z., Xu, G., & Wu, J. (2020). Probabilistic analysis of a cohesion-frictional slope using the slip-line field theory in a Monte-Carlo framework. *Computers and Geotechnics*, *120*, 103398. http://dx.doi.org/10.1016/j.compgeo.2019.103398.

Fernandes, N.F., Guimarães, R.F., Gomes, R.A.T., Vieira, B.C., Montgomery, D.R., & Greenberg, H. (2001). Condicionantes geomorfológicos dos deslizamentos nas encostas: avaliação de metodologias e aplicação de modelo de previsão de áreas susceptíveis. *Revista Brasileira de Geomorfologia*, *2*(1), 51-71.

Firincioglu, B.S., & Ercanoglu, M. (2021). Insights and perspectives into the limit equilibrium method from 2D and 3D analyses. *Engineering Geology*, *281*, 105968. http://dx.doi.org/10.1016/j.enggeo.2020.105968.

Fredlund, D.G. (1987). Slope stability analysis incorporating the effect of soil suction. In M.G. Anderson & K.S. Richards (Eds.), *Slope stability* (pp. 113-144). Hoboken: John Wiley & Sons.

Gerscovich, D.M.S. (2016). *Estabilidade de taludes* (2nd ed.). São Paulo: Oficina de Textos.

Li, X., Wu, Y., He, S., & Su, L. (2016). Application of the material point method to simulate the post-failure runout of the Wangjiayan landslide. *Engineering Geology*, *212*, 1-9. http://dx.doi.org/10.1016/j.enggeo.2016.07.014.

Liu, S.Y., Shao, L.T., & Li, H.J. (2015). Slope stability analysis using the limit equilibrium method and two finite element methods. *Computers and Geotechnics*, *63*, 291-298. http://dx.doi.org/10.1016/j.compgeo.2014.10.008.

Liu, X., Wang, Y., & Li, D.-Q. (2019). Investigation of slope failure mode evolution during large deformation in spatially variable soils by random limit equilibrium and material point methods. *Computers and Geotechnics*, *111*, 301-312. http://dx.doi.org/10.1016/j.compgeo.2019.03.022.

Reale, C., Xue, J., Pan, Z., & Gavin, K. (2015). Deterministic and probabilistic multi-modal analysis of slope stability. *Computers and Geotechnics*, *66*, 172-179. http://dx.doi.org/10.1016/j.compgeo.2015.01.017.

Riselo, B.C.D.T. (2021). *Análise de estabilidade de um talude rodoviário por meio de modelo determinístico e probabilístico e previsão do volume de massa mobilizada* [Master's dissertation, Federal University of Paraná]. Federal University of Paraná's repository (in Portuguese). Retrieved in April 15, 2022, from https://hdl.handle.net/1884/73640

Tonus, B.P.A. (2009). *Estabilidade de taludes: avaliação dos métodos de equilíbrio limite aplicados a uma encosta coluvionar e residual da serra do mar paranaense* [Master's dissertation, Federal University of Paraná].

Federal University of Paraná's repository (in Portuguese). Retrieved in April 15, 2022, from https://hdl.handle.net/1884/19152

Toro-Rojas, D., Cordão Neto, M.P., Farias, M.M., & Reinaldo, R.L. (2021). Analysis of the failure modes and development of landslides using the material point method. *Soils and Rocks*, *44*(1), 1-13. http://dx.doi.org/10.28927/SR.2021.057820.

Trevizolli, M.N.B. (2018). *Proposta de modelo para avaliação de risco de deslizamentos baseado em cenários de eventos pluviométricos: aplicação em um talude da Serra do Mar no trecho PR/SP* [Master's dissertation, Federal University of Paraná]. Federal University of Paraná's repository (in Portuguese). Retrieved in April 15, 2022, from https://hdl.handle.net/1884/58845

Troncone, A., Conte, E., & Donato, A. (2014). Two and three-dimensional numerical analysis of the progressive failure that occurred in an excavation-induced landslide. *Engineering Geology*, *183*, 265-275. http://dx.doi.org/10.1016/j.enggeo.2014.08.027.

Troncone, A., Conte, E., & Pugliese, L. (2019). Analysis of the slope response to an increase in pore water pressure using the material point method. *Water*, 11(7), *1446*. http://dx.doi.org/10.3390/w11071446.

US Army Corps of Engineers – USACE. (1999). *Engineering and design: risk-based analysis in geotechnical engineering for support of planning studies*. Washington DC: USACE. Technical Letter No. 1110-2-556.

Wang, B., Vardon, P.J., & Hicks, M.A. (2018). Rainfall-induced slope collapse with coupled material point method. *Engineering Geology*, *239*, 1-12. http://dx.doi.org/10.1016/j.enggeo.2018.02.007.

Wang, M.-Y., Liu, Y., Ding, Y.-N., & Yi, B.-L. (2020). Probabilistic stability analyses of multi-stage soil slopes by bivariate random fields and finite element methods. *Computers and Geotechnics*, *122*, 103529. http://dx.doi.org/10.1016/j.compgeo.2020.103529.

Soils and Rocks

An International Journal of Geotechnical and Geoenvironmental Engineering

www.soilsandrocks.com

ISSN 1980-9743
ISSN-e 2675-5475

Experimental study on the behavior of a new post-grouted micropile in a tropical soil

Joaquim Ribeiro Castro Neto[1], Paulo José Rocha de Albuquerque[1], Yuri Barbosa[1#], Luiz Felipe Goulart Fiscina[1]

Case Study

Keywords
Post-grouted micropiles
Static load tests
Instrumentation
Pile shaft bearing capacity
Tropical soils

Abstract

This work aims to analyze the behavior of a new post-grouted micropile setup developed in tropical soil. Its main innovation is the use of high mechanical resistance steel pipes (N80 class) for drilling and as a structural component of the micropiles. The pipes have special manchette valves uniformly spaced to allow neat cement grout injection into the soil. Two instrumented micropiles with 0.3 m diameter (after injection) and lengths of 19.4 m and 21 m were installed at Experimental Site III of the University of Campinas (Unicamp). The geological profile of this site presents a sandy clay surface layer (porous and collapsible) followed by a layer of sandy silt (diabase residual soil). The piles were subjected to compressive slow maintained loading tests and were instrumented along their depth with strain gages. No geotechnical failure was observed during the load test. The maximum load achieved by the MC1 and MC2 micropiles were 2.210 kN and 2.470 kN, respectively. The load test data were extrapolated to estimate the ultimate geotechnical pile capacity. The extrapolated geotechnical failure load was above 2.500 kN for both micropiles and similar to those estimated by the Federal Highway Administration FHWA (2005) load capacity method. It was verified that (1) the pile material undergoes creep under stress above 25 MPa on the transversal section of the pile and (2) the debonding effect during the loading process. The micropiles showed higher values of skin friction compared with other piles installed in the same geological-geotechnical context (tropical soil).

1. Introduction

The micropile was first conceived in Europe in the 1950s, when Fernando Lizzi developed the pali radice as a foundation technique. The main characteristic of the micropile installation technique is the performance of this type of deep foundation in high-resistance soils (including rocks), spaces with low ceilings and places with uneven surface (FHWA, 2005). Due to the small diameter (typically around 0.3 m) or the difficulty of assuring adequate cleaning of the borehole, tip resistance is generally disregarded and only load transfer by skin friction is considered (Allen et al., 2004). According to Choi & Cho (2010), neat cement grout injection may increase the load capacity of the micropiles by more than 100%, both in soil and rock.

Some authors (Finno et al., 2002; Holman & Barkauskas, 2007) point out that a relative displacement between the steel casing and the neat cement grout may occur. Allen et al. (2004) and Holman & Barkauskas (2007) suggest that this phenomenon, called debonding effect, results from inadequate preparation of the pile head or from eccentric loads. According to FHWA (2005), the debonding effect may be disregarded, and adhesion between the smooth metal tube and the neat cement grout varies from 1 to 1.75 MPa. Fiscina et al. (2021) conclude that the mobilized skin friction of the soil-micropile interface was 2.4 and 1.7 higher than other types of piles installed in similar underground conditions.

FHWA (2005) classifies micropiles into four types based on the injection technique and on the applied pressure. Table 1 shows these classifications.

Due to its complex behavior, several studies seek to understand the behavior of these deep foundation elements by using numeric tools, analytical models, or load tests. Numerical modeling is a widely employed tool for evaluating the pile load capacity and its load transfer mechanisms (Loukidis & Salgado, 2008; Han et al., 2017; Mendoza et al., 2017; Khanmohammadi & Fakharian, 2019; Ong et al., 2021). Park et al. (2012), Dias & Bezuijen (2018) and Kim et al. (2020) achieved acceptable results evaluating the load transfer mechanism of piles by using analytical

[#]Corresponding author. E-mail address: ybarbosa39@gmail.com
[1]Universidade Estadual de Campinas, School of Civil Engineering, Architecture and Urban Design, Campinas, SP, Brasil.

Submitted on May 25, 2022; Final Acceptance on October 10, 2022; Discussion open until February 28, 2023.
https://doi.org/10.28927/SR.2022.005322

Table 1. Micropile classification (FHWA, 2005).

Type of micropile	Description
Type A	Neat cement grout is tremied into the borehole. It does not use pressure grouting injection (Gravity Fill Technique).
Type B	Pressure grouting injection during withdrawal of the steel casing (0.5 to 1 MPa).
Type C IGU	First, the borehole is filled with neat cement grout. Then, neat cement grout is pressure injected from the head of the pile through a tube with valves (Post-grouting technique with pressures above 1 MPa).
Type D IRS	First, the annulus shealth is formed with neat cement grout via a single packer. Afterwards, neat cement grout is pressure injected, locally, via a double packer (pressures up to 2 MPa). The injection phases are usually spaced 24 hours apart and the process may be repeated up to four times. Lastly the borehole is filled with neat cement grout.

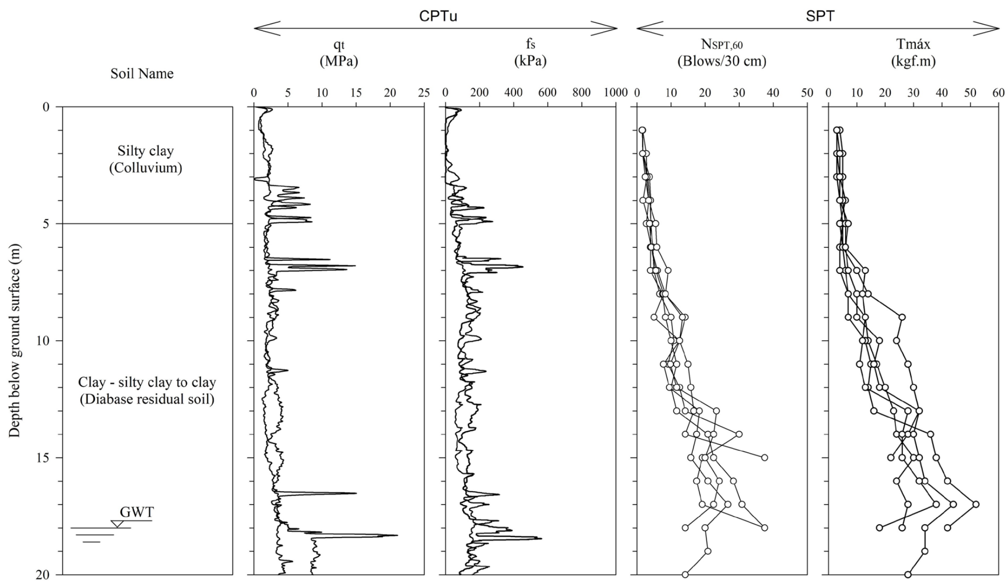

Figure 1. Physical and mechanical properties of the layered soil at ESIII.

models with emphasis in the discrete formulations, which considers different properties along the depth of the pile. Load tests are widely employed to understand the behavior of the piles and to validate computational tools and empirical and semiempirical calculation methodologies (Russo, 2004; Ko et al., 2018; Wan et al., 2019; Fattah et al., 2020; Freitas Neto et al., 2020).

Several papers evaluate the accuracy of empirical or semiempirical methods by using the results of load tests as a validation technique. In general, they suggest correction parameters to adjust the geotechnical characteristics of the subsoil conditions and the mechanical properties of the piles (Titi & Abu-Farsakh, 1999; Décourt, 2008; Niazi & Mayne, 2013; Wrana, 2015; Ebrahimian & Movahed, 2017; Eid et al., 2018; Moshfeghi & Eslami, 2018; Song et al., 2020; Jeong et al., 2021). Some methods were developed specifically for micropiles, such as: Bustamante & Doix (1985), Lizzi (1985) and FHWA (2005). Thereby, this study aims to present a new micropile technique in Brazil, evaluate its performance in a tropical soil by using instrumented load tests and compare its results with other piles installed in the same geological-geotechnical context.

2. Geological and geotechnical site characteristics

The load tests were performed at the Experimental Site III (ES III) of the University of Campinas, located in the city of Campinas, in the state of São Paulo, Brazil. Information on the site is provided in Albuquerque (2001), Castro Neto (2021), Fiscina (2020), and Fiscina et al. (2021).

Figure 1 shows the N_{SPT}, q_t, and f_s variation graphs based on five Standard Penetrations Tests (SPT) and two Piezocone Penetration Tests (CPTu). The upper layer is composed of porous silty clay (colluvial soil) about 5 m in depth, followed by ~25 m of silty clay (diabase residual soil). Lateritic concretion lenses of around 0.5 m were observed at a depth of 7 m. Such material can be identified in the peak values provided by the CPTu (q_t and f_s) along the test depth. Finally, the groundwater table (GWT) was found at a depth of 18 m.

Figure 2 shows the average geotechnical characteristics of the soil layers and the total length of the piles after their installation. The piles had a post-injection diameter of 0.3 m and lengths of 21 m (MC1) and 19.4 m (MC2). Both were installed according to the Type D methodology conforming to FHWA (2005). However, only the MC1 micropile had its manchette valves opened during the construction process.

3. Experimental set-up

The micropile in the present study is the result of a new construction technique that employs a special steel tube (ϕ = 200 mm - API N-80) with four main functionalities: drilling tool, casing protection, injection device (manchette valves system installed on the steel tube surface), and structural element. A brief description of the construction technique is presented below:

a) The first step is drilling by roto-percussion and water circulation using segments of steel tubes with threads. The initial segment has a drilling crown (Figure 3a) to facilitate cutting the soil. Tricone or eccentric bits with diamond or widia components can be used in case of more resistant bearing strata;
b) Then, a single packer (Figure 3b) is inserted inside the tube, at the tip of the micropile. Neat cement grout is injected with an ascending flux to fill the annulus space between the tube and the soil, constituting the annulus sheath, and removing any residual debris from drilling;
c) After the cure of the annulus sheath, a double packer (Figure 3c) is inserted for the post-grouting treatment. It is positioned at predetermined locations (starting from deeper positions), with the procedure being carried out from the bottom up. Note that the pressure injection can be carried out more than once – 1st phase, 2nd phase etc. – depending on the project/geotechnical consultant specifications;
d) Lastly, the steel tube is filled with neat cement grout from the bottom up. Figure 4 shows all phases of the construction process.

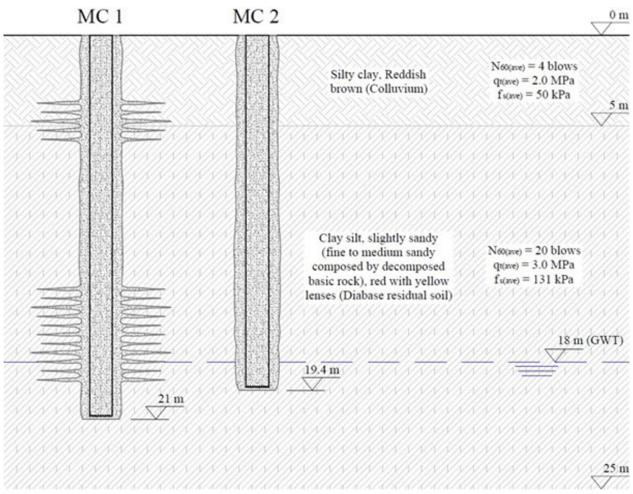

Figure 2. Estimated geotechnical profile of Experimental Site III.

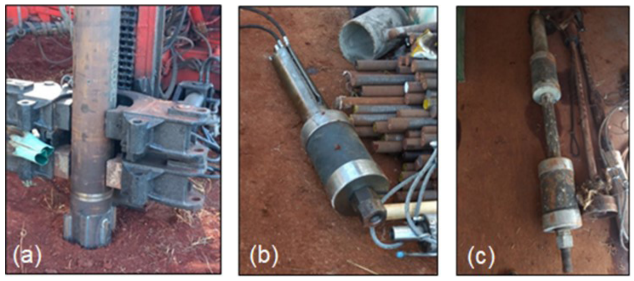

Figure 3. Tools used for the micropile construction: (a) tube coupled to the drill, (b) single packer and (c) double packer.

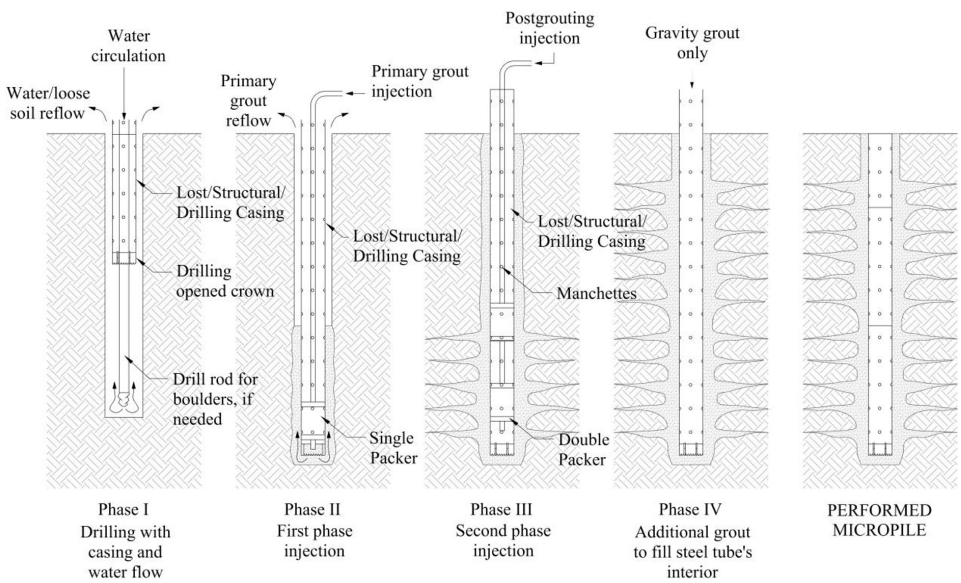

Figure 4. Micropile construction phases (Fiscina et al., 2021).

It is worthy to state that the manchette valves are previously installed in the walls of the steel tubes, in groups of four, diametrically opposed and vertically spaced by 0.5 m (industrial process). They have an aluminum body and a rubber packer, which opens with pressures up to 2 MPa, approximately (Figure 5). They close immediately after the pressure is released, preventing the neat cement grout from flowing back into the steel tube. To assure the correct operation of the device, the neat cement grout must have a cement-water factor of 0.5.

The instrumentation of the micropiles was performed using strain gages previously installed in steel bars of 12.5 mm in diameter and 0.5 m in length (instrumented bars). They were inserted after the post-grouting treatment (between Phase III and IV – Figure 4). Figure 6 shows the position of the instrumented bars alongside the pile depth, highlighting the MC1's manchette valves which opened after receiving the post-grouting treatment. Post-grouting injections were not performed for MC2 pile.

The reaction system of the load tests was designed to apply a maximum load of 3000 kN. It was composed of four reaction micropiles, a steel double I-beam, a hydraulic jack and a load cell (Figure 7). The static load-maintained test (SLMT) was conducted according to the instructions of the Brazilian Standard ABNT NBR 12131 (ABNT, 2006) with load increments of 130 kN.

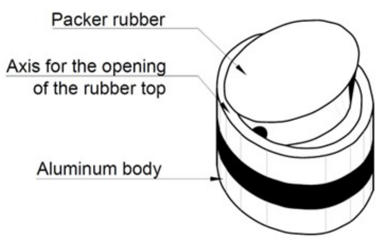

Figure 5. Neat cement grout injection valve.

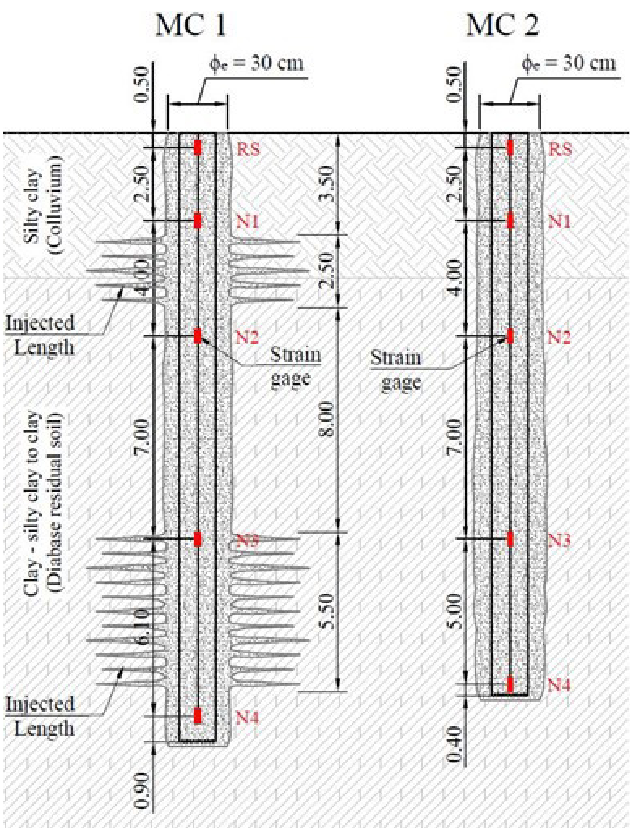

Figure 6. Instrumentation levels.

4. Analysis and results

Figure 8 shows the load *vs* movement curve of the micropiles studied. The MC1 reached a maximum load of 2210 kN with a movement of 24 mm while the MC2 reached a load of 2470 kN and a movement of 26 mm. The SMLT for MC1 was paralyzed due to a sudden failure of the pile cap/pile system, similar experience was evidenced by Fiscina et al. (2021). For MC2, the movement evolved continuously with

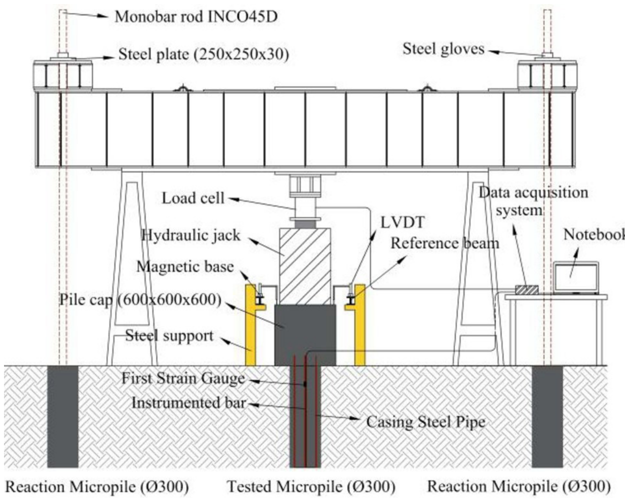

Figure 7. Load test assembly scheme (adapted from Fiscina et al., 2021).

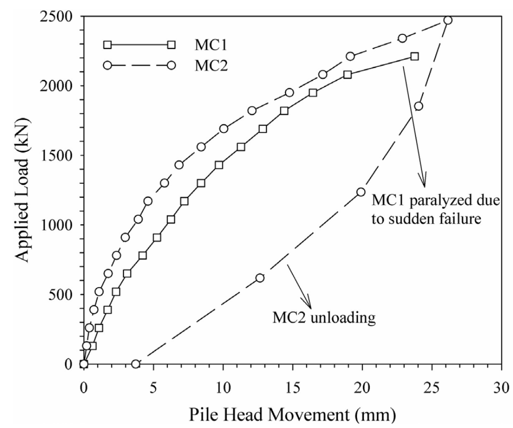

Figure 8. Load-displacement curves for micropiles.

the increase of the load without characterizing a conventional failure (close to 10% pile diameter). The test was stopped due to excessive deformation of the reaction system.

Since the results do not characterize a geotechnical failure, the Van der Veen (1953) method modified by Aoki (1976) was employed to extrapolate the data results, which resulted in an ultimate load capacity of 2560 kN and 2764 kN for the MC1 and MC2 micropiles, respectively. The ultimate load capacity was also estimated by the Bustamante & Doix (1985), Lizzi (1985) and FHWA (2005) semiempirical methods. Table 2 shows the results obtained by those methods.

Figure 9 presents the ratio of the estimated values for ultimate load capacity to the experimental ultimate load capacity obtained via SMLT. The FHWA (2005) and Lizzi (1985) methods showed similar results for both micropiles. This did not occur for the Bustamante & Doix (1985) method, which considers the initial annulus sheath volume and the post-grouting phases. Moreover, the Bustamante & Doix (1985) method also considers the tip resistance in the overall pile capacity calculation while the FHWA (2005) and Lizzi (1985) methods do not take it into account. The FHWA (2005) method showed results in the range of ± 20% of the variation which indicates to be a fit model to predict the geotechnical capacity of these types of piles embedded in tropical soil.

Figure 10 shows the load *vs* deformation curves along the micropile depth. The reference section exhibits deformations with an elastic behavior up to 1800 kN (25 MPa stress at the cross-section area, approximately), manifesting a creep response from this load up. Note that the MC2 micropile showed an unexpected behavior at level N2, with progressive stiffness loss after the tenth stage load.

The pile stiffness was obtained using the Incremental Stiffness Method (Fellenius, 1989; Fellenius, 2021) modified by Komurka & Moghaddam (2020). The tangential stiffness *vs* strain graphs (Figure 11) had a linear trend after 500 με, indicating that the skin friction was fully mobilized for the three upper levels (SR, N1, and N2). According to Fellenius (1989, 2001, 2021), after the graph converges to a straight line, the deep foundation element has the mechanical behavior of a column, so the calculated deformation module does not suffer interference from the surrounding soil. Therefore, considering the micropile diameter as 0.3 m, the deformation module of the micropiles is approximately equal to 11 GPa and 16 GPa for MC1 and MC2, respectively. These values are inferior to those of concrete piles, which are, in general, around 20 to 25 GPa (Albuquerque, 2001; Albuquerque et al., 2007, 2014). This can be explained by the fact that the neat cement grout does not use aggregates in its composition, which reduces the overall pile stiffness (Laister et al., 2014).

Table 2. Ultimate load capacity of the micropiles.

Method	MC1(in kN)	MC2(in kN)
FHWA (2005)	2555	2339
Lizzi (1985)	2227	2000
Bustamante & Doix (1985)	5518	4920

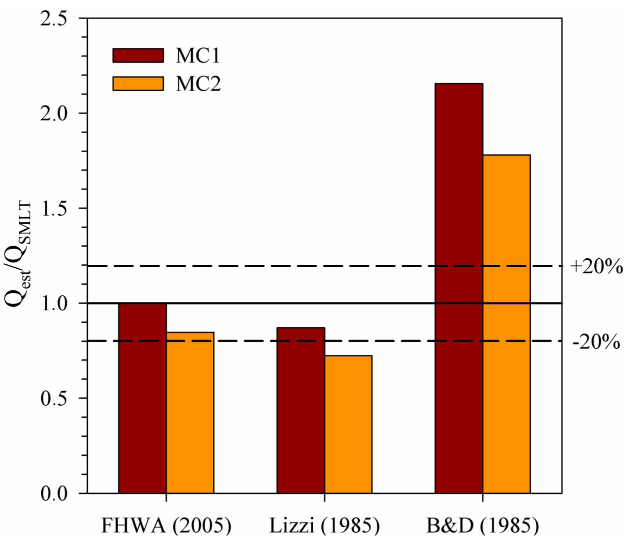

Figure 9. Comparison of estimated results.

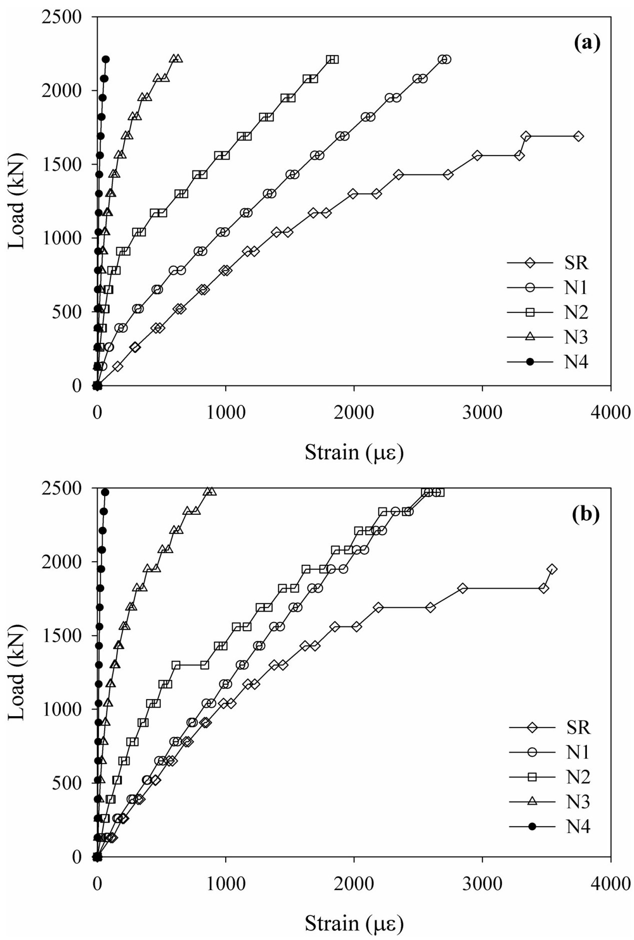

Figure 10. Load *vs* deformation graphs for micropiles (a) MC1 and (b) MC2.

Figure 12a shows the load transfer along the depth of the MC1 micropile. It indicates a linear behavior after 1820 kN and constant skin friction up to 14 m of depth. According to Figure 12b, the micropile MC2 presented a variation of the load transfer mechanism after the load stage of 1170 kN (between 3.0 and 7.0 m), which indicates a loss of friction in that region. The load transfer in the soil/micropile interface is progressively reduced until reaching a constant value at the last load stage, i.e., at this region there is no load transfer from the pile to the soil. This is probably due to excessive fissuring of the neat cement grout, which may have compromised the adhesion between the pile and the surrounding soil. According to Gomez et al. (2003) and Fiscina et al. (2021), this phenomenon is called debonding effect and happens when the pile-soil interface is unable to retain significant shear resistance. It is worth mentioning that the strength values of the neat cement grout at 28 days used in the present study (approximately equal to 15MPa) were below the values recommended by the FHWA (2005), which vary between 28 MPa to 35 MPa. The maximum tip load was 63 kN and 75 kN for MC1 and MC2, respectively, which in terms of the overall pile capacity is negligible.

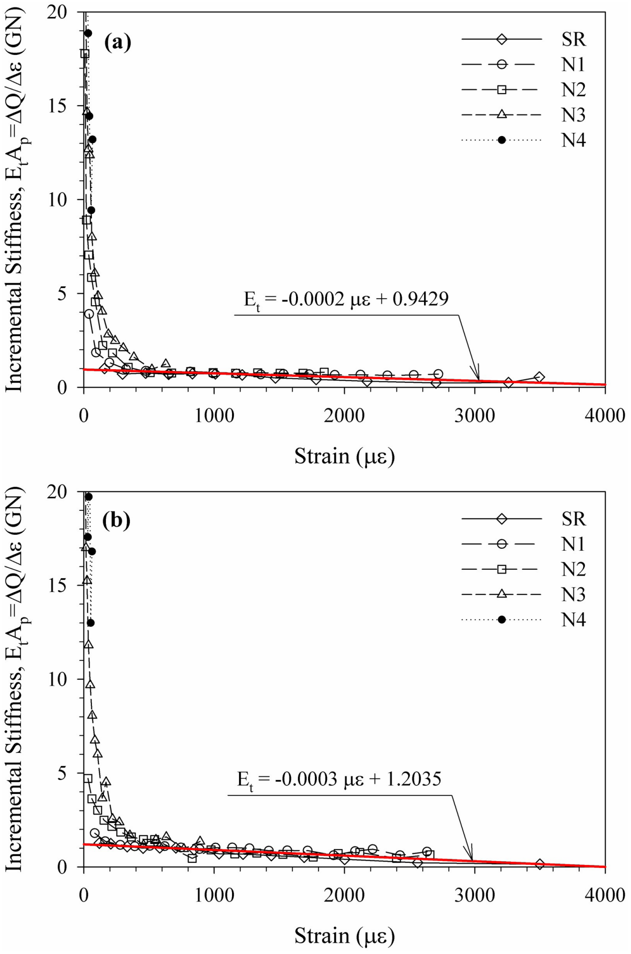

Figure 11. Incremental stiffness *vs* strain graphs for micropiles (a) MC1 and (b) MC2.

Figure 13a shows that the maximum mobilized skin friction on the MC1 micropile was in the region treated with neat cement grout (3 m to 7 m from the top of the pile), reaching a value equal to 150 kPa (last load stage). In addition, the weighted average skin friction along the micropiles depth was equal to 112 kPa (last load stage). For the MC2 micropile, the highest mobilized skin friction value was 222 kPa, in the region from 7 m to 14 m from the top of the pile (Figure 13b). At the last load stage, the weighted average skin friction along the length of the micropile was 137 kPa, showing that the post-grouting treatment with high pressures does nt necessarily guarantee the increasing of the skin friction of the micropile.

Figure 14 presents that the development of the unit skin friction (average value) with the displacement of the shaft follows the same trend for both piles, as verified by the B parameter (MC1 = 32 kPa/mm and MC2 = 38 kPa/mm). Also, the displacements for mobilizing the maximum skin friction were around 1.2% and 0.7% of the pile diameter for the MC1 and MC2 micropiles, respectively. These values are in accordance with the findings of Albuquerque (2001), Wada (2004) and Meyer & Żarkiewicz (2018).

Figure 15 shows the stiffness trend of current post-grouted micropile compared with other types performed at the Experimental Site I (Albuquerque, 2001; Albuquerque et al.,

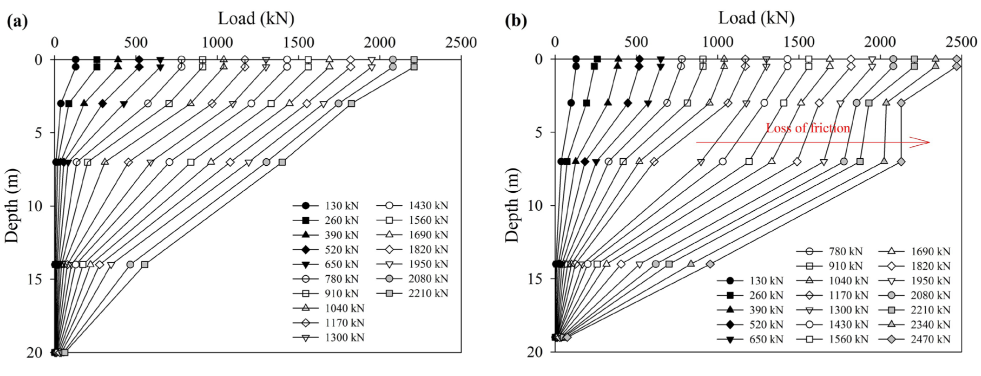

Figure 12. Load transfer for micropiles (a) MC1 and (b) MC2.

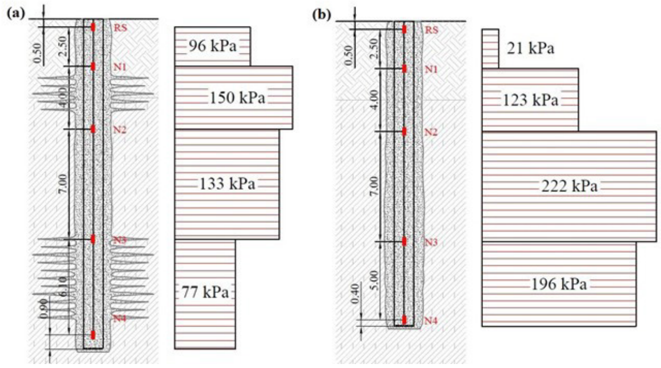

Figure 13. Maximum skin friction along depth for micropiles (a) MC1 and (b) MC2.

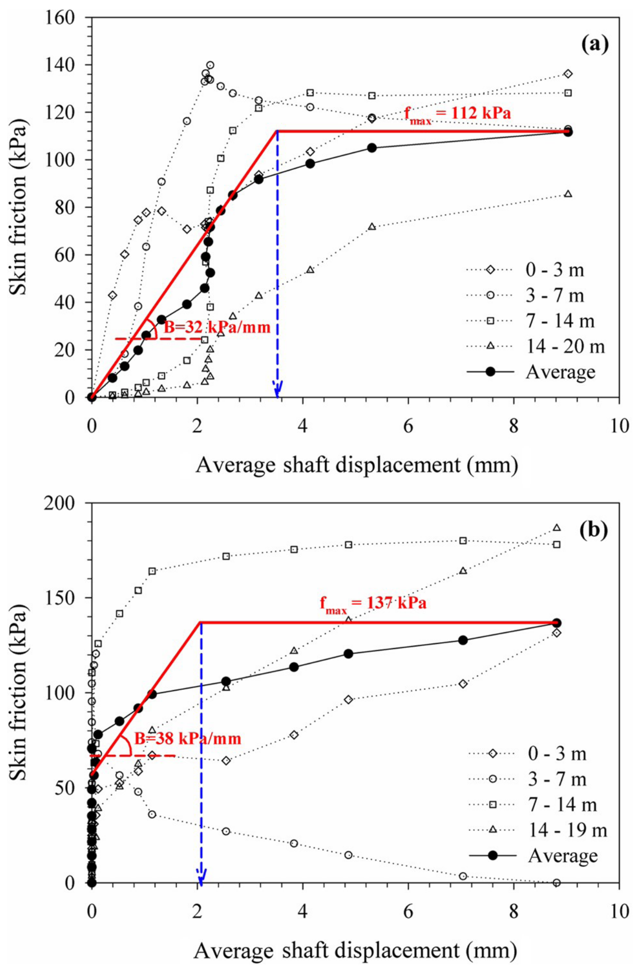

Figure 14. Average maximum unitary friction *vs* average shaft displacement for micropiles (a) MC1 and (b) MC2.

2005, 2007; Albuquerque & Carvalho, 2017; Fiscina et al., 2021). The upper stiffness bound varies between 45 and 25 kPa/mm and the lower bound between 25 and 5 kPa/mm, with the trend line varying between 35 and 15 kPa/mm. Traditional bored piles fully mobilized the skin friction for shaft displacements inferior to 1 mm, whereas root piles developed displacements close to 6 mm to mobilize the

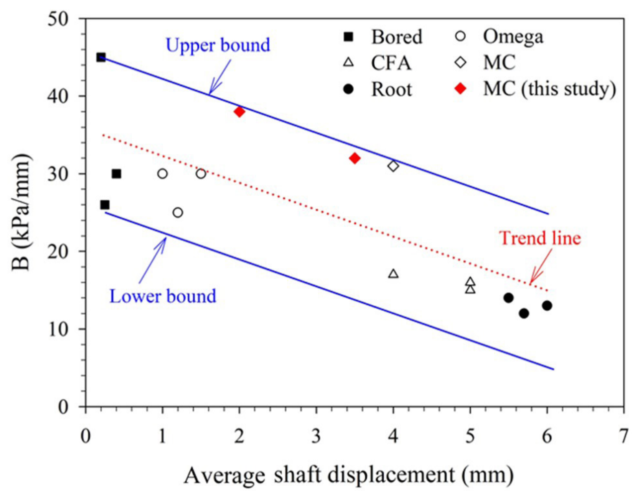

Figure 15. Variation in B parameter of piles performed at ESI.

maximum skin friction. The micropiles presented in this study were close to the upper stiffness bound with displacements between 2 mm and 4 mm.

Figure 16 presents the maximum skin friction variation for the piles performed at the ES I and the ES III. The maximum skin friction for the first layer of ES I (silty clay / depth of 0 to 5m / N_{SPT} = 4 blows) had an average value of 56 kPa (coefficient of variation = 34%). However, the same layer in the ES III – adding the results from Fiscina et al. (2021) for a micropile (MC 0) with ϕ = 0.3 m and L = 17 m – shows higher maximum skin friction in the first layer compared with that obtained for the piles installed at the ES I, with an average value of 101 kPa (CV = 22%). This value is 80% higher than the mobilized skin friction values from the ES1, showing that the construction process influences the performance of the pile. The first layer is a tropical lateritic soil, which, despite presenting low resistance values in the CPTu and SPT tests, results in higher skin friction due to the internal cementation inherit from this type of soil. This phenomenon was also observed by Décourt (2008), Schulze (2013) and Albuquerque et al. (2007) with piles performed in the same type of soil.

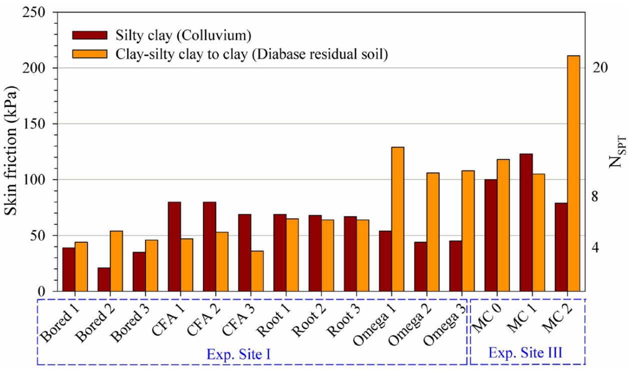

Figure 16. Skin friction variation for local soil profile.

Regarding the second representative soil layer, the piles installed in the ES I exhibit a maximum length of 12 m, with 7 m embedded in the residual soil layer with $N_{SPT,ave}$ = 8 blows, whereas in ES III, the micropiles vary between 16 and 21 m in length, with 11 to 16 m embedded in that same soil layer but with an $N_{SPT,ave}$ = 20 blows, which prevents a quantitative comparison. However, it was observed that, excluding the micropile MC2, the behavior was similar to that of omega piles from the ES I, with friction values around 110 kPa (114 kPa).

5. Conclusions

This work presented a new post-grouted micropile type installed in a tropical soil. Two instrumented static load-maintained tests were performed to verify its behavior and design parameters, and results were compared with other types of piles installed in the same subsoil profile. Main conclusions from results are as follows:

- The FHWA (2005) method of estimating the ultimate geotechnical pile capacity best fitted with the values from the load tests. The authors recommend using the average values of q_s suggested by the FHWA (2005) for this type of soil (tropical lateritic soil) and micropiles aiming to estimate the geotechnical capacity for future designs. The Bustamante & Doix (1985) method showed that the volume and injection correction parameters would be inadequate for the studied micropiles and for the local condition, thus requiring further studies. In addition, pile tip resistance can be ignored for these types of piles. The Lizzi (1985) method, despite being developed for root piles and showing results outside the ± 20% range, proved to be a usable method. However, further studies are required to propose a correction coefficient for this method.
- Comparing the maximum skin friction calculated from the method suggested by the FHWA (2005) and the values obtained from the load tests, the calculated values are lower, especially in the layers up to 7 m of depth. This suggests that this specific layer contain additional resistance due to its natural cementation (typical of lateritic soils).
- The instrumentation technique used was efficient. For stresses above 25 MPa, the instrumentation presents a creep response, indicating that the load vs deformation mechanism stops being proportional for values beyond that point, which should be avoided in load tests. The incremental stiffness method proposed by Komurka & Moghaddam (2020) is appropriate, considering that the behavior is non-linear and the transversal section is irregular;
- The deformation modules were inferior to those obtained for concrete piles, which was expected due to the use of neat cement grout instead of concrete (Fiscina et al., 2021). The loss of stiffness in part of the shaft of one of the piles suggests the occurrence of the debonding effect caused by the low resistance of the neat cement grout, which was lower than the values suggested by the FHWA (2005) standards.
- The piles showed that the maximum skin friction was mobilized for average shaft displacements of around 1% of the pile diameter (300 mm), similar to the behavior of other types of piles performed at Unicamp, which work mostly by friction. The stiffness of the micropiles showed higher values compared to the other piles installed at Unicamp, indicating that the installation process improves the friction performance.
- The new micropile construction methodology proved to be promising in terms of improving the shaft resistance, showing average skin friction above 110 kPa, which is 1.3 to 3.8 times higher than the average friction observed in other types of piles performed in similar ground conditions. However, there was no effective gain of resistance by lateral friction due to the post-grouting treatment, which indicates that only the injection of the annulus sheath is indicative of improvement in the performance by friction.

Acknowledgements

The authors thank the University of Campinas (Unicamp) and INCOTEP for the support given to build the experimental site and the micropiles. We also thank Coordenação de Aperfeiçoamento de Pessoal de Nível Superior (CAPES) for the study grants to the graduate students involved in this research.

Declaration of interest

The authors have no conflicts of interest to declare. All co-authors have observed and affirmed the contents of the paper and there is no financial interest to report.

Authors' contributions

Joaquim Ribeiro Castro Neto: conceptualization, data curation, investigation, methodology, writing – original draft. Paulo José Rocha de Albuquerque: conceptualization, methodology, supervision, validation, project administration, writing – review and editing. Yuri Barbosa: investigation, methodology, writing – review and editing. Luiz Felipe Goulart Fiscina: investigation, methodology, writing – review and editing.

List of symbols

q_t	Measured cone resistance
fs	Unit sleeve friction resistance
API	American Petroleum Institute
B	Stiffness
CPTu	Cone Penetration Test
CV	Coefficient of variation
ES I	Experimental Site I
ES III	Experimental Site III
MC 1	Micropile 1
MC 2	Micropile 2
N_{SPT}	Standard Penetration Test blows count
Q_{est}	Estimate Load by Method
Q_{SMLT}	Load Test Load Measured
SPT	Standard Penetration Test
SR	Reference Section

References

ABNT NBR 12131. (2006). *Estacas: prova de carga estática: método de ensaio.* ABNT - Associação Brasileira de Normas Técnicas, Rio de Janeiro, RJ (in Portuguese).

Albuquerque, P.J.R. (2001). *Estacas escavadas, hélice contínua e ômega: estudo do comportamento à compressão em solo residual de diabásio, através de provas de carga instrumentadas em profundidade* [Doctoral thesis]. Universidade de São Paulo (in Portuguese). https://doi.org/10.11606/T.23.2019.tde-07082019-100623.

Albuquerque, P.J.R., Carvalho, D., Alledi, C.T.D.B., & Polido, U.F. (2007). Behavior of instrumented continuous flight auger piles in sedimentary and residual soils. In *Proceedings of the 13th Panamerican Conference on Soil Mechanics and Geotechnical Engineering* (pp. 1-6). Venezuelan Geotechnical Society.

Albuquerque, P.J.R., Freitas Neto, O., & Garcia, J.R. (2014). Behavior of instrumented omega pile in porous soil. *Advanced Materials Research*, 1030, 732-735. http://dx.doi.org/10.4028/www.scientific.net/AMR.1030-1032.732.

Albuquerque, P.J.R., & Carvalho, D. (2017). Effect of second loading on the instrumented continuous flight auger concrete pile on porous soil. *Key Engineering Materials*, 753, 285-289. http://dx.doi.org/10.4028/www.scientific.net/KEM.753.285.

Albuquerque, P.J.R., Carvalho, D., & Massad, F. (2005). Bored, continuous flight auger and omega instrumented piles: Behavior under compression. In *Proceedings of the 16th International Conference on Soil Mechanics and Geotechnical Engineering* (pp. 339-345). IOS Press.

Allen, C., Jesús, G., Donald, B., & Tom, A. (2004). Micropiles: recente advances and future trends. In *Proceedings of the Current Practices and Future Trends in Deep Foundations* (pp. 140-415), Los Angeles. ASCE Geotechnical Special Publication. https://doi.org/doi:10.1061/40743(142)9.

Aoki, N. (1976). *Considerações sobre a capacidade de carga de estacas isoladas*. Rio de Janeiro*:* Universidade Gama Filho, 44p.

Bustamante, M., & Doix, B. (1985). Une méthode pour le calcul des tirants et des micropieux injectés. *Bulletin de Liaison des Laboratories des Ponts et Chaussées*, 140, 75-92 (in French).

Castro Neto, J.R. (2021). *Estaca injetada instrumentada tipo Incopile: avaliação do comportamento à compressão em solo tropical da região de Campinas/SP* [Master's dissertation]. Universidade Estadual de Campinas (in Portuguese). Retrieved in June 21, 2022, from https://hdl.handle.net/20.500.12733/1641142

Choi, C., & Cho, S.D. (2010). Field verification study for micropile load capacity. In *Proceedings of the 10th International Workshop on Micropiles* (pp. 1-10), Washington, DC.

Décourt, L. (2008). Loading tests: interpretation and prediction of their results. In *Proceedings of the Research to Practice in Geotechnical Engineering* (pp. 452-470). New Orleans: ASCE. http://dx.doi.org/10.1061/40962(325)16.

Dias, T.G.S., & Bezuijen, A. (2018). Load-transfer method for piles under axial loading and unloading. *Journal of Geotechnical and Geoenvironmental Engineering*, 144(1), 04017096. http://dx.doi.org/10.1061/(ASCE)GT.1943-5606.0001808.

Ebrahimian, B., & Movahed, V. (2017). Application of an evolutionary-based approach in evaluating pile bearing capacity using CPT results. *Ships and Offshore Structures*, 12(7), 937-953. http://dx.doi.org/10.1080/17445302.2015.1116243.

Eid, M., Hefny, A., Sorour, T., & Zagh, Y. (2018). Full-scale well instrumented large diameter bored pile load test in multi layered soil: a case study of damietta port new grain silos project. *International Journal of Current Engineering and Technology*, 8(01), 85-98. http://dx.doi.org/10.14741/ijcet.v8i01.10895.

Fattah, M.Y., Al-Omari, R.R., & Fadhil, S.H. (2020). Load sharing and behavior of single pile embedded in unsaturated swelling soil. *European Journal of Environmental and Civil Engineering*, 24(12), 1967-1992. http://dx.doi.org/10.1080/19648189.2018.1495105.

Fellenius, B.H. (1989). Tangent modulus of piles determined from strain data. In *Proceedings of the ASCE Geotechnical Engineering Division Foundation Congress* (pp. 500-510), Evanston. ASCE.

Fellenius, B.H. (2001). From strain measurements to load in an instrumented pile. *Geotechnical News Magazine*, 19(1), 35-38.

Fellenius, B.H. (2021). *Basics of foundation design*. (Electronic Edition). Retrieved in June 21, 2022, from https://www.fellenius.net

FHWA NHI-05-039. (2005). *Micropile design and construcion.* FHWA - Federal Highway Administration, U. S. Department of Transportation, Washington, DC.

Finno, R.J., Scherer, S.D., Paineau, B., & Roboski, J. (2002). Load transfer characteristics of micropiles in dolomite. In *Proceedings of the Deep Foundations 2002: An International Perspective on Theory, Design, Construction, and Performance* (pp. 1038-1053), Orlando. ASCE. http://dx.doi.org/10.1061/40601(256)73.

Fiscina, L.F.G. (2020). *On the interpretation of the failure mechanism of instrumented post-grouted micropiles submitted to compression and tensile axial loads in diabase soil* [Master's dissertation]. Universidade Estadual de Campinas. Retrieved in June 21, 2022, from https://hdl.handle.net/20.500.12733/1640794

Fiscina, L.F.G., Barbosa, Y., Albuquerque, P.J.R., & Carvalho, D. (2021). Field study on axial behavior of instrumented post-grouted steel pipe micropiles in tropical lateritic soil. *Innovative Infrastructure Solutions*, 6(2), 1-17. http://dx.doi.org/10.1007/s41062-020-00411-x.

Freitas Neto, O., Cunha, R.P., Albuquerque, P.J.R., Garcia, J.R., & Santos Júnior, O.F.D. (2020). Experimental and numerical analyses of a deep foundation containing a single defective pile. *Latin American Journal of Solids and Structures*, 17(3), 1-15. http://dx.doi.org/10.1590/1679-78255827.

Gomez, J., Cadden, A., & Bruce, D.A. (2003). Micropiles founded in rock: development and evolution of bond stress under repeated loading. In *Proceedings of 12th Panamerican Conference on Soil Mechanics and Geotechnical Engineering* (pp. 1911-1916), Cambridge. Verlag Glückauf GMBH.

Han, F., Salgado, R., Prezzi, M., & Lim, J. (2017). Shaft and base resistance of non-displacement piles in sand. *Computers and Geotechnics*, 83, 184-197. http://dx.doi.org/10.1016/j.compgeo.2016.11.006.

Holman, T.P., & Barkauskas, B.D. (2007). Mechanics of micropile performance from instrumented load tests. In *Proceedings of 7th FMGM 2007: Field Measurements in Geomechanics* (pp. 1-14). Boston: ASCE. http://dx.doi.org/10.1061/40940(307)8.

Jeong, S., Kim, D., & Park, J. (2021). Empirical bearing capacity formula for steel pipe prebored and precast piles based on field tests. *International Journal of Geomechanics*, 21(9), 04021165. http://dx.doi.org/10.1061/(ASCE)GM.1943-5622.0002112.

Khanmohammadi, M., & Fakharian, K. (2019). Numerical modelling of pile installation and set-up effects on pile shaft capacity. *International Journal of Geotechnical Engineering*, 13(5), 484-498. http://dx.doi.org/10.1080/19386362.2017.1368185.

Kim, D., Jeong, S., & Park, J. (2020). Analysis on shaft resistance of the steel pipe prebored and precast piles based on field load-transfer curves and finite element method. *Soil and Foundation*, 60(2), 478-495. http://dx.doi.org/10.1016/j.sandf.2020.03.011.

Ko, J., Seo, H., Kim, S., & Kim, S. (2018). Numerical analysis for mechanical behavior of pipe pile utilized for compressed air energy storage. In *Proceedings of the IFCEE 2018* (pp. 715-723). Orlando: ASCE. http://dx.doi.org/10.1061/9780784481578.068.

Komurka, V.E., & Moghaddam, R.B. (2020). The incremental rigidity method: more direct conversion of strain to internal force in an instrumented static loading test. In *Proceedings of the Geo-Congress 2020* (pp. 124-134), Minneapolis. ASCE. http://dx.doi.org/10.1061/9780784482780.013.

Laister, E., Albuquerque, P.J.R., Camarini, G., & Carvalho, D. (2014). The influence of cement and water to cement ratio on capillary absorption of root-pile mortars. *Soils and Rocks*, 37(2), 171-176. http://dx.doi.org/10.28927/SR.372171.

Lizzi, F. (1985). The pali radice (root piles): a state-of-the-art report. In *Proceedings of the Symposium on Recent Developments in Ground Improvement Techniques* (pp. 417-450). Bangkok: Balkema.

Loukidis, D., & Salgado, R. (2008). Analysis of the shaft resistance of non-displacement piles in sand. *Geotechnique*, 58(4), 283-296. http://dx.doi.org/10.1680/geot.2008.58.4.283.

Mendoza, C.C., Caicedo, B., & Cunha, R. (2017). Determination of vertical bearing capacity of pile foundation systems in tropical soils with uncertain and highly variable properties. *Journal of Performance of Constructed Facilities*, 31(1), 04016068. http://dx.doi.org/10.1061/(ASCE)CF.1943-5509.0000918.

Meyer, Z., & Żarkiewicz, K. (2018). Skin and toe resistance mobilisation of pile during laboratory static load test. *Studia Geotechnica et Mechanica*, 40(1), 1-5. http://dx.doi.org/10.2478/sgem-2018-0001.

Moshfeghi, S., & Eslami, A. (2018). Study on pile ultimate capacity criteria and CPT-based direct methods. *International Journal of Geotechnical Engineering*, 12(1), 28-39. http://dx.doi.org/10.1080/19386362.2016.1244150.

Niazi, F.S., & Mayne, P.W. (2013). Cone penetration test based direct methods for evaluating static axial capacity of single piles. *Geotechnical and Geological Engineering*, 31(4), 979-1009. http://dx.doi.org/10.1007/s10706-013-9662-2.

Ong, Y.H., Toh, C.T., Chee, S.K., & Mohamad, H. (2021). Bored piles in tropical soils and rocks: shaft and base resistances, t-z and q-w models. *Geotechnical Engineering*, 174(2), 193-224. http://dx.doi.org/10.1680/jgeen.19.00106.

Park, J.H., Kim, D., & Chung, C.K. (2012). Implementation of Bayesian theory on LRFD of axially loaded driven piles. *Computers and Geotechnics*, 42, 73-80. http://dx.doi.org/10.1016/j.compgeo.2012.01.002.

Russo, G. (2004). Full-scale load tests on instrumented micropiles. *Geotechnical Engineering*, 157(3), 127-135. http://dx.doi.org/10.1680/geng.2004.157.3.127.

Schulze, T. (2013). *Análise da capacidade de carga de estaca escavada instrumentada de pequeno diâmetro por meio de métodos semi-empíricos* [Master's dissertation]. Universidade Estadual de Campinas (in Portuguese). http://dx.doi.org/10.47749/T/UNICAMP.2013.909385.

Song, C.R., Bekele, B., Silvey, A., Lindemann, M., & Ripa, L. (2020). Piezocone/cone penetration test-based pile capacity analysis: calibration, evaluation, and implication of geological conditions. *International Journal of Geotechnical Engineering*, 16(3), 343-356. http://dx.doi.org/10.1080/19386362.2020.1778214.

Titi, H.H., & Abu-Farsakh, M.Y. (1999). *Evaluation of bearing capacity of piles from cone penetration test data.* Retrieved in June 21, 2022, from https://rosap.ntl.bts.gov/view/dot/22095

Van der Veen, C. (1953). The bearing capacity of pile. In *Proceedings of the International Conference on Soil Mechanics and Foundation Engineering* (pp. 84-90). Zürich: ICOSOMEF.

Wada, A. (2004). Skin friction and pile design. In *Proceedings of the 5th International Conference on Case Histories in Geotechnical Engineering* (pp. 1-7). New York: University of Missouri-Rolla. Retrieved in June 21, 2022, from https://scholarsmine.mst.edu/icchge/5icchge/session01/14

Wan, Z.H., Dai, G.L., & Gong, W.M. (2019). Field study on post-grouting effects of cast-in-place bored piles in extra-thick fine sand layers. *Acta Geotechnica*, 14(5), 1357-1377. http://dx.doi.org/10.1007/s11440-018-0741-7.

Wrana, B. (2015). Pile load capacity: calculation methods. *Studia Geotechnica et Mechanica*, 37(4), 83-93. http://dx.doi.org/10.1515/sgem-2015-0048.


DF+
TRANSFORMATIVE ENGINEERING, MANAGEMENT, AND INNOVATION DELIVERING RESULTS
DF+ IS AN INTEGRATED ENGINEERING CONSULTING FIRM WITH OVER 25 YEARS OF EXPERIENCE IN THE SECTORS OF MINING, INFRASTRUCTURE, AGRIBUSINESS, AND INDUSTRIAL.
WE DEVELOP PROJECTS BASED ON CONSOLIDATED TECHNICAL SOLUTIONS THAT ENCOMPASS THE STATE OF THE ART IN DIGITAL ENGINEERING.
AV. BARÃO HOMEM DE MELO, 4554 - 5th floor
ESTORIL, BELO HORIZONTE/MG
+55 31 2519-1001
dfmais.eng.br
comercial@dfmais.eng.br
DF+ ENGENHARIA

The Best Solution!

***Tecnilab Portugal, S.A.** will provide you with answers to your Geotechnical engineering needs.*

Tecnilab Portugal, S.A. is a professional Geotechnical engineering company and has a lot of experience as a professional group that mainly engages in measurement engineering in dam, subway(Metro), harbor, power plant, soft ground and structure construction.

WE ARE THE DISTRIBUTOR OF PORTUGAL OF ACE INSTRUMENT CO., LTD. IN KOREA.

ACE INSTRUMENT CO., LTD. is a company that obtains worldwide reputation for supplying high precision, high reliability products in all Geotechnical instruments, data logger and in-situ test equipments. Independently developed automatic monitoring system can be used anywhere in the world, including buildings, bridges, ground and any constructions.

Data Acquisition System & Web Monitoring Program

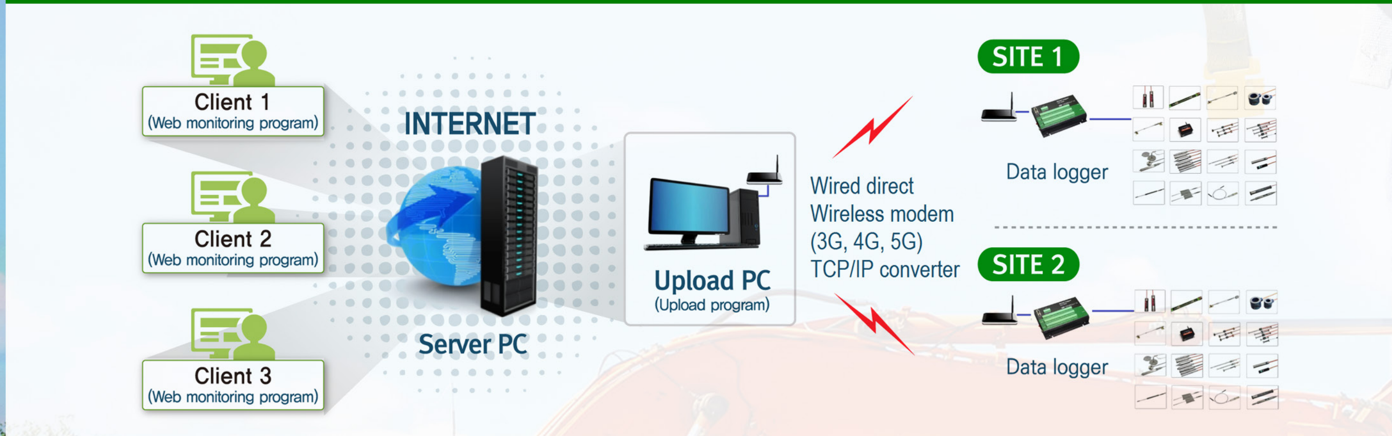

Sales company

Tecnilab Portugal, S.A.
A: Rua Gregorio Lopes, Lote 1512B 1449-041 Lisboa Portugal
T: +351 217 220 870 F: +351 217 264 550
www.tecnilab.pt

Manufacturer

ACE INSTRUMENT CO., LTD.
The first value in Geotechnical & Structural Instrumentation
A: 9, Dangjung-ro 27 beon-gil, Gunpo-si, Gyeonggi-do, Korea
T: +82 31 459 8753-7 F: +82 31 459 8758 E: acens@naver.com
www.aceinstrument.com

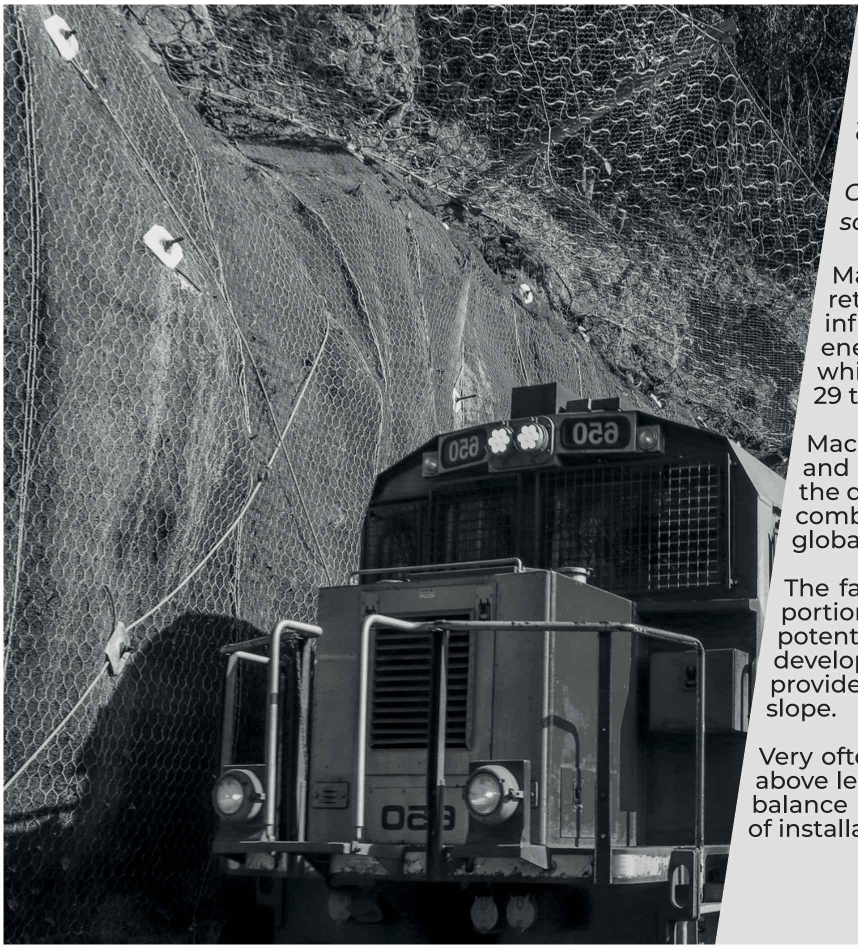


JET SJ
The Ground is our Challenge
MAIN ACTIVITY AREAS
Consultancy, Supervision and Training
· Earth Retaining Structures
· Special Foundations
· Ground Improvement
· Foundations Strengthening and Underpinning
· Façades Retention
· Tunnels and Underground Structures
· Slope Stability
· Geological and Geotechnical Investigation
· Demolition
www.jetsj.com
Tool Plazas P2 and P3
Santa Catarina, Brazil
Mining Shaft
Kamsar, Guiné
Lisbon Municipality Central Library and Archive
Lisboa, Portugal
Solar Santana Building
Lisboa, Portugal
Main Office
Rua Julieta Ferrão, 12 - Office 1501
1600-131 LISBOA, Portugal
Phone.: [+351] 210 505 150 / 51
Email: info@jetsj.com
www.linkedin.com/company/jetsj-geotecnia-lda/

Guide for Authors

Soils and Rocks is an international scientific journal published by the Brazilian Association for Soil Mechanics and Geotechnical Engineering (ABMS) and by the Portuguese Geotechnical Society (SPG). The aim of the journal is to publish original papers on all branches of Geotechnical Engineering. Each manuscript is subjected to a single-blind peer-review process. The journal's policy of screening for plagiarism includes the use of a plagiarism checker on all submitted manuscripts.

Soils and Rocks embraces the international Open Science program and is striving to meet all the recommendations. However, at this moment, the journal is not yet accepting preprints and open data, and has not adopted open peer reviews.

Soils and Rocks provides a manuscript template available at the journal's website.

1. Category of papers

Submissions are classified into one of the following categories:

Article – an extensive and conclusive dissertation about a geotechnical topic, presenting original findings.
Technical Note – presents a study of smaller scope or results of ongoing studies, comprising partial results and/or particular aspects of the investigation.
Case Study – report innovative ways to solve problems associated with design and construction of geotechnical projects. It also presents studies of the performance of existing structures.
Review Article – a summary of the State-of-the-Art or State-of-the-Practice on a particular subject or issue and represents an overview of recent developments.
Discussion – specific discussions about published papers.

Authors are responsible for selecting the correct category when submitting their manuscript. However, the manuscript category may be altered based on the recommendation of the Editorial Board. Authors are also requested to state the category of paper in their Cover Letter.

When submitting a manuscript for review, the authors should indicate the category of the manuscript, and is also understood that they:

a) assume full responsibility for the contents and accuracy of the information in the paper;
b) assure that the paper has not been previously published, and is not being submitted to any other journal for publication.

2. Paper length

Full-length manuscripts (Article, Case Study) should be between 4,000 and 8,000 words. Review articles should have up to 10,000 words. Technical Notes have a word count limit of 3,500 words. Discussions have a word count limit of 1,000 words. These word count limits exclude the title page, notation list (e.g., symbols, abbreviations), captions of tables and figures, acknowledgments and references. Each single column and double column figure or table is considered as equivalent to 150 and 300 words, respectively.

3. Scientific style

The manuscripts should be written in UK or US English, in the third person and all spelling should be checked in accordance with a major English Dictionary. The manuscript should be able to be readily understood by a Civil Engineer and avoid colloquialisms. Unless essential to the comprehension of the manuscript, direct reference to the names of persons, organizations, products or services is not allowed. Flattery or derogatory remarks about any person or organization should not be included.

The author(s) of Discussion Papers should refer to himself (herself/themselves) as the reader(s) and to the author(s) of the paper as the author(s).

The International System (SI) units must be used. The symbols are recommended to be in accordance with Lexicon in 14 Languages, ISSMFE (2013) and the ISRM List of Symbols. Use italics for single letters that denote mathematical constants, variables, and unknown quantities, either in tables or in the text.

4. Submission requirements and contents

A submission implies that the following conditions are met:

- the authors assume full responsibility for the contents and accuracy of the information presented in the paper;
- the manuscript contents have not been published previously, except as a lecture or academic thesis;
- the manuscript is not under consideration for publication elsewhere;
- the manuscript is approved by all authors;
- the manuscript is approved by the necessary authorities, when applicable, such as ethics committees and institutions that may hold intellectual property on contents presented in the manuscript;
- the authors have obtained authorization from the copyright holder for any reproduced material;
- the authors are aware that the manuscript will be subjected to plagiarism check.

The author(s) must upload two digital files of the manuscript to the Soils and Rocks submission system. The size limit for each submission file is 20 MB. The manuscript should be submitted in docx format (Word 2007 or higher) or doc format (for older Word versions). An additional PDF format file of the manuscript is also required upon submission. Currently, the journal is not accepting manuscripts prepared using LaTeX.

The following documents are required as minimum for submission:

- cover letter;
- manuscript with figures and tables embedded in the text (doc or docx format);

manuscript with figures and tables embedded in the text for revision (PDF format);

- permission for re-use of previously published material when applicable, unless the author/owner has made explicit that the image is freely available.

4.1 Cover letter

The cover letter should include: manuscript title, submission type, authorship information, statement of key findings and work novelty, and related previous publications if applicable.

4.2 Title page

The title page is the first page of the manuscript and must include:

- A concise and informative title of the paper. Avoid abbreviations, acronyms or formulae. Discussion Papers should contain the title of the paper under discussion. Only the first letter of the first word should be capitalized.
- Full name(s) of the author(s). The first name(s) should not be abbreviated. The authors are allowed to abbreviate middle name(s).
- The corresponding author should be identified by a pound sign # beside his/her and in a footnote.
- The affiliation(s) of the author(s), should follow the format: Institution, (Department), City, (State), Country.
- Affiliation address and e-mail must appear below each author's name.
- The 16-digit ORCID of the author(s) – mandatory
- Main text word count (excluding abstract and references) and the number of figures and tables

4.3 Permissions

Figures, tables or text passages previously published elsewhere may be reproduced under permission from the copyright owner(s) for both the print and online format. The authors are required to provide evidence that such permission has been granted at the moment of paper submission.

4.4 Declaration of interest

Authors are required to disclose conflicting interests that could inappropriately bias their work. For that end, a section entitled "Declaration of interest" should be included following any acknowledgments and prior to the "Authors' contributions" section. In case of the absence of conflicting interests, the authors should still include a declaration of interest.

4.5 Authors' contributions

Authors are required to include an author statement outlining their individual contributions to the paper according to the CASRAI CRediT roles (as per https://casrai.org/credit). The minimum requirements of contribution to the work for recognition of authorship are: a) Participate actively in the discussion of results; b) Review and approval of the final version of the manuscript. A section entitled "Authors' contributions" should be included after the declaration of interest section, and should be formatted with author's name and CRediT role(s), according to the example:

Samuel Zheng: conceptualization, methodology, validation. Olivia Prakash: data curation, writing - original draft preparation. Fatima Wang: investigation, validation. Kwame Bankole: supervision. Sun Qi: writing - reviewing and editing.

Do not include credit items that do not follow the Taxonomy established by CASRAI CRediT roles.

The authors' contributions section should be omitted in manuscripts that have a single author.

5. Plagiarism checking

Submitted papers are expected to contain at least 50 % new content and the remaining 50 % should not be verbatim to previously published work.

All manuscripts are screened for similarities. Currently, the Editorial Board uses the plagiarism checker Plagius (www.plagius.com) to compare submitted papers to already published works. Manuscripts will be rejected if more than 20 % of content matches previously published work, including self-plagiarism. The decision to reject will be under the Editors' discretion if the percentage is between 10 % and 20 %.

IMPORTANT OBSERVATION: Mendeley software plug-in (suggested in this guide) for MS-Word can be used to include the references in the manuscript. This plug-in uses a field code that sometimes includes automatically both title and abstract of the reference. Unfortunately, the similarity software adopted by the Journal (Plagius) recognizes the title and abstract as an actual written text by the field code of the reference and consequently increases considerably the percentage of similarity. Please do make sure to remove the abstract (if existing) inside Mendeley section where the adopted reference is included. This issue has mistakenly caused biased results in the past. The Editorial Board of the journal is now aware of this tendentious feature.

6. Formatting instructions

The text must be presented in a single column, using ISO A4 page size, left, right, top, and bottom margins of 25 mm, Times New Roman 12 font, and line spacing of 1.5. All lines and pages should be numbered.

The text should avoid unnecessary italic and bold words and letters, as well as too many acronyms. Authors should avoid to capitalize words and whenever possible to use tables with distinct font size and style of the regular text.

Figures, tables and equations should be numbered in the sequence that they are mentioned in the text.

Abstract

Please provide an abstract between 150 and 250 words in length. Abbreviations or acronyms should be avoided. The abstract should state briefly the purpose of the work, the main results and major conclusions or key findings.

Keywords

A minimum of three and a maximum of six keywords must be included after the abstract. The keywords must represent the content of the paper. Keywords offer an opportunity to include synonyms for terms that are frequently referred to in the literature using more than one term. Adequate keywords maximize the visibility of your published paper.

Examples:

Poor keywords – piles; dams; numerical modeling; laboratory testing

Better keywords – friction piles; concrete-faced rockfill dams; material point method; bender element test

List of symbols

A list of symbols and definitions used in the text must be included before the References section. Any mathematical constant, variable or unknown quantity should appear in italics.

6.1 Citations

References to other published sources must be made in the text by the last name(s) of the author(s), followed by the year of publication. Examples:

- Narrative citation: […] while Silva & Pereira (1987) observed that resistance depended on soil density
- Parenthetical citation: It was observed that resistance depended on soil density (Silva & Pereira, 1987).

In the case of three or more authors, the reduced format must be used, e.g.: Silva et al. (1982) or (Silva et al., 1982). Do not italicize "et al."

Two or more citations belonging to the same author(s) and published in the same year are to be distinguished with small letters, e.g.: (Silva, 1975a, b, c.).

Standards must be cited in the text by the initials of the entity and the year of publication, e.g.: ABNT (1996), ASTM (2003).

6.2 References

A customized style for the Mendeley software is available and may be downloaded from this link.

Full references must be listed alphabetically at the end of the text by the first author's last name. Several references belonging to the same author must be cited chronologically.

Some formatting examples are presented here:

Journal Article

Bishop, A.W., & Blight, G.E. (1963). Some aspects of effective stress in saturated and partly saturated soils. *Géotechnique*, 13(2), 177-197. https://doi.org/10.1680/geot.1963.13.3.177

Castellanza, R., & Nova, R. (2004). Oedometric tests on artificially weathered carbonatic soft rocks. *Journal of Geotechnical and Geoenvironmental Engineering*, 130(7), 728-739. https://doi.org/10.1061/(ASCE)1090-0241(2004)130:7(728)

Fletcher, G. (1965). Standard penetration test: its uses and abuses. Journal of the Soil Mechanics Foundation Division, 91, 67-75.

Indraratna, B., Kumara, C., Zhu S-P., Sloan, S. (2015). Mathematical modeling and experimental verification of fluid flow through deformable rough rock joints. *International Journal of Geomechanics*, 15(4): 04014065-1-04014065-11. https://doi.org/10.1061/(ASCE)GM.1943-5622.0000413

Garnier, J., Gaudin, C., Springman, S.M., Culligan, P.J., Goodings, D., Konig, D., ... & Thorel, L. (2007). Catalogue of scaling laws and similitude questions in geotechnical centrifuge modelling. *International Journal of Physical Modelling in Geotechnics*, 7(3), 01-23. https://doi.org/10.1680/ijpmg.2007.070301

Bicalho, K.V., Gramelich, J.C., & Santos, C.L.C. (2014). Comparação entre os valores de limite de liquidez obtidos pelo método de Casagrande e cone para solos argilosos brasileiros. *Comunicações Geológicas*, 101(3), 1097-1099 (in Portuguese).

Book

Lambe, T.W., & Whitman, R.V. (1979). *Soil Mechanics, SI version*. John Wiley & Sons.

Das, B.M. (2012). *Fundamentos de Engenharia Geotécnica*. Cengage Learning (in Portuguese).

Head, K.H. (2006). *Manual of Soil Laboratory Testing - Volume 1*: Soil Classification and Compaction Tests. Whittles Publishing.

Bhering, S.B., Santos, H.G., Manzatto, C.V., Bognola, I., Fasolo, P.J., Carvalho, A.P., ... & Curcio, G.R. (2007). *Mapa de solos do estado do Paraná*. Embrapa (in Portuguese).

Book Section

Yerro, A., & Rohe, A. (2019). Fundamentals of the Material Point Method. In *The Material Point Method for Geotechnical Engineering* (pp. 23-55). CRC Press. https://doi.org/10.1201/9780429028090

Sharma, H.D., Dukes, M.T., & Olsen, D.M. (1990). Field measurements of dynamic moduli and Poisson´s ratios of refuse and underlying soils at a landfill site. In *Geotechnics of Waste Fills - Theory and Practice* (pp. 57-70). ASTM International. https://doi.org/10.1520/STP1070-EB

Cavalcante, A.L.B., Borges, L.P.F., & Camapum de Carvalho, J. (2015). Tomografias computadorizadas e análises numéricas aplicadas à caracterização da estrutura porosa de solos não saturados. In *Solos Não Saturados no Contexto Geotécnico* (pp. 531-553). ABMS (in Portuguese).

Proceedings

Jamiolkowski, M.; Ladd, C.C.; Germaine, J.T., & Lancellotta, R. (1985). New developments in field and laboratory testing of soils. *Proc. 11th International Conference on Soil Mechanics and Foundation Engineering,* San Francisco, August 1985. Vol. 1, Balkema, 57-153.

Massey, J.B., Irfan, T.Y. & Cipullo, A. (1989). The characterization of granitic saprolitic soils. *Proc. 12th International Conference on Soil Mechanics and Foundation Engineering*, Rio de Janeiro. Vol. 6, Publications Committee of XII ICSMFE, 533-542.

Indraratna, B., Oliveira D.A.F., & Jayanathan, M. (2008b). Revised shear strength model for infilled rock joints considering overconsolidation effect. *Proc. 1st Southern Hemisphere International Rock Mechanics Symposium*, Perth. ACG, 16-19.

Barreto, T.M., Repsold, L.L., & Casagrande, M.D.T. (2018). Melhoramento de solos arenosos com polímeros. *Proc. 19º Congresso Brasileiro de Mecânica dos Solos e Engenharia Geotécnica*, Salvador. Vol. 2, ABMS, CBMR, ISRM & SPG, 1-11 (in Portuguese).

Thesis

Lee, K.L. (1965). *Triaxial compressive strength of saturated sands under seismic loading conditions* [Unpublished doctoral dissertation]. University of California at Berkeley.

Chow, F.C. (1997). *Investigations into the behaviour of displacement pile for offshore foundations* [Doctoral thesis, Imperial College London]. Imperial College London's repository. https://spiral.imperial.ac.uk/handle/10044/1/7894

Araki, M.S. (1997). *Aspectos relativos às propriedades dos solos porosos colapsíveis do Distrito Federal* [Unpublished master's dissertation]. University of Brasília (in Portuguese).

Sotomayor, J.M.G. (2018). *Evaluation of drained and non-drained mechanical behavior of iron and gold mine tailings reinforced with polypropylene fibers* [Doctoral thesis, Pontifical Catholic University of Rio de Janeiro]. Pontifical Catholic University of Rio de Janeiro's repository (in Portuguese). https://doi.org/10.17771/PUCRio.acad.36102*

* *official title in English should be used when available in the document.*

Report

ASTM D7928-17. (2017). Standard Test Method for Particle-Size Distribution (Gradation) of Fine-Grained Soils Using the Sedimentation (Hydrometer) Analysis. *ASTM International, West Conshohocken, PA.* https://doi.org/10.1520/D7928-17

ABNT NBR 10005. (2004). Procedure for obtention leaching extract of solid wastes. *ABNT - Associação Brasileira de Normas Técnicas*, Rio de Janeiro, RJ (in Portuguese).

DNIT. (2010). Pavimentação - Base de solo-cimento - Especificação de serviço DNIT 143. *DNIT -Departamento Nacional de Infraestrutura de Transportes*, Rio de Janeiro, RJ (in Portuguese).

USACE (1970). Engineering and Design: Stability of Earth and Rock-Fill Dams, Engineering Manual 1110-2-1902. Corps of Engineers, Washington, D.C.

Web Page

Soils and Rocks. (2020). *Guide for Authors*. Soils and Rocks. Retrieved in September 16, 2020, from http://www.soilsandrocks.com/

6.3 Artworks and illustrations

Each figure should be submitted as a high-resolution image, according to the following mandatory requirements:

- Figures must be created as a TIFF file format using LZW compression with minimum resolution of 500 dpi.
- Size the figures according to their final intended size. Single-column figures should have a width of up to 82 mm. Double-column figures should have a maximum width of 170 mm.
- Use Times New Roman for figure lettering. Use lettering sized 8-10 pt. for the final figure size.
- Lines should have 0.5 pt. minimum width in drawings.
- Titles or captions should not be included inside the figure itself.

Figures must be embedded in the text near the position where they are first cited. Cite figures in the manuscript in consecutive numerical order. Denote figure parts by lowercase letters (a, b, c, etc.). Please include a reference citation at the end of the figure caption for previously published material. Authorization from the copyright holder must be provided upon submission for any reproduced material.

Figure captions must be placed below the figure and start with the term "Figure" followed by the figure number and a period. Example:

Figure 1. Shear strength envelope.

Do not abbreviate "Figure" when making cross-references to figures.

All figures are published in color for the electronic version of the journal; however, the print version uses grayscale. Please format figures so that they are adequate even when printed in grayscale.

Accessibility: Please make sure that all figures have descriptive captions (text-to-speech software or a text-to-Braille hardware could be used by blind users). Prefer using patterns (e.g., different symbols for dispersion plot) rather than (or in addition to) colors for conveying information (then the visual elements can be distinguished by colorblind users). Any figure lettering should have a contrast ratio of at least 4.5:1

Improving the color accessibility for the printed version and for colorblind readers: Authors are encouraged to use color figures because they will be published in their original form in the online version. However, authors must consider the need to make their color figures accessible for reviewers and readers that are colorblind. As a general rule of thumb, authors should avoid using red and green simultaneously. Red should be replaced by magenta, vermillion, or orange. Green should be replaced by an off-green color, such as blue-green. Authors should prioritize the use of black, gray, and varying tones of blue and yellow.

These rules of thumb serve as general orientations, but authors must consider that there are multiple types of color blindness, affecting the perception of different colors. Ideally, authors should make use of the following resources: 1) for more information on how to prepare color figures, visit https://jfly.uni-koeln.de/; 2) a freeware software available at http://www.vischeck.com/ is offered by Vischeck, to show how your figures would be perceived by the colorblind.

6.4 Tables

Tables should be presented as a MS Word table with data inserted consistently in separate cells. Place tables in the text near the position where they are first cited. Tables should be numbered consecutively using Arabic numerals and have a caption consisting of the table number and a brief title. Tables should always be cited in the text. Any previously published material should be identified by giving the original source as a reference at the end of the table caption. Additional comments can be placed as footnotes, indicated by superscript lower-case letters.

When applicable, the units should come right below the corresponding column heading. Horizontal lines should be used at the top and bottom of the table and to separate the headings row. Vertical lines should not be used.

Table captions must be placed above the table and start with the term “Table” followed by the table number and a period. Example:

Table 1. Soil properties.

Do not abbreviate “Table” when making cross-references to tables. Sample:

Table 1. Soil properties

Parameter	Symbol	Value
Specific gravity of the sand particles	G_s	2.64
Maximum dry density (Mg/m^3)	$\rho_{d(max)}$	1.554
Minimum dry density (Mg/m^3)	$\rho_{d(min)}$	1.186
Average grain-size (mm)	d_{50}	0.17
Coefficient of uniformity	C_u	1.97

6.5 Mathematical equations

Equations must be submitted as editable text, created using MathType or the built-in equation editor in MS Word. All variables must be presented in italics.

Equations must appear isolated in a single line of the text. Numbers identifying equations must be flushed with the right margin. International System (SI) units must be used. The definitions of the symbols used in the equations must appear in the List of Symbols.

Do not abbreviate “Equation” when making cross-references to an equation.